UNIVERSITÀ
DEGLI STUDI
DI PADOVA

Sede Amministrativa: Università degli Studi di Padova

Dipartimento di Ingegneria Idraulica, Marittima, Ambientale e Geotecnica

SCUOLA DI DOTTORATO DI RICERCA IN Scienze dell'Ingegneria
Civile ed Ambientale

CICLO XXIII

THE CARDIOVASCULAR SYSTEM: A NUMERICAL STUDY

Direttore della scuola: Ch.mo Prof. Stefano Lanzoni
Supervisori: Ing. Francesca MAria Susin
Ch.mo Prof. Mario Putti
Ch.mo Prof. Stefano Lanzoni

Dottorando: Cesare Corrado

Abstract

The aim of this thesis concerns the mathematical and numerical study of the cardiovascular system. This work covers the three related main branches of study, dealing with artery modeling, valves modeling and heart modeling. The work is thus subdivided into three parts, each one dealing with a specific branch. In each part this work starts by a specific known in literature problem and suggests original improvements aimed at obtaining a more accurate solution and/or a cheaper computational cost.

In the first part a new one dimensional model for the compliant vessels is proposed, capable of reproducing also the effects related to the fluid-structure interaction which are loosed by the classical models present in literature. In particular it is show that with a cheaper modification it is possible to reproduce also in a one dimensional model the so called added mass effect, an effect related to the multidimensionality of the flow field as concerns the flows into compliant pipes. In the same parts an analytical solution for the unsteady motion in an undefined rigid pipe is proposed, taking into account of the transitory effects. As far as the pulsating flow is concerned, the reference solution classically adopted in literature is represented by the Womersley one. Even though accurate, this latter allows the only study of the motion when the flow is fully developed; conversely it is not capable of reproducing what happens, for example, immediately after a sudden pressure drop. In this work a new solution capable of reproducing also the motion when not fully developed is proposed. As far as applications is concerned, two particular cases are studied: the starting of an extra-corporeal device (fluid initially at rest) and a double variation of pressure (non-homogeneous initial conditions), consisting of a sudden drop followed by a sudden raise (i. e., this is what happens during a fainting).

In the second part a stability estimate concerning the immersed finite elements method is reported. Up to now, in literature the structural description is performed through linear piecewise continuous polynomial; in this work a new estimation is performed for a structural description performed by piecewise continuous polynomial of an arbitrary order, clearly comprehensive of the linear case. Moreover, for the implicit case only, it is demonstrated that a stability limit from below exists for the time step size; even though not determinable. Numerical examples will enforce the results obtained. A comparison between the ALE and the IFEM schemes is also performed for the simulation of an immersed structure. The results show that whenever the ALE computational cost increases proportionally to the structure displacement (as a consequence of the fluid mesh distortion), the IFEM formulation does not depend on structure displacement.

The third part deals with the heart electro-mechanical coupling. The heart electrical activity is typically reproduced through the data obtained by the electro-cardiogram, a non-invasive medical device furnishing the graphical representation in time of the extracellular potential differences between different body locations. Up to now the study of the heart activity was performed by treating independently the electro-physiology and the mechanics, i.e. without considering a feedback between them. In this work the solution is determined by considering the electro-mechanical feedback, arising a non-linear fully coupled problem, being both solutions (electro physiology and mechanics) depending on each other. As a results a changing in the heart conductivity is present, affecting the electro-cardiogram graph in some terminations. Moreover different distributions between the problem solved with feedback and the one solved without for both the trans-membrane and the extracellular potentials are present.

Riassunto

Lo scopo di questa tesi riguarda lo studio di matematico e numerico del sistema cardiovascolare. Questo lavoro comprende i tre rami principali correlati allo studio del sistema cardiovascolare, riguardanti la modellazione delle arterie, la modellazione valvole cardiache e la modellazione dell'elettromeccanica cardiaca. Il lavoro è suddiviso in tre parti, ognuna delle quali tratta un ramo specifico. In ogni parte questo lavoro il punto di partenza è rappresentato da un problema specifico e noto in letteratura; vengono quindi suggerite soluzioni originali finalizzate ad ottenere una soluzione più accurata e / o con un costo computazionale più conveniente.

Nella prima parte viene proposto un nuovo modello monodimensionale per le arterie, in grado di riprodurre anche gli effetti legati all'interazione fluido-struttura, non presenti nei modelli classici presenti in letteratura. In particolare, si dimostra che con una modifica molto economica in termini computazionali è possibile riprodurre anche in un modello unidimensionale il cosiddetto effetto massa aggiunta, un effetto legato alla multidimensionalità del campo di moto quando si ha a che fare con condotti deformabili. Viene inoltre proposta una soluzione analitica per il moto a transitorio del flusso in un condotto rigido di lunghezza indefinita. Per quanto riguarda i flussi a regime periodico, la soluzione classica di riferimento adottata in letteratura è rappresentata dal flusso alla Womersley. Anche se precisa, quest'ultima consente solamente lo studio del moto quando il flusso è completamente sviluppato; al contrario, non è in grado di riprodurre ciò che accade, per esempio, subito dopo una variazione improvvisa di pressione. In questa tesi viene proposta una soluzione in grado di riprodurre anche il moto quando non è pienamente sviluppato. Dal punto di vista applicativo vengono studiati due casi particolari: l'avvio di un dispositivo di circolazione extra-corporea (fluido inizialmente a riposo) e una doppia variazione di pressione (condizioni iniziali non omogenee), costituita da un calo improvviso di pressione seguito da un ristabilirsi della pressione iniziale, come accade nei casi di svenimento.

Nella seconda parte si determina una stima della stabilità relativamente al metodo degli elementi finiti immersi. Fino ad oggi, in letteratura la descrizione strutturale viene eseguita tramite polinomi continui lineari a tratti; in questo lavoro una nuova stima viene effettuata quando la struttura sia descritta da polinomi continui a tratti di ordine arbitrario, stima che chiaramente comprende come caso particolare quello dei polinomi lineari. Inoltre per il solo caso implicito, si dimostra che esiste anche un limite inferiore, anche se non determinabile esplicitamente, per l'incremento temporale, per avere stabilità dello schema numerico. Degli esempi numerici mostrano l'attendibilità dei risultati ottenuti. Si presenta inoltre un confronto fra i metodi ALE e IFEM per il caso della simulazione di una struttura immersa, come potrebbe essere una valvola cardiaca. I risultati hanno evidenziato che lo schema ALE presenta un costo di calcolo (in termini di sotto-iterazioni necessarie per arrivare a convergenza) proporzionale allo spostamento della struttura (come conseguenza della distorsione della griglia su cui viene risolto il moto del fluido), mentre la formulazione IFEM ne rimane indipendente.

La terza parte si occupa dell'accoppiamento elettromeccanico dell'attività cardiaca. L'attività elettrica cardiaca viene in genere analizzata attraverso i dati ottenuti dalla elettro-cardiogramma, un dispositivo medico non invasivo capace di rappresentare graficamente l'andamento nel tempo delle differenze di potenziale extracellulare sussistente tra differenti posizioni del corpo. Fino ad oggi lo studio della attività cardiaca è stato effettuato trattando in maniera indipendente l'elettro-fisiologia e la meccanica, cioè senza considerare l'esistenza di un feedback tra di loro. In questo lavoro la soluzione viene determinata considerando il feedback elettro-meccanico, attraverso la soluzione di un problema non lineare completamente accoppiato, essendo entrambe le soluzioni (elettro fisiologia e meccanica) reciprocamente dipendenti. A causa del cambiamento del tensore conduttività, dovuto alla deformazione cardiaca, in alcune terminazioni dell'elettro-cardiogramma si riscontrano risultati differenti dal caso in cui si supponga il cuore fisso nello spazio. Inoltre, si sono riscontrate distribuzioni differenti tra il problema risolto con feedback e quello risolto senza feedback, sia per quanto concerne il potenziale trans-membranale, sia per quanto concerne il potenziale extracellulare.

Aknowledgements

D'abord, je tiens particulièrement à remercier le Dr Jean Frédéric Gerbeau pour la merveilleuse expérience dans son équipe de recherche REO et ses explications trés claires et utiles à la compréhension de l'électrophysiologie du coeur. Je tiens également à remercier le Dr Miguel Angel Fernandez et le Dr Philippe Moireau pour l 'aide précieuse dans la compréhension des codes de l'INRIA et l'élaboration d'un code numérique très efficace. Je remercie également tous les batiment 16 pour l'amitié et de gentillesse à mon égard pendant mon séjour à Paris et a eu la patience pour l'enseignement de la langue française

Voglio inoltre ringraziare il Dr. Fabrizio Tamburini della facoltà di Astronomia per i preziosi consigli nella stesura del presente lavoro e per avermi dato l'onore di leggerla con occhio critico. Last but not the least, voglio ringraziare la mia famiglia tutta (gatto ciop compreso) per il supporto datomi in questi tre anni di dottortato, a loro dedico la tesi.

Contents

Introduction

The mathematical study of the cardiovascular system represents a significant tool to study the heart and circulation pathologies, allowing the knowledge of phenomena not detectable by the classical clinical devices. As a consequence, find models recasting as accurate as possible the behavior of this complex system is a very challenging task. The whole cardiovascular system can be roughly described as a network of compliant pipes of different dimensions alimented by a volumetric pump driven by an electrical stimulus. Being this complex system composed by different spatial scale, its whole detailed description is not an affordable task; typically, a detailed study is performed on only a part of interest, while the rest of the system is approximated through spatial reduced order methods (cf. [50], [28]), representing a boundary condition for the part under study. Moreover, the interactions between different physical phenomena (as, for example, the heart electrical propagation and the heart mechanical response or the fluid-structure interactions) add complexity to the problem.

This work is aimed in investigating deeply some aspects regarding the mathematical and numerical modeling of the cardiovascular system, covering its free typical branches of study:

- The unsteady flows in pipes
- The fluid-Structure Interaction problems
- The heart Electro-Mechanics

Part I is devoted to the study of the unsteady flows in pipes and aimed in:

- finding a more accurate description of the fluid-structure interaction problems in a compliant pipe when using a monodimensional model
- studying the effects related to the transitory effects of an unsteady flow in a rigid pipe

From a practical point of view, the results of this part could be also used to determine suitable boundary conditions for problems described in detail, thus describing also the effects typically neglected by the standard simplified models.

Chapter 1 deals with the so called added mass effect, an effects depending on the fluid-structure interaction which acts as a virtual mass on the structure. For example, considering the trivial case of a spring mass dumper system which moves into an ideal fluid at rest, the equation of motion takes the following form:

$$m\ddot{X} + c\dot{X} + kX = F(t) - m_a\ddot{X}$$

where X is the body displacement, m, c, k are the mass of the body, the dump coefficient and the elastic constant of the spring, $F(t)$ is the external force which act on the body and m_a the resulting added mass. The new term $m_a\ddot{X}$ is essentially due to the fact that the body, in it's motion, "pushes" the fluid. Synthesizing, the main conditions which determine the presence of the added mass effect could be summarized as follows:

- fluid-structure interaction
- non-orthogonality of fluid and structure displacement[1]
- unsteady motion

Although this effect is always present when one deals with a fluid-structure interaction problem, it is more evident when the structure and the fluid densities are comparable, as in the arterial tissue. This is an important

---

[1] This aspect will be clarified after

haemodynamic problem: a correct treatment of added mass affects both the quality of a solution (from a modeling point of view) and the efficiency in finding it (from a numerical point of view). Owing to the nature of flow in a compliant pipe, it is important to observe that a characteristic which gives rise to an added mass effect is the non-uni-dimensionality of the motion: indeed, if this is not the case, this effect disappears, being the fluid and the structure motion orthogonal.

In this work a new one dimensional model is proposed, able to reproduce the added mass effect, even though other effects related to the fluid-structure interaction could be reproduced by the same procedure. Indeed, up to now the one dimensional models present in the literature are not able to reproduce all the effects related to a fluid-structure interaction, because in the procedure adopted to obtain them the multidimensionality of the motion is completely loosed. The key idea in reproducing all the fluid-structure interaction effects consists in recovering the radial pressure variation and the radial velocity, even though these are smaller with respect to the corresponding radial ones and treating them as properties related to the structure. This hypothesis yields the following system of equations:

$$\begin{aligned}
&\frac{\partial A}{\partial t} + \frac{\partial Q}{\partial z} = 0 \\
&\frac{\partial Q}{\partial t} + \frac{\partial}{\partial z}\left(\alpha \frac{Q^2}{A}\right) + \frac{1}{\rho}\left(A\frac{\partial P}{\partial z} + \boxed{(P - p_w)\frac{\partial A}{\partial z}}\right) + K_r \frac{Q}{A} = 0 \\
&p_w = \beta\left(\frac{\sqrt{A} - \sqrt{A_0}}{\sqrt{\pi}}\right)
\end{aligned}$$

where a new term appears, related to the pressure radial distribution; clearly one needs to introduce a suitable model determining the mean pressure P. Even though other procedures could be affordable, the one here adopted is based on the integration of a simplified form of the radial momentum equation:

$$\begin{aligned} P - p_w = & -\frac{\rho}{A}\left(\frac{1}{4\pi}\left(\frac{\partial A}{\partial t}\right)^2 - 2\pi\frac{\partial}{\partial t}\int_0^R\left(r\int_r^R v_r(r')dr'\right)dr \right. \\ & \left. + \nu\left(A\left.\frac{\partial v_r}{\partial r}\right|_{r=R} - \frac{1}{2}\frac{\partial A}{\partial t}\right)\right) \\ = & -\frac{\rho}{A}\Big(L'(A,Q)\Big) \end{aligned}$$

the radial velocity profile is determined by experimental theory as a function of the radius and the wall velocity. Note that the new model represents a general case the classical one: indeed, if one neglects the radial variations a posteriori, then $P = p_w$ and so the classical system follows. Moreover, by considering the linearized form of $L'(A,Q)$, it is possible to consider the new system of equation as the classical one, where the structure is now described by the relation:

$$P = \beta\frac{\sqrt{A} - \sqrt{A_0}}{\sqrt{\pi}} + \mathcal{M}\frac{\partial^2 A}{\partial t^2} - \gamma\frac{\partial A}{\partial t}$$

resembling to the one introduced in [27] pag. 18, except for the fact that now the coefficients of the structural model depends on the fluid-structure interaction. In particular, this latter highlights that the fluid acts as a virtual inertia on the structure, through the coefficient $\mathcal{M}$. As depicted in figure 1, the added mass effect acts on the system as an additional inertia on the arterial wall.

In chapter 2 the effects related to the transitory of an unsteady flow are analyzed, i.e. the effects related to the initial conditions, for example when a sudden variation of pressure occurs. Typically, for the pulsating flow in a rigid pipe the classical analytical solution is represented by the Womersley one. Even though good for a developed motion, this solution is inadequate to reproduce the phenomena occurring until the motion is fully developed.

In this chapter a new general solution is proposed, taking into account of the phenomena depending on the initial condition: with this new approach it is now possible to study what happens during the assessment to the new

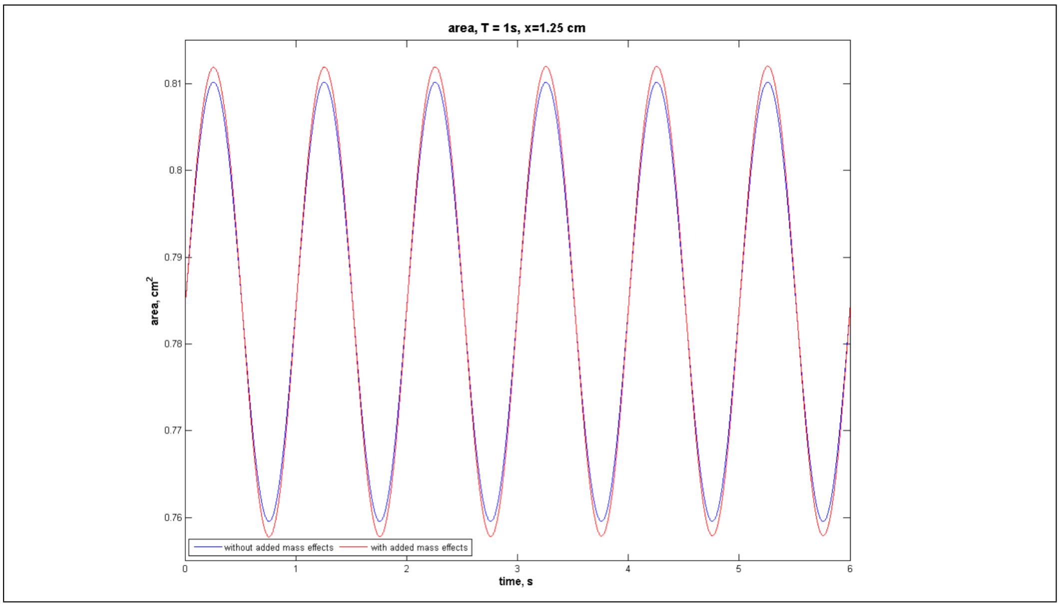

Figure 1: Comparison between area value vs time with (red line) and without (blue line) added mass effect, $T = 1\,s$

developed solution; moreover, it is possible to estimate the time needed to reach the new state of equilibrium. For a flow in an undefined rigid pipe, driven by a time-dependent pressure gradient, the system of the Navier-Stokes equations reduces to the only radial momentum:

$$\frac{\partial u_z}{\partial t} - \nu \left(\frac{\partial^2 u_z}{\partial r^2} + \frac{1}{r}\frac{\partial u_z}{\partial r} \right) = -\frac{1}{\rho}\frac{\partial p}{\partial z}$$

The general solution of which takes the form:

$$\begin{aligned} u_z &= \sum_{j=0}^{\infty} E_j e^{-\left(\frac{\gamma_j}{R_0}\right)^2 \nu t} J_0\left(\gamma_j y\right) \\ &+ \frac{A R_0^2}{2\mu}\frac{1}{i^3\alpha^2}\left[\left(1 - \frac{J_0\left(\alpha i^{3/2} y\right)}{J_0\left(\alpha i^{3/2}\right)}\right) e^{i\Omega t} - \left(1 - \frac{J_0\left(i\alpha i^{3/2} y\right)}{J_0\left(i\alpha i^{3/2}\right)}\right) e^{-i\Omega t}\right] \\ \alpha &= R_0\sqrt{\frac{\Omega}{\nu}} \\ y &= \frac{r}{R_0} \end{aligned}$$

the series of Bessel function representing the solution of the associated homogeneous axial momentum equation. Being this latter independent on the forcing therm (i.e. the right hand side), it is clear that the characteristic time scale will be independent on the pressure gradient temporal law; conversely, the effects related to the particular solution will influence the coefficient E_j of the series. In this chapter it is also demonstrated that the series totally converges on $\mathbb{R}$, so it is possible integrating the solution in the radial direction, obtaining also the flux temporal law . In the same chapter two applications are also reported:

- a flow initially at rest, representing the starting phase for an extra-corporeal circulation device
- a sudden decrease of pressure, followed by a raise to the previous value representing the flow during a fainting (cf figure 2).

In the latter case, the pressure gradient is obtained from a Fourier transformation of a set of experimental data sampled from a canine femoral artery, as described in [46].

Part II deals with the fluid-structure interaction problems when the structure is immersed in the fluid, as for the heart valves case. A fluid-structure interaction problem consists in determining the motion of two different continua, interacting each other along a portion of the common boundary. Typically the response of each continuum to external loads is not the same: fluids, for example, are governed by viscous-dissipative effects, while the solid response is mainly related to elastic-conservative effects; even though visco-elastic phenomena could be still active. Often the constitutive laws of each continuum are better described using different natural frames of reference. For example, the Eulerian framework could be used for the fluid portion while solid deformations are better described in Lagrangian coordinates. The resulting model yields a coupled system of equation; each must satisfy two conditions at the fluid-solid interface:

- fluid and solid must have the same velocity at the interface(no-slip condition, kinematic coupling);

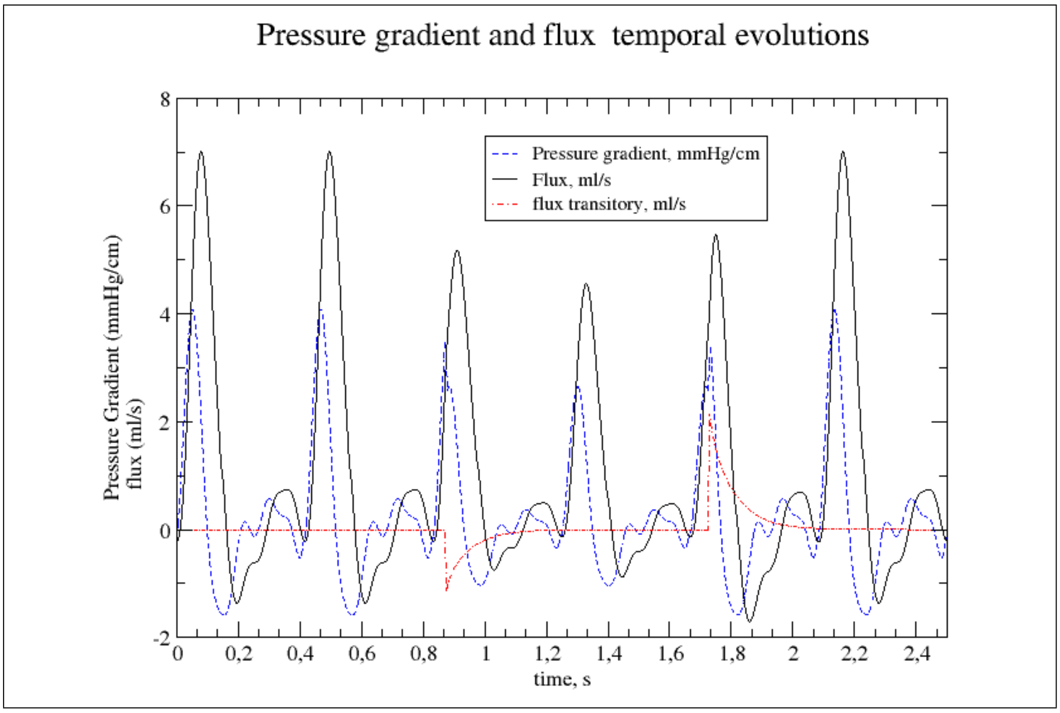

Figure 2: Pressure gradient (blue line), flux (black line) and flux transitory (red line) vs time. Pressure gradient is represented in $mmHg/cm$, while flux in ml/s.

- fluid and solid normal stresses must be mutually balanced at the interface (the action-reaction principle, dynamic coupling);

Clearly, being the displacement of the solid unknown, the fluid-structure interface is also unknown and is the shape of the fluid domain: this generates a non-linear problem that generates internal iterations when the problem is solved numerically. A second major difficulty is related to the remeshing the entire domain whenever deformations are large and the element aspect ratios become unacceptable. This can occurs at every internal iteration, leading to unsurmountable computational costs. In order to minimize these deficiency two approaches are the more viable and used:

- the Arbitrary Lagrangian Eulerian (ALE) [22, 23, 35]
- and the Immersed Finite Element (IFEM) / Immersed Boundary (IB) Method [44, 53]

A comparative description of the two approaches can be roughly summarized as follows. The former adapts the fluid domain to the solid, by rewriting the equation of the problem in a reference frame that moves by an arbitrary displacement. The latter models the solid as a source term for the fluid equations (c.f. fig. 3). A more detailed description of the ALE method could be found in chapter 3, while chapter 4 treats the IFEM method. In chapter 4 a stability estimates of the latter method is also reported. Stability analyses of the Immersed Boundary method are developed in [8, 9, 10], with extensions to the Immersed Finite Element Method described in [32]. In these works finite element spatial discretization is used in conjunction with first order finite differences in time. Two approaches are presented, both using the Backward Euler (BE) scheme to implicitly solve the fluid problem. The embedded body position is advanced in time by a Forward Euler (FE) scheme (first order extrapolation of previous data), in which case the coupled method is termed as semi-implicit (BE/FE). Otherwise, the embedded body evolution is numerically described by an implicit scheme (Backward Euler), leading to a fully implicit (BE/BE) approach. The key concept in order to obtain stability of the numerical scheme is to require that the energy of the discretized system does not increase at each time step. Time discretization by means of finite differences introduces a spurious energy term related to the truncation error. If this term is dissipative, the scheme is considered stable. Conversely if this spurious energy is larger than the energy dissipated by the

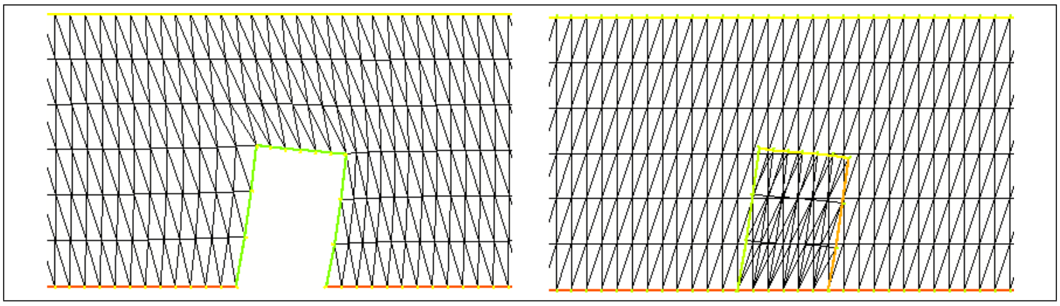

Figure 3: Comparison between ALE (right) and IFEM (left) methods with large structural displacement

fluid viscosity, the scheme becomes unstable. A fully implicit discretization is always stable, while the more efficient semi-implicit approach suffers a CFL-like stability restriction on time step size. Second order spatial discretization is often used for the fluid, in conjunction with first order discretization of the displacements of the embedded boundaries/bodies obtained by means of affine spaces. The stability analysis depends on this last assumption.

In this chapter we propose the use of higher order approximations for both the fluid and the Lagrangian finite element spaces (in particular, a $P2$ Lagrangian space) and we prove the stability of this higher order approach, developing a CFL-like stability condition for the semi-implicit approach, of the form:

$$\Delta t \leq \frac{h_x^{d-1}}{h_s^{m-2}} \frac{2\mu}{k_{max} L^n C_e^n}$$

where:

$$L^n = \max_{T_k \in \mathcal{S}_h} \left\{ \max_{\boldsymbol{s}_j, \boldsymbol{s}_i \in T_k \text{ and adjacent}} |\boldsymbol{X}_h^n(\boldsymbol{s}_j) - \boldsymbol{X}_h^n(\boldsymbol{s}_i)| \right\}$$

and C_e^n is the maximum number of mapped Lagrangian elements that touch the same Eulerian element at time $n\Delta t$. As it is possible to see by figure 4, when the CFL condition is not satisfied, the total energy of the system grows indefinitely in time.

Moreover, we show for the implicit scheme only that the difference between fluid and structure densities has an impact on the stability. After introducing some simplifications, we demonstrate only that a limitation on the minimum of the adopted time step exists, being a quantitative determination difficult to achieve. The stability estimate is performed by considering the temporal evolution of the fluid kinetic energy alone; the estimates yields:

$$\Delta t \geq -C \frac{\Delta\rho}{\mu} \frac{h_s^m}{h_f^d} \left[NTria \times (NBnode_T)^2 \right]$$

$$\Delta\rho = \rho_s - \rho_f$$

clearly, when $\Delta\rho \geq 0$ stability is always assured. Figure 5 summarizes the results for the case $\rho_s = 0$. In chapter 5 a comparison between ALE and

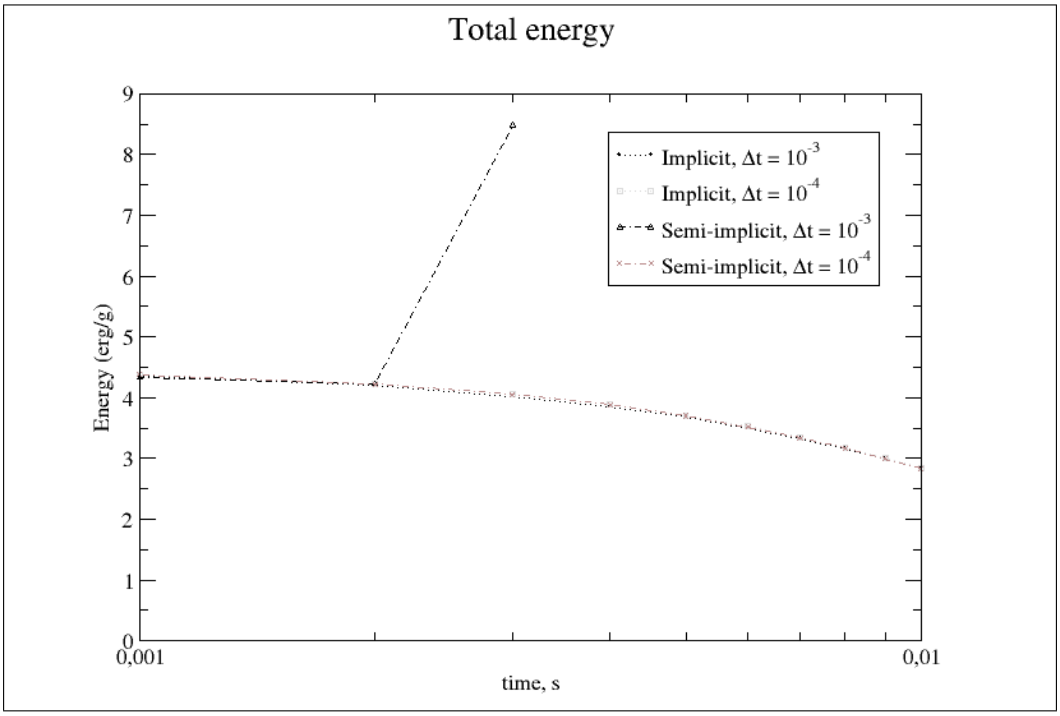

Figure 4: Total Energy temporal evolution, particular

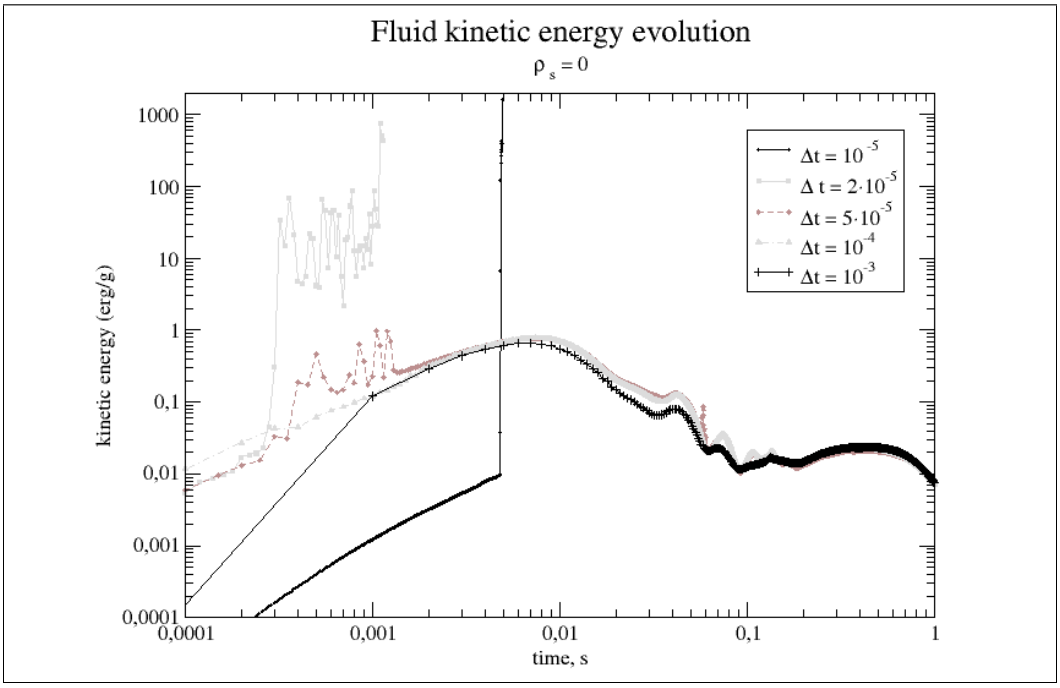

Figure 5: Fluid kinetic energy vs time

IFEM is performed, when dealing with immersed structure. As depicted in figure 6, when deformations becomes considerable, the ALE method computational cost, evaluated as a number of fixed point iterations needed for chive convergence, increases; conversely, the number of fixed point sub-iterations needed to achieve convergence for the ALE method is not affected by the deformation modulus

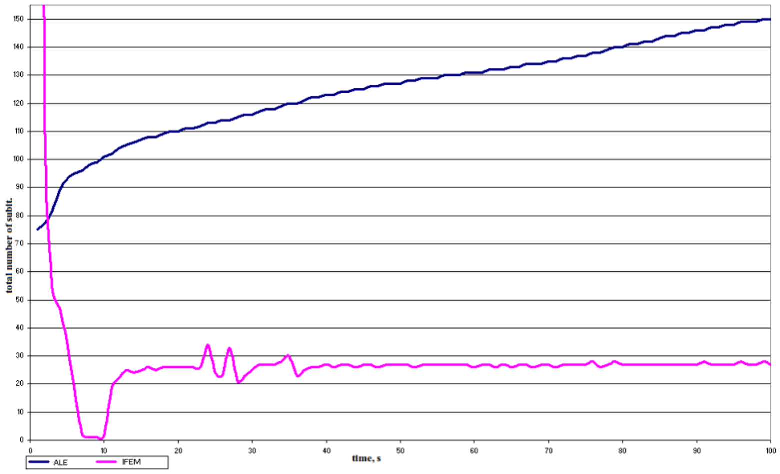

Figure 6: Number of sub-iteration for reach convergence vs time for ALE (blue line) and IFEM (magenta line)

Part III deals with heart electro-mechanics. Electro-mechanical problems have an important role in medicine, being the experimental investigation by medical devices leaking of informations. Conversely computer investigation furnishes also the informations which are not detectable by medical devices; as a consequence, computer investigation represents a significant tool in the study of heart disease, when addressed to reproduce as accurate as possible the physiology, i.e. to reproduce the same results coming from the experimental investigation.

As described in chapter 6, by the electrical point of view the heart could be described as a anisotropic conductor, being the electrical conduction greater along fiber directions, i.e. the direction of the sarcomeres, responsible of the heart contraction. Moreover, a capacity effect is also present. By the mechanical point of view, it could be described as an hyper-visco-elastic continuum, endowed of an active stiffness, driven by the electrical stimulus.

The heart electrical activity is typically reproduced through the data obtained by the electro-cardiogram, a non-invasive medical device furnishing the graphical representation in time of the extracellular potential differences between different body locations. Up to now the study of the heart activity has treated the two problems (mechanic and electro-physiology) independently, governing the active stiffness by a trans-membrane potential obtained on a fixed heart. Clearly, an electromechanical feed-back allows to obtain a solution more similar to the realistic case. The problem which arises is non-linear fully coupled, being both solutions (electro physiology and mechanics) depending on each other. By the numerical point of view, this corresponds to implementing an efficient coupling algorithm, capable of managing in an efficient manner the interaction between the two sub-problems. The heart movement has an impact on the electrocardiogram graph, being the fiber direction changed when the heart deforms. In chapter 8 an analysis on the influence of the electro-mechanical coupling on the ECG is performed. The major effect related to the electro-mechanical feed-back deals with the T wave. As depicted in fig 7 on aVF termination the wave is reversed. Moreover, in II and III the amplitude changes, while in V2 presents a larger amplitude and returns to the reference value without oscillations. The same behavior still when changing the heart frequency (as depicted in fig 8). The QRS wave is significantly modified in III, aVL, aVF and V3 terminations. In all the other terminations there are no significant modifications.

The changing of the conductivity tensor yields a different distribution for both the trans-membrane and the extracellular potentials on the heart, as depicted in 9. By the same figure, one could observe that the peak concerning the QRS wave is delayed in time when the electromechanical feedback is considered.

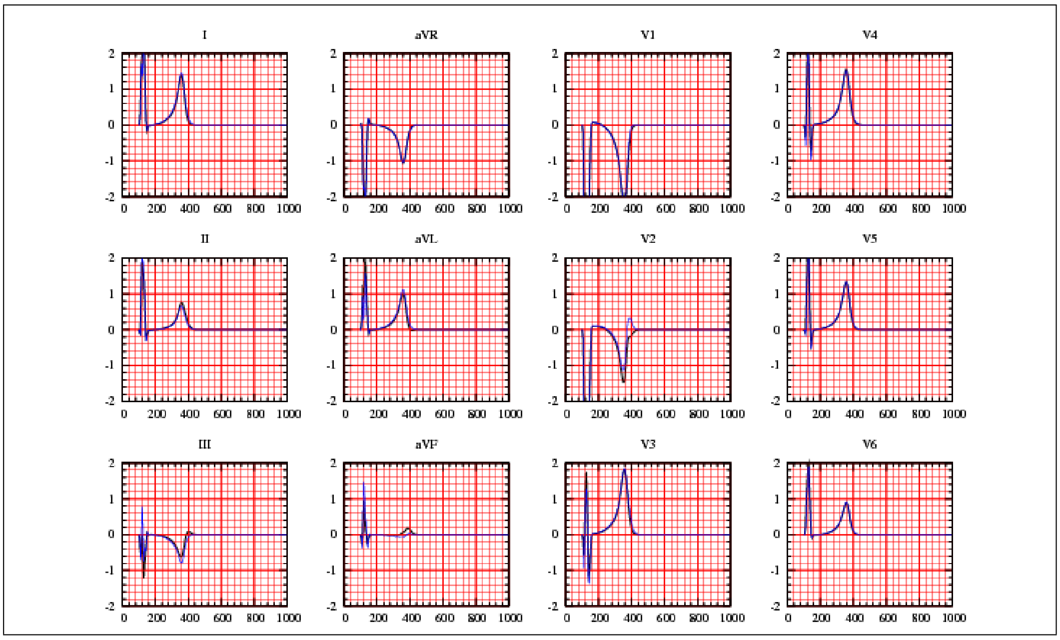

Figure 7: ECG with (black line) and without (blue line) electromechanical coupling, for a period $T = 1s$

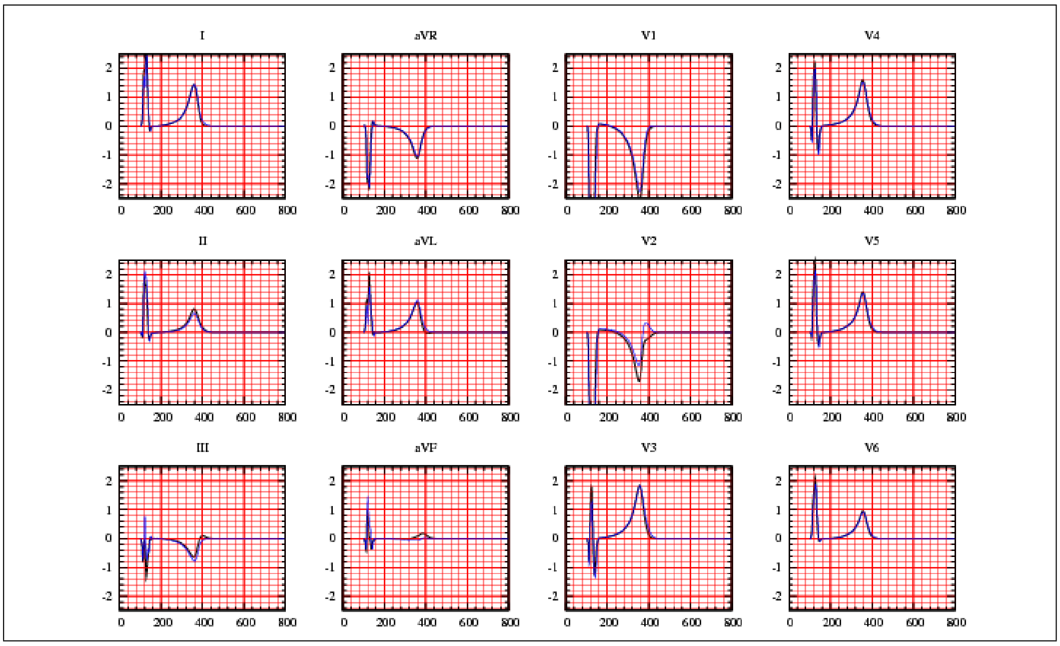

Figure 8: ECG with (black line) and without (blue line) electromechanical coupling, for a period $T = 0.8s$

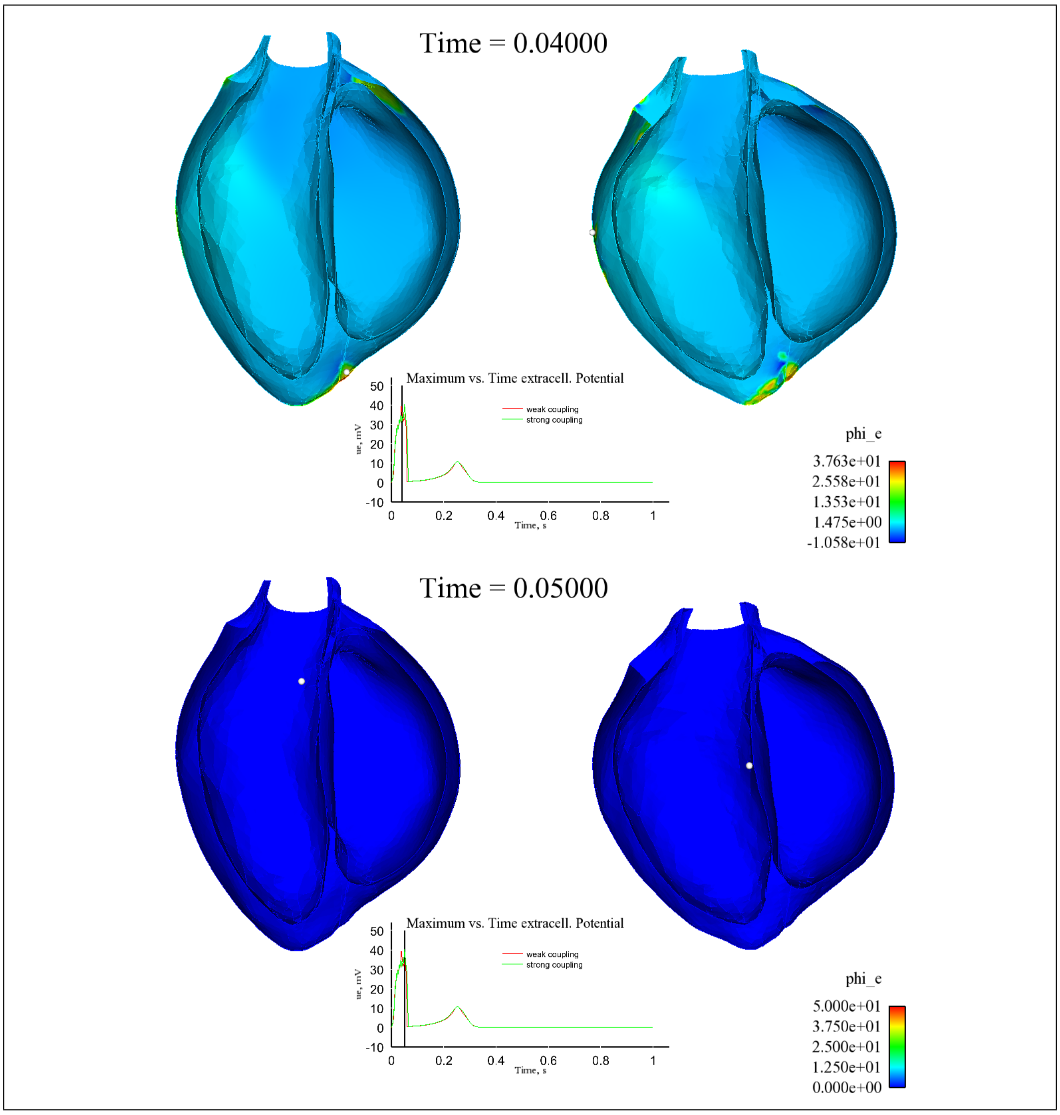

Figure 9: Extracellular potential for $t = 0.04s$ and $t = 0.05s$, with (right) and without (left) electromechanical feedback, Zygote geometry and a heart period of $T = 1.0s$. The white dot (where present) indicates the point of maximum transmembrane potential, for each time These two time values correspond to the R peak

Part I

Unsteady flows in pipes

Chapter 1

The added mass effect

1.1 Introduction

Added mass is an effect which derives from the fluid-structure interaction and determines, roughly speaking, a changement of the dynamic behavior of the structure, due to a virtual increment of its mass. Although this effect is always present when one deals with a fluid-structure interaction problem, it is more evident when the structure and the fluid densities are comparable. Synthesizing, the main conditions which determine this effect could be summarized as follows:

- fluid-structure interaction
- non-orthogonality of fluid and structure displacement[1]
- unsteady motion

Let us consider the simple case of a body attached to a spring-dumper system which moves into an ideal fluid at rest and with a density comparable to the one of the body; the fact that the body displaces a portion of fluid around it is traduced in an additional force. The equation of motion of the body

---

[1] This aspect will be clarified after

becomes:

$$m\ddot{X} + c\dot{X} + kX = F(t) - m_a\ddot{X}$$

where X is the body displacement, m, c, k are the mass of the body, the dump coefficient and the elastic constant of the spring, $F(t)$ is the external force which act on the body and m_a the resulting added mass. The new term $m_a\ddot{X}$ is essentially due to the fact that the body, in it's motion, "pushes" the fluid.

Typical examples of the added mass effect arise, when considering the problem of the interaction of a sea current with an off-shore structure, or the interaction of the water and a dam during an earthquake.

In the present thesis, I will to analyze the problem of the motion a particular fluid (the blood) in a particular compliant pipe (a vessel). This is an important haemodynamic problem: a correct treatment of added mass affects both the quality of a solution (from a modeling point of view) and the efficiency in finding it (from a numerical point of view). Owing to the nature of flow in a compliant pipe, it is important to observe that a characteristic which gives rise to an added mass effect is the non-uni-dimensionality of the motion: indeed, if this is not the case, this effect disappears, being the fluid and the structure motion orthogonal. As it is depicted in figure 1.1, the high frequency oscillations on the pressure history, which are present in the 2D axisymmetric model,disappear in the one dimensional case.

In this chapter a new one dimensional model is proposed, able to reproduce the added mass effect, even though other effects related to the fluid-structure interaction could be reproduced by the same procedure. Indeed, up to now the one dimensional model present in the literature are not able to reproduce all the effects related to a fluid-structure interaction, because in the procedure adopted to obtain them the multidimensionality of the motion is completely loosed. The key idea in reproducing all the fluid-structure interaction effects consists in recovering the radial pressure variation and the radial velocity, even though these are smaller with respect to the corresponding radial ones and treating them as properties related to the structure.

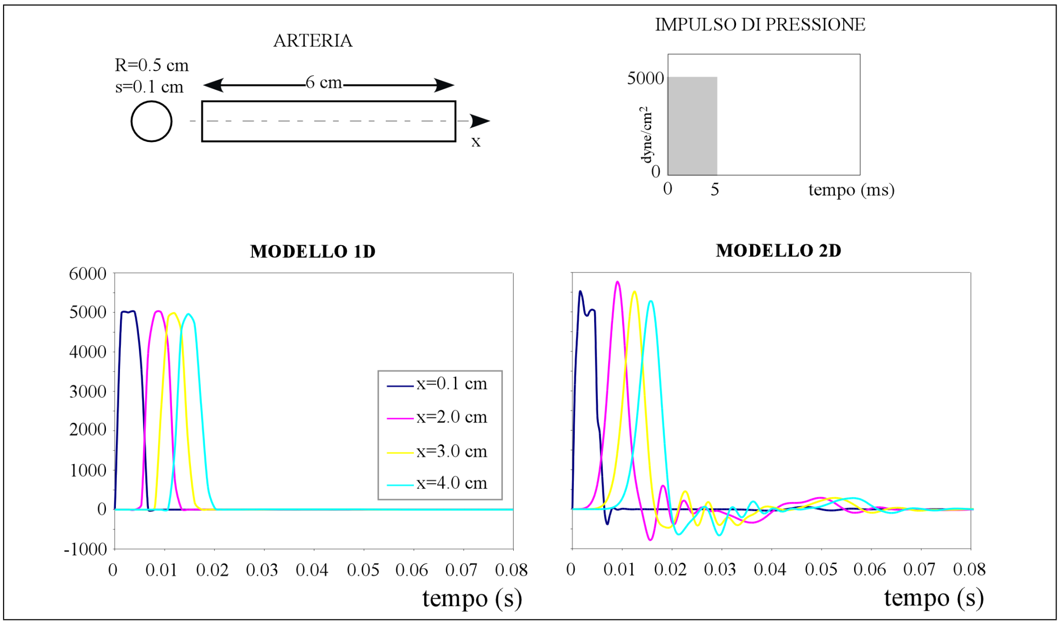

Figure 1.1: Comparison between 1D and 2D models. The pressure is plotted vs time

The procedure here adopted is based on the integration of a simplified form of the radial momentum equation, even though other procedures could be affordable.

1.2 Mathematical foundations of added mass effect in a compliant pipe

In this section, we recall the formulation described in [15], in order to explain from the mathematical point of view the added mass effect. Introducing a simplified model for both the fluid and the structure, it can be demonstrated that added mass is nothing else that a trace operator which derives from the continuity of the normal speed at the fluid-structure interface. Even though the model adopted is quite simple, the result is in a good agreement by a more complex fluid model. Equations similar to those of the simplified could be obtained by the incompressibility part of the solution which becomes by the Navier-Stokes equations after the application of the Ladizeskaya decomposition theorem. The notation of the following description is depicted if fig. 1.2

Let us consider the domain of Fig. 1.3, where Γ_f^1 and Γ_f^2 represent, respectively, the inlet and outlet fluid boundaries, Γ_f^3 represent the symmetry axis and $\Sigma = \Omega_s$ represent the interface boundary with the structure. This latter one has dimension $d-1$ with d the space dimension of the fluid domain. Let us assume a structural linear model for a cylindrical pipe of small thickness, under the assumption of membrane deformations. The reference configuration is a cylindrical surface of radius R_0 that is supposed to move only radially; moreover, let us consider the radial displacement with respect to a reference configuration R_0, namely:

$$\eta(z,t) = R(z,t) - R_0(z)$$

being z the axial coordinate. Denoting by ρ_s the structural density, h_s the structural thickness, E the Young modulus, σ the Poisson coefficient, f the external forcing term and with β the following quantity,

$$\beta = \frac{E h_s}{(1-\sigma^2) R_0^2}$$

for all time $t \in [0,T]$ the momentum equation reads:

$$\rho_s h_s \frac{\partial^2 \eta}{\partial t^2} + \beta \eta = f \qquad \text{in } [0,T] \times \Omega_s \tag{1.1}$$

$$\tag{1.2}$$

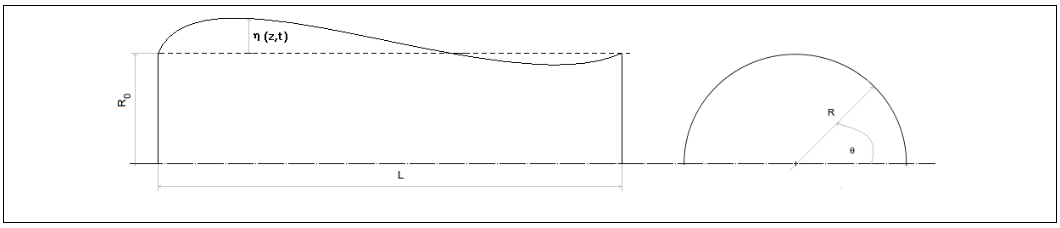

Figure 1.2: Notations

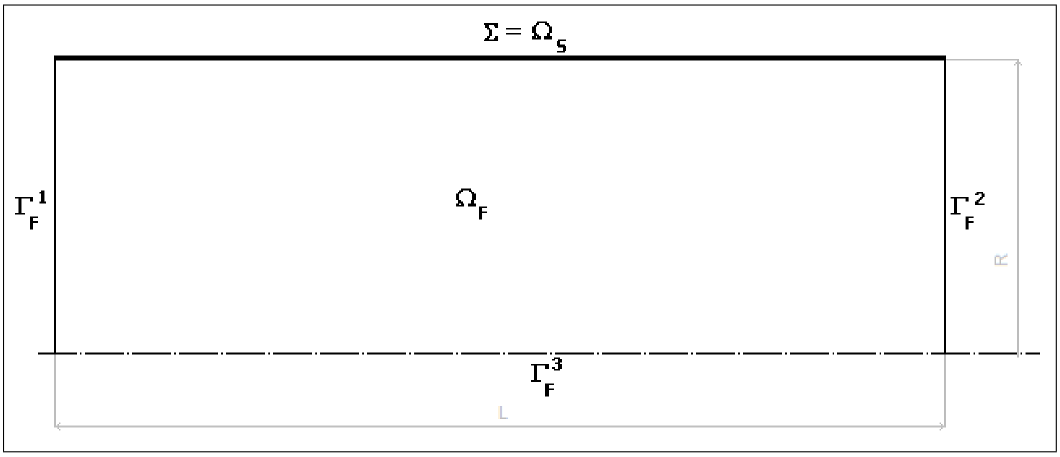

Figure 1.3: The computational domain

and is complemented by initial conditions:

$$\eta(z,0) = \eta_0(z) \qquad \text{in } \Omega_s \tag{1.3}$$

$$\frac{\partial \eta}{\partial t}(z,0) = \dot{\eta}_0(z) \qquad \text{in } \Omega_s \tag{1.4}$$

As far as the fluid is concerned, let us consider a simple ideal flow model in the pressure-velocity unknowns, which neglecting convective inertia yields:

$$\begin{array}{cl} \rho_f \frac{\partial \boldsymbol{u}}{\partial t} + \nabla p = 0 & \text{in } [0,T] \times \Omega_f \\ \nabla \cdot \boldsymbol{u} = 0 & \text{in } [0,T] \times \Omega_f \\ p = p_{in}(t) & \text{on } [0,T] \times \Gamma_f^1 \\ p = p_{out}(t) & \text{on } [0,T] \times \Gamma_f^2 \\ \boldsymbol{u} \cdot \boldsymbol{n} = 0 & \text{on } [0,T] \times \Gamma_f^3 \\ \boldsymbol{u} \cdot \boldsymbol{n} = w & \text{on } [0,T] \times \Sigma \end{array} \tag{1.5}$$

where ρ_f denotes the fluid density and p_{in}, p_{out} and w are given functions.

The problem (1.5) could be easily rewritten as follows:[2]

$$-\Delta p = 0 \qquad \text{in } [0,T]\times\Omega_f \tag{1.6}$$

$$p = p_{in}(t) \qquad \text{on } [0,T]\times\Gamma_f^1 \tag{1.7}$$

$$p = p_{out}(t) \qquad \text{on } [0,T]\times\Gamma_f^2 \tag{1.8}$$

$$\frac{\partial p}{\partial \boldsymbol{n}} = 0 \qquad \text{on } [0,T]\times\Gamma_f^3 \tag{1.9}$$

$$\frac{\partial p}{\partial \boldsymbol{n}} = -\rho_f \frac{\partial w}{\partial t} \qquad \text{on } [0,T]\times\Sigma \tag{1.10}$$

The fluid-structure coupling is then obtained by imposing the continuity of normal stress and normal velocity at the interface Σ:

$$\boldsymbol{u}\cdot\boldsymbol{n} = w = \frac{\partial \eta}{\partial t} \tag{1.11}$$

$$f = p|_{\Sigma} \tag{1.12}$$

Condition (1.10) on Σ then becomes:

$$\frac{\partial p}{\partial \boldsymbol{n}} = -\rho_f \frac{\partial^2 \eta}{\partial t^2} \tag{1.13}$$

We next consider the following functional spaces:

$$V = L^2(\Omega_s) \qquad Q = \{q \in H^1(\Omega_f)|\ q|_{\Gamma_f^1\cup\Gamma_f^2} = 0\}$$

where L^2 is the space of functions of compact support square integrable and Q is the space of the functions of compact support square integrable with their first derivatives and vanishing on the boundaries where a Dirichlet boundary condition is imposed. We also define the following inner product and bilinear forms:

$$(f,g) = \int_\Omega fg\,d\omega$$

$$a_f(p,q) = \int_{\Omega_f} \nabla p\cdot\nabla q\,d\omega_f \qquad \forall p,q\in H^1(\Omega_f)$$

$$a_s(\eta,\xi) = \int_{\Omega_s} \beta\eta\xi\,d\omega_s \qquad \forall \eta,\xi\in L^2(\Omega_s)$$

---

[2] the minus which appears in the laplacian is only for esthetic's reasons

Moreover, we make the following regularity assumptions for initial and boundary data:

$$p_{in,out} \in \mathcal{C}(0,\infty,H^{1/2}(\Gamma_f^1 \cup \Gamma_f^2)) \qquad \eta_0 \in V \qquad \frac{\partial \eta_0}{\partial t} \in V$$

The variational formulation of the problem thus becomes:

$$\begin{array}{c} a_f(p,q) = -\rho_f \int_\Sigma \frac{\partial^2 \eta}{\partial t^2} q \\ \left(\rho_s h_s \frac{\partial^2 \eta}{\partial t^2}, \xi\right) + a_S(\eta,\xi) = (p|_\Sigma, \xi) \end{array} \tag{1.14}$$

where $p|_\Sigma$ represents the restriction of p on Σ. Being the problem linear, we can apply the superposition of effects. In particular we decompose the pressure p in two parts: the first depends on all the boundary conditions except those on Σ (i.e., it vanishes on Σ); the second depends only on the boundary condition on Σ (i.e., it vanishes on $\Gamma_f^1 \cup \Gamma_f^2$). The first contribution is the solution of the following problem:[3]

$$\begin{array}{cc} -\Delta p^* = \Delta E_f \overline{p} & \text{in } \Omega_f \\ p* = 0 & \text{on } \Gamma_f^1 \cup \Gamma_f^2 \\ \frac{\partial p^*}{\partial \boldsymbol{n}} = -\frac{\partial E_f \overline{p}}{\partial \boldsymbol{n}} & \text{on } \Gamma_f^3 \\ \frac{\partial p^*}{\partial \boldsymbol{n}} = -\frac{\partial E_f \overline{p}}{\partial \boldsymbol{n}} & \text{on } \Sigma \end{array} \tag{1.15}$$

The second contribution, depending on the boundary condition on Σ is determined by considering the operator $\mathcal{R} \in Q$ which, applied to the value w of the boundary condition on Σ, gives the pressure on the whole domain Ω_f; this latter is defined by solving the following problem:

$$\begin{array}{cc} -\Delta \mathcal{R} w = 0 & \text{in } \Omega_f \\ \mathcal{R} w = 0 & \text{on } \Gamma_f^1 \cup \Gamma_f^2 \\ \frac{\partial \mathcal{R} w}{\partial \boldsymbol{n}} = 0 & \text{on } \Gamma_f^3 \\ \frac{\partial \mathcal{R} w}{\partial \boldsymbol{n}} = w & \text{on } \Sigma \end{array} \tag{1.16}$$

---

[3] because Q vanishes at the boundary, the solution p^* of the variational form should vanish too; in order to re-introduce the Dirichlet boundary conditions an arbitrary continuous extension operator $E_f \overline{p}$ is considered, which assumes the values $p_{in,out}$ on $\Gamma_f^1 \cup \Gamma_f^2$

Moreover, let us define the following trace operator:

$$\begin{aligned}&\mathcal{M}_A : H^{-1/2}(\Sigma) \to H^{1/2}(\Sigma)\\&\mathcal{M}_A w = \mathcal{R} w|_\Sigma\end{aligned}$$

which gives the value of the pressure at the boundary Σ obtained by a Neumann boundary condition on Σ.[4] Summarizing, the final pressure on the whole domain is given by:

$$p = p^* + E_F\overline{p} - \rho_f \mathcal{R}\frac{\partial^2\eta}{\partial t^2}$$

while it's restriction on Σ:

$$p|_\Sigma = p^*|_\Sigma + E_F\overline{p}|_\Sigma - \rho_f\mathcal{M}_A\frac{\partial^2\eta}{\partial t^2} = P_{ext} - \rho_f\mathcal{M}_A\frac{\partial^2\eta}{\partial t^2}$$

By relation (1.12) it is possible to re-write eq. (1.1) as follows:

$$\left(\rho_s h_s \mathcal{I} + \rho_f\mathcal{M}_A\right)\frac{\partial^2\eta}{\partial t^2} + \beta\eta = p_{ext} \tag{1.17}$$

where I is the identity operator.

It is possible to realize, with this simplified description, that the fluid acceleration influences the structure dynamic virtually increasing its mass (hence the term “added mass”). The operator $\mathcal{M}_A$ is difficult to determine, except when the domain is simple, as in our case. Recalling the results in [15], the spectrum of the added mass operator is given by the following expression:

$$\begin{aligned}&\mathcal{M}_A g = \sum_{k\geq 1} g_k \frac{L}{k\pi\tanh\left(\frac{k\pi R}{L}\right)}\sin\left(\frac{k\pi x}{L}\right)\\&g = \sum_{k\geq 1} g_k \sin\left(\frac{k\pi x}{L}\right)\end{aligned}$$

---

[4] This passage is crucial: by solving system (1.16) it is known the pressure on the whole domain, but the boundary data on Σ consists in the normal derivative of the pressure. What we need to know in order to apply the force exerted by the fluid on the structure is the value of the pressure on Σ. The operator $\mathcal{M}_A w$ gives this value.

[4] In this article a more complex structure model was considered, with an additional homogeneous boundary condition on structure displacement.

In particular, it is possible to demonstrate that the largest eigenvalue:

$$\mu_{max} = \frac{L}{\pi \tanh \frac{\pi R}{L}}$$

It is strictly related to geometrical properties, such as the ratio R/L characterizing the fluid domain.

1.3 The 1D problem: recovery of the added mass effect

In this section I introduce the mathematical 1D model for the compliant pipe in the flux-area (Q, A) unknowns. I follow the same procedure adopted in [59], except for the fact that I replace some hypotheses with other less restrictive on the radial velocity and on the pressure radial derivative. The result will be a system of three equation in four unknowns which is quite similar to the classical one. Moreover, I will show that this system could be reduced to the classical one and represents a sort of generalization. As far as the closure of the problem is concerned, I will introduce some model based on the experimental evidence which will give a well posed problem. It is however worthwhile to point out that the procedures here adopted for closing the problem is not the unique possible. The new term which appears in the momentum equation reintroduces the added mass effect, because takes into account of the variation in the radial direction of the pressure, variation which is related to the radial velocity and so to the multidimensionality of the problem.

Let us consider an axisymmetric incompressible flow field. The governing equations, written in cylindric coordinates, read:

$$\nabla \cdot \boldsymbol{v} = 0 \tag{1.18}$$

$$\frac{\partial p}{\partial z} = -\rho \left(\frac{\partial v_z}{\partial t} + \nabla \cdot (v_z \boldsymbol{v}) \right) + \mu \Delta v_z \tag{1.19}$$

$$\frac{\partial p}{\partial r} = -\rho \left(\frac{\partial v_r}{\partial t} + \nabla \cdot (v_r \boldsymbol{v}) \right) + \mu (\Delta v_r - \frac{v_r}{r^2}) \tag{1.20}$$

where:

$$\nabla \cdot (\alpha \boldsymbol{u}) = \frac{1}{r}\frac{\partial(r\alpha u_r)}{\partial r} + \frac{\partial \alpha u_z}{\partial z}$$
$$\Delta\alpha = \nabla \cdot (\nabla\alpha) = \nabla \cdot \left(\frac{\partial\alpha}{\partial r}, \frac{\partial\alpha}{\partial z}\right)$$

Let us consider a structure described by Koiter algebraic model [38, 39], which relates stress and strain through an algebraic law with a coefficient β and allows only radial displacement. Denoting by $\eta(z,t) = R(z,t) - R_0(z)$ the radial displacement with respect to the undeformed configuration R_0, in order to have a coupled system, the following conditions should be imposed at fluid-structure interface:

$$p = \beta\eta$$
$$v_r = \dot{\eta}$$
$$v_z = 0$$

ensuring the continuity of the normal stress (dynamic coupling) and of the velocity (kinematic coupling) at the fluid-structure interface. Summarizing, the hypotheses on which the model is based are:

- The flux is axisymmetric
- Only radial displacement is allowed
- Body forces are absent
- The axial component of the velocity dominates
- Pressure variations along the radial direction are sufficiently small

Remark The last two hypotheses do not imply that radial velocity and radial pressure variation are negligible, but that they are smaller than axial ones.

In order to obtain the 1D model by integrating the fluid equation, it is useful to recall (without proof) the lemma presented in [59]:

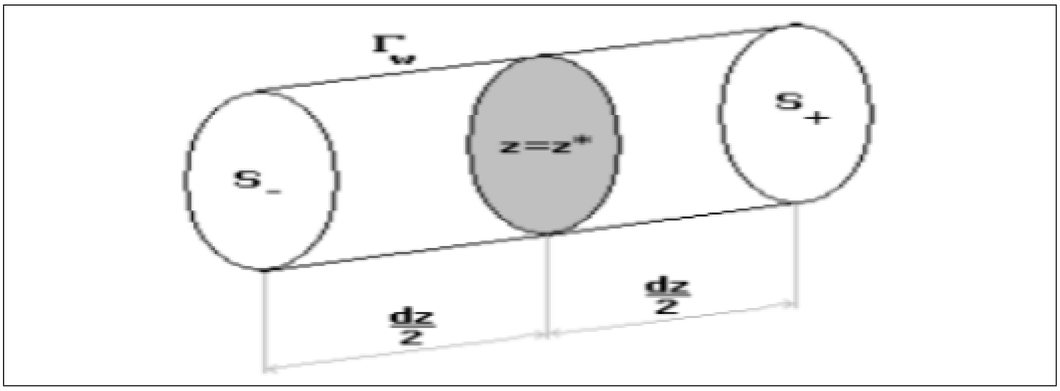

Figure 1.4: Control volume V

Lemma 1 *Let* $f : \Omega_t \times I \to \mathbb{R}$ *be an axisymmetric function, i.e.* $\frac{\partial f}{\partial \theta} = 0$ *Let us indicate by* f_w *the value of* f *on the wall boundary and by* $\overline{f}$ *its mean value on each axial section, defined by:*

$$\overline{f} = \frac{1}{A} \int_S f d\sigma$$

We have the following relations:

$$\frac{\partial A\overline{f}}{\partial t} = A\overline{\frac{\partial f}{\partial t}} + 2\pi R\dot{\eta} f_w$$

$$\frac{\partial A}{\partial t} = 2\pi R\dot{\eta}$$

Moreover, let us introduce the following notations:

$$\boldsymbol{n} = \frac{1}{R_0 g}\left(R\boldsymbol{e}_r - \frac{\partial R}{\partial \theta}\boldsymbol{e}_\theta - R\frac{\partial R}{\partial z}\boldsymbol{e}_z\right) \tag{1.21}$$

$$g = \frac{R}{R_0}\sqrt{1 + \left(\frac{1}{R}\frac{\partial R}{\partial \theta}\right)^2 + \left(\frac{\partial R}{\partial z}\right)^2} \tag{1.22}$$

$$d\sigma = gR_0 d\theta dz = g d\sigma_0 \tag{1.23}$$

In order to obtain the 1D problem, let us consider the cylindrical control domain of fig. 1.4 and integrate eqs (1.18), (1.19), using relations (1.21), (1.22) and (1.23) for integrals on Γ_w. From the continuity equation one finds:

$$
\begin{aligned}
0 &= \int_V \nabla \cdot \boldsymbol{v} dV = \int_{S_+} u_z d\sigma - \int_{S_-} u_z d\sigma + \int_{\Gamma_w} \boldsymbol{u} \cdot \boldsymbol{n} d\sigma \\
&= \left(\frac{\partial Q}{\partial z} + 2\pi R(z^*) \dot{\eta}(z^*) \right) dz + o(dz) \\
&= \left(\frac{\partial Q}{\partial z} + \frac{\partial A}{\partial t} \right) dz + o(dz)
\end{aligned}
$$

where Q is the flux evaluated on a section of area A. The same procedure can be applied to the axial momentum. In particular the term related to the pressure, becomes:

$$
\begin{aligned}
\int_V \frac{\partial p}{\partial z} dV &= \int_V (\nabla p) \cdot \boldsymbol{e}_z dV = \int_V (\nabla \cdot (pI)) \cdot \boldsymbol{e}_z dV \\
&= \int_{\partial V} p\boldsymbol{n} \cdot \boldsymbol{e}_z d\sigma = \int_{S_+} p d\sigma - \int_{S_-} p d\sigma + \int_{\Gamma_w} p\boldsymbol{n} \cdot \boldsymbol{e}_z \\
&= \frac{\partial AP}{\partial z} dz + o(dz) - 2\pi \int_{z^* - \frac{dz}{2}}^{z^* + \frac{dz}{2}} p_w(z) \overbrace{R(z) \frac{\partial R}{\partial z}}^{\frac{1}{2}\frac{\partial R^2}{\partial z}}(z) dz \\
&= \left(A \frac{\partial P}{\partial z} + (P - p_w) \frac{\partial A}{\partial z} \right) dz + o(dz)
\end{aligned}
$$

where P represents the cross-sectionally averaged pressure, while p_w is the pressure value on the boundary pipe. The 1D (not yet closed) system thus becomes:

$$
\frac{\partial A}{\partial t} + \frac{\partial Q}{\partial z} = 0 \tag{1.24}
$$

$$
\frac{\partial Q}{\partial t} + \frac{\partial}{\partial z} \left(\alpha \frac{Q^2}{A} \right) + \frac{1}{\rho} \left(A \frac{\partial P}{\partial z} + \boxed{(P - p_w) \frac{\partial A}{\partial z}} \right) + K_r \frac{Q}{A} = 0 \tag{1.25}
$$

$$
p_w = \beta \left(\frac{\sqrt{A} - \sqrt{A_0}}{\sqrt{\pi}} \right) \tag{1.26}
$$

where K_r is a coefficient which derives from the viscosity term and α is the Coriolis coefficient, defined as:

$$
\begin{aligned}
\alpha &= \frac{\int_S u_z^2 d\sigma}{A \overline{u}_z^2} \\
\overline{u}_z &= \frac{1}{A} \int_S u_z d\sigma
\end{aligned}
$$

Respect to the "classical" 1D system of equations which is used to study the flux in the compliant pipes, a new term appears in eq. (1.25) (the one highlighted by the box): this term take into account the effects of flow variations along the radial direction. It is easy to demonstrate that this new set of equations is a generalization of the classical one. Indeed, if one assume $v_r \approx 0$, the radial momentum equation yields:

$$\frac{\partial p}{\partial r} \approx 0$$

$$p_w = P$$

$$P = \beta \left(\frac{\sqrt{A} - \sqrt{A_0}}{\sqrt{\pi}} \right)$$

The problem given by (1.24)-(1.26) is not determined, since it involves three equation and four unknowns (Q, A, P, p_w). In order to close the problem, one possibility is to suitably integrate the equation of the radial momentum, in order to find a new independent relation. The problem now translates into the determination of a radial velocity profile depending on the wall movement. This can be done by using the experimental evidence. The simplified form of the radial momentum arises from the fact that only the terms that can be integrated are retained (i.e. convective terms are neglected, while the viscous term is assumed to depend only on the radial direction). Even though these assumptions could be seen as reductive, they are often introduced (see [69]). For the sake of completeness, another possible choice could be to integrate directly the pressure given by the relation described in [15], resulting form a simplified model, and thus close the problem.

1.3.1 The integration of the radial momentum

Let us consider two simplified forms of the radial momentum. The former (in the following called inertial form) takes into account only local inertia and reads:

$$\frac{\partial p}{\partial r} = -\rho \frac{\partial v_r}{\partial t} \tag{1.27}$$

while the latter (hereafter called viscous form) takes into account also viscous terms:

$$\frac{\partial p}{\partial r} = -\rho \frac{\partial v_r}{\partial t} + \mu \left(\frac{\partial^2 v_r}{\partial r^2} + \frac{1}{r}\frac{\partial v_r}{\partial r} - \frac{v_r}{r^2} \right) \tag{1.28}$$

Integrating (1.28) with respect to r, after some manipulations, one finds:

$$\begin{aligned} p_w - p(r) &= -\rho \left(\frac{\partial}{\partial t} \int_r^R v_r(r')dr' - v_r|_{r=R} \frac{\partial R}{\partial t} + v_r(r) \frac{\partial r}{\partial t} \right) \\ &+ \mu \int_r^R \left(\frac{\partial^2 v_r(r')}{\partial r'^2} + \frac{1}{r'}\frac{\partial v_r(r')}{\partial r'} - \frac{v_r(r')}{r'^2} \right) dr' \\ &= \frac{\rho}{4\pi A} \left(\frac{\partial A}{\partial t} \right)^2 - \rho \frac{\partial}{\partial t} \int_r^R v_r(r')dr' \\ &+ \mu \int_r^R \left(\frac{\partial^2 v_r(r')}{\partial r'^2} + \frac{1}{r'}\frac{\partial v_r(r')}{\partial r'} - \frac{v_r(r')}{r'^2} \right) dr' \end{aligned}$$

Integrating across the section and applying lemma 1 one finds:

$$\begin{aligned} P - p_w &= -\frac{\rho}{A} \left(\frac{1}{4\pi} \left(\frac{\partial A}{\partial t} \right)^2 - 2\pi \frac{\partial}{\partial t} \int_0^R \left(r \int_r^R v_r(r')dr' \right) dr \right. \\ &\left. + \nu \left(A \left. \frac{\partial v_r}{\partial r} \right|_{r=R} - \frac{1}{2}\frac{\partial A}{\partial t} \right) \right) \\ &= -\frac{\rho}{A} \Big(L'(A,Q) \Big) \end{aligned} \tag{1.29}$$

where $L'(A,Q)$ denotes the operator obtained considering the viscous terms; in the following, the operator related to the only inertial terms will be indicated with $L(A,Q)$.

Equation (1.25) can then be rewritten as:

$$\frac{\partial Q}{\partial t} + \frac{\partial}{\partial z} \left(\alpha \frac{Q^2}{A} \right) + \frac{1}{\rho} \left(A \frac{\partial p_w}{\partial z} - \rho \frac{\partial L'(A,Q)}{\partial z} \right) + K_r \frac{Q}{A} = 0$$

or in conservative form:

$$\frac{\partial Q}{\partial t} + \frac{\partial}{\partial z} \left(\alpha \frac{Q^2}{A} + \frac{\tilde{\beta}}{3\rho} \frac{A^{\frac{3}{2}} - A_0^{\frac{3}{2}}}{A_0} - L'(A,Q) \right) + K_r \frac{Q}{A} = 0 \tag{1.30}$$

$$\tilde{\beta} = \frac{\beta}{\sqrt{\pi}}$$

In both cases the differential equation differs from the classical form, obtained by neglecting variation in the radial direction, for the presence of the term constituting L' (or L).

1.3.2 Determining L' (and L) by experimental evidence

In order to determine the new operator, some considerations on the velocity profile should be made. By some deduction and by the experimental evidence, it is reasonable to approximate the radial velocity as a function of the wall velocity $\dot{\eta}$ in two forms:

- by a similarity profile,[5] of the form:

$$v_r = \left(\frac{r}{R(z,t)}\right)^m \frac{\partial \eta}{\partial t}, \qquad m > 0$$

- by a Womersley profile law of the form:

$$\begin{aligned} v_r &= \Re\left[\frac{i\omega D}{1 - F_{10}(\alpha)}\left(\frac{r}{R} - \frac{2J_1\left(\alpha i^{3/2}\frac{r}{R}\right)}{\alpha i^{3/2} J_0\left(\alpha i^{3/2}\right)}\right)\exp\left(i\omega\left(t - \frac{z}{c}\right)\right)\right] \\ &= \Re\left[v_1\left(\frac{r}{R}\right)\exp\left(i\omega\left(t - \frac{z}{c}\right)\right)\right] \\ \eta &= D\exp\left(i\omega\left(t - \frac{z}{c}\right)\right) \\ \alpha &= R\sqrt{\frac{\omega}{\nu}} \\ F_{10}(\alpha) &= \frac{2J_1\left(\alpha i^{3/2}\right)}{\alpha i^{3/2} J_0\left(\alpha i^{3/2}\right)} \end{aligned}$$

where J_0, J_1 are the Bessel functions of the first kind of first and second order, i is the complex unit, ν is the kinematic viscosity, c is a characteristic wave speed depending on the wall physical properties and α is the so called Womersley number. This approximation involves

---

[5] Or a weighted linear composition of similarity profiles:

$$v_r = \sum_{k=1}^{n} a_k \left(\frac{r}{R(z,t)}\right)^m \frac{\partial \eta}{\partial t}, \qquad m > 0, \qquad \sum_{k=1}^{n} a_k = 1$$

> small displacements, such that it is possible to approximate $R \approx R_0$. A derivation of the Womersley solution for the radial velocity is described in appendix A.

Derivating the operator L' for the first approximation of $v_r(r)$ is trivial; one obtains:

$$
\begin{aligned}
L'(A,Q) = {} & \frac{1}{4\pi}\left(1-\frac{2}{m+3}\right)\left(\frac{\partial A}{\partial t}\right)^2 \\
& - \frac{A}{2\pi}\left(\frac{1}{m+3}\right)\frac{\partial^2 A}{\partial t^2} \\
& + \nu\left(\frac{m-1}{2}\right)\frac{\partial A}{\partial t}
\end{aligned} \tag{1.31}
$$

Remark When the velocity profile is linear (i.e. $m = 1$) the viscous term vanishes.

The form of L' deduced by using the velocity profile proposed by Womersley one should consider both the complex and the complex conjugate form, in order to obtain a real solution. After some manipulation one finds:

$$
\begin{aligned}
L'(A,Q) = {} & \Bigg(\frac{1}{4\pi}\Bigg(1-\frac{\nu}{A\omega}\mathcal{I}\left[\frac{J_2\left(\alpha i^{3/2}\right)}{\left(1-F_{10}(\alpha)\right)J_0\left(\alpha i^{3/2}\right)}\right]\Bigg) \\
& + \frac{1}{2A}\sqrt{\frac{\pi}{A}}\mathcal{R}\left[\frac{R^3\left(i\alpha^2+8\left(1-F_{10}(\alpha)\right)\right)}{8i\alpha^2\left(1-F_{10}(\alpha)\right)}\right]\Bigg)\left(\frac{\partial A}{\partial t}\right)^2 \\
& + \Bigg(\frac{1}{2\pi}\frac{\nu}{\omega}\mathcal{I}\left[\frac{J_2\left(\alpha i^{3/2}\right)}{\left(1-F_{10}(\alpha)\right)J_0\left(\alpha i^{3/2}\right)}\right] \\
& - \sqrt{\frac{\pi}{A}}\mathcal{R}\left[\frac{R^3\left(i\alpha^2+8\left(1-F_{10}(\alpha)\right)\right)}{8i\alpha^2\left(1-F_{10}(\alpha)\right)}\right]\Bigg)\frac{\partial^2 A}{\partial t^2} \\
& + \Bigg(\sqrt{\frac{\pi}{A}}\omega\mathcal{I}\left[\frac{R^3\left(i\alpha^2+8\left(1-F_{10}(\alpha)\right)\right)}{8i\alpha^2\left(1-F_{10}(\alpha)\right)}\right] \\
& + \frac{\nu}{2}\Bigg(\mathcal{R}\left[\frac{J_2\left(\alpha i^{3/2}\right)}{\pi\left(1-F_{10}(\alpha)\right)J_0\left(\alpha i^{3/2}\right)}\right]-1\Bigg)\Bigg)\frac{\partial A}{\partial t}
\end{aligned} \tag{1.32}
$$

Remark Since (1.32). is obtained by assuming $R \approx R_0$, it is possible to neglect the nonlinear terms which appears in this relationship.

Remark The velocity profile given by Womersley is obtained by accounting for the viscous terms, and hence leads to determining the operator L'.

In both (1.31) and (1.32) the added mass term is this involving the second order time derivative of the section, which is proportional to an inertial force. The new terms (1.31) and (1.32) are obtained through integration of the pressure: remembering figure 1.1 we can expect that, even though the approximation of the radial velocity is still “coarse”, the oscillations which characterize the added mass effect are re-obtained.

Remark If one adds the algebraic relation which characterize the structure to the linearized form of (1.31) or (1.32), the results corresponds to a general structure model with an inertia given by the terms which multiply the second time derivative of the section and dissipation term which corresponds to the term which multiply the first time derivative of the section. Indeed, taking for example the similarity profiles, by relation

$$P = p_w - \frac{\rho}{A} L'(A, Q)$$

it follows:

$$P = \beta \frac{\sqrt{A} - \sqrt{A_0}}{\sqrt{\pi}} + \mathcal{M} \frac{\partial^2 A}{\partial t^2} - \gamma \frac{\partial A}{\partial t} \tag{1.33}$$

$$\mathcal{M} = \frac{\rho}{2\pi} \left(\frac{1}{m+3} \right) \tag{1.34}$$

$$\gamma = \frac{\mu}{A} \left(\frac{m-1}{2} \right) \tag{1.35}$$

Equation (1.33) resembles to the one introduced in [27] pag. 18, except for the fact that now the coefficient of the structural model depends on the fluid-structure interaction. It is so possible to consider the 1D model augmented by the added mass effect as a classical one dimensional problem where the structure has a complex form. Moreover, relation (1.33) shows that the fluid act as a virtual inertia on the structure, through the coefficient $\mathcal{M}$.

Vessel radius (R_0)	0.5 cm
Vessel length (L)	2.5 cm
Vessel thick (h_s)	0.05 cm
Vessel Poisson coef (σ)	0.5
Vessel Young mod. (E)	375000 $dyne/cm^2$
Vessel density (ρ_s)	0 g/cm^3
Fluid density (ρ_f)	1 g/cm^3
Fluid kin. viscosity (ν)	1 cm^2/s
Flux period (T)	1 s
Flux modulus (Q_0)	4 cm^3/s

Table 1.1: Physical and geometrical quantities

1.4 Comparison between radial velocity profiles

The aim of this section is to evaluate the accuracy of the radial velocity approximations discussed in subsection 1.3.2 with respect to a 2D numerical solution obtained with the finite element library Freefem++ [31]. The 2D problem is solved on a axisymmetrical domain, neglecting convective terms. The structural dynamic is embedded in the flow solution through a boundary condition of the Robin type imposed at the fluid-structure interface, [51]. Moreover, defective condition on the flux was chosen for the inlet section [26], while a non-reflecting condition is assumed at the outlet section [51]. An Arbitrary Lagrangian Eulerian frame of reference, [22, 23, 35], was adopted in order to account for the changing in time of the computational domain.

At the inlet the following harmonic flux condition is applied:

$$Q(t) = Q_0 \sin\left(\frac{2\pi}{T}t\right)$$

Physical and geometrical quantity adopted in the simulations, as well as the time step and the grid size are summarized in table 1.1 and 1.2 Approxima-

Time step size (Δt)	0.0005 s
Number of analyzed periods	3
Typical grid dimension h	0.0125 cm

Table 1.2: Numerical value used in 2D numerical simulation

tion through similarity profile is obtained by summing linearly 5 terms, as follows:

$$v_r(r,z,t) = a_1 \left(\frac{r}{R(z,t)}\right)\frac{\partial\eta}{\partial t} + \sum_{m=1}^{2}\left(a_{m+1}\left(\frac{r}{R(z,t)}\right)^{m+1} + a_{2+(m+1)}\left(\frac{r}{R(z,t)}\right)^{1/(m+1)}\right)\frac{\partial\eta}{\partial t}$$

The coefficients a_i are chosen with a least square criterion with respect to the numerical solution, with the additional condition:

$$\sum_{i=1}^{5} a_i = 1$$

The approximated and numerical radial profile are plotted in Figures 1.5 - 1.9, for 4 sections. It is possible to observe that:

- The analytical profiles and the numerical solution have a significant difference when the velocity changes sign
- The comparison between the analytical approximation and numerical profiles improves if the section is located far from the inlet/outlet (i.e., where boundary effects become negligible)
- The analytical approximation obtained by composing linearly five similarity profiles and that obtained by Womersley do not differ very much

The analytical profiles then appear to provide a reasonable approximation, even though they tend do depart from the numerical more refine solution when the radial velocity changes sign. We explain in section 1.5 how to take advantage of these profiles.

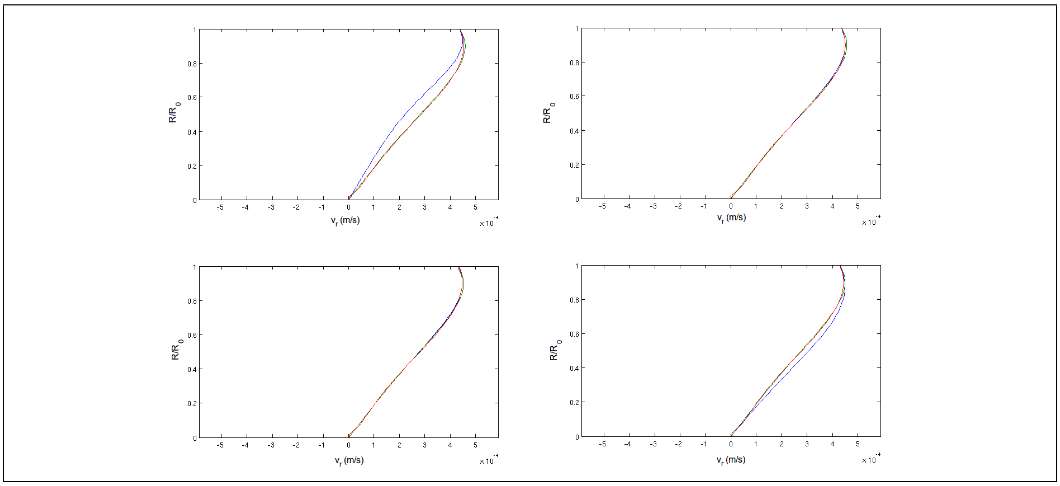

Figure 1.5: Comparison between interpolation $v_r(z,t)$ profile vs numerical $v_r(z,t)$ profile, for (from left to right and top to bottom) $x = 0.005cm$, $x = 0.01cm$, $x = 0.015cm$ and $x = 0.02cm$, at time $T = 2.0s$. Blue line: numerical solution; green line: interpolated from Womersley solution; red line: interpolated by 5 autosimilarity profiles.

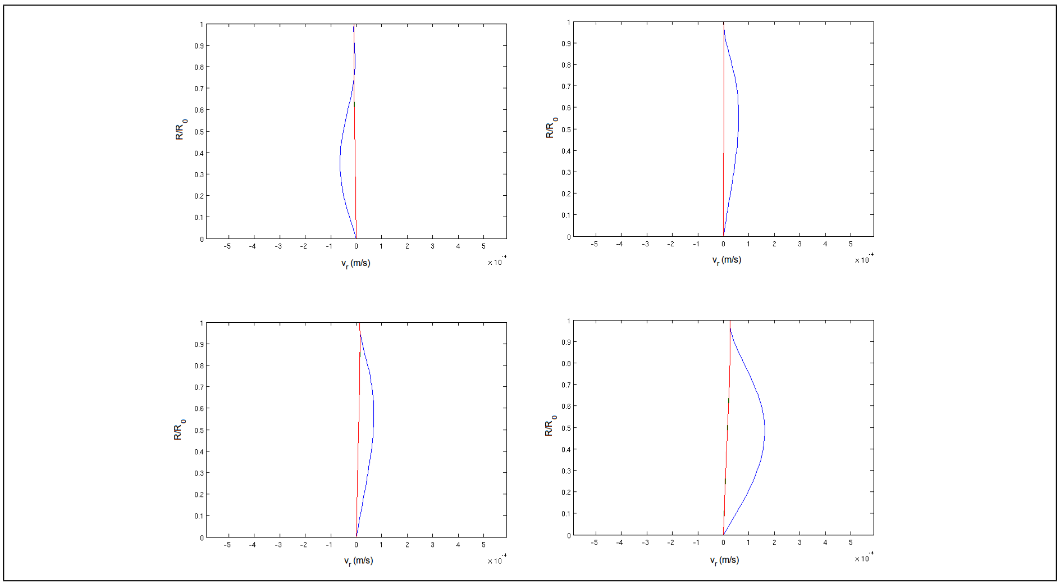

Figure 1.6: Comparison between interpolation $v_r(z,t)$ profile vs numerical $v_r(z,t)$ profile, for (from left to right and top to bottom) $x = 0.005cm$, $x = 0.01cm$, $x = 0.015cm$ and $x = 0.02cm$, at time $T = 2.25s$. Blue line: numerical solution; green line: interpolated from Womersley solution; red line: interpolated by 5 autosimilarity profiles.

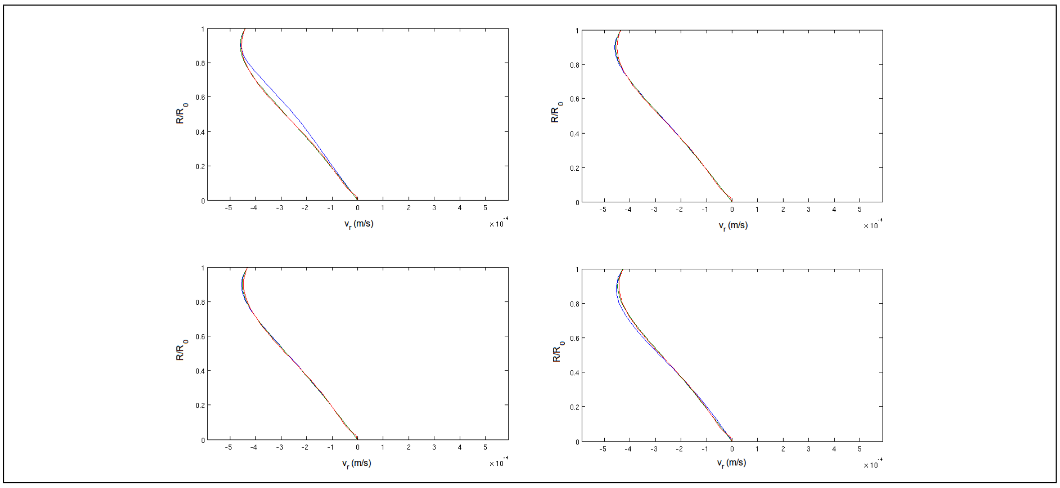

Figure 1.7: Comparison between interpolation $v_r(z,t)$ profile vs numerical $v_r(z,t)$ profile, for (from left to right and top to bottom) $x = 0.005cm$, $x = 0.01cm$, $x = 0.015cm$ and $x = 0.02cm$, at time $T = 2.5s$. Blue line: numerical solution; green line: interpolated from Womersley solution; red line: interpolated by 5 autosimilarity profiles.

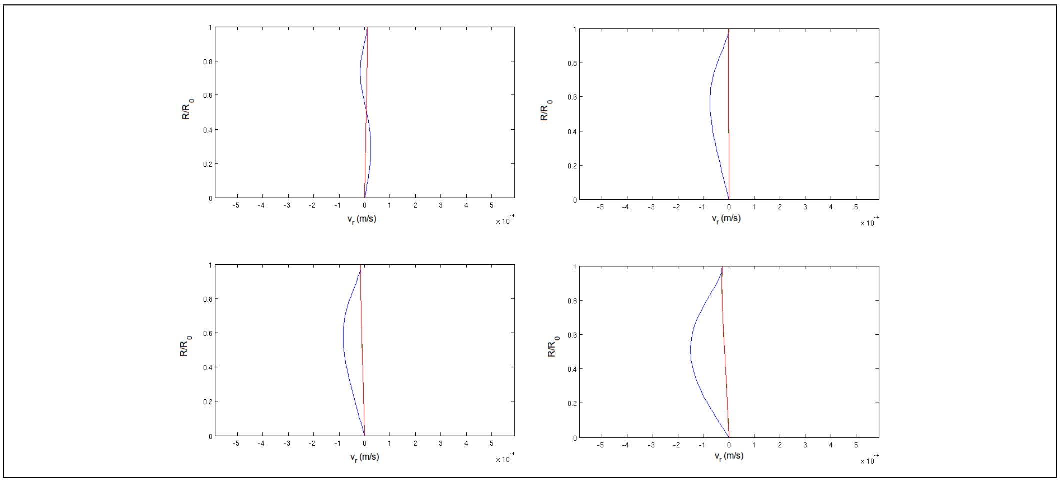

Figure 1.8: Comparison between interpolation $v_r(z,t)$ profile vs numerical $v_r(z,t)$ profile, for (from left to right and top to bottom) $x = 0.005cm$, $x = 0.01cm$, $x = 0.015cm$ and $x = 0.02cm$, at time $T = 2.75s$. Blue line: numerical solution; green line: interpolated from Womersley solution; red line: interpolated by 5 autosimilarity profiles.

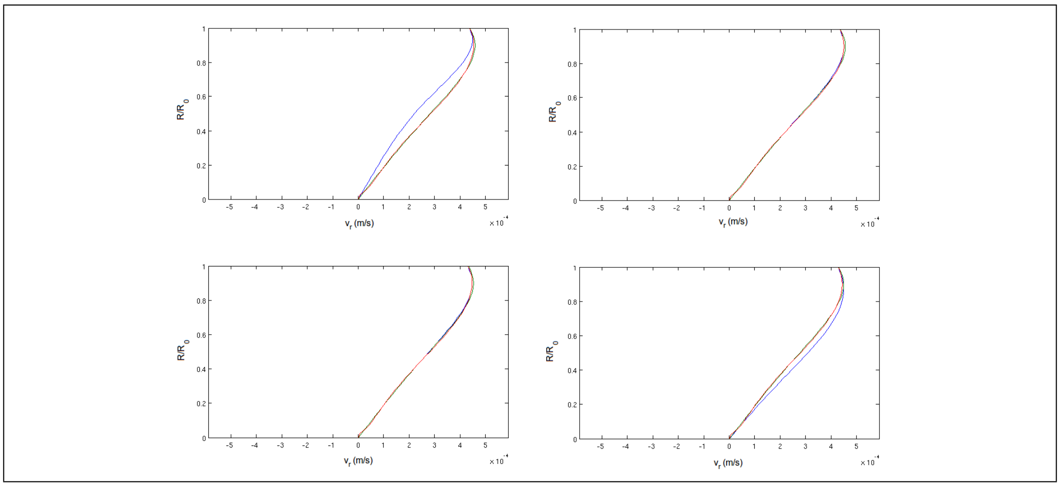

Figure 1.9: Comparison between interpolation $v_r(z,t)$ profile vs numerical $v_r(z,t)$ profile, for (from left to right and top to bottom) $x = 0.005cm$, $x = 0.01cm$, $x = 0.015cm$ and $x = 0.02cm$, at time $T = 3.0s$. Blue line: numerical solution; green line: interpolated from Womersley solution; red line: interpolated by 5 autosimilarity profiles.

1.5 How to use analytical approximations of velocity profiles

First of all it is worthwhile to point out that there is not any general criterion for selecting a reasonable analytical form of the radial velocity profile. Indeed, a linear composition of similarity solution has been show to provide good results. The value of the coefficients, however, is not known a priori. Now the question is: “how determine the coefficients of the linear composition, if they depend by the (unknown) solution?” The only way affordable is to create a sort of database of coefficients, obtained by 2D numerical simulations, for classical value of the problem as pipe length, pressure frequency and so on. After, if one desires to study a new problem with a set of parameters which does not belongs to the database, the new coefficients of the linear composition will be obtained by interpolation. I would like to point out that how to make this interpolation could represents a novel study field, being the linear one not necessary the best. The Womerlsey profile conversely works well when the input of the system is of the harmonic type, because it depends directly by the parameters under study. However, when the input is decomposed as a sum of harmonics,[6] in order to obtain a closed form for the added mass, some weight coefficients should be determined too.[7]

1.6 Numerical results

In this section I consider the effects of the added mass operator L and L' appearing in (1.30). The added mass operator determined by considering the linear composition of similarity profile discussed in 1.4, reads:

$$\begin{aligned}
L'(A,Q) &= -\frac{A_0}{2\pi}\left(\frac{a_1}{4}+\sum_{m=1}^{2}\left(\frac{a_{m+1}}{(m+1)+3}+\frac{a_{2+(m+1)}}{\frac{1}{(m+1)}+3}\right)\right)\frac{\partial^2 A}{\partial t^2}\\
&+\frac{\nu}{2}\sum_{m=1}^{2}\left(m a_{m+1}+\left(\frac{1}{m+1}-1\right)a_{2+(m+1)}\right)\frac{\partial A}{\partial t}\\
&= -\mathcal{M}\frac{\partial^2 A}{\partial t^2}+\gamma\frac{\partial A}{\partial t}
\end{aligned}$$

The continuity and momentum equations governing the flow field then reads:

$$\begin{aligned}
&\frac{\partial A}{\partial t}+\frac{\partial Q}{\partial z}=0\\
&\frac{\partial Q}{\partial t}+\frac{\partial}{\partial z}F_2(A,Q)-\mathcal{M}\frac{\partial^3 Q}{\partial z^2\partial t}+\gamma\frac{\partial^2 Q}{\partial z^2}=0\\
&F_2(A,Q)=\alpha\frac{Q^2}{A}+\frac{\tilde{\beta}}{3\rho}\frac{A^{\frac{3}{2}}-A_0^{\frac{3}{2}}}{A_0}
\end{aligned}$$

---

[6] Theoretically, if it is sufficiently smooth, every input could be decomposed in such a way

[7] It is however possible to consider only the first harmonic, if its contribution dominates the response. In this case it is possible to determine the fluid-structure interaction coefficients a priori by an analysis of the parameter and the coefficients which form the series.

where source term related to fluid dissipations is neglected for the sake of simplicity.[8] Momentum equation suggests the following splitting strategy:

$$\frac{A^{n+1}-A^n}{\Delta t}+\frac{\partial Q^n}{\partial z}=0 \tag{1.36}$$

$$\frac{Q^{n+1/2}-Q^n}{\Delta t}+\frac{\partial}{\partial z}F_2(A^n,Q^n)=0 \tag{1.37}$$

$$\frac{Q^{n+1}-Q^{n+1/2}}{\Delta t}-\frac{\mathcal{M}}{\Delta t}\left(\frac{\partial^2 Q^{n+1}}{\partial z^2}-\frac{\partial^2 Q^n}{\partial z^2}\right)+\gamma\frac{\partial^2 Q^{n+1}}{\partial z^2}=0 \tag{1.38}$$

where the convective terms (1.36),(1.37) are solved with an explicit scheme, whereas equation (1.38) is solved implicitly. A Finite Volume scheme was chosen for the convective terms, while for the added mass a Galerkin Finite Element scheme was adopted. In both cases a Dirichlet boundary condition was adopted at the inlet, while in the latter case an homogeneous Neumann one is assumed at the outlet.

Interpolation from Finite Element and to Finite Volume is performed by imposing the following relation:

$$u_i^{FVM}=\frac{1}{\Delta x}\int_{x_{i-1}}^{x_i} u^{FEM}dx, i=1,...,N$$

The same relation is used for interpolating from Finite Volume to Finite Element. However, in this latter case one has to determine $N+1$ value by N relations: the $N+1$th relation is obtained by imposing at one of the extremal node the boundary value (typically the flux at the first (inlet) node which is known as a boundary condition, while at the last (outlet) node the value of the section, obtained as solution of the first step of the algorithm).

The numerical results here presented were performed by imposing a flux rate of the following three different period: $T=2\,s$, $T=1\,s$, $T=0.5\,s$. The other data are the same summarized table 1.1. As depicted in figs. 1.10, 1.12 and 1.14, the added mass effect increase the range variation of the cross

---

[8] The added mass operator if evaluated by considering the radial velocity profile provided by Womersley, the momentum equation does not change if suitable expressions are introduced for $\mathcal{M}$ and γ

sectional area and the effect is more pronounced with increasing frequency. Conversely, the flux modulus is slightly affected.

Moreover, a time lag to return to the reference (undisturbed) conditions appears, both for the flux and the cross sectional area, as depicted in figs 1.16, 1.17 for a period $T = 2\,s$.

Table 1.3 resumes the principal indicator of the added mass effect. With $\tau_{A,Q}$ is denoted the time lag introduced by the added mass effect, while with $R_{A,Q}$ the ratio between the maximum value of the flux/area evaluated with the added mass effect and the corresponding one evaluated without the added mass effect.

In figs. 1.18, 1.20 and 1.22, the numerical results of the cross-sectional area with the operator $L'(A, Q)$ related to the viscous form are depicted; For the fluid, a coefficient $K_r = \pi\nu$ were considered. In figs. 1.19, 1.21 and 1.23, the corresponding flux values are depicted. In the numerical simulation here performed, the viscosity increase the wave amplitude of the cross-sectional area; this is in agreement by the fact that the drag generated by the viscosity accumulate mass, so the cross-sectional area must increase. The effect diminish advancing in time. This behavior is greater in the model without the added mass, while when added mass operator of the viscous form is considered, the term related to γ tends to counteract the effects related to K_r. This behavior is resumed in table 1.4, where the value of A_{peak_n}/A_{peak_1} are reported for both the solution with and without the added mass effect. The added mass operator here considered is the one yielded by the viscous form. The values correspond to a forcing term of period $T = 1\,s$.

	$T = 2\,s$	$T = 1\,s$	$T = 0.5\,s$
τ_A	$6.0713 \times 10^{-4} s$	$3.4146 \times 10^{-4} s$	$1.1384 \times 10^{-4} s$
R_A	1 .0694	1.0712	1.0804
τ_Q	$5.5869 \times 10^{-4} s$	$5.5564 \times 10^{-4} s$	$5.4815 \times 10^{-4} s$
R_Q	$9.9996 \times 10^{-1} s$	$9.9983 \times 10^{-1} s$	$9.9934 \times 10^{-1} s$

Table 1.3: Principal indicators of the added mass effect

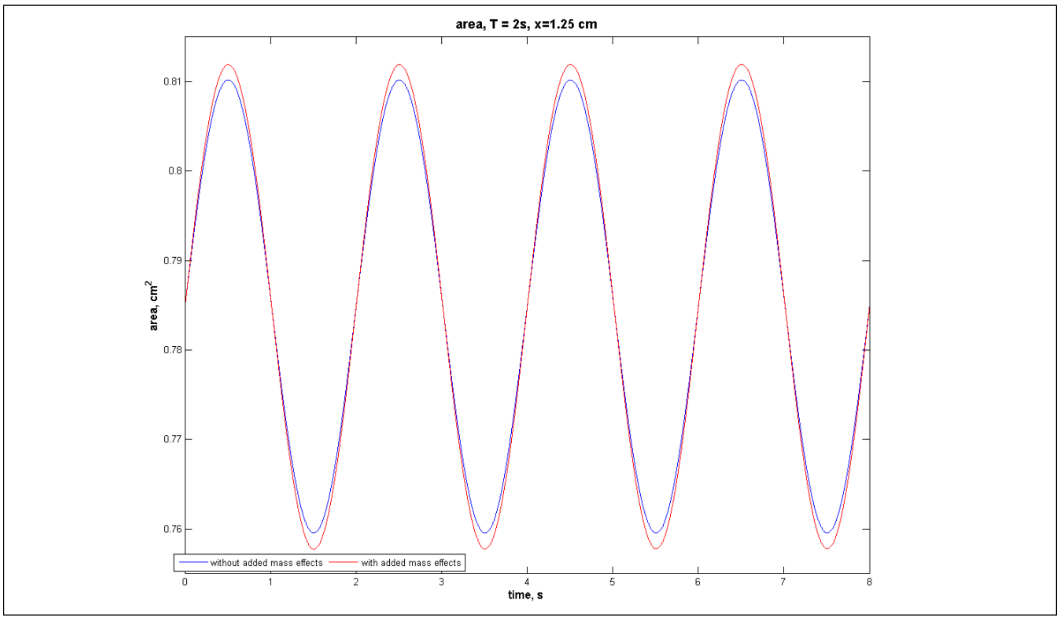

Figure 1.10: Comparison between area value vs time with (red line) and without (blue line) added mass effect, $T = 2\,s$

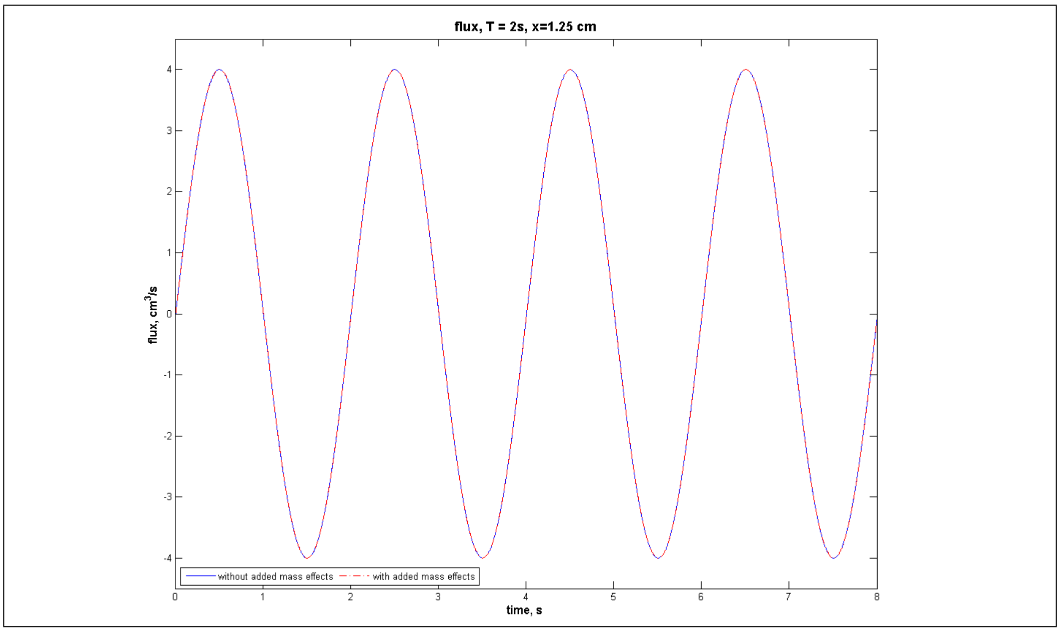

Figure 1.11: Comparison between flux value vs time with (red dotted line) and without (blue line) added mass effect, $T = 2\,s$

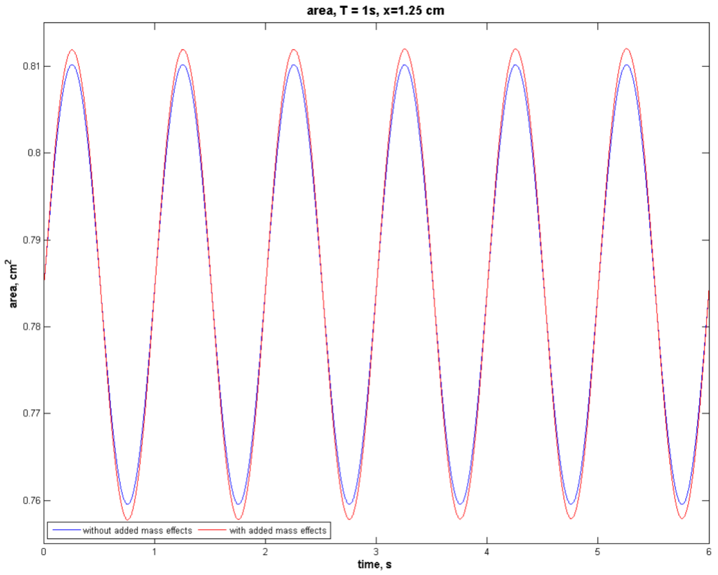

Figure 1.12: Comparison between area value vs time with (red line) and without (blue line) added mass effect, $T = 1\,s$

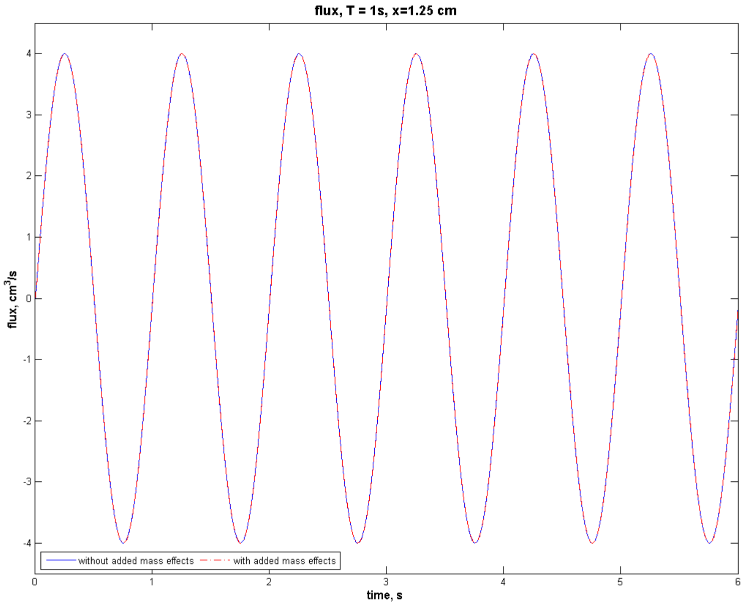

Figure 1.13: Comparison between flux value vs time with (red dotted line) and without (blue line) added mass effect, $T = 1\,s$

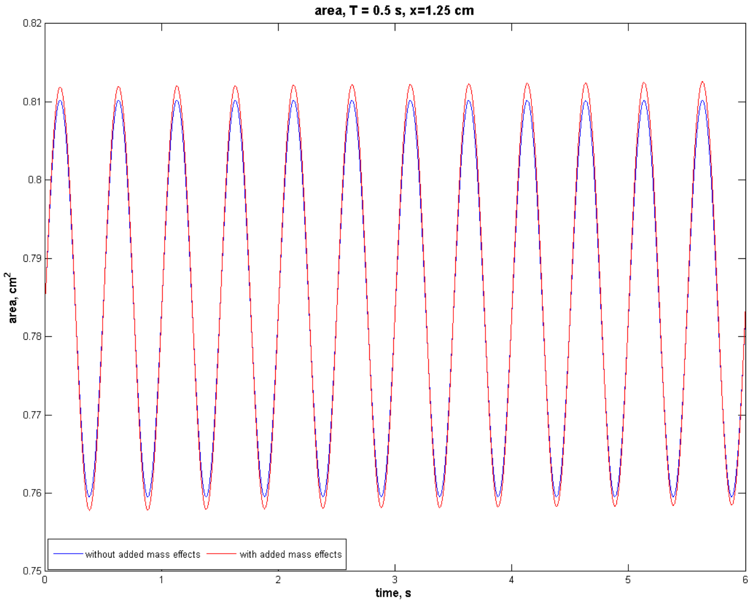

Figure 1.14: Comparison between area value vs time with (red line) and without (blue line) added mass effect, $T = 0.5\,s$

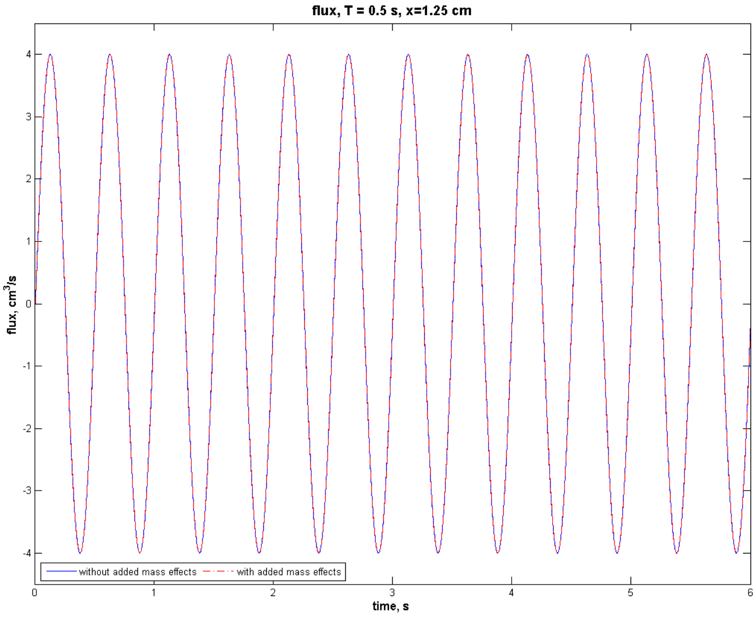

Figure 1.15: Comparison between flux value vs time with (red dotted line) and without (blue line) added mass effect, $T = 0.5\,s$

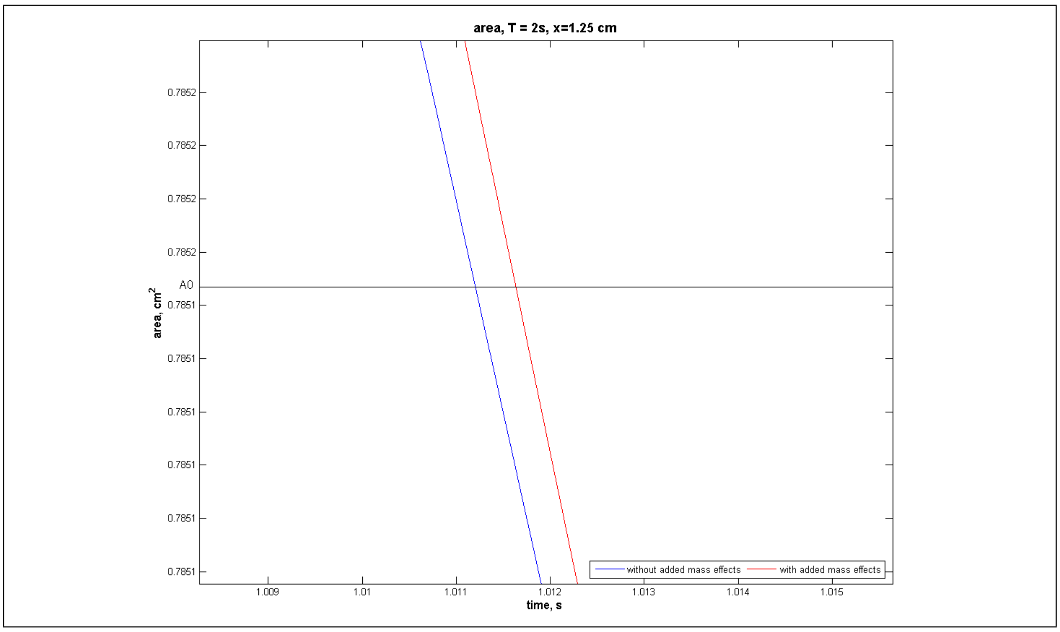

Figure 1.16: Comparison between area value vs time with (red line) and without (blue line) added mass effect, $T = 2\,s$, detail

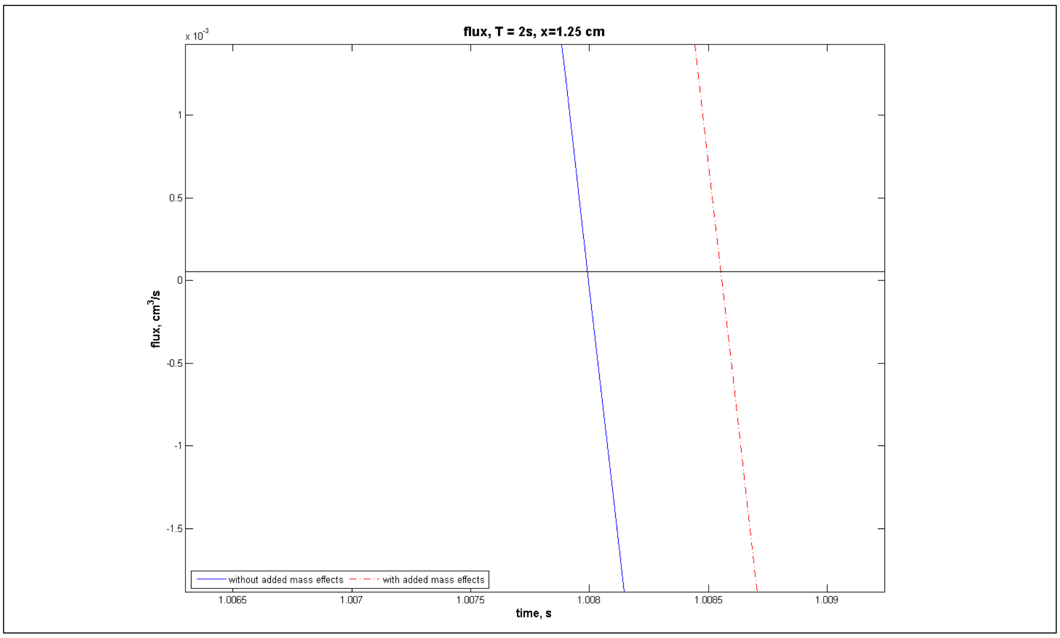

Figure 1.17: Comparison between flux value vs time with (red dotted line) and without (blue line) added mass effect, $T = 2\,s$, detail

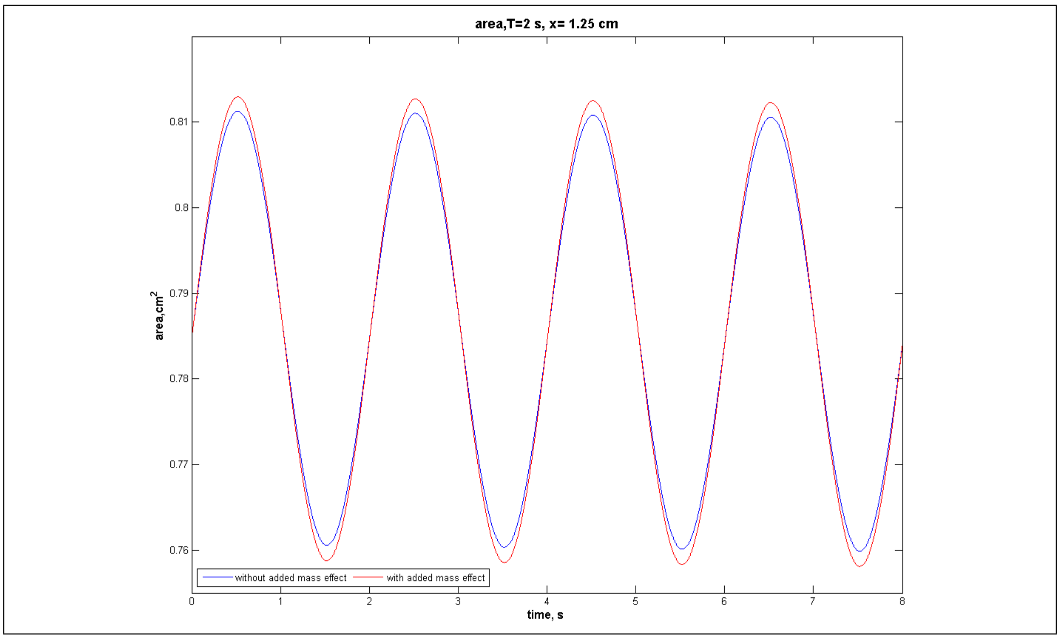

Figure 1.18: Comparison between area value vs time with (red line) and without (blue line) added mass effect for the operator L', $T = 2\,s$

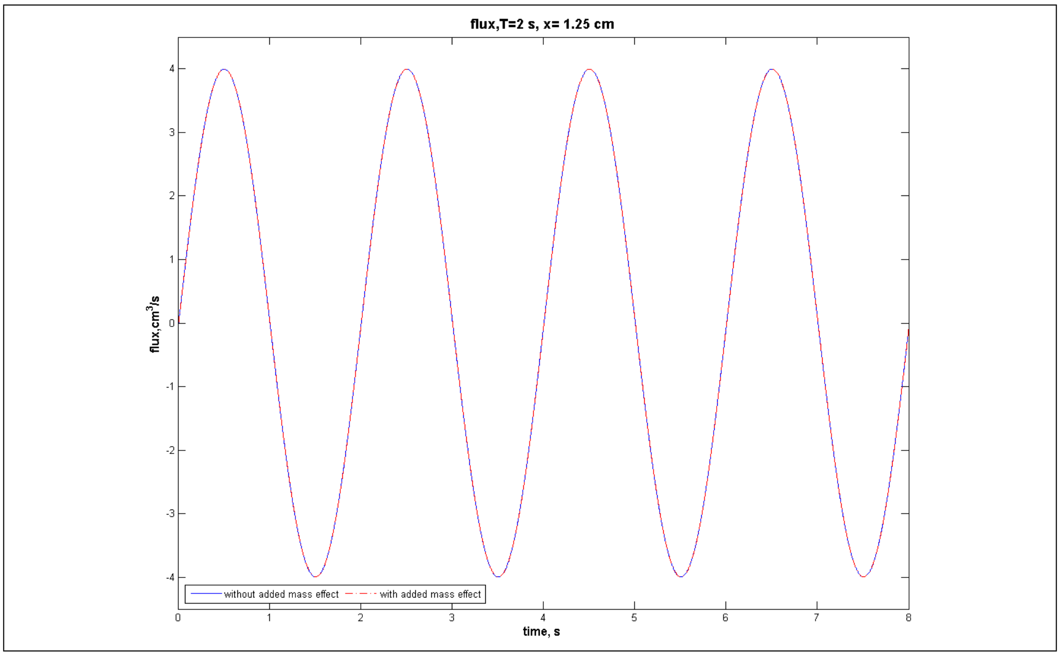

Figure 1.19: Comparison between flux value vs time with (red dotted line) and without (blue line) added mass effect for the operator L', $T = 2\,s$

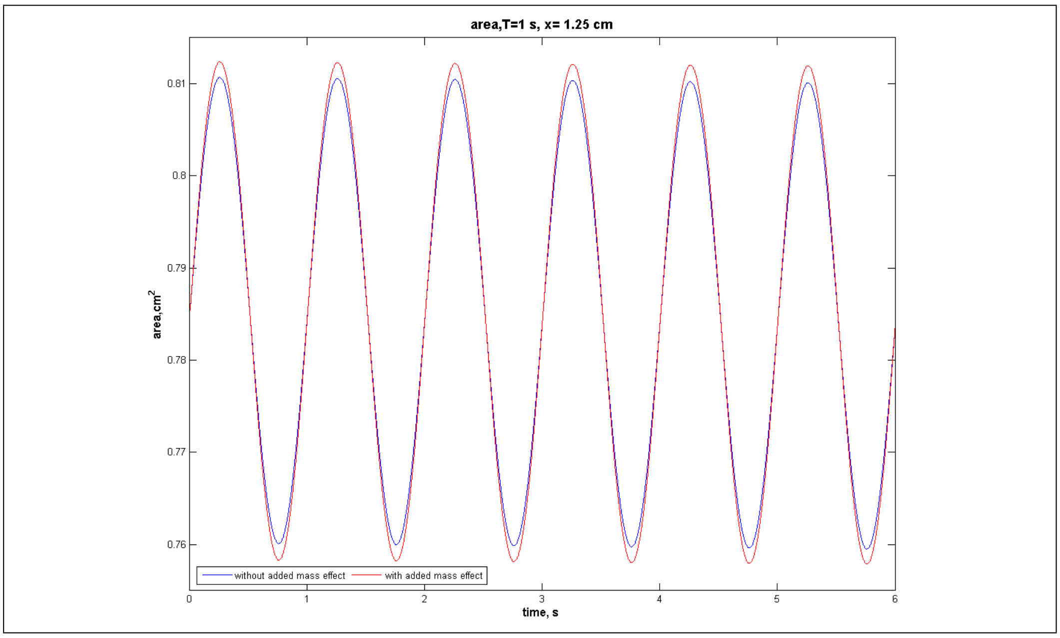

Figure 1.20: Comparison between area value vs time with (red line) and without (blue line) added mass effect for the operator L', $T = 1\,s$

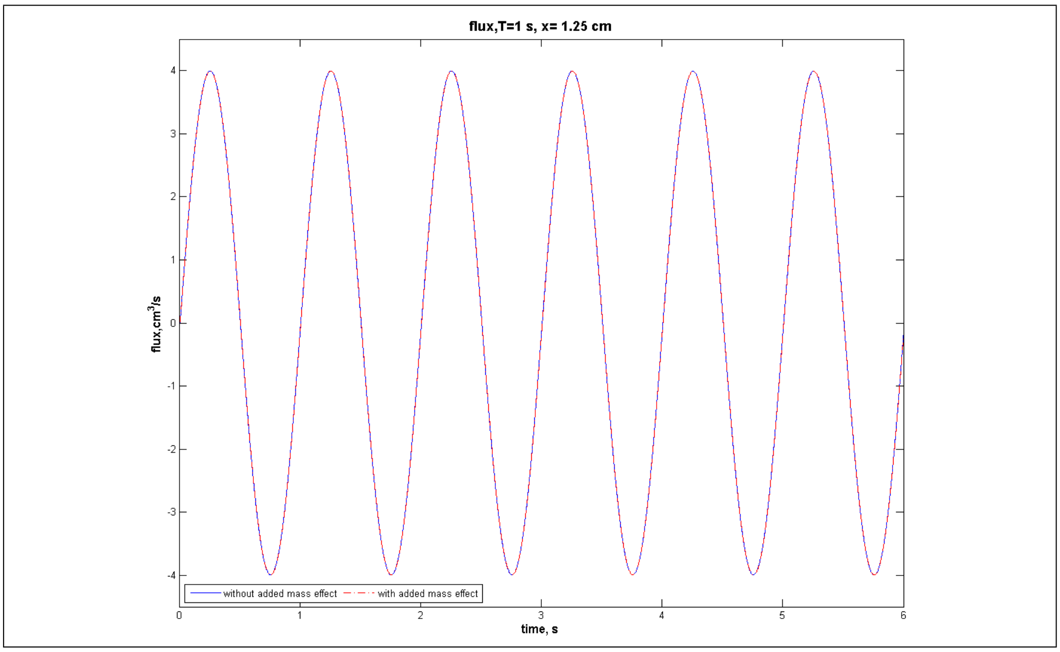

Figure 1.21: Comparison between flux value vs time with (red dotted line) and without (blue line) added mass effect for the operator L', $T = 1\,s$

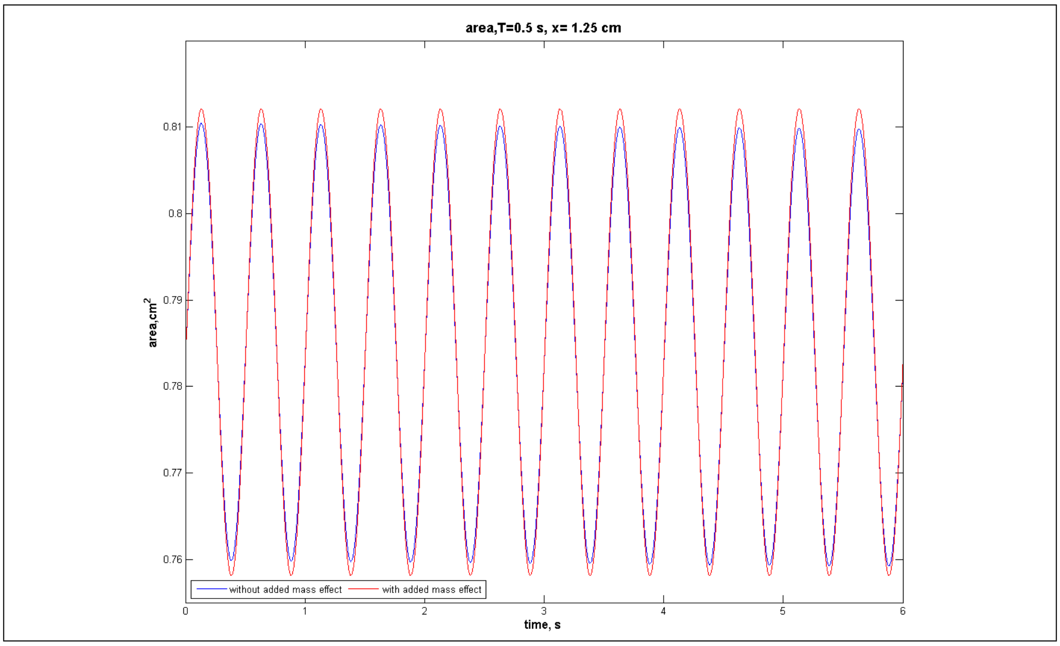

Figure 1.22: Comparison between area value vs time with (red line) and without (blue line) added mass effect for the operator L', $T = 0.5\,s$

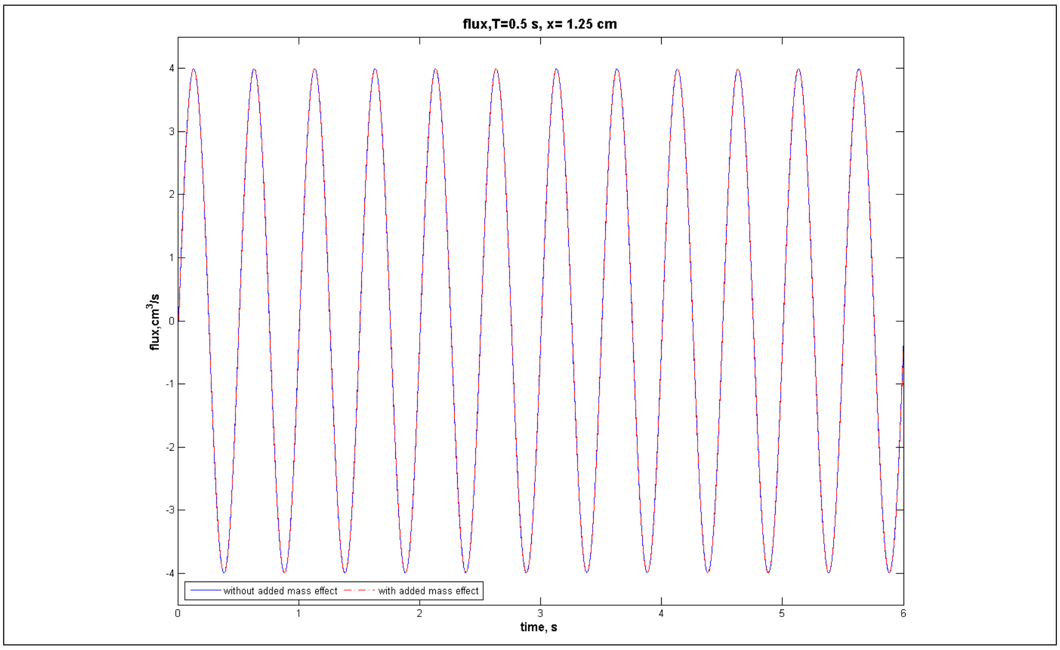

Figure 1.23: Comparison between flux value vs time with (red dotted line) and without (blue line) added mass effect for the operator L', $T = 0.5\,s$

peaks	without added mass	with added mass
1	1	1
2	0.9955	0.9968
3	0.9911	0.9936
4	0.9866	0.9904
5	0.9821	0.9872
6	0.9776	0.9840

Table 1.4: Ratio between the value of the cross-sectional area peaks $n = 1, .., 6$ and the first peaks with (2nd col.) and without (1st col) added mass. The period corresponds to $T = 1\,s$

1.7 Conclusions

The added mass effect represents an important phenomenon related to the fluid-structure interaction. The classical 1D approximation for the study of a flow in a compliant pipe is not capable to reproduce the part of response related to it. In this chapter a novel approach is proposed, which recast the same procedure used to obtain a 1D model, but with less restrictive hypotheses. The new set of equations represent a generalization of the classical one, being possible to re-obtain this latter by imposing a posteriori the conditions of null radial velocity and null pressure variation with respect to the radial coordinate.

Considering the pressure variation with respect to the radial coordinate introduces a new unknown, so a new equation is necessary in order to close the problem. The choose here adopted consist in integrating a simplified form of the equation of the radial momentum, adopting an approximation of the radial velocity based on the experimental evidence. The procedure yields a new operator $L'(A, Q)'$ (or, by considering the only inertial term, $L(A, Q)$), which takes into account of the fluid-structure interaction effects.

The problem is then solved numerically first by applying a splitting strategies on the momentum equation, and then solving the convective part with a Finite Volume scheme and the added mass part by a Galerkin-Finite Element scheme.

The result have demonstrated that neglecting the added mass effects yields a sub-estimation of the range of variation of the cross-sectional area, sub-estimation which becomes significant when the frequency of the forcing term increase; conversely, flux range is less affected, even though a decreasing of the maximum-to-minimum range where observed. Moreover, a small lag on the response for both cross sectional area and flux were highlighted.

Chapter 2

Analytical solution of a pulsating flow in a undefined rigid pipe

2.1 Introduction

The study of the flows driven by an unsteady pressure gradient represents an important branch of research in bio-fluid dynamics, even though some application exist also in the hydraulic engineering. Clearly, the problem of determining a velocity field is not a trivial task. Computer fluid dynamic represents an important tool to this aim, that can provide an accurate solution. Nevertheless, this procedure requires a relatively large computational cost that that can be not reasonable when one needs to analyze preliminary a given problem. Approximated analytical solutions then play an important role, since they can furnish an enough accurate solution in a reasonable time.

As far as flows driven by an unsteady pressure gradient are concerned, it is possible to find, under some simplifying hypotheses, an approximated analytical solution for the profile velocity which well mimic the real solution. Up to now, the most used solution of the pulsating flow in a rigid pipe is this derived by Womersley [30, 68], which is based on the following hypotheses:

1. The Reynolds number is small (typically less than 2300), so convective terms are negligible

2. The flow is axisymmetric
3. The axial dimension is much larger than pipe radius so that the pipe can be considered infinitely long
4. The influence to the solution of the inlet-outlet section is negligible (i.e., the section where the solution is determined is sufficiently far from the initial and final sections of the pipe)
5. The pressure gradient could be decomposed in a Fourier series
6. The solution describes an equilibrium state.

Hypothesis 6 means that the motion is fully developed in time, i.e. the solution although oscillatory is no more influenced by initial conditions. The system of equations which govern the flow field is linear: thanks to Hypothesis 5, it is possible to determine the solution for the generic harmonic of the Fourier series. Moreover, if the pressure mean value in time differs from zero (i.e. the time history is not symmetric with respect to the time Axis) , it is possible to "shift" the solution by a term which is formed by a Hagen-Poiseulle solution (i.e. which does not vary in time and represents the part of the solution related to the mean value of the pressure).

The pulsating flow field in a rigid pipe is characterized by two dimensionless parameters, defined as follows:

$$Re = \frac{2VR_0}{\nu}$$

$$\alpha = R_0\sqrt{\frac{\Omega}{\nu}}$$

Here R_0 is the radius of the pipe, ν is the kinematic viscosity of the fluid, V is a characteristic velocity and Ω the frequency of the pressure gradient. The first parameter is clearly the Reynolds number and does not need any comment. The second one, called "Womersley number", is a parameter which relates the frequency of the pulsating flow to the fluid viscosity and the radius of the pipe. The Womersley number is of particular importance in the study of pulsating flows; in particular, it is possible to verify that, in nature, blood vessel flows are characterized by a given range of this parameter (typically between 3 and 25). For example, if one compares blood flow in dog and human arterials, one find that in the latter case the heart frequency is smaller than in the former, being the typical values of the lumen radius greater. If the comparison is performed on α, one finds that each case is characterized by a specific range of variation of α.

Womersley solution is useful for the study of a developed motion. Clearly, if one want to study what happen before that the motion is fully developed (e.g., immediately after a sudden pressure increase), Womersley solution becomes inadequate. Nevertheless, this solution can be used as a particular solution (i.e., the regime solution) when one searches a complete solution. In this Chapter I determine the solution for an axisymmetric pulsating flow in a rigid pipe, accounting for also the transitory effects. Two particular cases will be analyzed: a fluid which at $t = 0$ is at rest (homogeneous initial condition) and a regime flow initially, subject to a sudden variation of the pressure (non homogeneous initial condition). For the sake of simplicity, the analysis is performed on a single harmonic, being the general case straightforward, according to the principle of superposition of the effects.

As a future work, this chapter could be represent a starting point for determine an analytical solution, more accurate than the Womersley one, for the compliant pipe. Moreover, the solution here evaluated can be integrated with the numerical analysis if utilized as inlet boundary condition. Indeed, a boundary condition of the Dirichlet type on the velocity avoid the use of a defective one, reducing significantly the computational cost.

2.2 Analytical formulation

For an axisymmetric flow in an infinitely long rigid pipe of radius R_0 subject to an unsteady pressure gradient, the system of Navier-Stokes equations reduces to the axial momentum balance only:[1]

$$\frac{\partial u_z}{\partial t} - \nu \left(\frac{\partial^2 u_z}{\partial r^2} + \frac{1}{r} \frac{\partial u_z}{\partial r} \right) = -\frac{1}{\rho} \frac{\partial p}{\partial z} \tag{2.1}$$

the pressure gradient at the right hand side being externally imposed. The solution of this equation could be decomposed as the sum of a particular solution, which takes into account the developed motion, and the general solution, which describes the transitory caused by the initial condition and corresponds to the solution of the homogeneous associated equation:

$$\frac{\partial u_z}{\partial t} - \nu \left(\frac{\partial^2 u_z}{\partial r^2} + \frac{1}{r} \frac{\partial u_z}{\partial r} \right) = 0 \tag{2.2}$$

Considering a pressure gradient of magnitude A and angular speed Ω with the form of a cosine wave,[2] written in the corresponding Euler form:

$$\frac{\partial p}{\partial z} = A \left(\frac{e^{i\Omega t} + e^{-i\Omega t}}{2} \right)$$

the associated Womersley solution, giving the particular solution of (2.1), becomes:

$$u_z(r,t) = \frac{AR_0^2}{2\mu} \frac{1}{i^3 \alpha^2} \left[\left(1 - \frac{J_0\left(\alpha i^{3/2} y\right)}{J_0\left(\alpha i^{3/2}\right)} \right) e^{i\Omega t} - \left(1 - \frac{J_0\left(i\alpha i^{3/2} y\right)}{J_0\left(i\alpha i^{3/2}\right)} \right) e^{-i\Omega t} \right]$$

$$\alpha = R_0 \sqrt{\frac{\Omega}{\nu}}$$

$$y = \frac{r}{R_0}$$

The solution of the homogeneous equation (2.2) could be found by a separation of variables, i.e. assuming that solution is of the form:

$$u_z(r,t) = F(r)G(t)$$

such that:

$$\frac{1}{\nu} \frac{G'}{G} = \left(\frac{F''}{F} + \frac{1}{r} \frac{F'}{F} \right) \tag{2.3}$$

---

[1] Indeed for this motion $v_r = 0$, so continuity equation reduces to $\frac{\partial v_r}{\partial z} = 0$ and radial momentum to $\frac{\partial p}{\partial r} = 0$

[2] The results for a sine wave could be determined by the same procedure

This equation implies that each member should be constant, being function of one variable only. Hence:

$$\begin{aligned} G'(t) &= -\nu\lambda^2 G(t) \\ F'' + \frac{1}{r}F' + \lambda^2 F &= 0 \end{aligned}$$

In order to ensure that the solution is limited is space, we have:

$$\begin{aligned} G(t) &= Be^{-\lambda^2 \nu t} \\ F(r) &= CJ_0(\lambda r) \end{aligned}$$

and, applying the boundary conditions:

$$\begin{aligned} \lambda_j &= \frac{\gamma_j}{R_0} & \gamma_j &: J_0(\gamma_j) = 0 \\ F(r) &= \sum_{j=0}^{\infty} C_j J_0(\gamma_j y) & y &= \frac{r}{R_0} \end{aligned}$$

we finally obtain:

$$u_{z_{\mathbf{hom}}} = \sum_{j=0}^{\infty} E_j e^{-\left(\frac{\gamma_j}{R_0}\right)^2 \nu t} J_0(\gamma_j y) \tag{2.4}$$

The following relations accounting for the orthogonality of Bessel functions will be used in the following for determining the coefficients E_j:[3]

$$\int_0^1 y J_p(\gamma_{i_p} y) J_p(\gamma_{j_p} y) dy = \delta_{ij} \frac{1}{2} \left(J'_p(\gamma_{i_p})\right)^2$$

$$f(r) = \sum_{j=0}^{\infty} f_j J_0\left(\gamma_j \frac{r}{R}\right) \tag{2.5}$$

$$f_j = \frac{2R_0^2}{(J'_0(\gamma_j))^2} \int_0^1 y f(y) J_0(\gamma_j y) dy \tag{2.6}$$

for:

- a fluid initially at rest

---

[3] Remembering that the Bessel solution for the axisymmetric problem depends on J_0 only

- a sudden variation of the pressure, starting from a developed flow condition

Remark The transitory determined for both the formulations come from the solution of an homogeneous equation; as a consequence, it does not depend on the frequency and thus on Womersley number a priori. Conversely, the time employed to reduce the homogeneous solution is affected by the values of the viscosity and of the radius pipe. The effects of the Womersley number on the transitory effects are introduced when one determines the coefficients E_j, being this coefficient dependent on the initial solution and so on the particular solution. The stronger effect is related to the phase-lag. Indeed, considering the case of a flux initially at rest and taking into account the analysis of the phase lag between the flux and the pressure gradient reported in [68], when $\alpha \to \infty$ the phase lag tends to $\pi/2$. As a consequence, the flux tends to 0 at the initial time and the coefficients E_j tend to vanish.

2.2.1 Flow initially at rest

In this case, imposing an homogeneous initial condition at $t = 0$ implies that the following relation must hold:

$$\sum_{j=1}^{\infty} E_j J_0(\gamma_j y) = \frac{AR_0^2}{2\mu}\frac{1}{i^3\alpha^2}\left(\frac{J_0\left(\alpha i^{3/2} y\right)}{J_0\left(\alpha i^{3/2}\right)} - \frac{J_0\left(i\alpha i^{3/2} y\right)}{J_0\left(i\alpha i^{3/2}\right)}\right) \tag{2.7}$$

$$y = \frac{r}{R_0}$$

From Eq. (2.7) and relation (2.5)-(2.6) it follows:

$$E_j = \frac{AR_0^2}{\mu}\frac{\gamma_j}{J_1\left(\gamma_j\right)}\frac{2}{\gamma_j^4 + \alpha^4}$$

and, therefore, the solution:

$$\begin{aligned}u_z(r,t) = &\sum_{j=0}^{\infty} \frac{AR_0^2}{\mu} \frac{2\gamma_j}{J_1\left(\gamma_j\right)\left(\gamma_j^4+\alpha^4\right)} e^{-\left(\frac{\gamma_j}{R_0}\right)^2 \nu t} J_0\left(\gamma_j y\right) \\ &+ \frac{AR_0^2}{2\mu} \frac{1}{i^3\alpha^2} \left(1 - \frac{J_0\left(\alpha i^{3/2} y\right)}{J_0\left(\alpha i^{3/2}\right)}\right) e^{i\Omega t} \\ &- \frac{AR_0^2}{2\mu} \frac{1}{i^3\alpha^2} \left(1 - \frac{J_0\left(i\alpha i^{3/2} y\right)}{J_0\left(i\alpha i^{3/2}\right)}\right) e^{-i\Omega t}\end{aligned}$$

2.2.2 Sudden variation of pressure

In this case the boundary condition is represented by a fully developed motion driven by an external pressure gradient which varies in time by a cosine law.[4] Let A_1 and Ω_1 be the magnitude of the pressure gradient and the frequency of the initial condition and α_1 it's Womersley number. At a time $t = t^*$ a sudden variation of pressure is imposed (generally both in frequency and amplitude), such that the initial velocity profile is represented by:

$$\begin{aligned}u_0 &= \frac{A_1 R_0^2}{2\mu i^3 \alpha_1^2} \left[\left(1 - \frac{J_0\left(\alpha_1 i^{3/2} y\right)}{J_0\left(\alpha_1 i^{3/2}\right)}\right) e^{i\phi} - \left(1 - \frac{J_0\left(i\alpha_1 i^{3/2} y\right)}{J_0\left(i\alpha_1 i^{3/2}\right)}\right) e^{-i\phi}\right] \\ \phi &= \Omega_1 t^*\end{aligned}$$

The problem does not depend on a translation in time, and it is possible to re-scale the time so that the origin of the new time axis coincides with t^*. Denoting by A_2 and Ω_2 the magnitude and the frequency of the new pressure gradient, by applying relation (2.5)-(2.6) it follows:

$$E_j = \frac{2\gamma_j R_0^2}{\mu J_1\left(\gamma_j\right)} \left[\frac{A_2}{\gamma_j^4+\alpha_2^4} - \frac{A_1}{\gamma_j^4+\alpha_1^4} \left(\frac{\alpha_1^2}{\gamma_j^2} \frac{e^{i\phi}-e^{i\phi}}{2i} + \frac{e^{i\phi}+e^{i\phi}}{2}\right)\right]$$

---

[4] As far as a pressure gradient which varies with a sine law is concerned, the modifications are straightforward. Moreover, it is possible to consider a field which is not fully developed as initial condition, retaining the exponential term and applying the same procedure for obtain terms E_j, but for the sake of simplicity, this case is not considered here

and finally:

$$
\begin{aligned}
u_z(r,t) = & \sum_{j=0}^{\infty} \frac{2\gamma_j R_0^2}{\mu J_1\left(\gamma_j\right)} \frac{A_2}{\gamma_j^4+\alpha_2^4} e^{-\left(\frac{\gamma_j}{R_0}\right)^2 \nu t} J_0\left(\gamma_j y\right) \\
& - \sum_{j=0}^{\infty} \frac{2\gamma_j R_0^2}{\mu J_1\left(\gamma_j\right)} \frac{A_1}{\gamma_j^4+\alpha_1^4} \left(\frac{\alpha_1^2}{\gamma_j^2} \frac{e^{i\phi}-e^{i\phi}}{2i} + \frac{e^{i\phi}+e^{i\phi}}{2}\right) e^{-\left(\frac{\gamma_j}{R_0}\right)^2 \nu t} J_0\left(\gamma_j y\right) \\
& + \frac{A_2 R_0^2}{2\mu} \frac{1}{i^3 \alpha_2^2} \left(1 - \frac{J_0\left(\alpha_2 i^{3/2} y\right)}{J_0\left(\alpha_2 i^{3/2}\right)}\right) e^{i\Omega_2 t} \\
& - \frac{A_2 R_0^2}{2\mu} \frac{1}{i^3 \alpha_2^2} \left(1 - \frac{J_0\left(i\alpha_2 i^{3/2} y\right)}{J_0\left(i\alpha_2 i^{3/2}\right)}\right) e^{-i\Omega_2 t}
\end{aligned}
$$

2.3 Evaluation of the convergence of the series

This section is devoted to demonstrate that the series appearing in the homogeneous solution obtained in (2.4) totally converges. This property will be used in section (2.4) to determine the flux, since it will be possible to exchange the integral with the sum and hence integrate every term.

The following consideration are used to determine the asymptotically behavior of each term of the series:

- Every exponential term $e^{-\left(\frac{\gamma_j}{R_0}\right)^2 \nu t}$ has its maximum for $t = 0$
- The Bessel function of order zero $J_0(z)$ is at least $C^0(\mathbb{R})$ and is equal to 1 at $z = 0$; moreover, observing that

  $$\lim_{z \to \infty} J_0(z) = \sqrt{\frac{2}{\pi z}} cos\left(z - \frac{\pi}{4}\right)$$

  it is possible to infer that

  $$|J_0(x)| \leq M_1$$

  with M_1 a finite quantity.
- By the derivation rule for Bessel functions it follows that

  $$J_1(x) = -\frac{d}{dx} J_0(x)$$

and, as a consequence, the zeros of $J_1(x)$ correspond to the maximum/minimum of $J_0(x)$; moreover for each γ_j an interval of radius δ exists where $J_0(x)$ changes sign. The zeros of $J_0(x)$ then aren't a maximum/minimum, and do not correspond to the zeros of $J_1(\gamma_j)$. Therefore, it is possible to write:

$$\left|\frac{1}{J_1(\gamma_j)}\right| \leq M_2$$

- by the relations:

$$\lim_{n\to\infty} a_{n+1} - a_n = \pi$$
$$\Rightarrow a_n \approx a_0 + n\pi,\ n \to \infty$$

  it is possible to approximate asymptotically γ_j with $n\pi$ as n tends to infinity; moreover the zeros of $J_0(x)$ are inferior limited by $\gamma_1 > 0$ and ordered

- all the others term which appear in the solution giving E_j are do not depend on j

Therefore, it follows that:

$$\begin{aligned} &|E_j J_0(\gamma_j y)| \leq M_j \\ &\lim_{n\to\infty} M_n = 0 \qquad\qquad O(n^3) \end{aligned} \tag{2.8}$$

The series $\sum_{n=1}^{\infty} M_n$ thus converges and, hence, the series $\sum_{j=1}^{\infty} E_j J_0(\gamma_j y)$ totally converges on $\mathbb{R}^{+}$[5].

2.4 Evaluation of the flux variation in time

Flux variation with time depends on a term related to the homogeneous solution and on a term related to the particular one. In this section only

---

[5] By symmetry considerations with respect to the axis $y = 0$ it is possible to infer the convergence on the whole $\mathbb{R}$

the former is determined, while the interested reader can find the details related to the determination of the latter in [68]. Taking advantage of the results reported in section 2.3, it is possible to exchange the integral with the summation in equation 2.4, the integral of $J_0(\gamma_j y)$, yielding:

$$2\pi R_0^2 \int_0^1 y J_0\left(\gamma_j y\right) dy = \frac{2\pi R_0^2}{\gamma_j} J_1\left(\gamma_j\right)$$

The total flux then becomes:

$$\begin{aligned} Q(t) =& 2\pi R_0^2 \sum_{j=0}^{\infty} \frac{E_j}{\gamma_j} J_1(\gamma_j) e^{-\left(\frac{\gamma_j}{R_0}\right)^2 \nu t} \\ &+ \frac{\pi R_0^4 A_2}{2\mu i^3 \alpha_2^2} \left(\left(1 - F_{10}(\alpha_2)\right) e^{i\Omega t} - \left(1 - F_{10}(i\alpha_2)\right) e^{-i\Omega t} \right) \\ F_{10}(\alpha) =& \frac{2 J_1\left(\alpha i^{3/2}\right)}{\alpha i^{3/2} J_0(\alpha i^{3/2})} \\ F_{10}(i\alpha) =& \frac{2 J_1\left(i\alpha i^{3/2}\right)}{i\alpha i^{3/2} J_0(i\alpha i^{3/2})} \end{aligned}$$

2.5 Numerical experiments

In this section the results of the new complete solution are showed for two case:

1. a flow initially at rest
2. a flow with double variation of pressure

The former resembles the beginning of a motion in a pulsating device aimed at supporting or replacing human blood circulation. The latter mimics although quite simply a sudden arterial pressure drop followed by normal pressure recovery.

The first example is quite simple and shows what happens for a motion under a pulsating gradient starting from rest; the physical parameters here considered are reported in table 2.1. For the transitory 30 coefficients were

Pipe radius (R_0)	$0.005\,m$
Fluid density (ρ)	$1055\,Kg/m^3$
Fluid viscosity (μ)	$0.0037\,Pa\cdot s$
Pressure gradient (dp/dx)	$-50000\,Pa/m$ ($-3.7603\,mmHg/cm$)
Pressure variation period T	$1.0\,s$

Table 2.1: Physical parameters for the case 1

adopted. As it is possible to see in figure 2.1 and in table 2.2, the flux requires three periods to reach the regime value. Denoting by

$$C = \Re\left[F_{10}\left(\alpha\right)\right] \qquad\qquad D = \Im\left[F_{10}\left(\alpha\right)\right]$$

The flux variation in time related to the particular solution could be rewritten as:

$$Q_{part}(t) = \frac{\pi R_0^4 A}{\mu\alpha^2}\left((C-1)\sin(\Omega t) + D\cos(\Omega t)\right) \tag{2.9}$$

the time value $\bar{t}$ corresponding to the positive peaks value of (2.9) are those which satisfy the following relation:

$$\begin{aligned} \tan\left(\Omega\bar{t}\right) &= \frac{C-1}{D} \\ \Omega\bar{t} &= \arctan\left(\frac{C-1}{D}\right) + k2\pi = \phi + k2\pi \end{aligned} \tag{2.10}$$

The ratio between the total solution and the particular solution, evaluated on the peaks, thus becomes:

$$\frac{Q}{Q_{part}}\left(t=\bar{t}\right) = 1 + \frac{4}{D\alpha^2\left(1+\left(\frac{C-1}{D}\right)^2\right)\cos\left(\phi\right)}\sum_{j=1}^{\infty}\frac{e^{-(\gamma_j/\alpha)^2(\phi+k2\pi)}}{1+\left(\frac{\gamma_j}{\alpha}\right)^4}$$

In table 2.2 the values of the ratio between the total solution and the particular solution evaluated at some peaks are reported. From the third period the difference between the regime value and the actual one is less than the 1%. For the same example, in figure 2.2 the axial velocity profile is depicted for the initial condition (i.e., $t = 0$) and for $t = 1\,s$, $t = 2\,s$ and $t = 4\,s$. In

peak n	1	2	3	4	6	7	8	9
ratio	0.81971	0.96762	0.99361	0.99874	0.99995	0.99999	1.0	1.0

Table 2.2: Ratio between the total solution and the particular solution evaluated on peaks for the flux, case 1

the same graphs the Womersley and the homogeneous solution are reported for the same time values. Except the initial condition, the weight of the homogeneous solution is greater near the axis of the pipe.

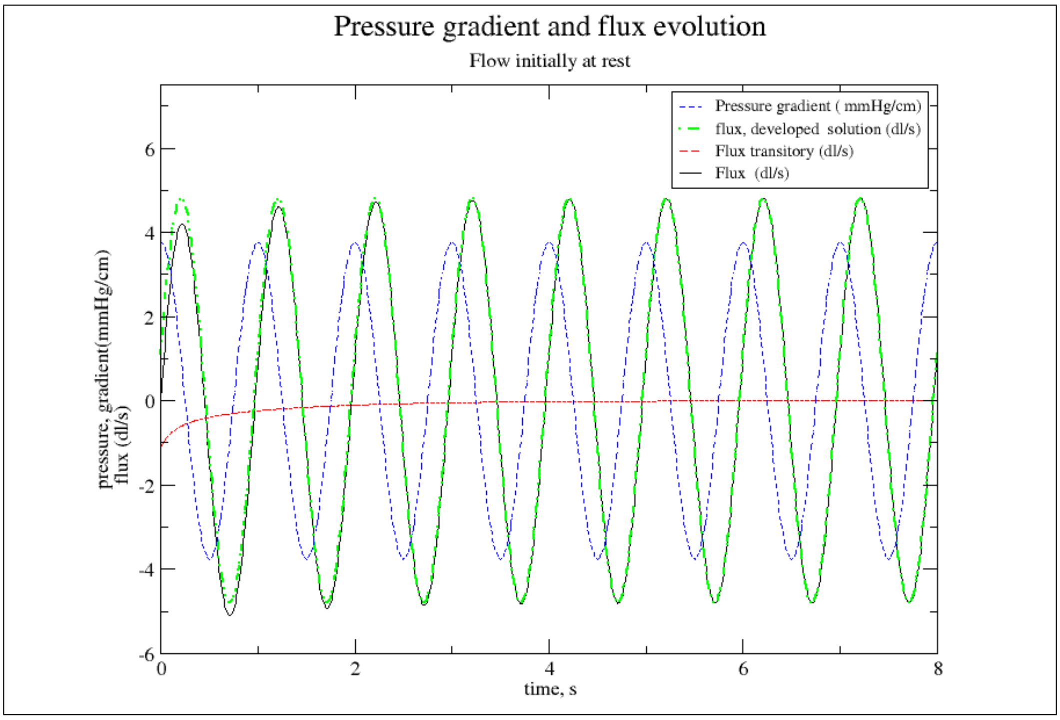

Figure 2.1: Flux and pressure gradient vs time for the first case. The blue line represents the pressure gradient. The black line represents the global solution, the green line the solution obtained by Womersley and the red line represents the homogeneous solution, which is responsible of the transitory.

For the second case the solution is obtained by applying twice the same procedure adopted for evaluating the coefficients E_j for a sudden variation of pressure; for the second transitory, terms related to the the transitory of the first variation appear; taking into account the property of orthogonality of

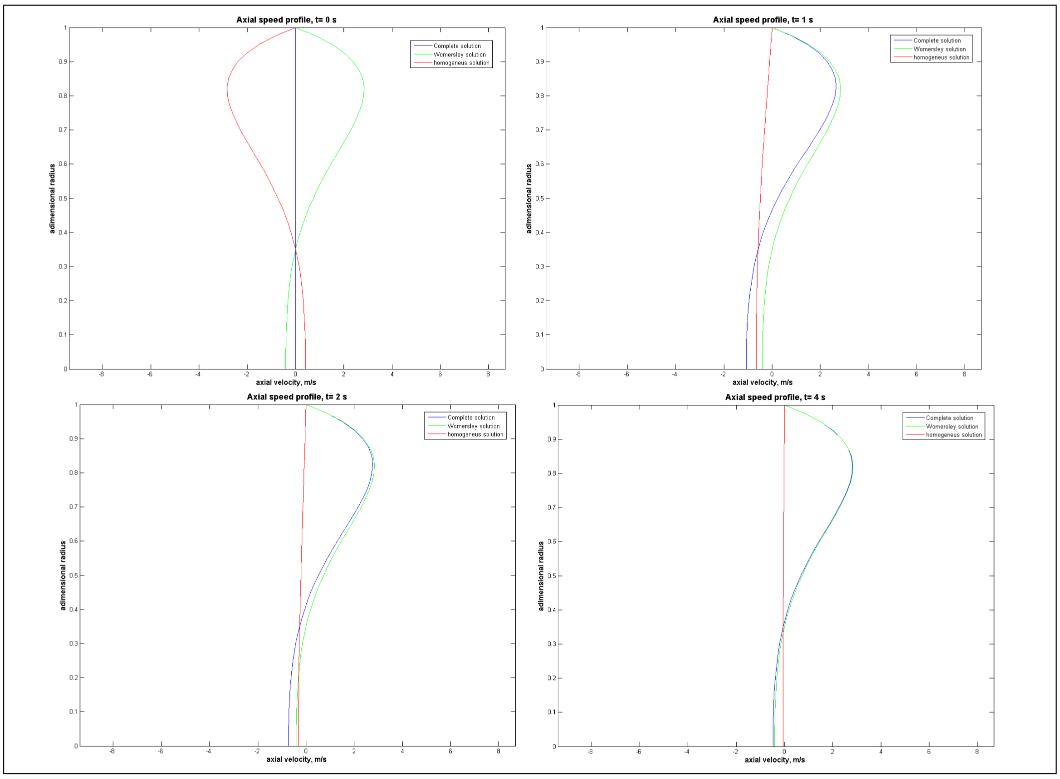

Figure 2.2: Axial velocity profile for case 1 for the initial condition (top left), $t = 1\,s$ (top right), $t = 2\,s$ (bottom left) and $t = 4\,s$ (bottom right). Blue line: global solution; green line: solution obtained from Womersley; red line: homogeneous solution.

the Bessel functions and denoting respectively by E_j^1 and E_j^2 the coefficients of the first and the second transitory, these new terms read:

$$E_j^2 = E_j^1 e^{-\left(\frac{\gamma_g}{R_0}\right)^2 \nu t^*}$$

being t^* the time elapsed between the first and the second variation. In this experiment, the transitory is evaluated through 50 coefficients. The pressure gradient is depicted in fig 2.3 (blue line), obtained from a Fourier transformation of a set of experimental data sampled from a canine femoral arteria, as described in [46]. Values adopted for the physical parameters are reported

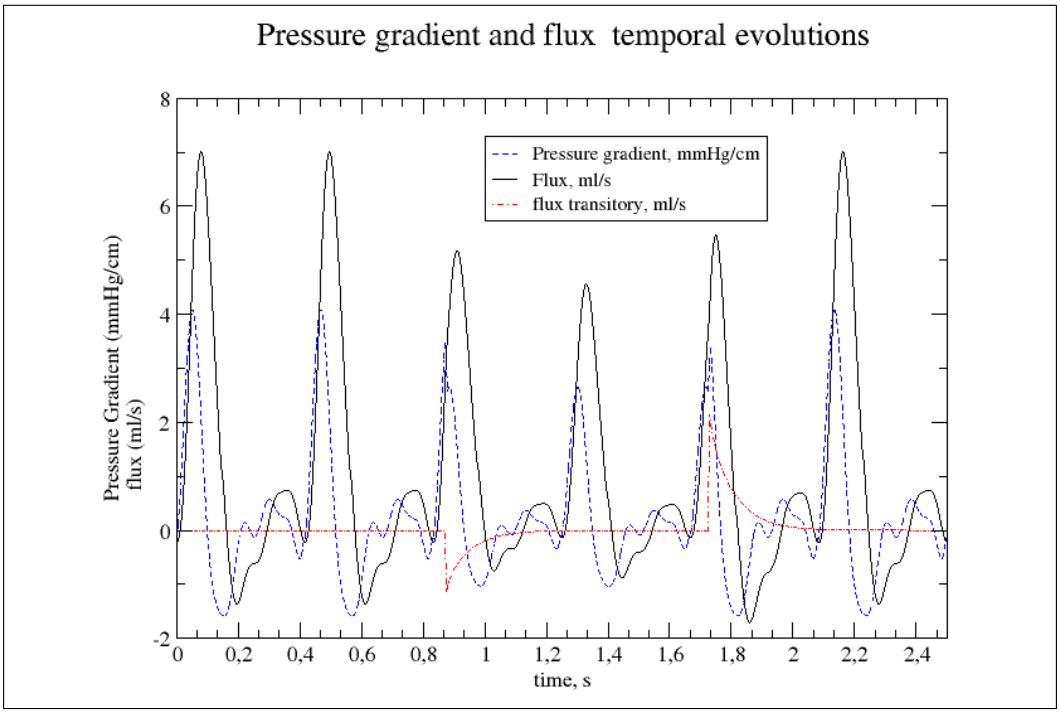

Figure 2.3: Pressure gradient (blue line), flux (black line) and flux transitory (red line) vs time. Pressure gradient is represented in $mmHg/cm$, while flux in ml/s.

in table 2.3 In figure 2.3 the flux vs time (black line) and the transitory vs time (red line) are also reported. Clearly, the sudden variation of the pressure gradient yields a variation on the blood flow with the appearance of a transitory until the onset of the new regime. In particular, the transitory yields a gradual settlement of the flow to the new conditions. In the simulated conditions, in particular, one could observe that the peak flow resulting

Pipe radius (R_0)	$0.0013\,m$
Fluid density (ρ)	$1055\,Kg/m^3$
Fluid viscosity (μ)	$0.004\,Pa \cdot s$
Pressure variation period T	$0.4167\,s$
Ratio between decreased and initial(final) pressures k	0.65
Global time at which the first variation occurs (t_1) :	$0.875\,s$ ($2.1T$)
Global time at which the second variation occurs (t_2) :	$1.7292\,s$ ($4.15T$)

Table 2.3: Physical parameter for the case 2

from the decrease in pressure gradient (3rd peak in figure 2.3) is initially, i.e., where there occurs the transition, the higher the peak is produced in the new regime. Of course, the same is lower as compared to the one (2nd peak in figure 2.3) of the previous period.

Similarly, when the pressure returns to the standard value (i.e., the value before the first pressure change), the peak flow (5th peak in figure 2.3) is initially less than that (6th peak in figure 2.3) of the next regime (compared with the last one of the previous period is higher of course). The figure also shows that the duration of the transient regime generated by the reduction in pressure gradient is less than the one generated by the increase of the pressure gradient; indeed, the time needed to restore the physiological flow conditions, is longer than the one needed to have the developed condition related to the smaller pressure gradient. In particular, the first transition has a duration approximately equal to 0.8T, while the second is about 1T. This is related to the phase at which the variation occurs, i.e. to the initial condition. Indeed, the pure exponential does not change, depending only on the viscosity and the pipe radius.

In table 2.4 the ratio between the first and the $i-th$ flux peak is reported; the flux needs in this case one period to adapting to the variation of the pressure gradient, diminishing if this decreases and increasing when it raises.

peak n	1	2	3	4	5	6	7
ratio	1.0	1.0	0.74	0.65	0.78	1.0	1.0

Table 2.4: Ratio between the first and the $i-th$ peak of the flux for case 2

Remark If the analysis related on the time needed to adapting to the new condition is performed in terms of the number of period, there is a dependence of the Womersley number on the exponent part too, as it is possible to find by a dimensionless form of the momentum equation in which the frequency is chosen for obtain a dimensionless time. This is not in contrast to Remark 6; in this regards, neglecting the effects of the Womersley number on the phase lag for the sake of simplicity, let us consider two fluid initially at rest, the first driven by a frequency f_1, while the second driven by a frequency f_2 such that $f_2 = 2f_1$. the time t_1 at which the first peak occurs for the first fluid corresponds to the time $t_2 = t_1$ at which the second peak occurs for the second fluid. Being the exponential independent on the frequency, the ratio between a peak of the developed motion and a peak at time t_1 does not change.

2.6 Conclusion

The analysis of this section has demonstrated that the transitory effects can have an important impact on the global solution if the time interval under analysis is not sufficiently long. Indeed, if this is not the case, the Womersley solution shows its limitation, being aimed at modeling a fully developed regime, a regime in which all the transient effects became negligible. Nevertheless, this solution can be used as the particular solution of the problem and "enriched" by the transitory effects, solution of the associated homogeneous equation. The effects related to the solution of the homogeneous equation have general validity, being independent on the right hand side; the effects related to the particular solution are re-introduced through the determination of the coefficients E_j. For which concerns a pulsating flow, the dependence on the Womersley number is related to the phase-lag between the pressure and the flux. In particular, if one consider a flow initially at rest driven by a cosine-law pressure gradient, when $\alpha \to \infty$ the phase-lag tends to $\pi/2$ so the particular solution tends to be at rest for $t = 0$. It follows that the coefficients E_j tend to vanishes.

The main parameters which affect the time interval in which the homogeneous solution expires are the viscosity (linear dependency) and the radius of the pipe (inverse quadratic dependency).

Two particular examples were analyzed:

1. The motion of a flow initially at rest, driven by a pulsating pressure gradient
2. A double pressure variation of a more complex pressure gradient, which tends to mimic what happens in the fainting

In these example it is showed that it is possible to study what happens before the flow is fully developed. This yields a new solution which corresponds in augmenting the previous one with a contribute which decrease exponentially in time. As far as the second case is concerned, it is possible to find a dependence of the transitory on the time in which the pressure changes, by applying the same considerations performed for dependency on the phase-lag.

Part II

Fluid-Structure Interaction problems

Introduction

A fluid-structure interaction problem consists in determining the motion of two different continua, interacting each other along a portion of the common boundary. Typically the response of each continuum to external loads is not the same: fluids, for example, are governed by viscous-dissipative effects, while the solid response is mainly related to elastic-conservative effects; even though visco-elastic phenomena could be still active. Often the constitutive laws of each continuum are better described using different natural frames of reference. For example, the Eulerian framework could be used for the fluid portion while solid deformations are better described in Lagrangian coordinates. The resulting model yields a coupled system of equation: each must satisfy two conditions at the fluid-solid interface:

- fluid and solid must have the same velocity at the interface(no-slip condition, kinematic coupling);
- fluid and solid normal stresses must be mutually balanced at the interface (the action-reaction principle, dynamic coupling);

Clearly, being the displacement of the solid unknown, the fluid-structure interface is also unknown and is the shape of the fluid domain: this generates a non-linear problem that generates internal iterations when the problem is solved numerically. A second major difficulty is related to the remeshing the entire domain whenever deformations are large and the element aspect ratios become unacceptable. This can occurs at every internal iteration, leading to unsurmountable computational costs. In order to minimize these deficiency two approaches are the more viable and used:

- the Arbitrary Lagrangian Eulerian (ALE) [22, 23, 35]
- and the Immersed Finite Element (IFEM) / Immersed Boundary (IB) Method [44, 53]

A comparative description of the two approaches can be roughly summarized as follows. The former adapts the fluid domain to the solid, by rewriting the equation of the problem in a reference frame that moves by an arbitrary displacement. The latter models the solid as a source term for the fluid equations.

Chapter 3

The Arbitrary Lagrangian Eulerian Method

The Arbitrary Lagrangian Eulerian method (ALE) combines the Lagrangian and Eulerian reference frames, exploiting the advantages of each. Typically a Lagrangian reference frame is useful in solid mechanics, because the resulting displacement defines the motion of each particle of the solid and so the mass conservation is satisfied implicitly. From the computational point of view this allows the use of a fixed computational mesh and defining and solving only the momentum conservation equation, being the mass conservation satisfied implicitly.

On the other hand, a Lagrangian frame of reference is "unfair" for fluid mechanics: fluid particles indeed are not cohesive as in the solid and can move away significantly from each another generating vortices, with the result that the position of a sample domain could be excessively deformed and/or overlap, resulting in a difficult description of the fluid motion, which is often better described with an Eulerian reference system. In this case, mass conservation must be explicitly enforced on the domain of interest. From a computational point of view this allows reuse of a fixed computational mesh where the mass and momentum conservation equations must be solved simultaneously. However, an Eulerian reference frame does not provide the fluid particle path, so is suboptimal for problems in which one or more boundaries move, such as for example a free surface.

An Arbitrary Lagrangian Eulerian formulation adapts the domain to the moving boundary, rewriting the equation of motion in a moving reference. It follows that time derivatives are expressed with respect to a fixed reference configuration and a homeomorphism (called ALE mapping and denoted by $\mathcal{A}_t : \Omega_0 \to \Omega(t)$) is used to match a point at time t in the current domain $\Omega(t)$ to the corresponding point in the reference configuration Ω_0. ALE mapping is arbitrary, but has ensure consistency of the domain to the evolution of the boundary interface. Hence the restriction of the mapping to the fluid boundary interface has to provide the configuration at time t of the structure boundary interface. Numerically, the mapping provides also the evolution of the spatial grid. In this case an ODE system, arising from the spatial discretization provides the evolution of the solution along trajectories, that are fully contained in the computational domain for each time. Moreover, after time discretization, the numerical scheme determines the temporal evolution of the unknowns at the nodes of the grid and consequently the evolution of the degrees of freedom as typical of classical finite element approach.

3.1 ALE formulation

Let $\mathcal{A}_t$ be a family of mappings, defined by the following homeomorphism:

$$\mathcal{A}_t : \Omega_0 \in \mathbb{R}^d \to \Omega_t \in \mathbb{R}^d, \qquad \boldsymbol{x}(\boldsymbol{Y}, t) = \mathcal{A}_t(\boldsymbol{Y}) \quad \forall t \in]t_0, T[$$

where $\boldsymbol{Y}$ denotes the coordinates in the reference fixed frame, while $\boldsymbol{x}$ denotes the coordinates in the time varying (current) frame. As we assumed that $\mathcal{A}_t$ is continuous on $\overline{\Omega}_0$ and has continuous inverse, and that the function:

$$t \to \boldsymbol{x}(\boldsymbol{Y}, t), \qquad \boldsymbol{Y} \in \Omega_0$$

is differentiable almost everywhere in $I = [t_0, T[$. For a generic function $f : \Omega_t \times I \to \mathbb{R}$ defined on an Eulerian reference frame, it is then possible to define the corresponding function on the ALE reference frame, as follows:

$$f : \Omega_0 \times I \to \mathbb{R}, \qquad f(\boldsymbol{Y}, t) = f(\mathcal{A}_t(\boldsymbol{Y}), t)$$

The time derivative on the ALE reference frame (i.e. on the ALE space coordinates) is defined as:

$$\left.\frac{\partial f}{\partial t}\right|_{\boldsymbol{Y}} : \Omega_t \times I \to \mathbb{R}, \qquad \left.\frac{\partial f}{\partial t}\right|_{\boldsymbol{Y}}(\boldsymbol{x}, t) = \frac{\partial \hat{f}}{\partial t}(\boldsymbol{Y}, t), \boldsymbol{Y} = \mathcal{A}_t^{-1}(\boldsymbol{x})$$

while velocity is:

$$\boldsymbol{w}(\boldsymbol{x}, t) = \left.\frac{\partial \boldsymbol{x}}{\partial t}\right|_{\boldsymbol{Y}}$$

Now it is possible to determine the ALE formulation for a time-dependent problem of the form:

$$\left.\frac{\partial u}{\partial t}\right|_{\boldsymbol{x}} + \mathcal{L}(u) = f$$

Applying the chain rule on time derivative, the following relation holds:

$$\left.\frac{\partial u}{\partial t}\right|_{\boldsymbol{Y}} = \left.\frac{\partial u}{\partial t}\right|_{\boldsymbol{x}} + \left.\frac{\partial \boldsymbol{x}}{\partial t}\right|_{\boldsymbol{Y}} \cdot \nabla_{\boldsymbol{x}} u = \left.\frac{\partial u}{\partial t}\right|_{\boldsymbol{x}} + \boldsymbol{w} \cdot \nabla_{\boldsymbol{x}} u$$

so the problem becomes:

$$\left.\frac{\partial u}{\partial t}\right|_{\boldsymbol{x}} - \boldsymbol{w} \cdot \nabla_{\boldsymbol{x}} u + \mathcal{L}(u) = f$$

The corresponding conservative form of the original problem reads:

$$\left.\frac{\partial u}{\partial t}\right|_{\boldsymbol{x}} + \nabla_{\boldsymbol{x}} \cdot \boldsymbol{F} = f$$

where $\boldsymbol{F}$ represents the flux of the unknown u. Denoting by $J_{\mathcal{A}_t}$ the Jacobian of the mapping, by the Euler expansion:

$$\left.\frac{\partial J_{\mathcal{A}_t}}{\partial t}\right|_{\boldsymbol{Y}} = J_{\mathcal{A}_t} \nabla_{\boldsymbol{x}} \cdot \boldsymbol{w}$$

$$J_{\mathcal{A}_{t_0}} = 1$$

Let V_t be an arbitrary sub-domain of Ω_t, such that $V_t = \mathcal{A}_t(V_0)$, it follows:

$$\frac{d}{dt}\int_{V_t} u d\Omega = \frac{d}{dt}\int_{V_0} u J_{\mathcal{A}_t} d\Omega = \int_{V_0} \left.\frac{\partial(uJ_{\mathcal{A}_t})}{\partial t}\right|_{\mathbf{Y}} d\Omega = \int_{V_t}\left[\left.\frac{\partial u}{\partial t}\right|_{\boldsymbol{Y}} + u\nabla_{\boldsymbol{x}}\cdot\boldsymbol{w}\right] d\Omega$$

so in the ALE reference frame:

$$\frac{d}{dt}\int_{V_t} u d\Omega + \int_{V_t} \nabla_{\boldsymbol{x}}\cdot(\boldsymbol{F} - \boldsymbol{w}u)\, d\Omega = \int_{V_t} f d\Omega$$

or, on the reference domain:

$$\int_{V_0}\left\{\left.\frac{\partial(uJ_{\mathcal{A}_t})}{\partial t}\right|_{\boldsymbol{Y}} + J_{\mathcal{A}_t}\left[\nabla_{\boldsymbol{x}}\cdot(\boldsymbol{F} - \boldsymbol{w}u) - f\right]\right\} d\Omega = 0$$

Since V_0 is arbitrary, it follows that:

$$\left.\frac{\partial(uJ_{\mathcal{A}_t})}{\partial t}\right|_{\boldsymbol{Y}} + J_{\mathcal{A}_t}\nabla_{\boldsymbol{x}}\cdot(\boldsymbol{F} - \boldsymbol{w}u) = J_{\mathcal{A}_t} f$$

3.2 Construction of the map $\mathcal{A}_t$

The construction of the ALE map $\mathcal{A}_t$ can be translated to the following:

Problem 1 *Given the time evolution of the interface boundary:*[1]

$$\boldsymbol{g} : \partial\Gamma_0 \times I \to \partial\Gamma_t$$

find the homeomorphism $\mathcal{A}_t$ *such that*

$$\begin{aligned} &\mathcal{A}_t(\boldsymbol{Y}) = \boldsymbol{g}(\boldsymbol{Y}, t), && \boldsymbol{Y} \in \partial\Gamma_0 \\ &\mathcal{A}_t(\boldsymbol{Y})\cdot\boldsymbol{n} = 0, && \mathbf{Y} \in \partial\Omega\backslash\partial\Gamma_0 \end{aligned}$$

where $\boldsymbol{n}$ *denotes the outward normal.*

Normally one needs to know $\mathcal{A}_t$ only at some time values, generally coming from the temporal discretization. Thus the typical approach to determine the required homeomorphism consists in a harmonic extension of the boundary conditions at a prescribed time $t = \bar{t}$; this is translated in the following:

---

[1] Or, more generally, the time evolution of the moving boundary

Problem 2 *Let* $\boldsymbol{g}(\boldsymbol{Y},\bar{t})$ *be the interface boundary position at time* $t=\bar{t}$*, find* $\boldsymbol{x}(\boldsymbol{Y})$ *such that:*

$$\begin{aligned} &\nabla_{\boldsymbol{Y}}\cdot(k\nabla_{\boldsymbol{Y}}\boldsymbol{x})=\boldsymbol{0} && \boldsymbol{Y}\in\Omega_0\\ &\boldsymbol{x}(\boldsymbol{Y})=\boldsymbol{g}(\boldsymbol{Y},\bar{t}) && \boldsymbol{Y}\in\partial\Gamma_0\\ &\boldsymbol{x}(\boldsymbol{Y})\cdot\boldsymbol{n}=0 && \boldsymbol{Y}\in\partial\Omega_0\backslash\partial\Gamma_0 \end{aligned}$$

with k *a positive constant.*

3.3 Variational formulation of the Navier-Stokes Equations in an ALE reference frame

The Navier-Stokes equations can be rewritten as a particular case of the problem treated in section 3.1, where the flux $\boldsymbol{F}$ is decomposed in a (non-linear) convective part (i.e. a term which does not contain space derivatives) and in a part containing first order spatial derivatives in the $\boldsymbol{u}$ unknown. Navier-Stokes equations in a non-conservative ALE formulation become:

$$\begin{aligned} &\left.\left(\frac{\partial\boldsymbol{u}}{\partial t}\right)\right|_{\mathbf{Y}}+\left((\boldsymbol{u}-\boldsymbol{w})\cdot\nabla_{\boldsymbol{x}}\right)\boldsymbol{u}+\nabla_{\boldsymbol{x}}p-\nu\nabla^2_{\boldsymbol{x}}\boldsymbol{u}=0\\ &\nabla_{\boldsymbol{x}}\cdot\boldsymbol{u}=0 \end{aligned}$$

Note that only temporal derivatives are affected by the changing of reference frame.

Introducing the following functional spaces:

$$V(\Omega_t)=[H^1_0(\Omega_t)]^d \qquad\qquad Q(\Omega_t)=L^2(\Omega_t)$$

the variational formulation for the Navier-Stokes problem in an ALE frame becomes:

Problem 3 *Find* $\boldsymbol{u} \in V$ *such that:*

$$\begin{aligned}
&\int_{\Omega_t} \boldsymbol{v} \cdot \left(\left.\frac{\partial \boldsymbol{u}}{\partial t}\right|_{\boldsymbol{Y}} + (\boldsymbol{u} - \boldsymbol{w}) \cdot \nabla_{\boldsymbol{x}} \boldsymbol{u} \right) d\Omega + \\
&+ \int_{\Omega_t} (\nu \nabla_{\boldsymbol{x}} \boldsymbol{u} \cdot \nabla_{\boldsymbol{x}} \boldsymbol{v} - p \nabla_{\boldsymbol{x}} \cdot \boldsymbol{v})\, d\Omega = 0 \qquad \forall \boldsymbol{v} \in V(\Omega_t) \qquad (3.1) \\
&\int_{\Omega_t} q \cdot \nabla_{\boldsymbol{x}} \cdot \boldsymbol{u} = 0 \qquad \forall q \in Q(\Omega_t) \qquad (3.2) \\
&\boldsymbol{u} = \frac{\partial \boldsymbol{g}}{\partial t} \qquad \text{on } \partial\Gamma_t \qquad (3.3)
\end{aligned}$$

where $u \in H^1(\Omega_t)$, $q \in L^2(\Omega_t)$.

The aforementioned formulation is defined on an Eulerian frame of reference; moreover, the test functions are assumed to vanish on the boundary. To enforce this last condition on the moving domain we proceed as follows.First we rewrite the formulation in the reference domain. To this aim $\hat{V}(\Omega_0) = V(\Omega_0)$, $\hat{Q}(\Omega_0) = Q(\Omega_0)$. Then the ALE mapping defines the following set of functions in the current configuration:

$$\chi(\Omega_t) = \{v_i : \Omega_t \times I \to \mathbb{R},\ \ v_i = \hat{v}_i \circ \mathcal{A}_t^{-1},\ \hat{v}_i \in \hat{V}(\Omega_0)\} \qquad (3.4)$$

$$\chi_p(\Omega_t) = \{p : \Omega_t \times I \to \mathbb{R},\ \ p = \hat{p} \circ \mathcal{A}_t^{-1},\ \hat{p} \in \hat{Q}(\Omega_0)\} \qquad (3.5)$$

In order to have admissible spaces, the conditions $\chi(\Omega_t) \subset V(\Omega_t)$ and $\chi_p(\Omega_t) \subset Q(\Omega_t)$ must hold. This translates into conditions enforced on the ALE mapping. A sufficient but too restrictive condition is that the $\mathcal{A}_t$ be a $C^1(\Omega)$ dipheomorphism, i.e, $\forall t \in I$:

$$\begin{aligned}
&\mathcal{A}_t \in \boldsymbol{C}^1(\overline{\Omega_0}) && \mathcal{A}_t^{-1} \in \boldsymbol{C}^1(\overline{\Omega_t}) \\
&\boldsymbol{J}_{\mathcal{A}_t} \in \boldsymbol{L}^\infty(\Omega_0) && \boldsymbol{J}_{\mathcal{A}_t^{-1}} \in \boldsymbol{L}^\infty(\Omega_t)
\end{aligned}$$

This requirement is too restrictive and numerical methods do not satisfy them (indeed a function which belonging to H^1 does not be belongs to C^1). The following less restrictive criteria (and the correlated proof) can be found in [25]:

Proposition 1 *Let Ω_0 a bounded domain with Lipschitz-continuous boundary; moreover, let $\mathcal{A}_t$ be invertible on $\overline{\Omega}_0$ and satisfy the following conditions, $\forall t \in I$:*

- *$\Omega_t = \mathcal{A}_t(\Omega_0)$ be bounded and Lipschitz-continuous;*
- *$\mathcal{A}_t \in \boldsymbol{W}^{1,\infty}(\Omega_0)$, $\mathcal{A}_t^{-1} \in \boldsymbol{W}^{1,\infty}(\Omega_t)$*

Then, $v \in H^1(\Omega_t)$ if and only if $\hat{v} = v \circ \mathcal{A}_t \in H^1(\Omega_0)$; moreover the norms $\|v\|_{H^1(\Omega_t)}$ and $\|\hat{v}\|_{H^1(\Omega_0)}$ are equivalent.

Proposition 2 *Let*

$$\boldsymbol{x}(\boldsymbol{Y}, t) \in H^1(I; \boldsymbol{W}^{1,\infty}(\Omega_0))$$

if $\hat{v} \in H^1(I, H^1(\Omega_0))$, then $v = \hat{v} \circ \mathcal{A}_t^{-1} \in H^1(I, H^1(\Omega_t))$; moreover:

$$\left.\frac{\partial v}{\partial t}\right|_{\boldsymbol{Y}} \in L^2(I, H^1(\Omega_t))$$

3.4 Discretization of ALE mapping by finite element method

The discrete spaces chosen for the discretization of the problem affect the discretization type of the ALE mapping. During the movement of the computational domain the mapping must guarantee that triangulation remains consistent with the space chosen for the domain discretization. With referencing to a Lagrangian finite element space, we use the following notation to define the finite element space:

$$\mathcal{F}_{n,k}(\mathcal{T}_{0,h}) = \left\{ \hat{\psi}_h \in C^0(\overline{\Omega_0}),\, \left.\hat{\psi}_h\right|_{K_0} \circ \mathcal{M}_k^{K_0} \in P_n(K_R), \right. \\ \left. \forall K_0 \in \mathcal{T}_{0,h} \right\} \tag{3.6}$$

where $\hat{\psi}_h$ a function defined on the reference element K_0 and $\mathcal{M}_k^{K_0} \in P_k(K_R)$ is the homeomorphism that relates the coordinate system on the reference

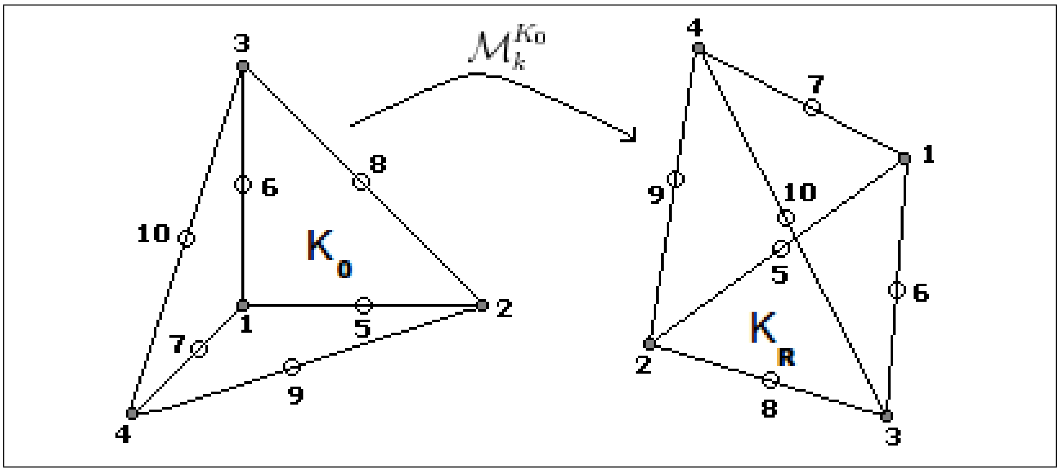

Figure 3.1: Mapping between unitary tetrahedron and mesh element for a Lagrangian $P2$ space

element K_0 (i.e. the unit simplex in 2D or the unit tetrahedron in 3D) to the global coordinates of the element of the mesh K_R (see figure 3.1 for an example for a $P2$ space). this homeomorphism is defined as follows:

$$\begin{aligned}\mathcal{M}_k^{K_0} : K_R \to K_0, \boldsymbol{Y}(\boldsymbol{\eta}) = \mathcal{M}_k^{K_0}(\boldsymbol{\eta}) = \\ = \sum_{i \in \mathcal{N}_k} \boldsymbol{Y}_i \tilde{\phi}_i(\boldsymbol{\eta}),\ \boldsymbol{\eta} \in K_r, \tilde{\phi}_i \in P_k(K_R)\end{aligned} \tag{3.7}$$

where $\tilde{\phi}$ is the $i-th$ shape function related to the $i-th$ node of the reference element that defines the parametric mapping, while $\boldsymbol{Y}_i$ are nodal coordinates on the transformed mesh element K_R and $\mathcal{N}_k$ are the total number of nodes defining the parametric mapping. Typical choice for $\mathcal{F}_{n,k}$ are the affine, $\mathcal{F}_{n,1}$ and the isoparametric, $\mathcal{F}_{n,n}$ spaces. For an admissible finite element formulation, space $V(\Omega_0)$ is to be approximated by the space $\mathcal{X}_h(\Omega_0) = \mathcal{F}_{n,k}(\mathcal{T}_{0,h})$, which implies that $\forall K_0 \in \mathcal{T}_{0,h}$, $\mathcal{M}_k^{K_0} \in P_k(K_R)$; moreover, the following relation must hold:

$$\chi_h(\Omega_t) = \Big\{\psi_h : \Omega_t \times I \to \mathbb{R}, \psi_h \circ \mathcal{A}_{h,t} = \hat{\psi}_h,\ \hat{\psi}_h \in \chi_h(\Omega_0)\Big\} \tag{3.8}$$

Considering the (3.8) implies that, for every time t, the following condition has to be verified:

$$\chi_h(\Omega_t) = \mathcal{F}_{n,k}(\mathcal{T}_{t,h})$$

where $\mathcal{T}_{t,h}$ represents the image of $\mathcal{T}_{0,h}$ through $\mathcal{A}_{h,t}$. The proof can be found in [25]. Hence we can state:

Proposition 3 *If at every time t the discretized ALE mapping satisfies:*

$$\mathcal{A}_{h,t}|_{K_0} \circ \mathcal{M}_k^{K_0} = \mathcal{M}_k^{K_t}, \qquad \forall K_0 \in \mathcal{T}_{0,h},\, K_t = \mathcal{A}_t(K_0) \tag{3.9}$$

(in particular, $\mathcal{A}_{h,t}|_{K_0} = \mathcal{M}_k^{K_t} \circ (\mathcal{M}_k^{K_0})^{-1}$), and for $t = t_0$:

$$\chi_h(\Omega_0) = \mathcal{F}_{n,k}(\mathcal{T}_{0,h})$$

then $\forall t \in I$, $\chi_h(\Omega_t)$, defined as in (3.8), satisfies:

$$\chi_h(\Omega_t) = \mathcal{F}_{n,k}(\mathcal{T}_{t,h})$$

As a consequence, a finite element space satisfying the proposition 3 is the isoparametric finite element space $\mathcal{F}_{k,k}(\mathcal{T}_{0,h})$ (For more details, see [25], pagg. 13-14).

3.5 Discretization of the Navier-Stokes equation in an ALE reference frame

The discretization of the Navier-Stokes problem is obtained by using the finite element spaces described above together with a a backward Euler time stepping scheme.

The finite element space on the domain Ω_t given by $\mathcal{F}_{n,k}(\mathcal{T}_{t,h})$, corresponding (through the ALE mapping) to the space $\mathcal{F}_{n,k}(\mathcal{T}_{0,h})$ of functions defined on Ω_0, as defined in (3.6). Denoting by $\mathcal{N}$ the total number of mesh nodes and by $\mathcal{N}_{int} < \mathcal{N}$ the number of nodes that do not belong to the Dirichlet boundaries, set of basis functions for the problem unknowns is represented by:

$$\{v_i,\ \ v_i \in \chi_h(\Omega_t),\ i = 1, ..., \mathcal{N}\}$$
$$\{q_i,\ \ q_i \in \chi_{p_h}(\Omega_t),\ i = 1, ..., \mathcal{N}\}$$

while trial function spaces are defined by:[2]

$$\chi_{0,h}(\Omega_t) = \chi_h(\Omega_t) \cap H^1_0(\Omega_t) = \{v_i, \ \ i = 1, ..., \mathcal{N}_{int}\}$$
$$\chi_{p_{0,h}}(\Omega_t) = \chi_{p_h}(\Omega_t) \cap L^2_0(\Omega_t) = \{q_i, \ \ i = 1, ..., \mathcal{N}\}$$

We denote by $\boldsymbol{u}_h^n = \boldsymbol{u}_h(n\Delta t)$, the approximation at time $t_n = n\Delta t$, where Δt the time step size. The discrete formulation is given by:

Problem 4 *Find $\boldsymbol{u}_h^{n+1}, p_h^{n+1}$ satisfying:*

$$\begin{aligned}
&\int_{\Omega_t} \left(\frac{\boldsymbol{u}_h^{n+1} - \boldsymbol{u}_h^n}{\Delta t} \cdot \boldsymbol{v}_h + (\boldsymbol{u}_h^{n+1} - \boldsymbol{w}_h) \cdot \nabla_{\boldsymbol{x}} \boldsymbol{u}_h^{n+1} \cdot \boldsymbol{v}_h \right) d\Omega \\
&\quad + \nu \int_{\Omega_t} \nabla_{\boldsymbol{x}} \boldsymbol{u}_h^{n+1} \cdot \nabla_{\boldsymbol{x}} \boldsymbol{v}_h d\Omega \\
&\quad - \int_{\Omega_t} p_h^{n+1} \nabla_{\boldsymbol{x}} \cdot \boldsymbol{v}_h = 0 && \forall \boldsymbol{v}_h \in \boldsymbol{\chi}_{0,h}(\Omega_t) \qquad (3.10) \\
&\int_{\Omega_t} q_h \nabla_{\boldsymbol{x}} \cdot \boldsymbol{u}_h^{n+1} = 0 && \forall q_h \in \chi_{p_{0,h}}(\Omega_t) \qquad (3.11) \\
&\quad \boldsymbol{u}_h^{n+1} = \boldsymbol{u}_\Gamma && \forall \boldsymbol{x} \in \partial\Gamma_t, \ t \in I \\
&\quad \boldsymbol{u}_h^{n+1} = \boldsymbol{u}_D && \forall \boldsymbol{x} \in \partial\Omega_t \backslash \partial\Gamma_t, \ t \in I \\
&\quad \boldsymbol{u}_h^0 = \boldsymbol{u}_0 && \forall \boldsymbol{x} \in \Omega_0, \ t = t_0
\end{aligned}$$

where $\boldsymbol{u}_h^0$ is the given initial condition, $\boldsymbol{u}_D$ and $\boldsymbol{u}_\Gamma$ are the given boundary values.

3.6 Stability of the ALE formulation

In this section we briefly recall some stability results for the ALE formulation In practice, we require that the norm of the energy (i.e. total energy) decreases in time, if no sources are present in the system. The estimates reported here are taken from [25]. Using the discrete solution of problem 4

---

[2] Space L^2_0 corresponds to the function belonging to L^2 with zero mean value; if however Neumann boundary conditions are imposed, it is possible to use L^2 as is

as test functions in (3.10) and(3.11), after some manipulations we obtain:

$$\begin{aligned}\|\boldsymbol{u}_h^{n+1}\|^2_{L^2(\Omega_{t^{n+1}})} + \Delta t\ \nu\|\nabla_{\boldsymbol{x}}\boldsymbol{u}_h^{n+1}\|^2_{L^2(\Omega_{t^{n+1}})} &\leq \|\boldsymbol{u}_h^n\|^2_{L^2(\Omega_{t^n})} \\ + \left(\int_{t^n}^{t^{n+1}}\int_{\Omega_t} \nabla_{\boldsymbol{x}}\cdot\boldsymbol{w}_h|u_h^n|^2 d\Omega dt - \Delta t\int_{\Omega_{t^{n+1}}} \nabla_{\boldsymbol{x}}\cdot\boldsymbol{w}_h|u_h^{n+1}|^2 d\Omega\right)\end{aligned} \tag{3.12}$$

By (3.12) it is possible to infer that stability depends on the mesh velocity $\mathbf{w}_h$ through the term:

$$\left(\int_{t^n}^{t^{n+1}}\int_{\Omega_t} \nabla_{\boldsymbol{x}}\cdot\boldsymbol{w}_h|u_h^n|^2 d\Omega dt - \Delta t\int_{\Omega_{t^{n+1}}} \nabla_{\boldsymbol{x}}\cdot\boldsymbol{w}_h|u_h^{n+1}|^2 d\Omega\right)$$

so scheme (3.10),(3.11) is only conditionally stable, as this latter can assume positive and negative values.

Chapter 4

The Immersed Finite Element Method

4.1 Introduction

The Immersed Finite Element Method (IFEM) is both a matematical formulation and a a numerical discretization method developed to provide a flexible framework for the description of a fluid-structure interaction problem. This method is quite similar to the Immersed Boundary method [53], except for the fact that the immersed structure has the same spatial dimension of the fluid domain. In this formulation each continuum is described with the most appropriate reference frames [53, 73]. Effects of the fluid-embedded bodies are summarized into a volumetric source term that describes the fluid-structure interaction forces. This approach aims at avoiding mesh updates or remeshing, leading to considerable savings in computational time.

As aforementioned, the original IFEM formulation [73] was born as an extension of the Immersed Boundary Method [53], which was developed to treat bodies with geometries having a lower spatial dimension with respect to the fluid domain. The IFEM approach is capable of handling embedded bodies and fully discretize them independently of the fluid domain. In both approaches Eulerian (fluid) variables are related to a fixed Cartesian mesh, while Lagrangian quantities (structure) are defined on a curvilinear deformable grid. Hence, interpolation between the two meshes is a key ingredient of IFEM. Coupling between Eulerian and Lagrangian quantities is performed by an interpolation kernel. The earlier versions [53] employ approximate interpolation Kernel functions. Typically for this task approximations of the Dirac delta distribution are used, but more sophisticated kernels, such that the Reproducing Kernel Particle Method (RKPM), [67], have been developed. In the following description, we employ a different approach, developed by [6, 7] that recasts the problem in a variational framework, thus avoiding the explicit construction of the discrete Dirac Delta function.

Stability analyses of the Immersed Boundary method are developed in [8, 9, 10], with extensions to the Immersed Finite Element Method described in [32]. In these works finite element spatial discretization is used in conjunction with first order finite differences in time. Two approaches are presented, both using the Backward Euler (BE) scheme to implicitly solve the fluid problem. The embedded body position is advanced in time by a Forward Euler (FE) scheme (first order extrapolation of previous data), in which case the coupled method is termed as semi-implicit (BE/FE). Otherwise, the embedded body evolution is numerically described by an implicit scheme (Backward Euler), leading to a fully implicit (BE/BE) approach. The key concept in order to obtain stability of the numerical scheme is to require that the energy of the discretized system does not increase at each time step. Time discretization by means of finite differences introduces a spurious energy term related to the truncation error. If this term is dissipative, the scheme is considered stable. Conversely if this spurious energy is larger than the energy dissipated by the fluid viscosity, the scheme becomes unstable. A fully implicit discretization is always stable, while the more efficient semi-implicit approach suffers a CFL-like stability restriction on time step size. Second order spatial discretization is often used for the fluid, in conjunction with first order discretization of the displacements of the embedded boundaries/bodies obtained by means of affine spaces. The stability analysis depends on this last

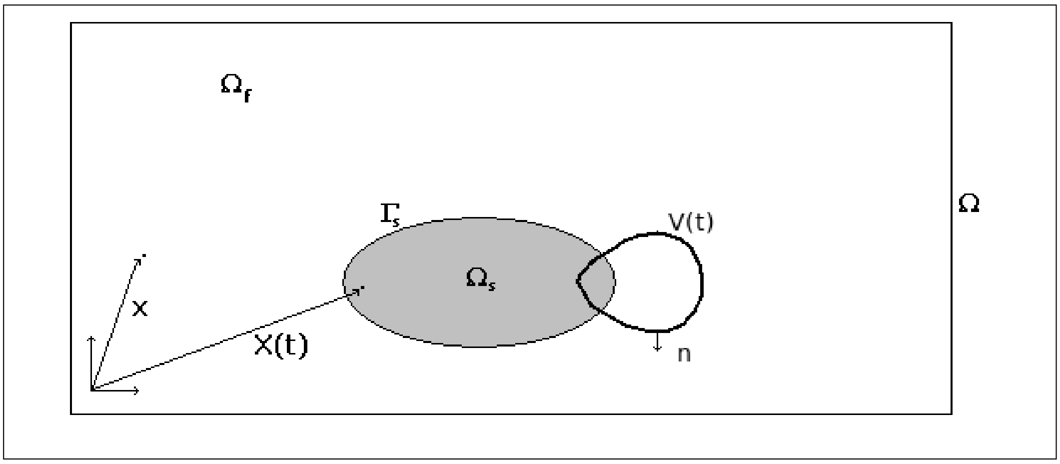

Figure 4.1: Domain partition, $m = d = 2$

assumption.

In this chapter we propose the use of higher order approximations for both the fluid and the Lagrangian finite element spaces (in particular, a $P2$ Lagrangian space) and we prove the stability of this higher order approach, developing a CFL-like stability condition for the semi-implicit approach. Some numerical example will enforce the obtained results. If the assumption of visco-elastic behavior of the constitutive law of the immersed body is adopted, [11] and [32] show that FEM discretization enjoys strong consistency. We prove that strong consistency is lost when the dissipative terms of the solid stress tensor do not behave like a fluid and show that weak consistency has an impact on the stability properties of the scheme. Moreover, we show for the implicit scheme only that the difference between fluid and structure densities has an impact on the stability. After introducing some simplifications, we demonstrate only that a limitation on the minimum of the adopted time step exists, being a quantitative determination difficult to achieve. The stability estimate is performed by considering the temporal evolution of the fluid kinetic energy alone.

4.2 The Equation of motion

Consider a domain $\Omega \in \mathbb{R}^d$, $d = 2, 3$ partitioned in two sub-domains Ω_f and Ω_s having the common boundary Γ_s, with $\Omega = \Omega_f \cup \Omega_s$, $\Omega_f \subset \mathbb{R}^d$, $\Omega_s \subset \mathbb{R}^m$, $m \leq d$, $\Gamma_s = \Omega_s \cap \Omega_f$ (Fig. 4.1). The first domain is filled with fluid, and the second represents the region where a solid continuum is present. Since the solid is deformable, the geometry of Ω_s, and thus of Γ_s, changes in time. In the following, $\Omega_s = \Omega_s(t)$ denotes the configuration at time t, while $\Omega_{0s} = \Omega_s(0)$ the initial (reference) configuration. Because of the no-slip condition, at the interface Γ_s both continua must have the same velocity; moreover, the dynamic equilibrium imposes equality of the forces exerted by the fluid on the structure and the forces exerted by the structure on the fluid, thus implying continuity of the normal stresses.

It is possible to treat the union of both continua in a unified way as follows: let $\boldsymbol{u}$ the velocities of both the fluid and the structure, ρ_α and $\boldsymbol{\sigma}_\alpha, \alpha = f, s$ the densities and the Cauchy stress tensors of the fluid and the structure respectively and $\boldsymbol{n}$ the outward unit normal $\boldsymbol{n}$; for a generic volume V(t) mapped by a reference configuration $V(0)$, which moves with the same velocity $\boldsymbol{u}$ of the particles in it contained the Virtual Work Principle states that, for any virtual displacement $\delta\boldsymbol{u}$, the following relation holds:

$$\begin{aligned}
&\int_{V(t)} \rho_f \frac{d\boldsymbol{u}}{dt} \cdot \delta\boldsymbol{u} \, d\boldsymbol{x}(t) + \int_{V(t)} \boldsymbol{\sigma}_f : \nabla\left(\delta\boldsymbol{u}\right) \, d\boldsymbol{x}(t) \\
&\quad + \int_{V(t)\cap\Omega_s(t)} \left(\rho_s - \rho_f\right) \frac{d\boldsymbol{u}}{dt} \cdot \delta\boldsymbol{u} \, d\boldsymbol{X}(t) \\
&\quad + \int_{V(t)\cap\Omega_s(t)} \left(\boldsymbol{\sigma}_s - \boldsymbol{\sigma}_f\right) : \nabla\left(\delta\boldsymbol{u}\right) \, d\boldsymbol{X}(t) \\
&\quad = \int_{\partial V(t)} \boldsymbol{\sigma}_f \boldsymbol{n} \cdot \delta\boldsymbol{u} \, da(t) + \int_{\partial V(t)\cap\Omega_s(t)} \left(\boldsymbol{\sigma}_s - \boldsymbol{\sigma}_f\right) \boldsymbol{n} \cdot \delta\boldsymbol{u} \, da(t)
\end{aligned}$$

Denoting by $\boldsymbol{X}(\boldsymbol{s}, t)$ the Lagrangian coordinates of the structure, where $\boldsymbol{s}$ represents the position of the material point at initial time, so $d\boldsymbol{u}/dt = \partial^2\boldsymbol{X}(\boldsymbol{s}, t)/\partial t^2$, integrating by parts and using the following identity:

$$\partial\left(\Omega_s \cap V\right) = \left(\partial\Omega_s \cap V\right) \cup \left(\Omega_s \cap \partial V\right) \tag{4.1}$$

the principle of virtual works yields:

$$\begin{aligned}\int_{V(t)} \left(\rho_f \frac{d\boldsymbol{u}}{dt} - \nabla \cdot \boldsymbol{\sigma}_f\right) \cdot \delta \boldsymbol{u}\, d\boldsymbol{x}(t) \\ = - \int_{V(t)\cap\Omega_s(t)} \Big((\rho_s - \rho_f)\, \ddot{\boldsymbol{X}} - \nabla \cdot (\boldsymbol{\sigma}_s - \boldsymbol{\sigma}_f)\Big) \cdot \delta \boldsymbol{u}\, d\boldsymbol{X}(t) \\ - \int_{V(t)\cap\partial\Omega_s(t)} (\boldsymbol{\sigma}_s - \boldsymbol{\sigma}_f)\, \boldsymbol{n} \cdot \delta \boldsymbol{u}\, dA(t)\end{aligned} \tag{4.2}$$

The last term that appears in (4.2) vanishes due to the continuity of the normal stress. The fluid-structure interaction term can be represented using the function:

$$\boldsymbol{f}_s^{FSI} = -(\rho_s - \rho_f)\ddot{\boldsymbol{X}} + \nabla \cdot (\boldsymbol{\sigma}_s - \boldsymbol{\sigma}_f) \tag{4.3}$$

Proceeding as in [11] it is possible to rewrite relation (4.2) on the domain $V(t)$, thanks to the following relations:

$$\boldsymbol{F}(\boldsymbol{x}, t) = \int_{V(t)} \boldsymbol{f}_s^{FSI}(\boldsymbol{X}(t), t)\delta(\boldsymbol{x} - \boldsymbol{X}(t))d\boldsymbol{X}(t) \tag{4.4}$$

where $\delta(\cdot)$ is the classical Dirac delta distribution.

For the continuity equation, by the conservation of mass inside $V(t)$, follows:

$$\begin{aligned}\frac{dm}{dt} &= \frac{d}{dt}\int_{V(t)} \rho d\boldsymbol{x}(t) = \frac{d}{dt}\int_{V(t)} \rho_f d\boldsymbol{x}(t) + \frac{d}{dt}\int_{V(t)\cap\Omega_s(t)} (\rho_s(t) - \rho_f)\, d\boldsymbol{x}(t) \\ &= \frac{d}{dt}\int_{V(0)} J\rho_f d\boldsymbol{x}(0) + \frac{d}{dt}\int_{V(0)\cap\Omega_s(0)} J_s\,(\rho_s(0) - \rho_f)\, d\boldsymbol{X}(0) \\ &= \int_{V(0)} \rho_f \frac{dJ}{dt} d\boldsymbol{x}(0) + \int_{V(0)\cap\Omega_s(0)} (\rho_s(0) - \rho_f)\, \frac{dJ_s}{dt} d\boldsymbol{X}(0) \\ &= \int_{V(t)} \rho_f \nabla \cdot (u)\, d\boldsymbol{x}(t) + \int_{V(t)\cap\Omega_s(t)} (\rho_s(t) - \rho_f)\, \nabla \cdot \dot{\boldsymbol{X}} d\boldsymbol{X}(t) \\ &= \int_{V(t)} \Big(\rho_f \nabla \cdot (u) + \delta\,(\boldsymbol{x} - \boldsymbol{X}(t))\,(\rho_s(t) - \rho_f)\, \nabla \cdot \dot{\boldsymbol{X}}\Big)\, d\boldsymbol{x}(t) = 0\end{aligned}$$

Continuity equation thus becomes:

$$\rho_f \nabla \cdot \boldsymbol{u} = G(\boldsymbol{x}, t)$$

where:

$$G(\boldsymbol{x},t) = -\int_{V(t)} (\rho_s(t) - \rho_f)\, \nabla \cdot \dot{\boldsymbol{X}}(t)\delta(\boldsymbol{x} - \boldsymbol{X}(t))d\boldsymbol{X}(t) \tag{4.5}$$

Hence, writing the fluid stress tensor as $\boldsymbol{\sigma}_f = -p + \mu\left(\nabla\boldsymbol{u} + \nabla^t\boldsymbol{u}\right)$, the interaction between fluid and structure can be embedded as a source term in the classical Navier-Stokes equations, leading to the following problem:

Problem 5 *Find $\boldsymbol{u}$, p and $\boldsymbol{X}$ that satisfy:*

$$\begin{aligned}
&\rho_f\left(\frac{\partial\boldsymbol{u}}{\partial t} + \boldsymbol{u}\cdot\nabla\boldsymbol{u}\right) - \mu\Delta\boldsymbol{u} + \nabla p = \boldsymbol{F}(\boldsymbol{x},t) && \text{in } \Omega\times]0,T[\\
&\rho_f\nabla\cdot(u) = G(\boldsymbol{x},t) && \text{in } \Omega\times]0,T[\\
&\boldsymbol{F}(\boldsymbol{x},t) = \int_\Omega \boldsymbol{f}_s^{FSI}(\boldsymbol{X}(t),t)\delta(\boldsymbol{x}-\boldsymbol{X}(t))d\boldsymbol{x} && \text{in } \Omega\times]0,T[\\
&G(\boldsymbol{x},t) = -\int_\Omega (\rho_s(t)-\rho_f)\,\nabla\cdot\dot{\boldsymbol{X}}(t)\delta(\boldsymbol{x}-\boldsymbol{X}(t))d\boldsymbol{x} &&\\
&\dot{\boldsymbol{X}} = \int_\Omega \boldsymbol{u}(\boldsymbol{x},t)\delta(\boldsymbol{x}-\boldsymbol{X}(t))d\boldsymbol{x} && \text{in } \Omega\times]0,T[\\
&\boldsymbol{u}(\boldsymbol{x},t) = 0 && \text{on } \partial\Omega\times]0,T[\\
&\boldsymbol{u}(\boldsymbol{x},0) = \boldsymbol{u}_0(\boldsymbol{x}) && \text{on } \Omega\\
&\boldsymbol{X}(\boldsymbol{s},0) = \boldsymbol{X}_0(\boldsymbol{s}) && \text{on } \Omega_s
\end{aligned}$$

and $\boldsymbol{f}_s^{FSI}$, defined as in (4.3).

This problem is now defined in the fixed domain Ω, taking into account the interaction term between fluid and structure variables within Ω_s through the sources $\boldsymbol{F}(\boldsymbol{x},t)$ and $G(\boldsymbol{x},t)$.

4.2.1 Variational formulation

The variational formulation of problem 5 requires special attention to the interaction terms. In [6] the authors prove that (4.4) belongs to $H^{-1}(\Omega)^d$ even when $m \leq d$, so integral (4.6) is well defined even when the space dimension of the embedded bodies is lower than the space dimension of the fluid domain. Multiplying (4.3) by $\boldsymbol{v}$, a test function belonging to $[H_0^1(\Omega)]^d$, and integrating over the moving domain $\Omega_s(t)$, one obtains the equation:

$$\int_{\Omega_s(t)} \left((\rho_s - \rho_f)\ddot{\boldsymbol{X}} - \nabla \cdot (\boldsymbol{\sigma}_s - \boldsymbol{\sigma}_f) + \boldsymbol{f}_s^{FSI}\right) \cdot \boldsymbol{v} d\Omega_s = 0 \tag{4.6}$$

The transformation from the current structure configuration $\Omega_s(t)$ to the reference domain is achieved using the first Piola-Kirchoff stress. To this aim, denoting with $\mathbb{F}(\boldsymbol{s}, t) = \partial X_i \backslash \partial s_j$ the Jacobian matrix, with $J(\boldsymbol{s}, t) = det(\mathbb{F}(\boldsymbol{s}, t))$, its determinant, with $\boldsymbol{P} = J\boldsymbol{\sigma}(\mathbb{F}^{-1})^T$ the first Piola-Kirchoff stress tensor, and with $\rho_s^0 = J\rho_f$ the density in the reference configuration, taking into account the continuity of the normal stress at the interface, and integrating by parts, eq (4.6) can be rewritten as:

$$\begin{aligned}\int_{\Omega_s} \boldsymbol{F} \cdot \boldsymbol{v} = &- \int_{\Omega_{0s}} J_s \left(\rho_s^0 - \rho_f\right) \ddot{\boldsymbol{X}} \cdot \boldsymbol{v}(\boldsymbol{X}(\boldsymbol{s}, t)) d\Omega_{0s} \\ &- \int_{\Omega_{0s}} (\boldsymbol{P}_s - \boldsymbol{P}_f) : \nabla \boldsymbol{v}(\boldsymbol{X}(\boldsymbol{s}, t)) d\Omega_{0s}\end{aligned}$$

In the same way, recalling the Reynolds transport theorem, for the continuity equations it is possible to write:

$$\int_{\Omega_s} qG = - \int_{\Omega_{0s}} \left(\rho_s^0 - \rho_f\right) \frac{d}{dt} \left(J_s - 1\right) q(\boldsymbol{X}(\boldsymbol{s}, t)) d\Omega_{0s}$$

The problem can now be given in the following variational formulation:

Problem 6 *Given* $\boldsymbol{u}_0 \in [H_0^1(\Omega)]^d$, $\boldsymbol{X}_0 \in [H_0^1(\Omega_{0s})]^m$, $\dot{\boldsymbol{X}}_0 \in [H_0^1(\Omega_{0s})]^m$, *for all* $t \in]0, T[$, *find* $(\boldsymbol{u}(t), p(t), \boldsymbol{X}(t)) \in [H_0^1(\Omega)]^d \times L_0^2(\Omega) \times [H_0^1(\Omega_{0s})]^m$ *such* *that:*

$$\rho_f \left((\frac{\partial \boldsymbol{u}}{\partial t}, \boldsymbol{v}) + (\boldsymbol{u} \cdot \nabla \boldsymbol{u}, \boldsymbol{v}) \right)$$

$$+ \mu(\nabla \boldsymbol{u}, \nabla \boldsymbol{v}) - (p, \nabla \cdot (v)) = \int_{\Omega_s} \boldsymbol{F} \cdot \boldsymbol{v} \qquad \forall \boldsymbol{v} \in [H_0^1(\Omega)]^d \tag{4.7}$$

$$\rho_f(\nabla \cdot (u), q) = \int_{\Omega_s} qG \qquad \forall q \in L_0^2(\Omega) \tag{4.8}$$

$$\int_{\Omega_s} \boldsymbol{F} \cdot \boldsymbol{v} = - \int_{\Omega_{0s}} J_s(\rho_s^0 - \rho_f) \ddot{\boldsymbol{X}} \cdot \boldsymbol{v}(\boldsymbol{X}(\boldsymbol{s}, t)) d\Omega_{0s}$$

$$- \int_{\Omega_{0s}} (\boldsymbol{P}_s - \boldsymbol{P}_f) : \nabla \boldsymbol{v}(\boldsymbol{X}(\boldsymbol{s}, t)) d\Omega_{0s} \qquad \forall \boldsymbol{v} \in [H_0^1(\Omega)]^d \tag{4.9}$$

$$\int_{\Omega_s} qG = - \int_{\Omega_{0s}} \left(\rho_s^0 - \rho_f\right) \frac{d}{dt} \left(J_s - 1\right) q(\boldsymbol{X}(\boldsymbol{s}, t)) d\Omega_{0s} \qquad \forall q \in L_0^2(\Omega) \tag{4.10}$$

$$\dot{\boldsymbol{X}}(\boldsymbol{s}, t) = \boldsymbol{u}(\boldsymbol{X}(\boldsymbol{s}, t), t) \qquad \textit{on } \Omega_{0s} \tag{4.11}$$

$$\boldsymbol{u}(\boldsymbol{x}, t) = 0 \qquad \textit{on } \partial\Omega$$

$$\boldsymbol{u}(\boldsymbol{x}, 0) = \boldsymbol{u}_0(\boldsymbol{x}) \qquad \textit{in } \Omega$$

$$\boldsymbol{X}(\boldsymbol{s}, 0) = \boldsymbol{X}_0(\boldsymbol{s}) \qquad \textit{in } \Omega_s$$

$$\dot{\boldsymbol{X}}(\boldsymbol{s}, 0) = \dot{\boldsymbol{X}}_0(\boldsymbol{s}) \qquad \textit{in } \Omega_s$$

where $(.,.)$ *denotes the* L^2 *inner product, defined as:*

$$(\boldsymbol{u}, \boldsymbol{v}) = \int_{\Omega} \boldsymbol{u} \cdot \boldsymbol{v} \; d\Omega$$

4.3 Numerical discretization

Discretization of Problem 6 is naturally obtained by means of Finite Element (FE) in space and Finite Difference (FD) in time. Even though other discrete approaches can be used, we follow [64] and use classical FE in space and single first order FD in time. The fluid pressure and velocities are discretized in the entire domain Ω, while the structure displacement $\boldsymbol{X}$ is discretized only in Ω_{0s}

4.3.1 Space discretization

Let $\mathcal{T}_h$ be a triangulation of Ω and $\mathcal{S}_h$ a triangulation of Ω_{0s} and denote with h_x the diameter of $\mathcal{T}_h$ and with h_s the diameter of $\mathcal{S}_h$. Note that $\mathcal{S}_h \nsubseteq \mathcal{T}_h$, even though $\Omega_s \subset \Omega_f$. Hence, it is possible to introduce the following finite dimensional subspaces:

$$\begin{array}{ll}
\boldsymbol{R}_h^r \subseteq [H^1(\Omega_{0s})]^m & \boldsymbol{R}_h^r = \left\{\boldsymbol{\phi}_h \in [C^0(\Omega_{0s})]^m : \boldsymbol{\phi}_h|_{T_k} \in [\mathbb{P}^r]^m \ \ \forall T_k \in \mathcal{S}_h\right\} \\
\boldsymbol{V}_h^p \subseteq [H_0^1(\Omega)]^d & \boldsymbol{V}_h^p = \left\{\boldsymbol{v}_h \in [C^0(\Omega)]^d : \boldsymbol{v}_h|_{T_k} \in [\mathbb{P}^p]^d \ \ \forall T_k \in \mathcal{T}_h\right\} \\
Q_h^l \subseteq L_0^2(\Omega) & Q_h^l = \left\{q_h \in C^0(\Omega) : q_h|_{T_k} \in \mathbb{P}^l \ \ \forall T_k \in \mathcal{T}_h\right\}
\end{array}$$

where $\mathbb{P}^p$ is the space of Lagrangian polynomials of degree p defined on the generic element T_k of $\mathcal{T}_h$ or $\mathcal{S}_h$ respectively. Clearly, spaces $\boldsymbol{V}_h$ and Q_h must be related in order to satisfy the inf-sup condition (see [13, 33]).

Let denote with $\mathcal{N}_j^\alpha$ and $Ndof_\alpha$, $\alpha = s\ ,\ f\ ,\ q$ the generic Lagrangian basis functions and the number of degrees of freedom associated to the spaces $\boldsymbol{R}_h$, $\boldsymbol{V}_h$ and Q_h respectively, and with v_i the i-th spatial component of the function $\boldsymbol{v}$. In order to evaluate integral (4.9), one needs to know the values of the fluid unknowns on nodes of Ω_{0s} and the values of the fluid test functions on the mapped structural domain, i.e. as a function of the reference configuration. So, one needs to build an interpolation operator between the fluid and the structure, defined on the reference domain as follows:

$$\Pi_h(v_i, t) = \sum_{j=1}^{Ndof_s} v_{i,j}^{f\to s}(t)\mathcal{N}_j^s \tag{4.12}$$

$$\Pi_h(q, t) = \sum_{j=1}^{Ndof_s} q_j^{f\to s}(t)\mathcal{N}_j^s \tag{4.13}$$

where:

$$v_{i,j}^{f\to s}(t) = v_i(\boldsymbol{X}(\boldsymbol{s}_j, t)) = \sum_{l=1}^{Ndof_f} v_{i,l}\mathcal{N}_l^f(\boldsymbol{X}(\boldsymbol{s}_j, t)) \tag{4.14}$$

$$q_j^{f\to s}(t) = q(\boldsymbol{X}(\boldsymbol{s}_j, t)) = \sum_{l=1}^{Ndof_q} q_l\mathcal{N}_l^q(\boldsymbol{X}(\boldsymbol{s}_j, t)) \tag{4.15}$$

Where $\boldsymbol{s}_j$ are the j-th coordinates of the j-th node on the reference configuration. Relation (4.12) and (4.13) can be used to evaluate integrals over Ω_{0s}, the domain of the structure in its reference (initial) position. The following semi-discrete Finite Element formulation of Problem 6 can be written:

Problem 7 *Given* $\boldsymbol{u}_{0h} \in \boldsymbol{V}_h$*,* $\boldsymbol{X}_{0h} \in \boldsymbol{R}_h$*,* $\dot{\boldsymbol{X}}_{0h} \in \boldsymbol{R}_h$*, for all* $t \in]0, T[$ *find* $(\boldsymbol{u}_h(t), p_h(t), \boldsymbol{X}_h(t)) \in \boldsymbol{V}_h \times Q_h \times \boldsymbol{R}_h$ *such that:*

$$\rho_f\left(\left(\frac{\partial \boldsymbol{u}_h}{\partial t}, \boldsymbol{v}_h\right) + (\boldsymbol{u}_h \cdot \nabla \boldsymbol{u}_h, \boldsymbol{v}_h)\right)$$

$$+\,\mu(\nabla \boldsymbol{u}_h, \nabla \boldsymbol{v}_h) - \left(p_h, \nabla \cdot (v)_h\right) = \int_{\Omega_s} \boldsymbol{F}_h \cdot \boldsymbol{v}_h \qquad \forall \boldsymbol{v}_h \in \boldsymbol{V}_h \tag{4.16}$$

$$\rho_f(\nabla \cdot (u)_h, q_h) = -\int_{\Omega_s} q_h G_h \qquad \forall q_h \in Q_h \tag{4.17}$$

$$\begin{aligned}\int_{\Omega_s} \boldsymbol{F}_h \cdot \boldsymbol{v}_h = &-\int_{\Omega_{0s}} J_{s_h}(\rho_s^0 - \rho_f)\ddot{\boldsymbol{X}}_h \cdot \Pi_h(\mathbf{v}_h, t) d\Omega_{0s} \\ &- \int_{\Omega_{0s}} \boldsymbol{P}_{sh} : \nabla \Pi_h(\mathbf{v}_h, t) d\Omega_{0s} \\ &+ \int_{\Omega_{0s}} \boldsymbol{P}_{fh} : \nabla \Pi_h(\mathbf{v}_h, t) d\Omega_{0s}\end{aligned} \tag{4.18}$$

$$\int_{\Omega_s} q_h G_h = -\int_{\Omega_{0s}} \left(\rho_s^0 - \rho_f\right) \frac{d}{dt}(J_{s_h} - 1)\Pi_h(q_h, t) d\Omega_{0s} \tag{4.19}$$

$$\dot{\boldsymbol{X}}_h = \Pi_h(\mathbf{u}_h, t) \tag{4.20}$$

$$\boldsymbol{u}_h = 0 \qquad \text{on } \partial\Omega$$

$$\boldsymbol{u}_h(0) = \boldsymbol{u}_{0h} \qquad \text{in } \Omega$$

$$\boldsymbol{X}_h(0) = \boldsymbol{X}_{0h} \qquad \text{in } \Omega_{0s}$$

$$\dot{\boldsymbol{X}}_h(0) = \dot{\boldsymbol{X}}_{0h} \qquad \text{in } \Omega_{0s}$$

Where subscript h denotes the space discrete version of the function, tensor, etc defined previously at continuum level.

4.3.2 Time discretization by finite difference

Time discretization is obtained using the first order Euler scheme in the derivatives appearing in (4.16). This is complemented by central and forward differencing of $\ddot{\boldsymbol{X}}$ appearing in (4.18) and $\dot{\boldsymbol{X}}$ appearing in (4.20), respectively. If the Backward Euler is used everywhere, i.e., all time-dependent terms in equations (4.16), (4.18) and (4.20) are evaluated at the new time, t^{n+1}, the method is termed BE/BE method and is unconditionally stable, but requires at each time step the solution of a system of nonlinear equations. A computationally more efficient approach is to use Forward Euler in (4.18) and (4.20), leading to a semi-implicit approach termed FE/BE. This approach allows the decoupling of equations (4.18) and (4.20) from (4.16), yielding a sequential algorithm that in principal requires smaller computational resources. However, it suffers from stability constraints that are explicated as a CFL-like restriction on the maximum allowable time step [8, 10, 32].

Subdividing the time interval in N steps of size Δt, such that $T \leq N\Delta t$ and using superscript $n, n+1, n+\theta,\ \theta \in \{0, 1\}$, to indicate quantities defined at $t^{n+\theta} = t^n + \theta\Delta t$, the fully discrete problem can be written as:

Problem 8 *Given* $\boldsymbol{u}_h^0 \in \boldsymbol{V}_h$, $\boldsymbol{X}_h^0 \in \boldsymbol{R}_h$, $\boldsymbol{X}_h^{-1} = \boldsymbol{X}_h(-\Delta t) \in \boldsymbol{R}_h$, *for all*

$n \leq N$ find $(\boldsymbol{u}_h^{n+1}, p_h^{n+1}, \boldsymbol{X}_h^{n+1}) \in \boldsymbol{V}_h \times Q_h \times \boldsymbol{R}_h$ *such that:*

$$\begin{aligned}\int_{\Omega_s} \boldsymbol{F}_h^{n+1} \cdot \boldsymbol{v}_h = &- \int_{\Omega_{0s}} \boldsymbol{P}_{sh}^{n+1}(\nabla \boldsymbol{X}^{n+\theta}) : \nabla \Pi_h(\mathbf{v}_h, t^{n+\theta}) d\Omega_{0s} \\ &- \int_{\Omega_{0s}} J_{s_h}(\nabla \boldsymbol{X}^{n+\theta})(\rho_s^0 - \rho_f) \frac{\boldsymbol{X}_h^{n+\theta} - 2\boldsymbol{X}_h^{n-1+\theta} + \boldsymbol{X}_h^{n-2+\theta}}{\Delta t^2} \cdot \Pi_h(\mathbf{v}_h, t^{n+\theta}) d\Omega_{0s} \\ &+ \int_{\Omega_{0s}} \boldsymbol{P}_{fh}^{n+1}(\boldsymbol{u}_h^{n+\theta}, p_h^{n+\theta}) : \nabla \Pi_h(\mathbf{v}_h, t^{n+\theta}) d\Omega_{0s}\end{aligned} \tag{4.21}$$

$$\begin{aligned}\int_{\Omega_s} G_h^{n+1} q_h = & \\ &- \int_{\Omega_{0s}} \left(\rho_s^0 - \rho_f\right) \frac{\big(J_h(\nabla \boldsymbol{X}^{n+\theta}) - 1\big) - \big(J_h(\nabla \boldsymbol{X}^{n-1+\theta}) - 1\big)}{\Delta t} \Pi_h(q_h, t^{n+\theta})\end{aligned} \tag{4.22}$$

$$\begin{aligned}\rho_f &\left(\left(\frac{\boldsymbol{u}_h^{n+1} - \boldsymbol{u}_h^n}{\Delta t}, \boldsymbol{v}_h \right) + (\boldsymbol{u}_h^{n+1} \cdot \nabla \boldsymbol{u}_h^{n+1}, \boldsymbol{v}_h) \right) \\ &+ \mu(\nabla \boldsymbol{u}_h^{n+1}, \nabla \boldsymbol{v}_h) - (p_h^{n+1}, \nabla \cdot (v)_h) = \int_{\Omega_s} \boldsymbol{F}_h^{n+1} \cdot \boldsymbol{v}_h \qquad \forall \boldsymbol{v}_h \in \boldsymbol{V}_h\end{aligned} \tag{4.23}$$

$$\rho_f(\nabla \cdot (u)_h^{n+1}, q_h) = \int_{\Omega_s} G_h^{n+1} q_h \qquad \forall q_h \in Q_h \tag{4.24}$$

$$\frac{\boldsymbol{X}_h^{n+1} - \boldsymbol{X}_h^n}{\Delta t} = \Pi_h(\mathbf{u}_h(t^{n+1}), t^{n+\theta}) \tag{4.25}$$

$$\begin{aligned}\boldsymbol{u}_h^0 &= \boldsymbol{u}_{0h} && \textit{in } \Omega \\ \boldsymbol{X}_h^0 &= \boldsymbol{X}_{0h} && \textit{in } \Omega_{0s} \\ \boldsymbol{X}_h^{-1} &= \boldsymbol{X}_h^0 - \Delta t \dot{\boldsymbol{X}}_{0h} && \textit{in } \Omega_{0s}\end{aligned}$$

where $\theta \in \{0, 1\}$*;* $\theta = 1$ *yields BE/BE scheme, FE/BE otherwise.*

The FE/BE sequential algorithm can be summarized as follows:

1. compute the integrals $\int_{\Omega_s} \boldsymbol{F}_h^{n+1} \cdot \boldsymbol{v}_h$, $\int_{\Omega_s} G_h^{n+1} q_h$ in (4.21), (4.22)
2. solve the fluid problem (4.23)-(4.24) with the source terms previously evaluated by (4.21), (4.22)
3. update the structure position $(\boldsymbol{X}_h^{n+1})$ by extrapolation using (4.25)

Conversely, BE/BE needs linearization as steps 1 to 3 must be solved fully coupled.

4.4 Stability analysis

It is well known that in the continuous problem the total energy must equate the dissipative terms. The numerical problem can not have the same property because of truncation error, thus we require, as in [8, 10, 11, 32], that the energy of the system remain non increasing. In the following analysis it is assumed that the structure is incompressible, so the embedded body shall satisfy the additional constraint $J = 1$. This implies the following Lagrangian mixed formulation for the aforementioned continuum:

$$\begin{aligned}&\rho_s^0 \ddot{\boldsymbol{X}} - \nabla \cdot \boldsymbol{P}_s + \nabla p_s = 0\\&J - 1 = 0\end{aligned}$$

where p_s represent the pressure related to the embedded solid, obtained in the usual way from the classical Lagrange-multipliers formulation. Regarding the formulation of the FSI problem, one has to impose a divergence-free velocity field; moreover the pressure that appears in (4.7) takes into account of p_s so the term related to the fluid stress tensor which appears in (4.3), (4.6) consist of only the deviatoric part (i.e. $-\mu\Delta\boldsymbol{u}$). In the sequel the constant difference between body and fluid densities is denoted by $\Delta\rho = \rho_s - \rho_f$.

The specific elastic energy of the system $\mathcal{E}$ coincides with that of the structure and can be defined as:

$$\mathcal{E} = \boldsymbol{P}_s : \mathbb{F} \tag{4.26}$$

so first Piola-Kirchoff tensor can be expressed as:

$$\boldsymbol{P}_s^{kl} = \frac{\partial \mathcal{E}}{\partial \mathbb{F}_{kl}} \tag{4.27}$$

The total elastic energy of the system is defined by:

$$E = \int_{\Omega_{0s}} \mathcal{E}$$

Assuming $\mathcal{E} \in C^2(\Omega_{0s})$, the following fourth order tensor is defined:

$$\mathbb{H}^{ijkl} = \frac{\partial^2 \mathcal{E}}{\partial \mathbb{F}_{ij} \partial \mathbb{F}_{kl}}$$

Tensor $\mathbb{H}$ is assumed bounded an positive definite, i.e. there exist two positive constants k_{min} and k_{max} such that:

$$k_{min} \mathbb{F} : \mathbb{F} \leq \mathbb{F}^T \mathbb{H} \mathbb{F} \leq k_{max} \mathbb{F} : \mathbb{F} \tag{4.28}$$

So the elastic energy, defined as $\mathcal{E} = \mathbb{F}^T \mathbb{H} \mathbb{F}$ is assumed bounded an positive definite too.

4.4.1 Stability of the continuous and semi-discretized problems

Following [32] it is possible to prove the following stability estimate for the continuous Problem 6:

Lemma 2 *For $t \in]0, T[$, the solution $(\boldsymbol{u}(t), p(t), \boldsymbol{X}(t)) \in [H_0^1(\Omega)]^d \times L_0^2(\Omega) \times H_0^1(\Omega_{0s})^m$, $m \geq d - 1$, of Problem 6 satisfies the following energy equation:*

$$\frac{\rho_f}{2} \frac{d}{dt} \|\boldsymbol{u}\|_{L^2(\Omega)} + \mu \|\nabla \boldsymbol{u}\|_{L^2(\Omega_f)} + \frac{\Delta\rho}{2} \frac{d}{dt} \|\dot{\boldsymbol{X}}\|_{L^2(\Omega_{0s})} + \frac{d}{dt} E(\nabla \boldsymbol{X}) = 0 \tag{4.29}$$

Proof Take $\boldsymbol{v} = \boldsymbol{u}$ and $q = p$ in (4.7)-(4.9), use (4.11) and (4.27).

The equation (4.29) states that during time the total energy of the system, sum of the elastic energy and the kinetic energy, is dissipated by the fluid viscosity. Ideally one would like to preserve this equilibrium also for the numerical approximation. Actually, for the semi-discrete Problem 7 a similar result holds, the only difference consisting on the interpolation term of the fluid stress to the structure subspace, as shown in the following Lemma.

Lemma 3 *For $t \in]0, T[$ the solution $(\boldsymbol{u}_h(t), p_h(t), \boldsymbol{X}_h(t)) \in \boldsymbol{V}_h \times Q_h \times \boldsymbol{R}_h$ of Problem 7 satisfies the following energy equation:*

$$\begin{aligned} &\frac{\rho_f}{2} \frac{d}{dt} \|\boldsymbol{u}_h\|_{L^2(\Omega)} + \mu \|\nabla \boldsymbol{u}_h\|_{L^2(\Omega)} + \frac{\Delta\rho}{2} \frac{d}{dt} \|\dot{\boldsymbol{X}}_h\|_{L^2(\Omega_{0s})} \\ &\quad + \frac{d}{dt} E(\nabla \boldsymbol{X}_h) - \int_{\Omega_{0s}} \boldsymbol{P}_{fh} : \nabla \Pi_h(\mathbf{u}_h, t) = 0 \end{aligned} \tag{4.30}$$

Proof As in the continuous case, taking $\boldsymbol{v}_h = \boldsymbol{u}_h$, $q_h = p_h$ in (4.23)-(4.18) and using (4.20) yields the result.

Remark Under the hypothesis of a visco-elastic behavior of the structure with the same viscosity of the fluid (as done in [11, 32]), the last term that appears in (4.30) vanishes, showing the strong consistency of the FE semi-discrete problem. This shows also that no stability restrictions arise for the space discretization. If the hypothesis is dropped, a stability estimate related to the interpolation operator should be found; this will be a topic of future works.

In the sequel, a visco-elastic behavior is assumed, so it is possible to neglect terms that arise from the interpolator.

4.4.2 Stability of the space and time discretized problem

The Euler time discretization in problem 8 introduces a residual on the elastic energy, which can be interpreted as an artificial viscosity, that is not always positive. The following Lemma 4 shows that the BE/BE approach is unconditionally stable, while FE/BE is only conditionally stable. Lemma 5 gives a CFL-like condition for the time step size that ensures the stability FE/BE.

Lemma 4 *Let $\boldsymbol{u}_h^{n+1}$, p_h^{n+1}, $\boldsymbol{X}_h^{n+1}$ be the solution of Problem 8 and assume that the tensor $\mathbb{F}$ and the elastic energy $\mathcal{E}$ satisfy (4.28); then scheme BE/BE is unconditionally stable, while FE/BE does not.*

Proof Substituting $\boldsymbol{v}_h$, q_h with $\boldsymbol{u}_h^{n+1}$, p_h^{n+1} in (4.23), using (4.24) and the skew-symmetry of the convective term one obtains:

$$\begin{aligned} &\frac{\rho_f}{2\Delta t}\left(\|\boldsymbol{u}_h^{n+1}\|_{L^2(\Omega)} - \|\boldsymbol{u}_h^{n}\|_{L^2(\Omega)} + \|\boldsymbol{u}_h^{n+1} - \boldsymbol{u}_h^{n}\|_{L^2(\Omega)}\right) \\ &\quad + \mu\|\nabla \boldsymbol{u}_h^{n+1}\|_{L^2(\Omega)} = \left\langle \boldsymbol{F}_h^{n+1}, \boldsymbol{u}_h^{n+1}\right\rangle \end{aligned} \tag{4.31}$$

where the right hand side can be evaluated as:

$$\left\langle \boldsymbol{F}_h^{n+1}, \boldsymbol{u}_h^{n+1} \right\rangle = -\int_{\Omega_{0s}} \boldsymbol{P}_{sh}^{n+1} : \nabla \Pi_h \left(\boldsymbol{u}_h^{n+1}, t^{n+\theta} \right)$$

$$-\int_{\Omega_{0s}} \frac{\Delta\rho}{\Delta t} \left(\frac{\boldsymbol{X}_h^{n+\theta} - \boldsymbol{X}_h^{n-1+\theta}}{\Delta t} - \frac{\boldsymbol{X}_h^{n-1+\theta} - \boldsymbol{X}_h^{n-2+\theta}}{\Delta t} \right) \cdot \Pi_h \left(\boldsymbol{u}_h^{n+1}, t^{n+\theta} \right)$$

and substituting (4.25):

$$\begin{aligned}
\left\langle \boldsymbol{F}_h^{n+1}, \boldsymbol{u}_h^{n+1} \right\rangle &= -\frac{1}{\Delta t} \int_{\Omega_{0s}} \boldsymbol{P}_{sh}^{n+1} : \left(\nabla \boldsymbol{X}_h^{n+1} - \nabla \boldsymbol{X}_h^{n} \right) \\
&- \frac{\Delta\rho}{2\Delta t} \Bigg(\frac{\|\boldsymbol{X}_h^{n+1} - \boldsymbol{X}_h^{n}\|_{L^2(\Omega_{0s})}}{\Delta t^2} - \frac{\|\boldsymbol{X}_h^{n} - \boldsymbol{X}_h^{n-1}\|_{L^2(\Omega_{0s})}}{\Delta t^2} \\
&+ (1-\theta) \left(\frac{\|\boldsymbol{X}_h^{n} - \boldsymbol{X}_h^{n-1}\|_{L^2(\Omega_{0s})}}{\Delta t^2} - \frac{\|\boldsymbol{X}_h^{n-1} - \boldsymbol{X}_h^{n-2}\|_{L^2(\Omega_{0s})}}{\Delta t^2} \right) \\
&+ \theta \frac{\|\boldsymbol{X}_h^{n+1} - 2\boldsymbol{X}_h^{n} + \boldsymbol{X}_h^{n-1}\|_{L^2(\Omega_{0s})}}{\Delta t^2} \\
&+ (1-\theta) \frac{\|\boldsymbol{X}_h^{n+1} - \boldsymbol{X}_h^{n} - \boldsymbol{X}_h^{n-1} + \boldsymbol{X}_h^{n-2}\|_{L^2(\Omega_{0s})}}{\Delta t^2} \Bigg)
\end{aligned}$$

Define the function:

$$w_n(t)\,[0,1] \to \mathbb{R}^+ : \qquad w_n(t) = \mathcal{E}\left(\mathbb{F}^n + t(\mathbb{F}^{n+1} - \mathbb{F}^n) \right) \tag{4.32}$$

Assuming that the elastic energy is sufficiently smooth, i.e. for each time interval $[t^n, t^{n+1}]$, $\mathcal{E} \in C^2([t^n, t^{n+1}])$, (4.32) could be expanded in Taylor series up to first order, noting that $t = 1$ yields for BE/BE while $t = 0$ yields FE/BE:

$$w_n(1) - w_n(0) = \mathcal{E}(\mathbb{F}^{n+1}) - \mathcal{E}(\mathbb{F}^n) = w_n'(1) - \frac{1}{2} w_n''(\xi)$$

$$w_n(1) - w_n(0) = \mathcal{E}(\mathbb{F}^{n+1}) - \mathcal{E}(\mathbb{F}^n) = w_n'(0) + \frac{1}{2} w_n''(\xi)$$

The derivatives of $w_n(t)$ can be evaluated as:

$$w_n'(t) = \frac{\partial \mathcal{E}}{\partial \mathbb{F}_{ij}}(t) \cdot \left(\mathbb{F}_{ij}^{n+1} - \mathbb{F}_{ij}^{n} \right) = \boldsymbol{P}_s(t) : \left(\mathbb{F}^{n+1} - \mathbb{F}^n \right)$$

$$\begin{aligned}
w_n''(t) &= \frac{\partial^2 \mathcal{E}}{\partial \mathbb{F}_{ij} \partial \mathbb{F}_{kl}}(t) \cdot \left(\mathbb{F}_{ij}^{n+1} - \mathbb{F}_{ij}^{n} \right) \cdot \left(\mathbb{F}_{kl}^{n+1} - \mathbb{F}_{kl}^{n} \right) \\
&= \left(\mathbb{F}^{n+1} - \mathbb{F}^n \right)^T \mathbb{H} \left(\mathbb{F}^{n+1} - \mathbb{F}^n \right)
\end{aligned}$$

and hence:

$$\begin{aligned}\boldsymbol{P}_s(t) : \left(\mathbb{F}^{n+1} - \mathbb{F}^n\right) &= \mathcal{E}(\mathbb{F}^{n+1}) - \mathcal{E}(\mathbb{F}^n) \\ &- 2\left(\frac{1}{2} - \theta\right)\frac{1}{2}\left(\mathbb{F}^{n+1} - \mathbb{F}^n\right)^T \mathbb{H}\left(\mathbb{F}^{n+1} - \mathbb{F}^n\right) \qquad (4.33)\end{aligned}$$

Substituting into (4.31) one obtains:

$$\begin{aligned}&\frac{\rho_f}{2\Delta t}\left(\|\boldsymbol{u}_h^{n+1}\|_{L^2(\Omega)} - \|\boldsymbol{u}_h^n\|_{L^2(\Omega)} + \|\boldsymbol{u}_h^{n+1} - \boldsymbol{u}_h^n\|_{L^2(\Omega)}\right) \\ &+ \mu\|\nabla\boldsymbol{u}_h^{n+1}\|_{L^2(\Omega)} + \frac{1}{\Delta t}\left(E^{n+1}(\nabla\boldsymbol{X}_h) - E^n(\nabla\boldsymbol{X}_h)\right) \\ &+ \frac{\Delta\rho}{2\Delta t}\left(\frac{\|\boldsymbol{X}_h^{n+1} - \boldsymbol{X}_h^n\|_{L^2(\Omega_{0s})}}{\Delta t^2} - \frac{\|\boldsymbol{X}_h^n - \boldsymbol{X}_h^{n-1}\|_{L^2(\Omega_{0s})}}{\Delta t^2}\right. \\ &+ \left.\frac{\|\boldsymbol{X}_h^{n+1} - 2\boldsymbol{X}_h^n + \boldsymbol{X}_h^{n-1}\|_{L^2(\Omega_{0s})}}{\Delta t^2}\right) = \\ &\left(\frac{1}{2} - \theta\right)\frac{1}{\Delta t}\int_{\Omega_{0s}}\left(\mathbb{F}^{n+1} - \mathbb{F}^n\right)^T \mathbb{H}\left(\mathbb{F}^{n+1} - \mathbb{F}^n\right) \qquad (4.34)\end{aligned}$$

The fully implicit scheme (BE/BE, $\theta = 1$) thus is unconditionally stable:

$$-\frac{1}{2\Delta t}\int_{\Omega_{0s}}\left(\mathbb{F}^{n+1} - \mathbb{F}^n\right)^T \mathbb{H}\left(\mathbb{F}^{n+1} - \mathbb{F}^n\right) \leq -\frac{k_{min}}{2\Delta t}\|\mathbb{F}^{n+1} - \mathbb{F}^n\|_{L^2(\Omega_{0s})} \leq 0$$

while FE/BE ($\theta = 0$) is stable only if:

$$\begin{aligned}0 &\leq \frac{1}{2\Delta t}\int_{\Omega_{0s}}\left(\mathbb{F}^{n+1} - \mathbb{F}^n\right)^T \mathbb{H}\left(\mathbb{F}^{n+1} - \mathbb{F}^n\right) \\ &\leq \frac{k_{max}}{2\Delta t}\|\mathbb{F}^{n+1} - \mathbb{F}^n\|_{L^2(\Omega_{0s})} \leq \mu\|\nabla\boldsymbol{u}^{n+1}\|_{L^2(\Omega)}\end{aligned}$$

Lemma 4 gives only a qualitative stability estimate, while one needs to know a condition on Δt for FE/BE in order to achieve stability. Lemma 5 gives the desired estimate in term of a CFL-like restriction on Δt.

In order to prove Lemma 5 the following result is introduced, without proof.

Proposition 4 *Given a finite element function f_h described by a n-th degree Lagrange polynomial, it is possible to express its gradient ∇f_h element by element by a polynomial of degree $n-1$ involving from first to $n-1$ discrete derivatives, evaluated through nodal values of the function.*

Lemma 5 *Let $\boldsymbol{u}_h^{n+1}$, p_h^{n+1}, $\boldsymbol{X}_h^{n+1}$ be the solution of the FE/BE ($\theta = 0$) scheme of Problem 8; if the reference Lagrangian mesh is quasi-uniform, FE/BE is stable under the condition:*

$$\Delta t \leq \frac{h_x^{d-1}}{h_s^{m-2}} \frac{2\mu}{k_{max} L^n C_e^n} \tag{4.35}$$

where:

$$L^n = \max_{T_k \in \mathcal{S}_h} \left\{ \max_{\boldsymbol{s}_j, \boldsymbol{s}_i \in T_k \text{ and adjacent}} |\boldsymbol{X}_h^n(\boldsymbol{s}_j) - \boldsymbol{X}_h^n(\boldsymbol{s}_i)| \right\}$$

and C_e^n is the maximum number of mapped Lagrangian elements that touch the same Eulerian element at time $n\Delta t$.

Proof Proceeding as in Lemma 4, the goal is to obtain an explicit form for the right term of (4.34), in order to have:

$$\frac{k_{max}}{2\Delta t} \|\mathbb{F}^{n+1} - \mathbb{F}^n\|_{L^2(\Omega_{0s})} - \mu \|\nabla \boldsymbol{u}_h^{n+1}\|_{L^2(\Omega)} \leq 0 \tag{4.36}$$

which is translated ina an estimation of $\|\mathbb{F}^{n+1} - \mathbb{F}^n\|_{L^2(\Omega_{0s})}$ respect to $\|\nabla \boldsymbol{u}_h^{n+1}\|_{L^2(\Omega)}$. Summing over all triangles of triangulation and using (4.25), (4.12) and (4.14) the following relation follows:

$$\|\mathbb{F}^{n+1} - \mathbb{F}^n\|_{L^2(\Omega_{0s})} = \Delta t^2 \sum_{k=1}^{N_{el}} |\nabla \boldsymbol{\Pi}_h(\boldsymbol{u}_{\boldsymbol{h}}^{n+1}, t^{n+\theta})|_{0,T_k}^2 \tag{4.37}$$

denoting from now on the generic component of $\boldsymbol{\Pi}_h(\boldsymbol{u}_{\boldsymbol{h}}^{n+1}, t^{n+\theta})$ by f_h, and by $\hat{}$ the quantities related to the reference element, being the mesh quasi-uniform it is possible to write:

$$|\nabla f_h|_{0,K}^2 \leq C h_s^{m-2} \|\hat{\nabla} \hat{f}_h\|_{0,\hat{K}}^2 \tag{4.38}$$

referring for example to the unitary simplex (for unitary tetrahedron one proceeds in the same way) with Lagrangian piecewise-continuous elements, by Proposition 4 it is possible to express the gradient on the k-th element as a linear combination of discrete derivatives, $G_{j,i}$ that depend on nodal values, so relation (4.38) becomes:

$$|\nabla f_h|_{0,K}^2 \leq C h_s^{m-2} \sum_{i=1}^{m} \left(\sum_{j=1}^{Ndof_G} G_{j,i} \right)^2 \leq C h_s^{m-2} \sum_{i=1}^{m} \sum_{j=1}^{Ndof_G} G_{j,i}^2 \tag{4.39}$$

where, for a space of piecewise-continuous Lagrangian polynomials of degree k in a domain of dimension m,

$$Ndof_G = \binom{m + (k-1)}{k-1}$$

It is possible to express $G_{j,i}$ in (4.39) as a line integral of ∇f; for example for piecewise-continuous quadratic elements in a 2D domain one has:

$$\begin{aligned}
G_{1,x} &= -4\left(\int_0^{\frac{l_{12}}{2}} \nabla f dl_{12} - \int_{\frac{l_{12}}{2}}^{l_{12}} \nabla f dl_{12}\right)\\
G_{2,x} &= \frac{1}{4}\left(\int_{\frac{l_{12}}{2}}^{l_{12}} \nabla f dl_{12} - \int_0^{\frac{l_{13}}{2}} \nabla f dl_{13} + \int_0^{\frac{l_{23}}{2}} \nabla f dl_{23}\right)\\
G_{3,x} &= -\left(3\int_0^{\frac{l_{12}}{2}} \nabla f dl_{12} - \int_{\frac{l_{12}}{2}}^{l_{12}} \nabla f dl_{12}\right)\\
G_{1,y} &= \frac{1}{4}\left(\int_{\frac{l_{13}}{2}}^{l_{13}} \nabla f dl_{13} - \int_0^{\frac{l_{12}}{2}} \nabla f dl_{12} - \int_{\frac{l_{23}}{2}}^{l_{23}} \nabla f dl_{23}\right)\\
G_{2,y} &= -4\left(\int_0^{\frac{l_{13}}{2}} \nabla f dl_{13} - \int_{\frac{l_{13}}{2}}^{l_{13}} \nabla f dl_{13}\right)\\
G_{3,y} &= -\left(3\int_0^{\frac{l_{13}}{2}} \nabla f dl_{13} - \int_{\frac{l_{13}}{2}}^{l_{13}} \nabla f dl_{13}\right)
\end{aligned}$$

so:

$$
\begin{aligned}
|G_{1,x}| &\leq C_1 \left(\left| \int_0^{\frac{l_{12}}{2}} \nabla f dl_{12} \right| + \left| \int_{\frac{l_{12}}{2}}^{l_{12}} \nabla f dl_{12} \right| \right) \\
|G_{2,x}| &\leq C_2 \left(\left| \int_{\frac{l_{12}}{2}}^{l_{12}} \nabla f dl_{12} \right| + \left| \int_0^{\frac{l_{13}}{2}} \nabla f dl_{13} \right| + \left| \int_0^{\frac{l_{23}}{2}} \nabla f dl_{23} \right| \right) \\
|G_{3,x}| &\leq C_3 \left(\left| \int_0^{\frac{l_{12}}{2}} \nabla f dl_{12} \right| + \left| \int_{\frac{l_{12}}{2}}^{l_{12}} \nabla f dl_{12} \right| \right) \\
|G_{1,y}| &\leq C_2 \left(\left| \int_{\frac{l_{13}}{2}}^{l_{13}} \nabla f dl_{13} \right| + \left| \int_0^{\frac{l_{12}}{2}} \nabla f dl_{12} \right| + \left| \int_{\frac{l_{23}}{2}}^{l_{23}} \nabla f dl_{23} \right| \right) \\
|G_{2,y}| &\leq C_1 \left(\left| \int_0^{\frac{l_{13}}{2}} \nabla f dl_{13} \right| + \left| \int_{\frac{l_{13}}{2}}^{l_{13}} \nabla f dl_{13} \right| \right) \\
|G_{3,y}| &\leq C_3 \left(\left| \int_0^{\frac{l_{13}}{2}} \nabla f dl_{13} \right| + \left| \int_{\frac{l_{13}}{2}}^{l_{13}} \nabla f dl_{13} \right| \right)
\end{aligned}
$$

and applying Schwartz inequality:

$$
\begin{aligned}
\sum_{i=1}^{m} \sum_{j=1}^{3} G_{j,i}^2 \leq C \Bigg(& |\boldsymbol{X}_4 - \boldsymbol{X}_1| \left(\int_0^{\frac{l_{12}}{2}} |\nabla f|^2 \, dl_{12} \right) + |\boldsymbol{X}_2 - \boldsymbol{X}_4| \left(\int_{\frac{l_{12}}{2}}^{l_{12}} |\nabla f|^2 \, dl_{12} \right) \\
& + |\boldsymbol{X}_6 - \boldsymbol{X}_1| \left(\int_0^{\frac{l_{13}}{2}} |\nabla f|^2 \, dl_{13} \right) + |\boldsymbol{X}_3 - \boldsymbol{X}_6| \left(\int_{\frac{l_{13}}{2}}^{l_{13}} |\nabla f|^2 \, dl_{13} \right) \\
& + |\boldsymbol{X}_5 - \boldsymbol{X}_2| \left(\int_0^{\frac{l_{23}}{2}} |\nabla f|^2 \, dl_{23} \right) + |\boldsymbol{X}_3 - \boldsymbol{X}_5| \left(\int_{\frac{l_{23}}{2}}^{l_{23}} |\nabla f|^2 \, dl_{23} \right) \Bigg) \\
& \leq \max_{|\boldsymbol{X_i} - \boldsymbol{X_j}| \text{ adjacent}} |\boldsymbol{X_i} - \boldsymbol{X_j}| \sum \int_{l_{ij}} |\nabla f|^2 dl
\end{aligned}
$$

Same results follow for polynomial with a degree higher than the second, the only difference consists of segment $\|\boldsymbol{X}_i - \boldsymbol{X}_j\|$, not necessarily belonging to one edge of reference triangle/tetrahedron, because from the third order there exist node inside the triangle.

When $d = 2$, denoting with $\hat{T}_k$ the union of the elements of fluid grid touched by structural element T_k, one can apply an inverse estimate and a trace inequality to obtain:

$$\begin{aligned}\|\nabla f_h\|_{0,l_{ij}} &= |f_h|_{1,l_{ij}} \le C_0 h_x^{-1/2} |f_h|_{1/2,l_{ij}} \\ &\le C_0 C_1 h_x^{-1/2} |f_h|_{1,\hat{T}_k} = C h_x^{-1/2} \|\nabla f_h\|_{0,\hat{T}_k}\end{aligned}$$

When $d = 3$ previous reasoning is applied as in [32], iterating on a set of region $\hat{F}_{ij}$ intersection between a plane passing through l_{ij} and $\hat{T}_k$:

$$\begin{aligned}\|\nabla f_h\|_{0,l_{ij}} &= |f_h|_{1,l_{ij}} \le C_0 h_x^{-1/2} |f_h|_{1/2,l_{ij}} \\ &\le C_0 C_1 h_x^{-1/2} |f_h|_{1,\hat{F}_{ij}} \le C_0 C_1 C_2 h_x^{-1} |f_h|_{1/2,\hat{F}_{ij}} \\ &\le C_0 C_1 C_2 C_3 h_x^{-1} |f_h|_{1,\hat{T}_K} = C h_x^{-1} \|\nabla f_h\|_{0,\hat{T}_k}\end{aligned}$$

so:

$$|\nabla f_h|^2_{0,l_{ij}} \le \frac{C}{h_x^{d-1}} |\nabla f_h|^2_{0,\hat{T}_k}$$

and:

$$|\nabla f_h|^2_{0,K} \le C \frac{h_s^{m-2}}{h_x^{d-1}} \max_{|\boldsymbol{X_i}-\boldsymbol{X_j}| \text{ adjacent}} |\boldsymbol{X_i} - \boldsymbol{X_j}| |\nabla f_h|^2_{0,\hat{T}_k}$$

Hence:

$$\begin{aligned}|\nabla f_h|^2_{0,\Omega_{0s}} &\le C \frac{h_s^{m-2}}{h_x^{d-1}} \sum_{k=1}^{N_{el}} \max_{|\boldsymbol{X_i}-\boldsymbol{X_j}| \text{ adjacent}} |\boldsymbol{X_i} - \boldsymbol{X_j}| |\nabla f_h|^2_{0,\hat{T}_k} \\ &\le C \frac{h_s^{m-2}}{h_x^{d-1}} \max_k \left\{ \max_{|\boldsymbol{X_i}-\boldsymbol{X_j}| \text{ adjacent}} |\boldsymbol{X_i} - \boldsymbol{X_j}| \right\} \sum_{k=1}^{N_{el}} |\nabla f_h|^2_{0,\hat{T}_k} \\ &\le C \frac{h_s^{m-2}}{h_x^{d-1}} L^n C_e^n |\nabla f_h|^2_{0,\Omega} \end{aligned} \tag{4.40}$$

Thanks to (4.40) it is now possible to write:

$$\frac{k_{max}}{2\Delta t} \|\mathbb{F}^{n+1} - \mathbb{F}^n\|_{L^2(\Omega_{0s})} \le \frac{k_{max}\Delta t}{2} \frac{h_s^{m-2}}{h_x^{d-1}} L^n C_e^n \|\nabla \boldsymbol{u}_h^{n+1}\|_{L^2(\Omega)} \tag{4.41}$$

so, from (4.36) and (4.41) (4.35) follows.

Remark While in [32] $|\boldsymbol{X}_h^n(\boldsymbol{s}_j) - \boldsymbol{X}_h^n(\boldsymbol{s}_i)|$ represents effectively the distance between two vertices in the deformed configuration, here and in the sequel this quantity represents the distance between two adjacent nodes (i.e. the straight line that joins no more than two nodes), not necessarily on a side.

Corollary. Numerical viscosity due to time discretization is given by

$$-\frac{k_{max}\Delta t}{2}\frac{h_s^{m-2}}{h_x^{d-1}}L^n C_e^n \tag{4.42}$$

for FE/BE scheme and by:

$$\frac{k_{min}\Delta t}{2}\frac{h_s^{m-2}}{h_x^{d-1}}L^{n+1} C_e^{n+1} \tag{4.43}$$

for BE/BE scheme.

Proof Relation (4.42) follows by (4.41), while (4.43) is obtained in the same way, using $n+1$ instead of n.

4.5 Some considerations on the stability criteria related to the inertial term

As far as the stability related on the inertial term is concerned, some considerations for the only implicit scheme are introduced in this section. When one deals with a problem where the density of the immersed structure is greater than (or equal to) the fluid one, the unconditional stability is always assured. Conversely when this is not the case, a limitation on the minimum value of the time step has to be satisfied to achieve stability.

This section is intended in demonstrating that this limitation exists, being the determination of its minimum value a difficult task involving the estimation of the constants introduced in the used inequality.

Nevertheless, numerical results of section 4.6.2 will show the existence of this limitation, even though not determined.

In order to focus on the only inertial term related to the kinetic energy, the elastic term is neglected for the sake of simplicity.

The criterion here adopted to check the stability deals with the temporal variation of the kinetic energy of the fluid alone, evaluated on the whole domain Ω. The reason of this choice comes from the difficulties to separate the fluid domain Ω_f from the whole domain Ω in the discretized problem. Nevertheless, if the fluid kinetic energy defined on the whole domain tends to increase in time, an instability in the numerical algorithm occurs. Indeed, being the system isolated, at continuum level the maximum value of the total energy has to be the one of the initial condition; as a consequence, the fluid kinetic energy is bounded from above by this value. If the value of the fluid kinetic energy increases unbounded in time, the numerical scheme is introducing a spurious energy in the system, thus making the algorithm unstable.

Denoting by $\Delta\rho$ the difference between the structure and fluid densities, when $0 \le \rho_s < \rho_f$ the energy estimation yields:

$$\begin{aligned}\frac{\rho_f}{2\Delta t}\left(\|\boldsymbol{u}_h^{n+1}\|_{L^2(\Omega)} - \|\boldsymbol{u}_h^{n}\|_{L^2(\Omega)} + \|\boldsymbol{u}_h^{n+1} - \boldsymbol{u}_h^{n}\|_{L^2(\Omega)}\right) &= -\mu\|\nabla\boldsymbol{u}_h^{n+1}\|_{L^2(\Omega)} \\ &+ \frac{|\Delta\rho|}{2\Delta t}\left(\frac{\|\boldsymbol{X}_h^{n+1} - \boldsymbol{X}_h^{n}\|^2_{L^2(\Omega_{0s})}}{\Delta t^2} - \frac{\|\boldsymbol{X}_h^{n} - \boldsymbol{X}_h^{n-1}\|^2_{L^2(\Omega_{0s})}}{\Delta t^2}\right. \\ &+ \left.\frac{\|\boldsymbol{X}_h^{n+1} - 2\boldsymbol{X}_h^{n} + \boldsymbol{X}_h^{n-1}\|^2_{L^2(\Omega_{0s})}}{\Delta t^2}\right)\end{aligned}$$

The only positive term on the right hand side deals with the contribution of the structure inertial force and could be bounded as follows:

$$\begin{aligned}&\frac{|\Delta\rho|}{2\Delta t}\left(\frac{\|\boldsymbol{X}_h^{n+1} - \boldsymbol{X}_h^{n}\|^2_{L^2(\Omega_{0s})}}{\Delta t^2} - \frac{\|\boldsymbol{X}_h^{n} - \boldsymbol{X}_h^{n-1}\|^2_{L^2(\Omega_{0s})}}{\Delta t^2}\right. \\ &+ \left.\frac{\|\boldsymbol{X}_h^{n+1} - 2\boldsymbol{X}_h^{n} + \boldsymbol{X}_h^{n-1}\|^2_{L^2(\Omega_{0s})}}{\Delta t^2}\right) \\ &\le \frac{|\Delta\rho|}{2\Delta t}\left(\frac{\|\boldsymbol{X}_h^{n+1} - \boldsymbol{X}_h^{n}\|^2_{L^2(\Omega_{0s})}}{\Delta t^2} - \frac{\|\boldsymbol{X}_h^{n} - \boldsymbol{X}_h^{n-1}\|^2_{L^2(\Omega_{0s})}}{\Delta t^2}\right. \\ &+ \left.\frac{\|\boldsymbol{X}_h^{n+1} - \boldsymbol{X}_h^{n}\|^2_{L^2(\Omega_{0s})}}{\Delta t^2} + \frac{\|\boldsymbol{X}_h^{n} - \boldsymbol{X}_h^{n-1}\|^2_{L^2(\Omega_{0s})}}{\Delta t^2}\right) \\ &= \frac{|\Delta\rho|}{\Delta t}\frac{\|\boldsymbol{X}_h^{n+1} - \boldsymbol{X}_h^{n}\|^2_{L^2(\Omega_{0s})}}{\Delta t^2}\end{aligned}$$

denoting with superscripts f, s the test function of fluid and structure respectively and neglecting the temporal index, the interpolation can be rewritten as

$$\frac{\boldsymbol{X}_h^{n+1} - \boldsymbol{X}_h^n}{\Delta t} = \sum_i u_i \left(\sum_m N_i^f(\boldsymbol{X}_m) N_m^s(\boldsymbol{q}) \right) = \sum_i u_i \tilde{N}_i(\boldsymbol{q})$$

where $\tilde{N}_i(\boldsymbol{q})$ is a test function defined on the structural grid for the $i-th$ fluid node. It follows:

$$\frac{\|\boldsymbol{X}_h^{n+1} - \boldsymbol{X}_h^n\|^2_{L^2(\Omega_{0s})}}{\Delta t^2} = \sum_{i,j} u_i u_j \int_{\Omega_{0s}} \tilde{N}_i(\boldsymbol{q}) \tilde{N}_j(\boldsymbol{q})$$

$$= \sum_{T_k \in \mathcal{S}_h} \sum_{i,j} u_i u_j \int_{\Omega_{T_k}} \left(\sum_{m_k} N_i^f(\boldsymbol{X}_{m_k}) N_{m_k}^s(\boldsymbol{q}) \right) \left(\sum_{p_k} N_j^f(\boldsymbol{X}_{p_k}) N_{p_k}^s(\boldsymbol{q}) \right)$$

Being the maximum absolute value of the Lagrange functions at least one, considering a quasi-uniform mesh and denoting by $NTria$ the total number of triangles/tetrahedra on the structure triangulation and by $NBnode_T$ the total number of node on the reference triangle/tetrahedron of the structural mesh, it follows:

$$\begin{aligned}
&\sum_{T_k \in \mathcal{S}_h} \sum_{i,j} u_i u_j \int_{\Omega_{T_k}} \left(\sum_{m_k} N_i^f(\boldsymbol{X}_{m_k}) N_{m_k}^s(\boldsymbol{q}) \right) \left(\sum_{p_k} N_j^f(\boldsymbol{X}_{p_k}) N_{p_k}^s(\boldsymbol{q}) \right) \\
&\quad \le \sum_{T_k \in \mathcal{S}_h} \sum_{i,j} u_i u_j \left(\sum_{m_k} N_i^f(\boldsymbol{X}_{m_k}) \right) \left(\sum_{p_k} N_j^f(\boldsymbol{X}_{p_k}) \right) \int_{\Omega_{T_k}} dT_K \\
&\quad \le C h_s^m \sum_{T_k \in \mathcal{S}_h} \sum_{i,j} \left(u_i \sum_{m_k} N_i^f(\boldsymbol{X}_{m_k}) \right) \left(u_j \sum_{p_k} N_j^f(\boldsymbol{X}_{p_k}) \right) \\
&\quad \le C h_s^m \sum_{T_k \in \mathcal{S}_h} (NBnode_T)^2 \sum_{i,j} u_i u_j \\
&\quad = C h_s^m \left[NTria \times (NBnode_T)^2 \right] \sum_{i,j} u_i u_j \\
&\quad \le C h_s^m \left[NTria \times (NBnode_T)^2 \right] \left(\sum_i (u_i)^2 + \sum_j (u_j)^2 \right) \\
&\quad = 2 C h_s^m \left[NTria \times (NBnode_T)^2 \right] \sum_i (u_i)^2
\end{aligned}$$

for a quasi-uniform mesh the following relation holds:

$$C_1 h_f^d \sum_i (u_i)^2 \le \|u_h\|^2_{L^2(\Omega)} \le C_2 h_f^d \sum_i (u_i)^2$$

by applying the Poincarè inequality:

$$\sum_i (u_i)^2 \leq \frac{C_3}{h_f^d} \|u_h\|^2_{L^2(\Omega)} \leq \frac{C_4}{h_f^d} \|\nabla u_h\|^2_{L^2(\Omega)}$$

so:

$$\frac{\|\boldsymbol{X}_h^{n+1} - \boldsymbol{X}_h^n\|^2_{L^2(\Omega_{0s})}}{\Delta t^2} \leq C \frac{h_s^m}{h_f^d} \left[NTria \times (NBnode_T)^2 \right] \|\nabla u_h\|^2_{L^2(\Omega)}$$

Generalizing for every value of $\Delta\rho$ it follows:

$$\Delta t \geq -C \frac{\Delta\rho}{\mu} \frac{h_s^m}{h_f^d} \left[NTria \times (NBnode_T)^2 \right] \tag{4.44}$$

clearly, if $\Delta\rho \geq 0$ stability is assured, being always $\Delta t > 0$.

Being the total number of triangle a great quantity, this estimation shows only that this limitation exists, but does not furnish any information on the minimum value of the time step size. In section 4.6.2 some results are depicted that show the existence of this limitation.

4.6 Numerical results

The stability properties of BE/BE and FE/BE schemes, in conjunction with a second order spatial interpolation are tested on a simple numerical problem. To this aim, denoting by $\boldsymbol{S}$ the second Piola-Kirchoff stress tensor, the temporal evolution of total energy, given by:

$$\begin{aligned}
E_T &= \int_\Omega \frac{1}{2} \|\boldsymbol{u}\|^2 + \int_{\Omega_{0s}} \boldsymbol{S}^{kl} \mathbb{E}_{kl} \\
\mathbb{E}_{kl} &= \frac{1}{2} \left(\frac{\partial d_k}{\partial s_l} + \frac{\partial d_l}{\partial s_k} + \sum_m \frac{\partial d_m}{\partial s_k} \frac{\partial d_m}{\partial s_l} \right) \\
\boldsymbol{d} &= \boldsymbol{X}(\boldsymbol{s}, t) - \boldsymbol{X}_0(\boldsymbol{s})
\end{aligned}$$

is recorded as a function of time. We use an example consisting of an insulated system, for which the total energy monotonically decreases in time until it reaches a constant value. Thus spurious effects due to time-stepping can be easily visualized.

4.6.1 Problem setup

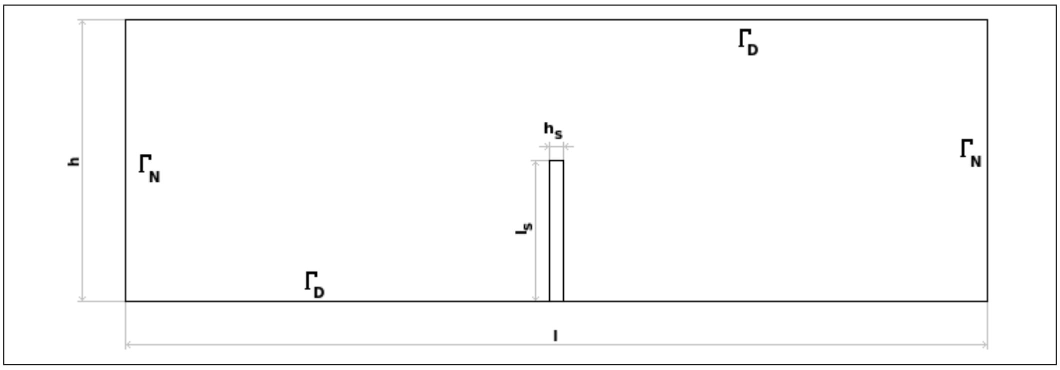

Figure 4.2: Domain

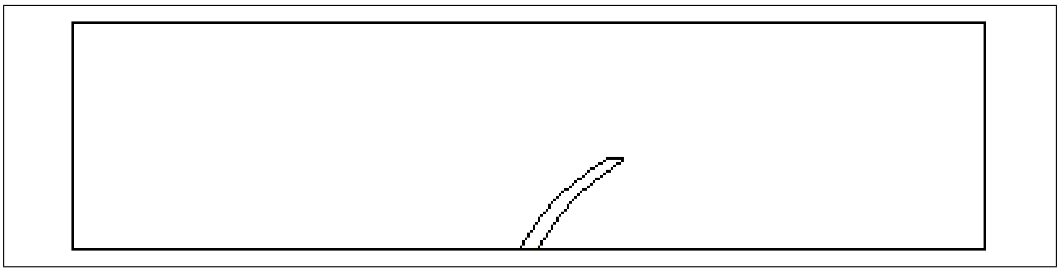

Figure 4.3: Initial condition

The computational domain of Fig. 4.2 consists in a structure constrained at bottom, embedded in a viscous fluid. For time $t < 0$ the structure is constrained in a pre-loaded configuration and the fluid is at rest, like in Fig. 4.3. At time $t = 0$ the structure is released and evolves to an unstrained configuration, driving the fluid in it's neighborhood. From the physical point of view, the motion that arises is damped by the fluid viscosity and consequently the total energy is dissipated.

Fluid is assumed to be Newtonian incompressible, described by Navier-Stokes equations, while structure is a Hookean isotropic massless one, described by it's first Piola-Kirchoff tensor:

$$\boldsymbol{P} = \frac{c_1}{2} tr \left(\mathbb{F}^T \mathbb{F} - \mathbb{I} \right) \mathbb{F} + c_2 \left(\mathbb{F}^T \mathbb{F} - \mathbb{I} \right) \mathbb{F}$$

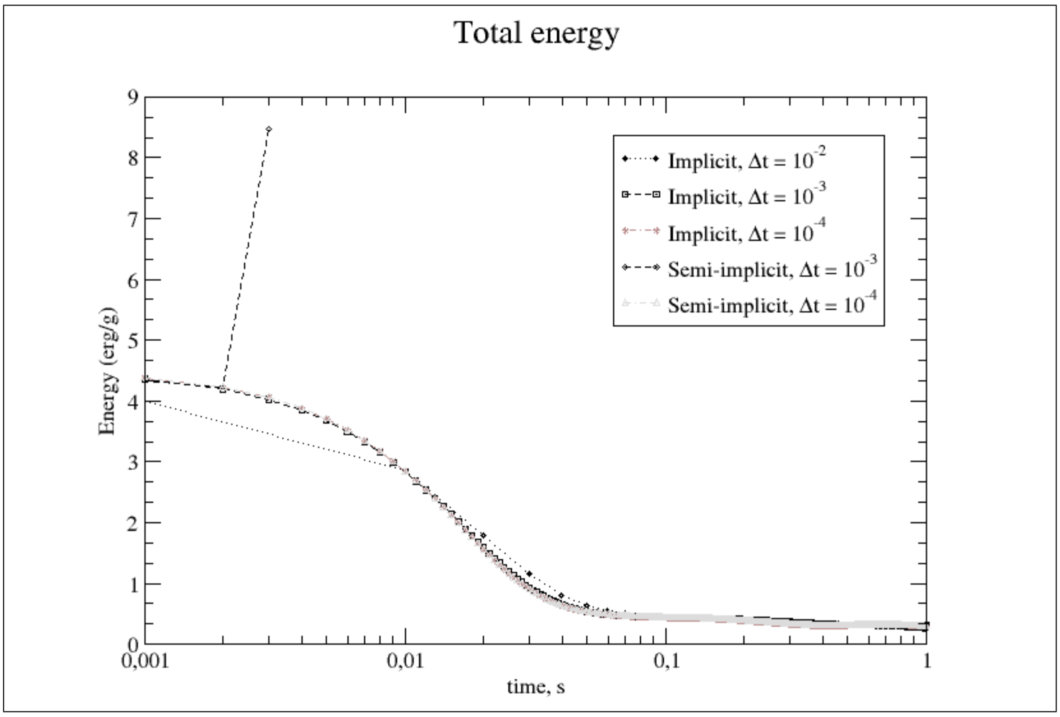

Figure 4.4: Total Energy temporal evolution

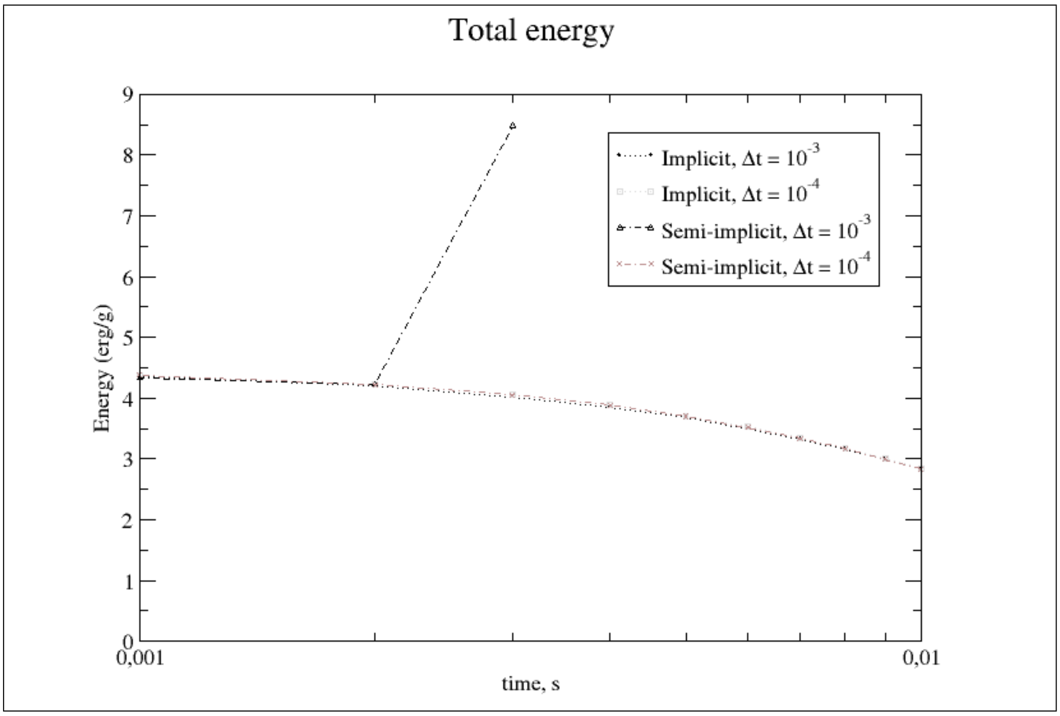

Figure 4.5: Total Energy temporal evolution, particular

Fluid domain Ω $(l \times h)$	4×1 (cm)
Structure dimension Ω_s $(l_s \times h_s)$	0.5×0.05 (cm)
Fluid density ρ_f	1 (g/cm^3)
Structure density ρ_s	1 (g/cm^3)
Kinematic viscosity ν	1 (cm^2/s)
Young Modulus E	4200 $(dyne/cm^2)$
Poisson Modulus σ	0.45
Pre-load force density f	85 $(dyne/cm^3)$

Table 4.1: Physical and geometrical properties

being c_1 and c_2 the two Lamé constants, thus defined:

$$c_1 = \frac{E\sigma}{(1+\sigma)(1-2\sigma)} \qquad\qquad c_2 = \frac{E}{2(1+\sigma)}$$

Physical and geometrical properties are shown in table 4.1. The domain is discretized by 80×20 nodes, while structure by 4×40. For the fluid $\mathbb{P}_2 - \mathbb{P}_1$ Lagrangian finite elements spaces are adopted, [64], whereas the structure is approximated by $\mathbb{P}_2$ Lagrangian finite elements. Considering the same simplification for L^n and C_e^n adopted in [32], the constraint on the time step size for the semi-implicit algorithm becomes:

$$\Delta t \leq \frac{h_x^{d-1}}{h_s^{m-2}} \frac{1}{k_{max} C}$$

Since the constant C typically is close to one, choosing for k_{max} the maximum between c_1 and $2c_2$. With data of Table 4.1 it is possible to show that a time-step of $\Delta t = 10^{-4}s$ ensures stability, while another one of at least one order of magnitude greater yields an unstable semi-implicit scheme. Figure 4.4 shows the temporal behavior of energy for both implicit and semi-implicit algorithm when $\Delta t = 10^{-4}s$ and $\Delta t = 10^{-3}s$. In the same figure the total energy decay for $\Delta t = 10^{-2}s$ for the implicit scheme is depicted, while in figure 4.5 depict the energy behavior at the earlier simulation time for the implicit and semi-implicit schemes, evaluated with time steps of $\Delta t = 10^{-4}s$

Fluid domain Ω ($l \times h$)	4×1 (cm)
Structure dimension Ω_s ($l_s \times h_s$)	0.5×0.05 (cm)
Fluid density ρ_f	1 (g/cm^3)
Kinematic viscosity ν	0.035 (cm^2/s)
Young Modulus E	420 ($dyne/cm^2$)
Poisson Modulus σ	0.45

Table 4.2: Physical and geometrical properties common to all the test case

and $\Delta t = 10^{-3}s$. As it is possible to see the results are so in agreement with the theory introduced in section 4.4; moreover, the behavior of the total energy, when algorithms are stable, is slightly different: this is caused by the different numerical viscosity, which depends on the time step size.

4.6.2 Numerical result related to the inertial term

The numerical simulations here performed are intended in demonstrating the validity of results described in section 4.5. In order to highlight the energy evolution when $\rho_s < \rho_f$, a small Young modulus is adopted for the structure thus reducing the numerical viscosity defined in (4.43). The initial configuration of the structure is the same used for the simulations performed in subsection 4.6.1. The data common to all the test case are summarized in table 4.2

The first test case is performed by adopting the same densities for both the fluid and the solid and considering a time step of $\Delta t = 10^{-5}s$ and another of $\Delta t = 10^{-2}s$. As depicted in figure 4.6, the scheme presents a time-decreasing fluid kinetic energy.

Conversely, when the structure density is smaller than the fluid one, as in the second and in the third case, the fluid kinetic energy increases in time for some values of the time step size (respectively, for a time step smaller than $\Delta t = 2 \cdot 10^{-5}$ for $\rho_s = 0$ and for a time step smaller than $\Delta t = 2 \cdot 10^{-6}$ for $\rho_s = \rho_f/2$). In figure 4.7 the fluid kinetic energies for $\rho_s = 0$ and $\Delta t = 10^{-5}$,

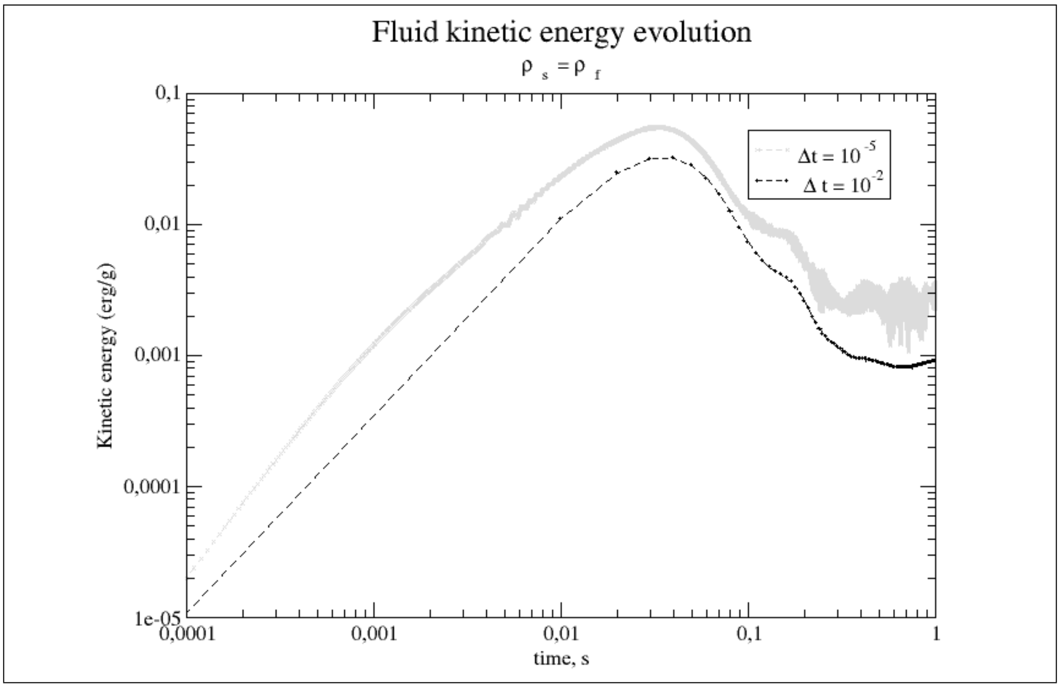

Figure 4.6: Fluid kinetic energy vs time for the first test case

$\Delta t = 2 \cdot 10^{-5}$, $\Delta t = 5 \cdot 10^{-5}$, $\Delta t = 10^{-4}$ and $\Delta t = 10^{-3}$. are depicted. The time steps $\Delta t = 10^{-5}$ and $\Delta t = 2 \cdot 10^{-5}$ yield instability, while the others show a stable temporal behavior. Moreover, in stable cases, the energies temporal evolutions are similar each others. By the intermediate value of structural density $\rho_s = \rho_f/2$ analogous results are found. In particular, the instability appears for a time step smaller than $2 \cdot 10^{-6}$, a value grater than the one of the previous test case, in agreement with formula (4.44). The results for test case 3 are depicted in figure 4.8.

4.7 Conclusion

In this chapter we have extend the formulation of [7, 11, 32] to a compressible structure of generic density. Moreover, we have proposed a discretization of this latter by finite element in space and finite difference in time and two algorithmic strategies (one implicit and one semi-implicit) for obtaining a numerical solution. By considering the particular case of an incompressible

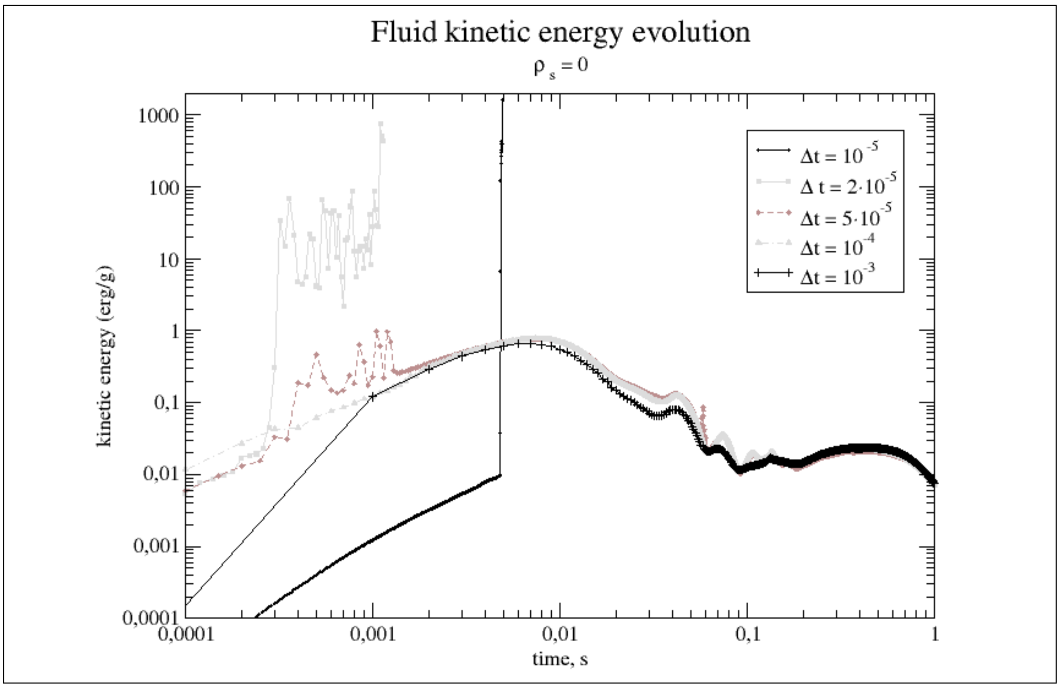

Figure 4.7: Fluid kinetic energy vs time for the second test case

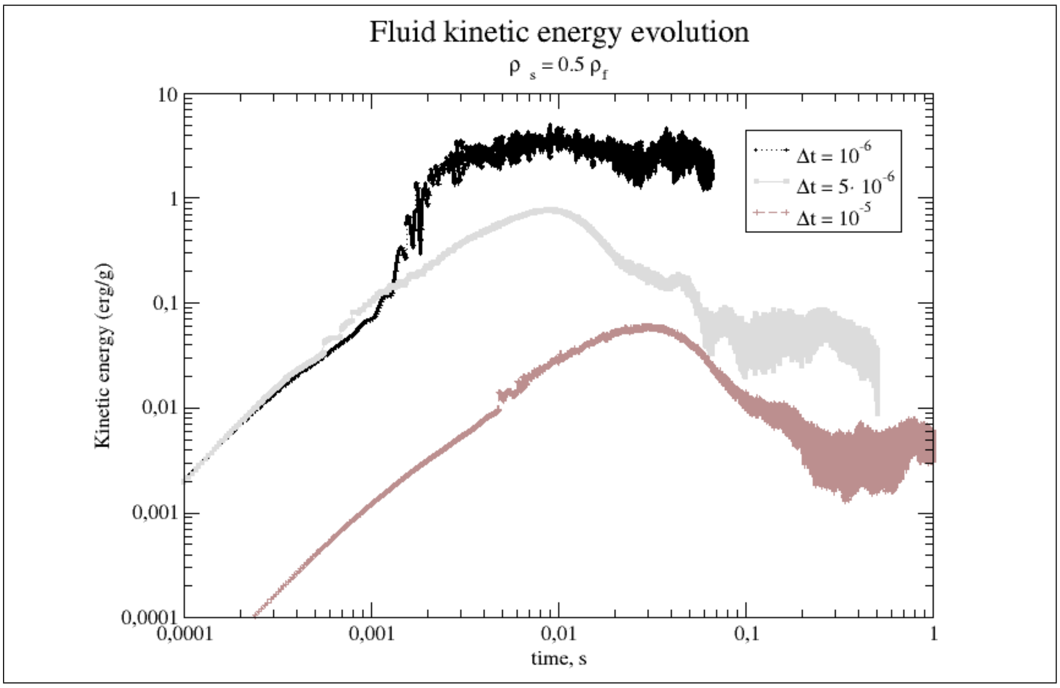

Figure 4.8: Fluid kinetic energy vs time for the third test case for testing the instability related to the inertial terms

structure, with the same density and visco-elastic behavior of the fluid, we have furnished a stability estimation based on the total energy time evolution for each strategy. We have shown that the implicit algorithm yields a decreasing of the total mechanical energy and thus is unconditionally stable, while the semi-implicit one achieve stability only if a restriction on the maximum time step size is satisfied. Differently from [32], we have considered a generic Lagrangian polynomial description for the structure, and we have demonstrated that the case of an affine polynomial description, as adopted in [32], represents a particular case of the estimation here obtained.

Moreover, we have demonstrate for the implicit algorithm that a lower-limitation exists on the time step size if the structure density is smaller than the fluid density. The analysis on this latter condition was performed by considering the only fluid kinetic energy, on the whole domain Ω, being difficult to separate the fluid domain from the solid one after the geometrical discretization. Nevertheless if the value of this latter energy increases unbounded in time, the algorithm is without doubts unstable. Indeed, the the kinetic energy has to be limited from above by the total mechanical energy, which assumes its maximum value at the initial time. The condition here introduced shows only that a limitation exists, but does not furnish a quantitative value of the limit.

Numerical results here reported have shown the consistency of the results in this work explained.

Chapter 5

Comparison of Arbitrary Lagrangian Eulerian and Immersed finite Element methods for immersed structures

5.1 Introduction

In this chapter we present a comparison between the Arbitrary Lagrangian Eulerian method and the Immersed finite element method. The aim of this chapter is to show that when dealing with problems of fluid motion with immersed continuum a reasonable choice for the numerical approximation is represented by the IFEM method , thus we compare the total number of sub-iterations required to reach the convergence at each time step between the IFEM and the ALE schemes. Note that whenever the ALE method yields a highly deformed fluid mesh, remeshing must be performed to avoid the linear system ill-conditioning. In the following comparison we do not perform remeshing but highlight the ALE “bad” behavior by counting linear iterations, whose number increases with ill-conditioning. The IFEM does not suffers for this problem, as shown in figure 5.1. Hence, while IFEM is well

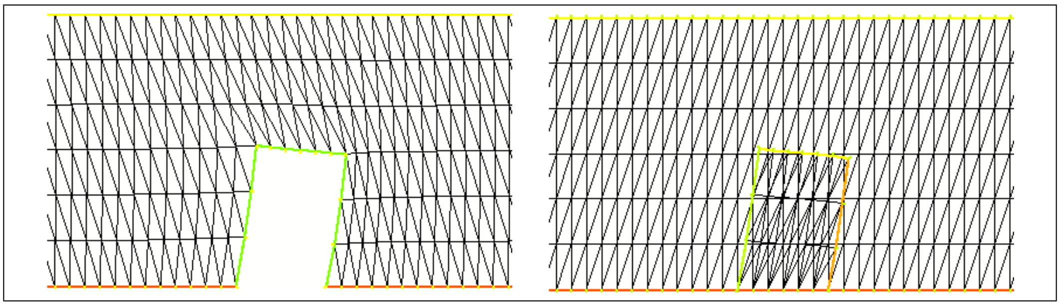

Figure 5.1: Comparison between ALE (right) and IFEM (left) methods with large structural displacement

suited for modeling a structure immersed in a fluid, as is the case of valves dynamic, the study of the arterial wall displacement is better described by an ALE formulation, which allows direct enforcement of the coupling boundary condition.

5.2 Problem description

The case under study consists of a bounded fluid domain with an immersed structure, fixed at bottom (see figure 5.2). The fluid is driven by a constant pressure gradient between the inlet (Γ_{in}) and the outlet (Γ_{out}) sections. The fluid is initially at rest and the structure is initially unloaded. For the sake of simplicity, a linear elasticity model is adopted, with its stress tensor defined as:

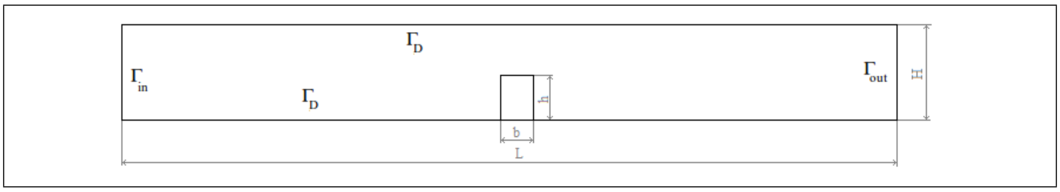

Figure 5.2: Problem geometry and symbol conventions

$$\boldsymbol{\sigma} = (\lambda \nabla \cdot \boldsymbol{d})\, \boldsymbol{I} + 2\mu \boldsymbol{\epsilon}$$

$$\epsilon_{ij} = \frac{1}{2}\left(\frac{\partial d_i}{\partial s_j} + \frac{\partial d_j}{\partial s_i}\right)$$

Domain dimension ($L \times h$):	40×3(m)
Fluid density (ρ_f):	$999.1(\frac{Kg}{m^3})$
Structure dimension ($b \times h$):	1×1.5 (m)
Structure density (ρ_s):	$7792.28(\frac{Kg}{m^3})$
Poisson coefficient (σ)	0.33
Young Modulus(E)	210000 $(\frac{N}{m^2})$
Time step size (Δt)	5×10^{-3} (s)
Total number of fluid mesh nodes	1687
Total number of structural mesh nodes	28

Table 5.1: Common parameters to case 1 and case 2

parameter	case 1	case 2
Kinematic viscosity (ν)	$1(\frac{m^2}{s})$	$10^{-6}(\frac{m^2}{s})$
Pressure at inlet	$5 \cdot 10^4\, Pa$	$8.9 \cdot 10^{-7}\, Pa$
Pressure at outlet	$-5 \cdot 10^4\, Pa$ bar	$-8.9 \cdot 10^{-7}\, Pa$

Table 5.2: Common parameters to case 1 and case 2

Two cases are here analyzed, they have in common the parameters reported in table 5.1, while the parameter that distinguish the two test cases in table 5.2.

Parameters here adopted have no physical meaning; the chosen values are finalized to obtain typical numerical results without excessive computing time and at the same time highlight the relevant numerical results of the analyzed schemes

5.3 Algorithm description

The numerical discretization of the problem is performed by finite element in space and finite difference in time, as described in chapter 3 for the ALE formulation and in chapter 4 for the IFEM one. In particular, fluid is described through a $P2 - P1$ finite element space [64], while structural deformations with $P2$ elements.

5.3.1 ALE algorithm

ALE mapping is of the type isoparametric with $P2$ element. The boundary conditions used to evaluate the ALE mapping are homogeneous Dirichlet on Γ_D, while on Γ_{in}, Γ_{out} only tangential displacements are allowed. Clearly, at the fluid-structure interface the mesh displacement has to be the same of the structure displacement.

Given initial an guess $(k = 0)$ $\boldsymbol{d}_0^{n+1}$, $\boldsymbol{w}_0^{n+1}$ the iterative cycle reads as follows:

1. solve the Navier-Stokes problem, by imposing the continuity of velocity at the interface, obtaining $(\boldsymbol{u}_{k+1}^{n+1}, p_{k+1}^{n+1})$;
2. evaluate the weak form of the fluid force on the structure;
3. solve the structural problem, by imposing the force previously determined as Neumann boundary condition, obtaining $(\tilde{\boldsymbol{d}}_{k+1}^{n+1})$;
4. apply relaxation (if required) to the new displacement:

$$\boldsymbol{d}_{k+1}^{n+1} = \omega \, \tilde{\boldsymbol{d}}_{k+1}^{n+1} + (1 - \omega) \, \boldsymbol{d}_k^{n+1}$$

   ;
5. determine the news mesh displacement and velocity $(\boldsymbol{s}_{k+1}^{n+1}, \boldsymbol{w}_{k+1}^{n+1})$ vectors by solving the mapping formulation;
6. move the mesh ;
7. if convergence is not reached, set $k = k + 1$ and go to 1.

5.3.2 IFEM algorithm

The IFEM algorithm employed in these simulations slightly differs from the one described in chapter 4 because structure displacement is evaluated by solving an additional equation on the structural mesh, where a Dirichlet Boundary condition is imposed on the whole boundary. Moreover, the forcing term $\boldsymbol{F}$ takes into account the contribution that comes from the fluid stress tensor, so no visco-elastic terms are considered.

Given initial guess ($k = 0$) $\boldsymbol{d}_0^{n+1}$, $\boldsymbol{w}_0^{n+1}$ the iterative algorithm reads as follows:

1. evaluate the weak form of the source forcing $\int_{\Omega_s} \boldsymbol{F}_{k+1}^{n+1} \cdot \boldsymbol{v}$;
2. solve the Navier-Stokes equation, obtaining ($\boldsymbol{u}_{k+1}^{n+1}$, p_{k+1}^{n+1});
3. solve the elasticity equation, with the following Dirichlet boundary condition at interface:

   $$\boldsymbol{d}_{k+1}^{n+1}\big|_{\partial\Omega_s} = \boldsymbol{d}^{n+1}\big|_{\partial\Omega_s} + \boldsymbol{u}_{k+1}^{n+1}\big|_{\partial\Omega_s}$$

   thus obtaining ($\boldsymbol{d}_{k+1}^{n+1}$);
4. go back to 1 if convergence was not reached.

5.4 Numerical results

In fig 5.3 the total number of sub-iterations required to reach convergence is plotted for case 1, while in figure 5.4 the same is plotted for case 2. For the immersed finite element method the number of sub-iterations decreases in time, converging to a number between $25 - 30$ for case 1 and around 6 for case 2. Conversely, for the Arbitrary Lagrangian Eulerian method, the number of sub-iterations increases in time, when the displacement becomes large and the fluid mesh becomes too deformed. In case 1 where the displacement is larger (see figure 5.5, 5.6) the total number of sub-iteration increases rapidly; conversely in case 2, where displacements are about 10 order of magnitudes smaller (see figure 5.7, 5.8), the total number of sub-iterations increases slower.

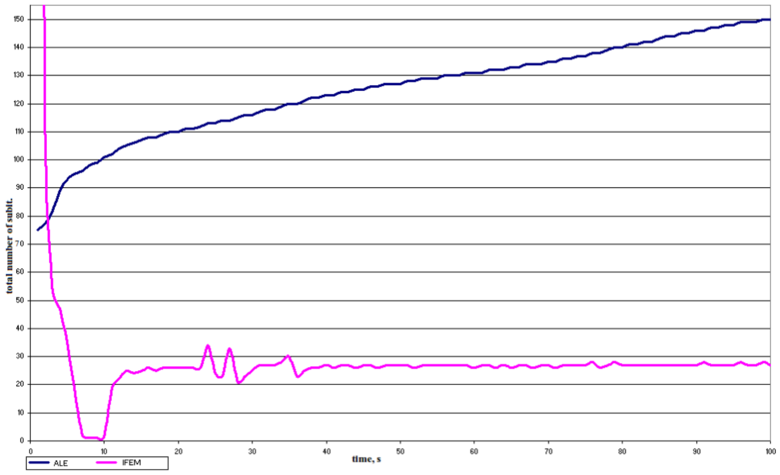

Figure 5.3: Number of sub-iteration for reach convergence vs time of case 1 for ALE (blue line) and IFEM (magenta line)

The solution obtained by the ALE method and the one obtained by IFEM method do not differ so much, as it is possible to see by comparing the structural mesh position, figs 5.9, 5.10

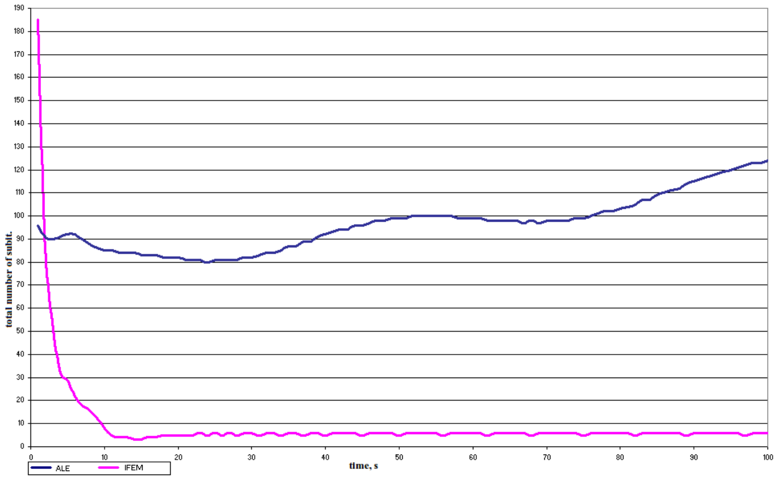

Figure 5.4: Number of sub-iteration for reach convergence vs time of case 2 for ALE (blue line) and IFEM (magenta line)

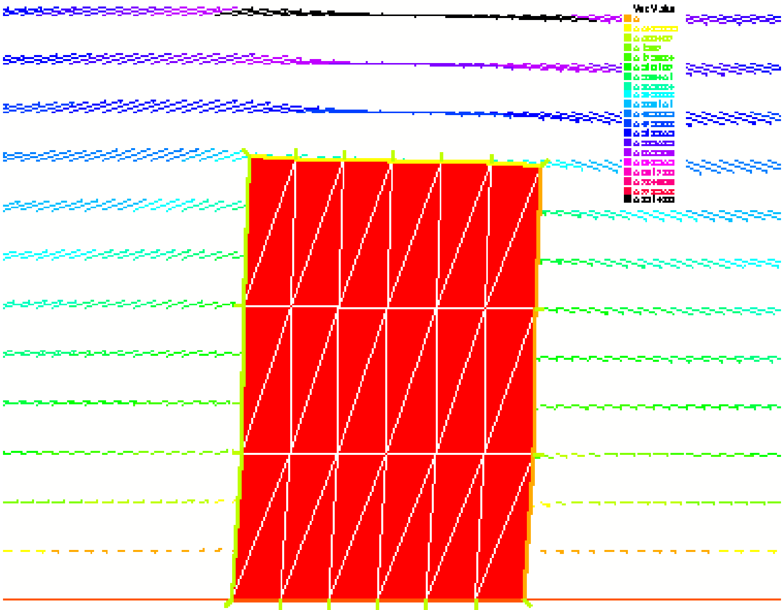

Figure 5.5: Solution at time $t = 0.25s$, case 1

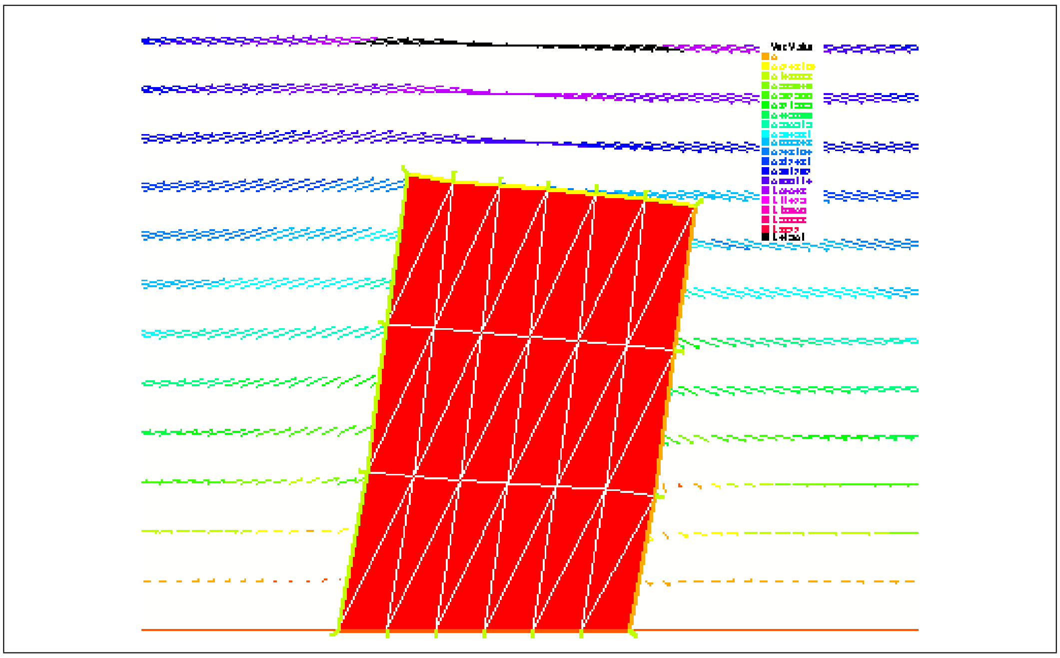

Figure 5.6: Solution at time $t = 0.5s$, case 1

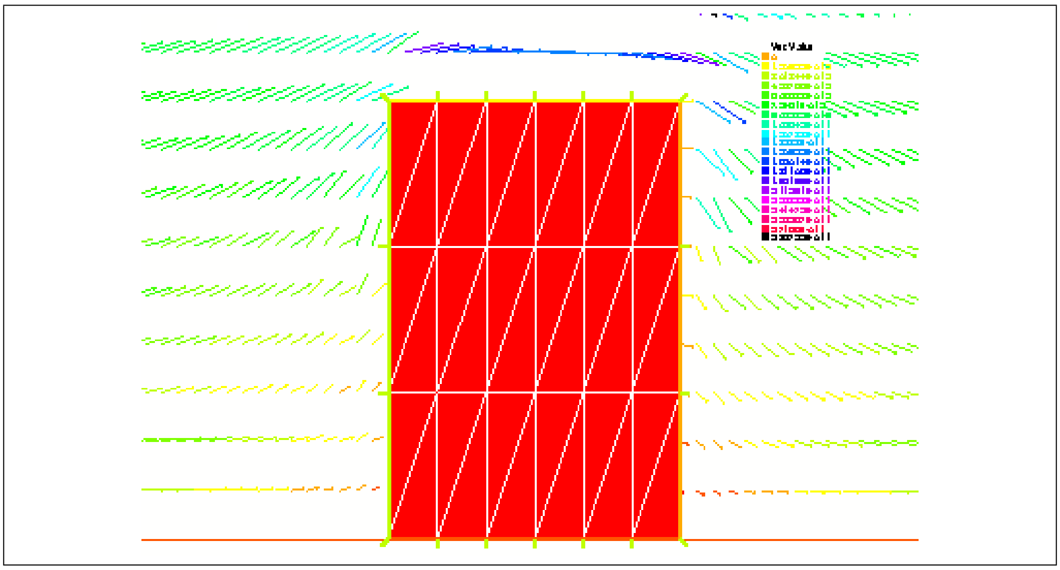

Figure 5.7: Solution at time $t = 0.25s$, case 2

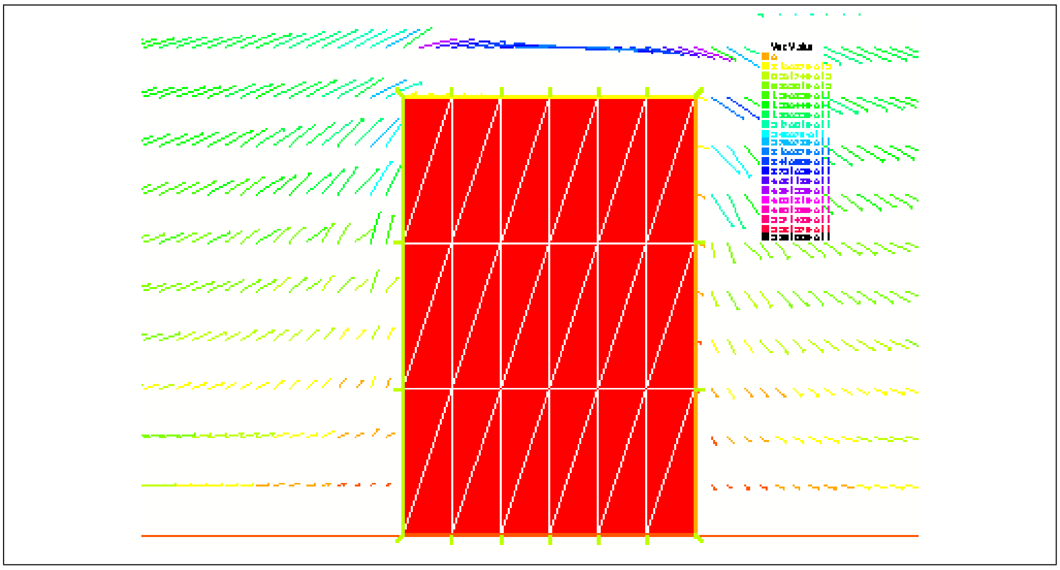

Figure 5.8: Solution at time $t = 0.5s$, case 2

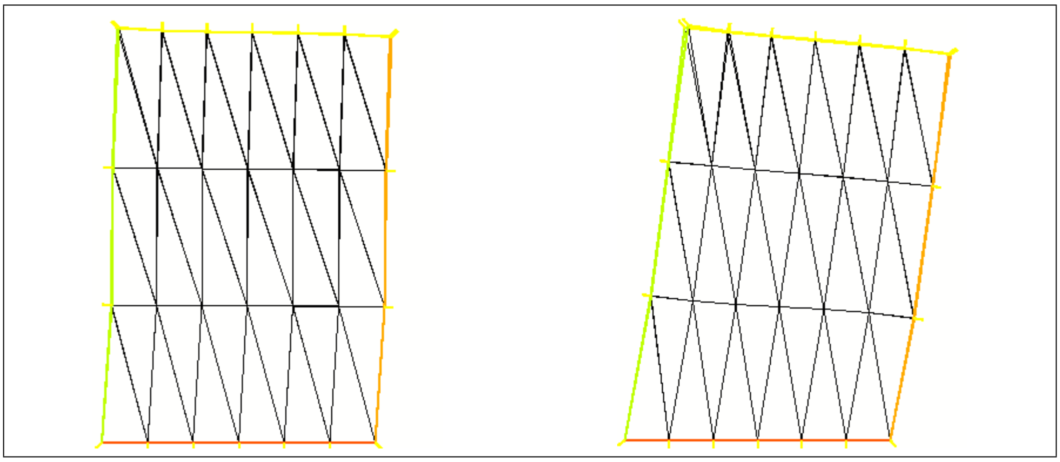

Figure 5.9: Structural mesh for ALE and IFEM methods, time $t = 0.25s$ (left) and $t = 0.5s$ (right), case 1

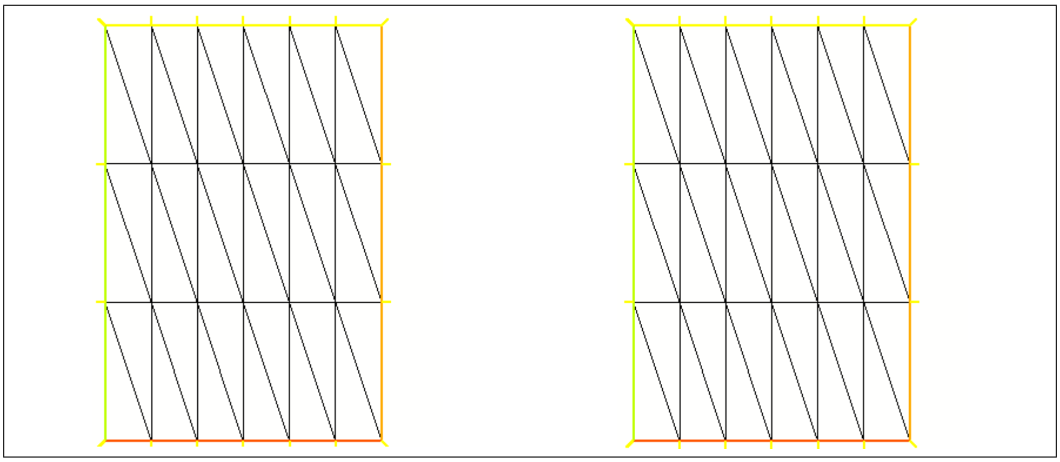

Figure 5.10: Structural mesh for ALE and IFEM methods, time $t = 0.25s$ (left) and $t = 0.5s$ (right), case 2

Part III

Heart Electro-Mechanics

Chapter 6

The Heart electro-physiology

6.1 Introduction

The heart is a complex organ which could be approximated as a volumetric pump, constituted by the heart muscle and activated by an electric signal. The study of this complex organ yields mainly two branch of interest:

- The electro-physiology, aimed at determine how an electrical wave travels in the heart
- The mechanics, aimed at determine the mechanical response of the heart, when inserted in a circulatory system

The final task of this part of the thesis is devoted to the study of the coupling of these two branches, determining the so called “electromechanical activity” of the heart. In this chapter the heart electro-physiology is explained, while in chapter 7 the mechanical model is treated. Finally, in chapter 8 the characteristics of a coupled electro-mechanics problem are introduced.

The heart electro-physiology is description of the electrical wave propagation which is based on two different spatial scales: the cellular (microscopic) one, modeling the electrical wave propagation inside the heart muscular cell and the macroscopic one, describing the propagation of the electrical wave

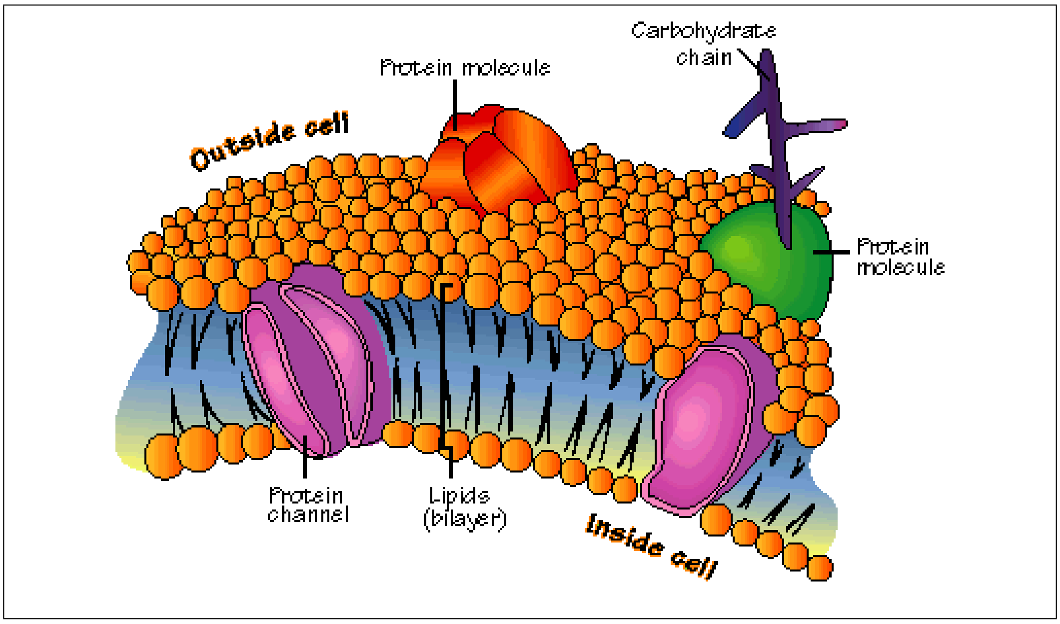

Figure 6.1: Sketch of the cell membrane

inside the heart (i.e. from a cell to another) and from the heart to the rest of the body.

At microscopic level, the electrical propagation is related to the ionic exchange between the intra-cellular and extra-cellular regions; the ionic exchange occurs through the cell membrane, a surface perforated by proteins which assures the flux of the electrical ion from the extern into the cell and vice-versa and so the cellular polarization and depolarization (fig. 6.1). There exists three different type of ionic exchange, depending on their characteristic:

- ionic channels
- pumps
- exchangers

Ionic channels are passive elements which allow the flow of a chemical species in only one side, depending on its electrochemical gradient. Ionic channels are therefore modeled as a a variable conductivity (in particular, they could be closed, i.e. zero conductivity) and their opening/closing is the cause of cell depolarization (for sodium channels) and re-polarization (for potassium channels). The current generate by ionic channels is proportional to the concentration of ions at intra and extra cellular level.

Conversely, *pumps* are active elements responsible for the flow of chemical species in the electrochemical gradient opposite direction; the necessary energy to do so is extracted by the molecule of Adenosine Tri Phosphate (ATP) by the cell metabolism. Pumps act after ionic channels and restore the initial ionic concentration.

Exchangers are channels which exchange ionic species using the energy which becomes by the ionic gradient of another ionic specie. A typical exchange is the one of the sodium-calcium species, where the calcium gradient is the one generated by a sodium-potassium pump.

At macroscopic level, the electrical wave propagation was introduced [60] treating the heart as continuum medium; in literature there exists many models to treat the heart as a continuum, however the most used is the so called "bidomain model" [65] which describes the evolution of the electrical potential in two different microscopic domain, the intracellular one and the extracellular one (by this the name bidomain). The solution of this latter furnishes the intra and extracellular potential, the difference of which, called transmembrane potential, constitutes the electrical activation responsible of the heart contraction. The intra-cellular and the trans-membrane potentials are not evaluable by clinical equipment; however it is possible to determine the difference between some body location of the extracellular potential, through a medical device called electro-cardiogram (ECG). The extra-cellular potential has so a strong impact for which concerns the clinical point of view.

6.2 The bidomain model

As pointed out in section 6.1, the heart tissue is formed by two different media (the intra-cellular medium, $\Omega_{H,i}$, representing the set of cells forming the heart muscle and the extra-cellular medium, $\Omega_{H,e}$, representing the space between the cells), separated by the cell membrane, figure 6.2. The total heart volume Ω_H is formed by the union of both domains domain $\Omega_{H,i}$ and $\Omega_{H,e}$, as follows:

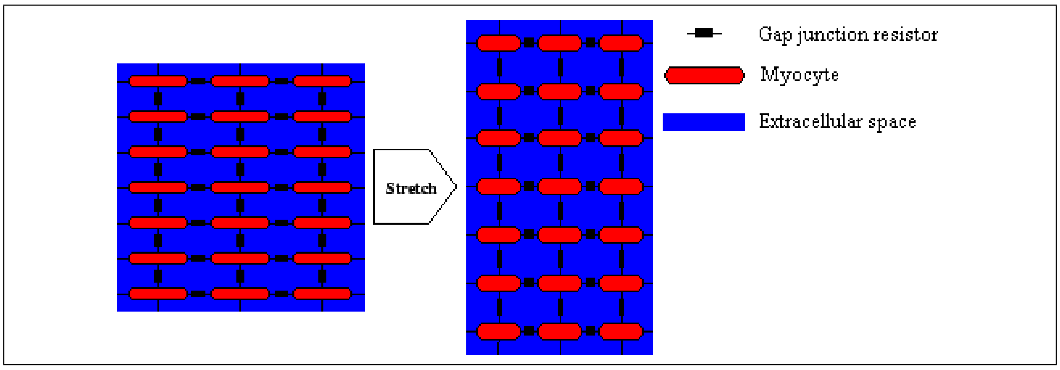

Figure 6.2: The extra and intra cellular level

$$\overline{\Omega}_H = \overline{\Omega}_{H,e} \cup \overline{\Omega}_{H,i}$$

where by $\overline{\Omega}_{H,e,i}$ and $\overline{\Omega}_H$ the closure each domain is denoted.

Each media is assumed to be a passive conductor, with an anisotropic conductivity $\boldsymbol{\sigma}_{i,e}$; the current-potential relation corresponds to the Ohm's law, as follows:

$$\boldsymbol{j}_{i,e} = -\boldsymbol{\sigma}_{i,e} \nabla u_{i,e}$$

where $u_{i,e}$ denotes the intra or extra cellular potential and $\boldsymbol{j}_{i,e}$ denotes the intra or extra cellular current density. The intersection of the boundaries of the two domains corresponds to the cell membrane Γ_m previously described in 6.1. Cell membrane is crossed by a surface current density I_m, obtained by the continuity equation:

$$I_m = \boldsymbol{j}_i \cdot \boldsymbol{n}_H = -\boldsymbol{j}_e \cdot \boldsymbol{n}_H$$

where $\boldsymbol{n}_H$ represents the outward unit normal to $\Omega_{H,i}$. Typically, the membrane electrical behavior is described as a circuit formed by a parallel of a resistance and a capacity, yielding to the following relation:

$$I_m = I_{ion} + C_m \frac{\partial V_m}{\partial t} + i_{app}$$

where i_{app} represents an applied external current, C_m denotes the capacity for a unitary surface, V_m the trans-membrane potential $V_m = u_i - u_e$, and I_{ion} the ionic current depending on the ionic exchanges at microscopic level, as described in section 6.1. Even though different models exist in literature for determining I_{ion}, [58, 63] each one depends on the trans-membrane potential, V_m and on the ionic activity of the cell membrane. Indeed, in each model exists a variable, denoted by $\boldsymbol{w}$ which models these aspects and has to obey to an ODE's system as follows:

$$\frac{\partial \boldsymbol{w}}{\partial t} + \boldsymbol{g}\left(V_m, \boldsymbol{w}\right) = 0$$

here $\boldsymbol{g}$ depends on the model chosen for describing the ionic model.

Through an homogenization procedure as described in [40, 54], it is possible to model the propagation phenomena at continuum level on the domain Ω_H; this leads to the following set PDEs:

$$A_m \left(C_m \frac{\partial V_m}{\partial t} + I_{ion}\left(v_m, w\right) \right) - \nabla \cdot \left(\boldsymbol{\sigma}_i \nabla u_i \right) = I_{app} \qquad \text{in } \Omega_H \qquad (6.1)$$

$$A_m \left(C_m \frac{\partial V_m}{\partial t} + I_{ion}\left(v_m, w\right) \right) + \nabla \cdot \left(\boldsymbol{\sigma}_e \nabla u_e \right) = I_{app} \qquad \text{in } \Omega_H \qquad (6.2)$$

$$\frac{\partial w}{\partial t} + g\left(v_m, w\right) = 0 \qquad \text{in } \Omega_H \qquad (6.3)$$

or, in it's typical differential-algebraic (DAE) formulation:

$$A_m \left(C_m \frac{\partial V_m}{\partial t} + I_{ion}\left(v_m, w\right) \right) - \nabla \cdot \left(\boldsymbol{\sigma}_i \left(\nabla V_m + \nabla u_e \right) \right) = I_{app} \quad \text{in } \Omega_H \quad (6.4)$$

$$\nabla \cdot \left(\left(\boldsymbol{\sigma}_i + \boldsymbol{\sigma}_e \right) \nabla u_e \right) + \nabla \cdot \left(\boldsymbol{\sigma}_i \nabla V_m \right) = 0 \quad \text{in } \Omega_H \quad (6.5)$$

$$\frac{\partial w}{\partial t} + g\left(v_m, w\right) = 0 \quad \text{in } \Omega_H \quad (6.6)$$

System (6.1)-(6.2), is the so called “bidomain model“. System (6.1)-(6.2) (or the corresponding DAE form, (6.4)-(6.5)) fas to be endowed by suitable boundary conditions.

Heart boundary is formed by an internal region (endocardium) corresponding to the surface delimiting the ventricles and by an external surface (epicardium) surrounded by the human tissue (bones, lungs, etc). Through some experimental observations [52], was noted that the intracellular current is not transmitted outside the heart; conversely, the extracellular current propagates at the exterior only on the epicardium, leading to the continuity of the potential and the extra-cellular current at the epicardium surface. However, when the study of the electrical activity is limited to the heart only, a typical practice consists in imposing no flux on the epicardium for the extracellular current (i.e. the heart is considered as isolated). For system (6.1)-(6.2) the following boundary conditions [41, 65] thus follow:

$$\begin{aligned} \boldsymbol{\sigma}_i \nabla u_i \cdot \boldsymbol{n}_H &= 0 \\ \boldsymbol{\sigma}_e \nabla u_e \cdot \boldsymbol{n}_H &= 0 \end{aligned}$$

while for the DAE system:

$$\begin{aligned} \boldsymbol{\sigma}_i \nabla V_m \cdot \boldsymbol{n}_H &= -\boldsymbol{\sigma}_i \nabla u_e \cdot \boldsymbol{n}_H \\ \boldsymbol{\sigma}_e \nabla u_e \cdot \boldsymbol{n}_H &= 0 \end{aligned}$$

In both cases, dealing with boundary conditions of the Neumann type only, the following additional condition:

$$\int_{\Omega_h} u_e = 0$$

has to be imposed for the well-posedness of the problem.

6.2.1 The ionic models

The expressions for $I_{ion}(v_m, w)$ and $\boldsymbol{w}$ depend on the ionic model chosen; the most simple is the one called Fizhugh and Nagumo, [24, 37]:

$$\begin{aligned} I_{ion}(v_m, w) &= k v_m (v_m - a)(v_m - 1) + w \\ g(v_m, w) &= \epsilon (\beta v_m - \gamma w) \end{aligned}$$

Other models exist in literature (Aliev and Panfilov, [2], Mitchell and Schaeffer, [47]); in the present work the model of Mitchell and Schaeffer, [47] will be assumed. This is defined by the following relations:

$$I_{ion}\left(v_m, w\right) = -\frac{w}{\tau_{in}} \frac{\left(v_m - V_{min}\right)^2 \left(V_{max} - v_m\right)}{V_{max} - V_{min}} + \frac{1}{\tau_{out}} \frac{v_m - V_{min}}{V_{max} - V_{min}}$$

$$g\left(v_m, w\right) = \begin{cases} \frac{w}{\tau_{open}} - \frac{1}{\tau_{open}\left(V_{max} - V_{min}\right)^2} & v_m < V_{gate} \\ \frac{w}{\tau_{close}} & v_m > V_{gate} \end{cases}$$

where τ_{in}, τ_{out}, τ_{open}, τ_{close}, V_{gate} are given parameters and V_{min}, V_{max} scaling constants. This model integrates relevant physiological properties of the cell membrane (trans-membrane potential, activation dynamics and two currents). In particular, it is capable of reproducing the cell heterogeneity, as described in section 6.4.3.

6.3 The thorax model

With the term "thorax model" here and in the following is intended the electrical model which describes the propagation of the extra-cellular potential and of the extracellular current in the whole human body. When the thorax potential is known, it is possible to determine the electro-cardiogram by evaluating the potential differences between some typical point of the body as, for example, those marked in figure 6.3 .

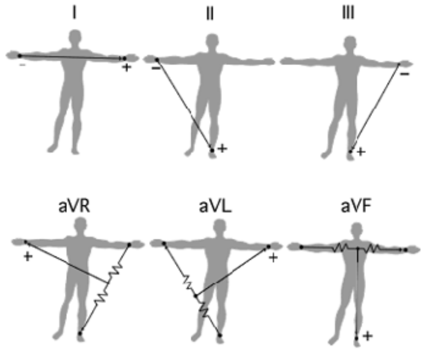

Figure 6.3: Electrode position for leads I, II, III, aVR, aVL and aVF

Thorax domain Ω_T as depicted in fig. 6.4 includes bones and lungs and is delimited by the epicardium Σ and by the body skin Γ_{ext} By the electrical point of view is considered as in a quasi-static state as demonstrated in [45] and behaves like a passive conductor, described by the following Ohm's law:

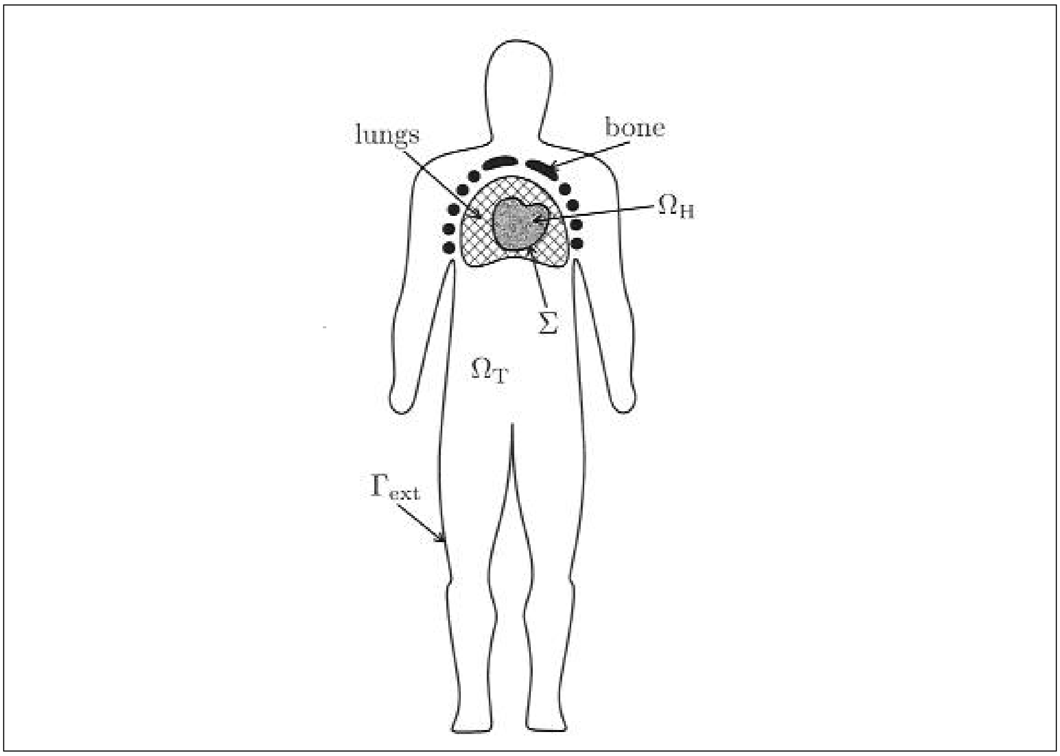

Figure 6.4: Domain decomposition

$$\boldsymbol{j}_T = \boldsymbol{\sigma}_T \nabla u_T$$

where u_T represents the thorax potential, and $\boldsymbol{\sigma}_T$ the heterogeneous conductivity tensor. Being any source of charge absent, by the continuity equation it follows:

$$\nabla \cdot (\boldsymbol{\sigma}_T \nabla u_T) = 0 \qquad \text{in } \Omega_T \tag{6.7}$$

As far as for the boundary condition is concerned, the surface Γ_{ext} is electrically isolated, [42, 54, 58, 63]:

$$\boldsymbol{\sigma}_T \nabla u_T \cdot \boldsymbol{n}_T = 0 \qquad \text{on } \Gamma_{ext} \tag{6.8}$$

where $\boldsymbol{n}_T$ denotes the outward unit normal on Γ_{ext}. On the epicardium Σ however the continuity of potential and current with the one of the heart has to be imposed; it follows:

$$u_e = u_T \qquad \text{on } \Sigma \tag{6.9}$$

$$\boldsymbol{\sigma}_T \nabla u_T \cdot \boldsymbol{n}_T + \boldsymbol{\sigma}_e \nabla u_e \cdot \boldsymbol{n}_H = 0 \qquad \text{on } \Sigma \tag{6.10}$$

where $\boldsymbol{n}_H$ represents the heart outward unit normal.

When the solution is determined numerically, conditions (6.9),(6.10) imply the coupling between the heart and the thorax model, yielding to an algorithm in which heart-thorax sub-iteration are required. In literature however, there exist some works ([12, 43, 55, 57]) where the condition (6.10) is relaxed by imposing an homogeneous boundary condition for each model (the model is named “heart isolated”), thus avoiding sub-iterations. This latter hypothesis produces good results in terms of ECG only when one deals with non-pathological case.

The interested reader can find the proof of the existence and the uniqueness of the bidomain-thorax coupled system in [72].

6.4 Other modeling aspects

The description of the heart electro-physiology is completed by the following three aspects:

- The modeling of the heart and thorax conductivity
- The modeling of the electrical external stimulus
- The modeling of the cell heterogeneity

6.4.1 Heart and thorax conductivity

As mentioned in section 6.2, the heart conductivity is anisotropic, being the heart muscle made of fibers. Thus, the electrical conductivity is higher

σ_i^l (Scm^{-1})	σ_i^t (Scm^{-1})	σ_e^l (Scm^{-1})	σ_e^t (Scm^{-1})
3.0×10^{-3}	3.0×10^{-4}	3.0×10^{-3}	1.2×10^{-3}

Table 6.1: Heart conductivity values

along the fiber direction than in the transverse one. Denoting by $\boldsymbol{a}(x)$ the unit vector parallel to the fiber local direction, with σ^l the conductivity along the fiber and with σ^t the conductivity in the transverse direction, the conductivity tensors for the intra and extra cellular currents become:

$$\boldsymbol{\sigma}_{i,e} = \sigma_{i,e}^t \boldsymbol{I} + \left(\sigma_{i,e}^l - \sigma_{i,e}^t\right) \boldsymbol{a}(x) \otimes \boldsymbol{a}(x)$$

where $\boldsymbol{I}$ denotes the identity matrix and $\otimes$ the tensorial product.

Different heart conductivity values for $\sigma_{i,e}^l$ and $\sigma_{i,e}^t$ are available in literature ([18, 45, 63]); in the present work the ones originally reported in [56] and resumed in table 6.1 are assumed. The fiber directions is the one plotted in figure 6.5, obtained as as described in [61]. Other procedures based on an harmonic extension could be found in [48, 72].

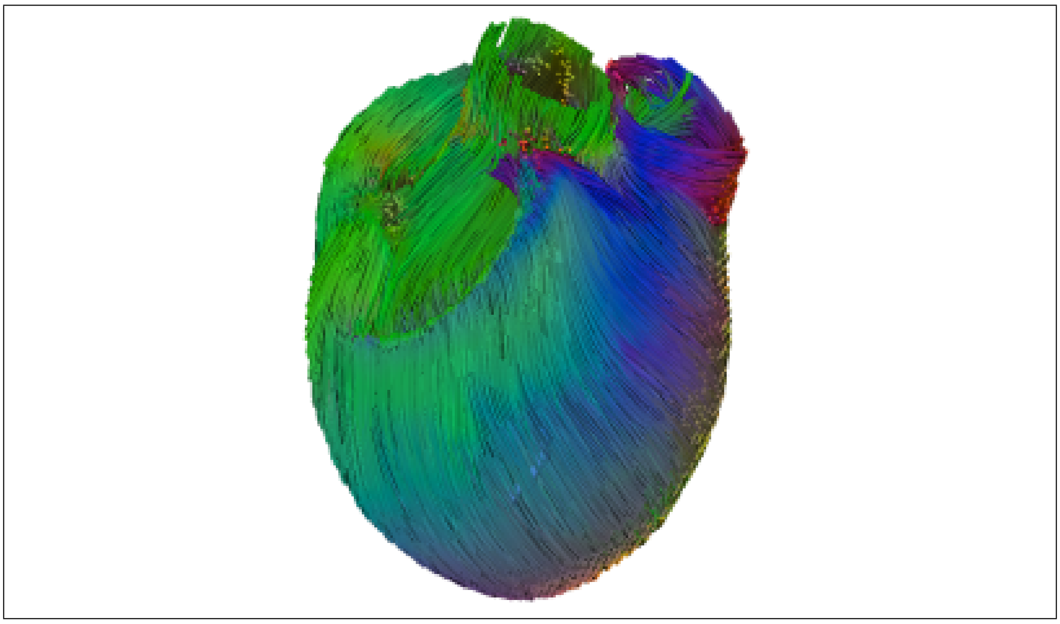

Figure 6.5: Fiber visualization with MedINRIA (Equipe Asclepios)

σ_T^l (Scm^{-1})	σ_T^b (Scm^{-1})	σ_T^t (Scm^{-1})
2.4×10^{-4}	4.0×10^{-5}	6.0×10^{-4}

Table 6.2: Thorax conductivity values

Thorax conductivity is assumed to be heterogeneous isotropic, being its tensor defined as:

$$\boldsymbol{\sigma}_T = \sigma_T \boldsymbol{I}$$

$$\sigma_T = \begin{cases} \sigma_T^l & \text{lungs} \\ \sigma_T^b & \text{bones} \\ \sigma_T^t & \text{remaining regions} \end{cases}$$

Typical value for the thorax conductivity are the one defined in [14] and reported in table 6.2. These values will be assumed in the present work.

6.4.2 External stimulus

Physiologically, the activation wave begins at the sinusal node in the right atria and propagates to the ventricle through the atrioventricular node and join the His-bundle, a complex structure composed of three main branches (see fig. 6.6) located in the septum. His-bundle activates the Purkinje fibers to stimulate all the endocardium (see [45] for a detailed description). Even though there are in literature interesting attempts at modeling the complex system of His-bundle and Purkinje fibers (see, for example, [21, 66]), the coupling of them with a 3D model of the myocardium raises many modeling and computational difficulties: the fiber network has to be manually defined whereas it cannot be non-invasive obtained from classical imaging techniques; the results are strongly dependent on fiber density, a quantity difficult to determine; the time and space scales are quite different between this fast conductive network and the rest of the tissue which can be challenging from the computational standpoint.

To circumvent these issues, in the present work the Purkinje fibers are roughly modeled by considering the external stimulus as an external volume current, during a small period of time t_{act} and acting on a thin subendocardial layer, both for the left and right ventricles.

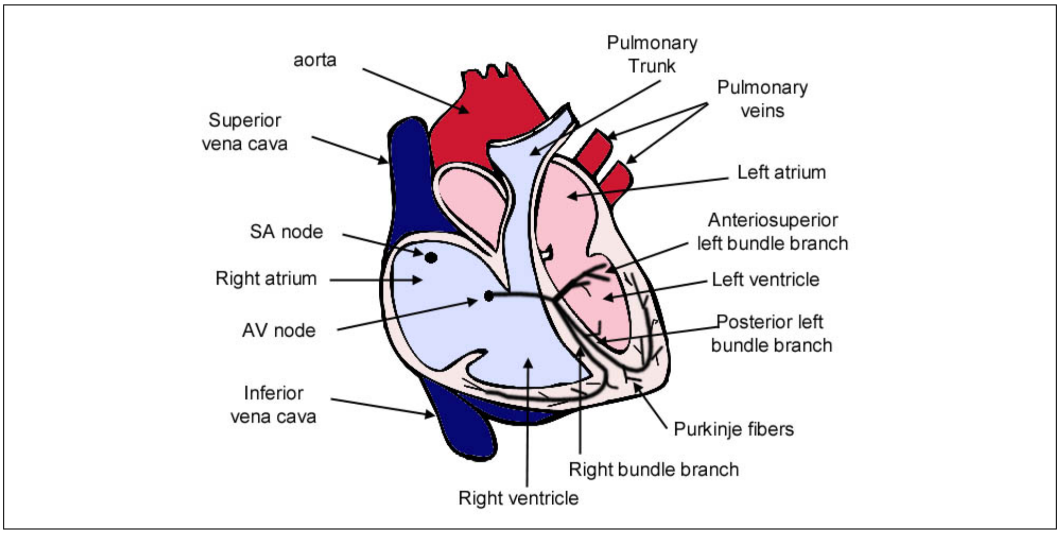

Figure 6.6: Sketch of of His bundle and Purkinje fibers locations

In the left ventricle the layer is defined by the set:

$$S = \left\{(x, y, z) \in \Omega_H : c_1 \leq ax^2 + by^2 + cz^2 \leq c_2\right\}$$

where a, b, c, c_1, c_2 are given constants. The source current is thus parametrized as follows:

$$\begin{aligned} I_{app}(x, y, z, t) &= I_0(x, y, z)\chi_S(x, y, z)\chi_{[0,t_{act}]}(t)\psi(x, z, t) \\ I_0(x, y, z) &= i_{app}\left[\frac{c_2}{c_2 - c_1} - \frac{1}{c_2 - c_1}\left(ax^2 + by^2 + cz^2\right)\right] \end{aligned}$$

where i_{app} is the amplitude of the external applied stimulus, χ_S and $\chi_{[0,t_{act}]}$ are the following characteristic functions:

$$\chi_S = \begin{cases} 1 & (x, y, z) \in S \\ 0 & (x, y, z) \notin S \end{cases}$$

$$\chi_{[0,t_{act}]} = \begin{cases} 1 & t \in [0, t_{act}] \in S \\ 0 & \quad t \notin [0, t_{act}] \end{cases}$$

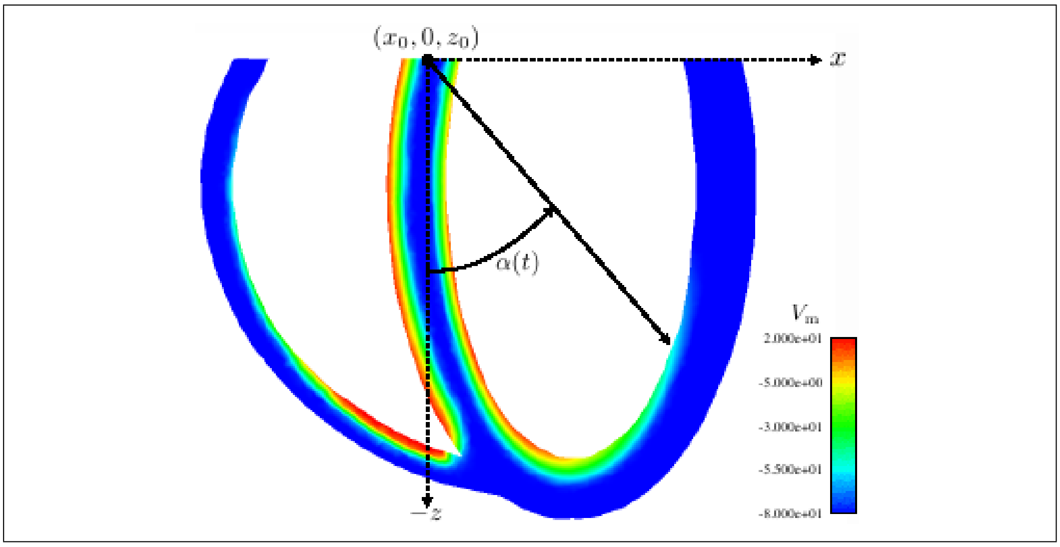

Figure 6.7: Geometrical description of the external stimulus, cut plane at $y = 0$

while $\psi(x, z, t)$ is defined as follows:

$$\psi(x, z, t) = \begin{cases} 1 & atan\left(\frac{x-x_0}{z-z_0}\right) \leq \alpha(t) \\ 0 & atan\left(\frac{x-x_0}{z-z_0}\right) > \alpha(t) \end{cases}$$

The quantity $\alpha(t)$, defined as:

$$\alpha(t) = \frac{t\pi}{2t_{act}}$$

is called activated angle and denotes the portion of ventricle reached by the electrical stimulus, as depicted in figure 6.7; a typical value for t_{act}, here and in the following used, is $10\,ms$.

6.4.3 Cell heterogeneity

Another significant issue related to the electro-physiology deals with the cell heterogeneity. Cell heterogeneity has an impact on the so called action potential duration (APD). The action potential represents a short-lasting event in which the electrical membrane potential of a cell rapidly rises and falls, following a stereotyped trajectory; for which concerns the heart cells, the action potential is the first step in the chain of events leading to the contraction.

A_m	C_m	τ_{in}	τ_{out}	τ_{open}	τ_{close}^{RV}	τ_{close}^{endo}	τ_{close}^{mcell}	τ_{close}^{epi}	V_{Gate}	V_{min}	V_{max}
200	10^{-3}	4.5	90	100	120	130	140	90	-67	-80	20

Table 6.3: Cell membrane parameters for the left ventricle

The heterogeneity of the APD can be found in different myocardium locations ([29, 45]) and is the most important factor in the genesis of the normal ECG T-wave shape and polarity ([3, 20, 29, 34, 70]; it is assumed a correlation between the heterogeneity of the APD and the anisotropy of the heart tissues ([19]).

In this work cell heterogeneity is considered on the left ventricle only, as trans-mural variation of APD. Thus, it is assumed that epicardial cells have the shortest APD, while endocardial cells have an intermediate values between mid-myocardial cells (M-cells) and epicardial cells ([70]). From the analysis reported in [47], the leading order of the maximum APD provided by the Mitchell-Schaeffer ionic model is proportional to the parameter τ_{close}, so cell heterogeneity is modeled as a variation of this parameter across the trans-mural direction. Typical values of the heart parameters are summarized in table 6.3. These values will be assumed in the numerical examples.

Chapter 7

The Heart Mechanics

7.1 introduction

From the mechanical standpoint, the heart is similar to a volumetric pump, formed by heart muscles and activated by an electric signal. Inside is divided into two cavities called ventricles, each one connected to a complex arterial system, in particular:

- the left ventricle is connected to the big circulation, i.e. the arterial branch which transports the oxygenated blood from the heart to the peripheral organs (big circulation)
- the ventricle is connected to the pulmonary artery, transporting the blood rich of CO_2 from the heart to the lungs (small circulation).

The filling of the ventricle is performed by the emptying of the atria, two cavities each one communicating with its ventricle. The flux direction and the heart phases are governed by the overture/closure of some moving parts called valves.

The heart is an anisotropic continuum, which contracts along preferred directions, called heart fiber; many studies were consecrated to the determination of the fiber orientation as, for example, [49]. The most used theory is the one presented in [62], in which the fibers are nested in a set of layer, and their orientation changes progressively, passing from the endocardium to the epicardium. From the structural point of view, it is possible to distinguish two type of mechanical response:

- A passive response (passive stiffness), which depends only on the load applied
- An active response (active stiffness) which acts along the heart fibers and depends on the applied electrical stimulus.

Ventricles has the shape of a thick truncated ellipsoid, the left corresponding to a revolution solid, while the right fitting on the former, as depicted in figure 7.1. In order to determine the heart orientation, the so called "big axis" is defined, corresponding to the smaller principal axis of inertia on the left ventricle; heart elevation coordinate coincides with the big axis. The lower ventricular part is called "apex", while the upper, where the atria are attached, is called "base".

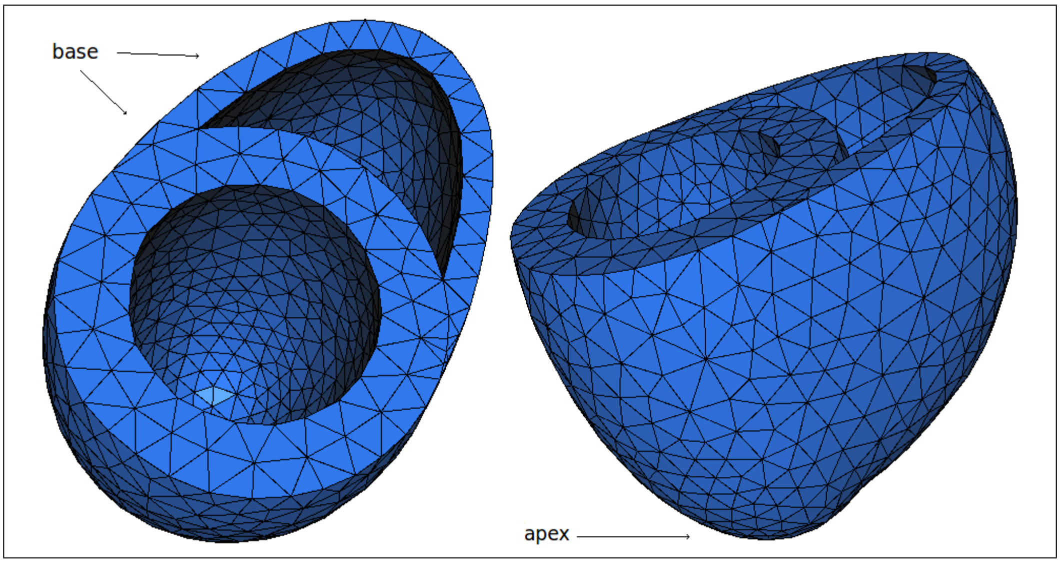

Figure 7.1: Typical approximation for the heart geometry

Of significant importance is the determination of the cardiac cycle consisting in the time evolution of the pressure and the volume of each ventricles. The cardiac cycle represents indeed an important indicator by the clinical standpoint. We point out that our interest is devoted to the study of the ventricle dynamic, thus the atria are neglected, being their pressure laws described through known temporal laws.

The heart cycle could be decomposed in the following four phases:

- **The contraction (systole)**:
  this phase employs typically $50\,ms$; the ventricles are contracted by the depolarization wave. All the valves are closed and the pressure increases rapidly until overcoming the aorta pressure (left ventricle, $80\,mmHg$) or the pulmonary artery pressure (right ventricle, $10\,mmHg$). When these values are reached, the sigmoid valves open. Being all the valves closed during the contraction, this phase is often called ”isovolumic contraction“;

- **The ejection**:
  this phase employs typically $210\,ms$; the pressure in the ventricles and in the aorta (resp. pulmonary artery) increases up to the systolic pressure (at rest $120\,mmHg$). The maximum flow rate is reached at the beginning of this phase, while just before the end the electric excitation stops and the ventricular pressure decreases until a value lower than that in the aorta (resp. in the pulmonary artery). Hence, the valves close.

- **The isovolumic relaxation**:
  this phase employs typically $60\,ms$; the atria are filled with the blood coming from the peripheral or from the lungs; the ventricular pressure suddenly decreases until a value lower than that in the atria. The mitral and the pulmonary valves open.

- **The refilling phase (diastole)**:
  this phase employs typically $500\,ms$; during this phase the blood flows from the atria to the ventricles; typically the 80% of the refilling employs one quarter of the total time of the phase (rapid refill); after, the atria contract and the refill finish.

In figs. 7.2, 7.3, 7.4 the variation of pressure, volume and ejected flux vs time are depicted for the left ventricle.

Remark The aforementioned description is intended for a subject at rest; if the heart frequency increases, the total heart cycle time decrease at expense of the diastole phase. In this latter case, the role of the atrial pressure becomes significant for the refilling of the ventricles.

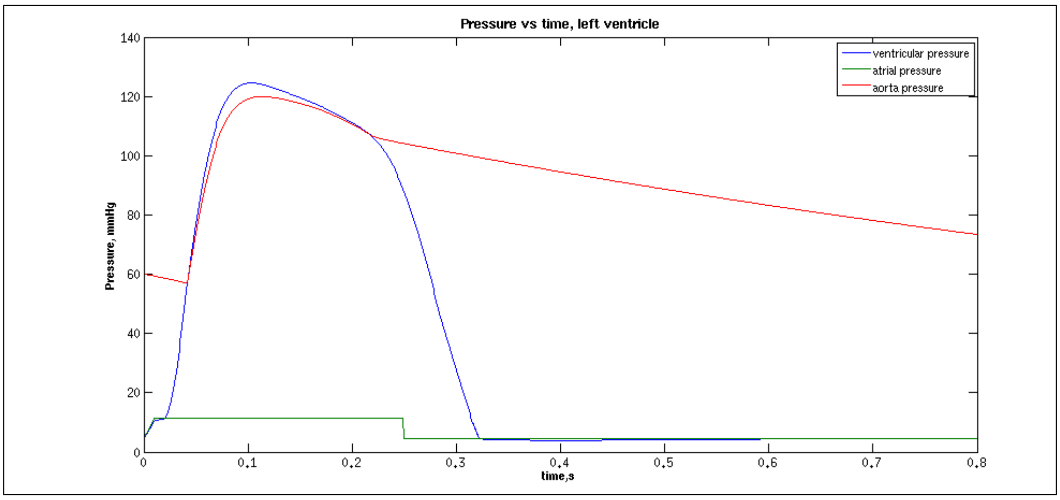

Figure 7.2: Left ventricle, ventricular (blue line), atrial (green line), and aorta (red line) pressures variation with respect to time for one period $T = 0.8s$.

The total heart work performed by the ventricle in a single heart cycle corresponds to the area enclosed in the pressure vs volume graph, fig. 7.5. Typical values of this work are about of $1.07\,J$ for the left ventricle and of $0.16\,J$ for the right ventricle respectively.

7.2 Heart mechanical model

By the mechanical point of view, the heart behaves as an hyper-elastic incompressible continuum, with a viscoelastic contribution; moreover the fibers contraction produce an active stiffens contribution dependent on the electrical stimulus. Clearly, the best frame of reference describing the heart mechanics is the Lagrangian one.

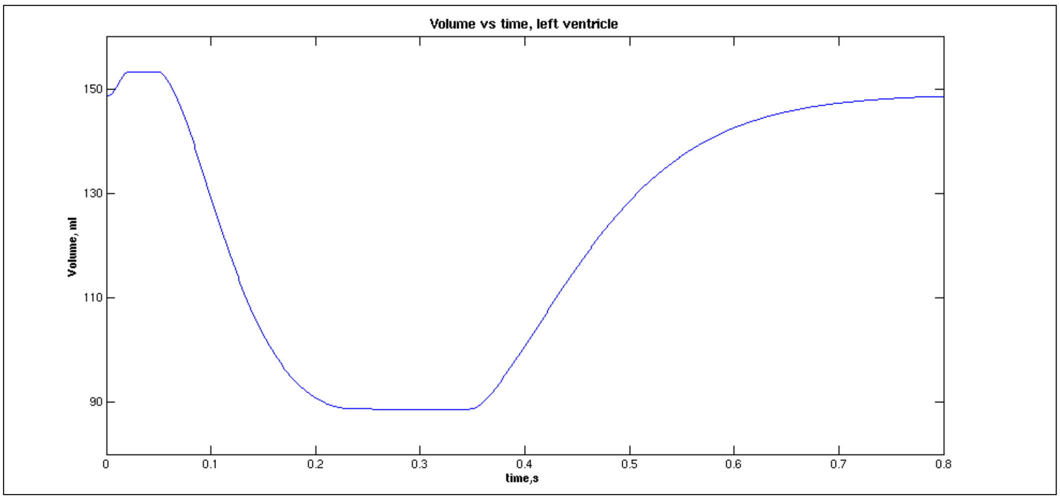

Figure 7.3: Left ventricle, volume variation vs time for one period $T = 0.8s$

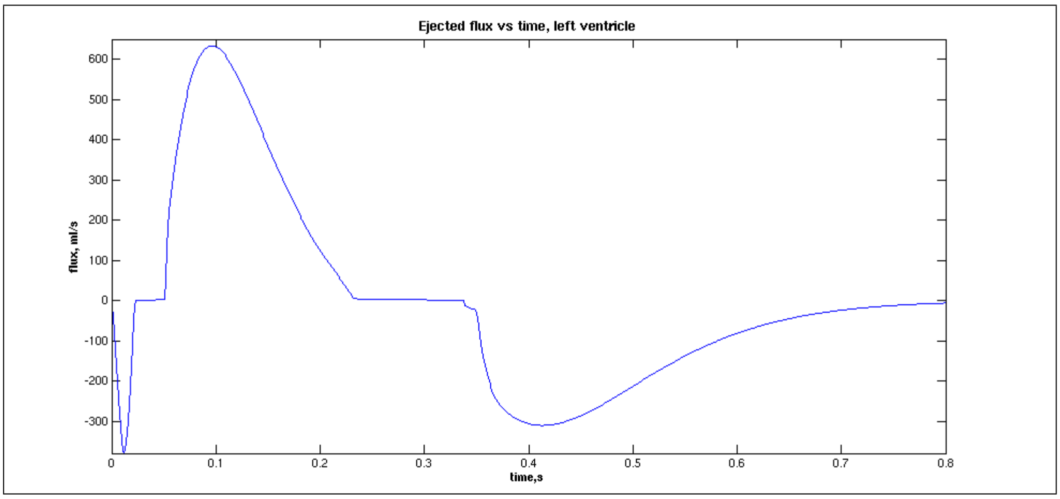

Figure 7.4: Left ventricle flux variation vs time for one period $T = 0.8s$; negative values correspond to the refill of the ventricle.

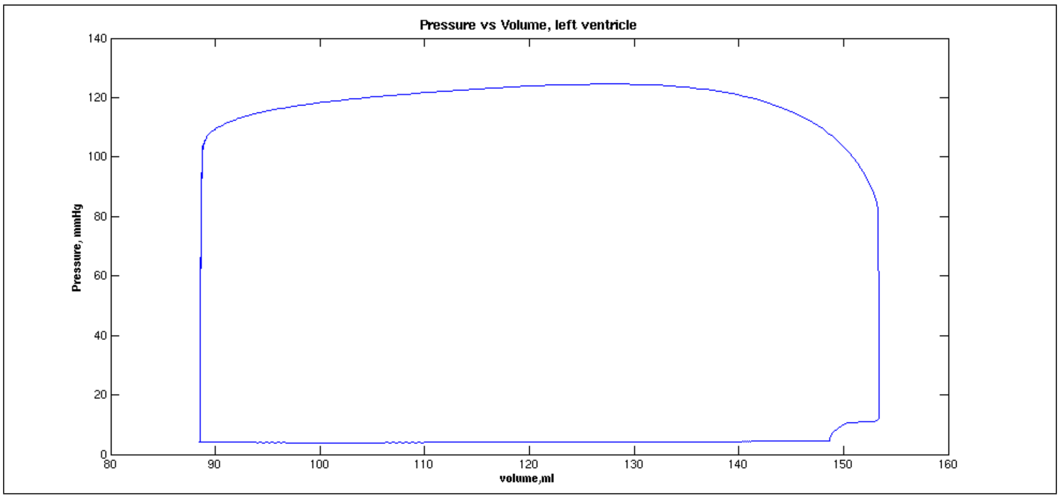

Figure 7.5: Pressure vs volume graph for the left ventricle for standard (at rest) conditions

The internal energy related to the passive part could be decomposed into two contributions, the first one, here and in the following denoted by W^e, takes into account of the hypereleasticity while the other, here and in the following denoted by W^v takes into account of the dissipative effects.

As far as for all hyper-elastic continua, the deformation energy depends on the only three invariants of the right Cauchy-Green tensor $\boldsymbol{C} = \boldsymbol{F}^T\boldsymbol{F}$ (see [17] for a complete description), being $\boldsymbol{F}$ the Jacobian matrix with respect to the undeformed configuration. Thus:

$$
\begin{aligned}
&W^e\left(I_1, I_2, I_3\right) = k_1\left(I_1 - 3\right) + k_2\left(I_2 - 3\right) + ak_1\left(I_3 - 1\right) - (k_1 + 2k_2 + a)ln(I_3)\\
&I_1 = tr(\boldsymbol{C})\\
&I_2 = \frac{1}{2}(tr(\boldsymbol{C})^2 - tr(\boldsymbol{C}^2))\\
&I_3 = det(\boldsymbol{C}) = J^2
\end{aligned}
$$

where k_1, k_2, a are parameters depending on the continuum properties. The second Piola Kirchoff stress tensor $\boldsymbol{S}$ is thus obtained by deriving the internal energy W^e with respect to the Green-Lagrange strain tensor.

Remark Typically the deformation energy is defined through the so called reduced invariants, defined as:

$$J_1 = I_1 I_3^{-1/3} J_2 = I_2 I_3^{-2/3} \qquad\qquad J_3 = J^{1/2}$$

yielding the following decomposition of the second Piola-Kirchoff stress tensor:

$$\begin{aligned} \boldsymbol{S}_d &= 2 \sum_{j=1,2} \frac{\partial W^e}{\partial J_i} \frac{\partial J_i}{\partial \boldsymbol{C}} \\ p &= -\frac{\partial W^e}{\partial J} \end{aligned}$$

Here $\boldsymbol{S}_d$ denotes the deviatoric part of the Stress tensor, while p the hydrostatic pressure of the system, i.e. the contribution of the stress balancing an applied isotropic stress state.

For the incompressible materials, as the biological tissue, the elastic energy is a function of the only two invariants J_1, J_2 being $J = 1$; as a consequence, the principle of virtual work is augmented by a Lagrange multiplier, yielding the following optimization problem:

Problem 9 *Find ($\boldsymbol{d}$,p) which satisfy:*

$$\min_{\boldsymbol{d}} \max_{p} \left(\int_{\Omega_0} W^e + p(1-J) d\Omega - \mathcal{W}^{ext} \right)$$

where $\mathcal{W}^{ext}$ represents the energy associated to the external forces.

The second Piola-Kirchoff stress tensor thus becomes:

$$\begin{aligned} \boldsymbol{S} &= \frac{\partial W^e}{\partial \boldsymbol{E}} - p\frac{\partial J}{\partial \boldsymbol{E}} = \frac{\partial W^e}{\partial \boldsymbol{E}}(J_1, J_2) - pJ\boldsymbol{C}^{-1} \\ \boldsymbol{E} &= \frac{1}{2}(\boldsymbol{C} - \boldsymbol{I}) \end{aligned}$$

Remark In the present work, the incompressibility is imposed through a penalization technique, rewriting the Ciarlet-Geymonat elastic energy as:

$$W^e = k_1(J_1 - 3) + k_2(J_2 - 3) + k(J-1) - k\ln(J)$$

and choosing k sufficiently big. The hydrostatic pressure thus becomes:

$$p = k\frac{1-J}{J}$$

The dissipative effects are described introducing the convex functional $W^v(\dot{\boldsymbol{E}})$, yielding the following expression for the second Piola-Kirchoff stress tensor:

$$\boldsymbol{S} = \frac{\partial W^e}{\partial \boldsymbol{E}} + \frac{\partial W^v}{\partial \dot{\boldsymbol{E}}} = \boldsymbol{S}^e + \boldsymbol{S}^v$$

Typically the following simplified form for W^v is adopted:

$$W^v = \frac{\eta}{2} tr \left(\dot{\boldsymbol{E}}^2 \right)$$

where $\eta \geq 0$ represents a viscosity parameter; the viscous contribution to the stress tensor thus reads:

$$\boldsymbol{S}^v = \frac{\partial W^v}{\partial \dot{\boldsymbol{E}}} = \eta \dot{\boldsymbol{E}}$$

The active stiffness depends on the sarcomeres contraction driven by the electrical wave, a process described by Huxley, [36], modeling by Bestel, [4] and Bestel, Clément and Sorine, [5] through the so called "Bestel-Clément-Sorine model" for the muscle contraction. This model consists in the following system of ODEs:

$$\begin{aligned}
&\dot{k}_c = -\left(\alpha|\dot{e}_c| + |u|\right) k_c + k_0 |u|_+ \\
&\dot{\tau}_c = k_c \dot{e}_c - \left(\alpha|\dot{e}_c| + |u|\right) \tau_c + \sigma_0 |u|_+ \\
&\tau_c(0) = 0 \\
&k_c(0) = 0 \\
&\sigma_0 = \left(\frac{1}{2} + s_0\right) k_0
\end{aligned}$$

where k_c denotes the active stiffness, τ_c is denotes a quantity similar to the stress along the sarcomeres, u represents the electrical activation and it is proportional to the trans-membrane cell potential V_m and s_0, k_0 are two constants, the meaning of which is explained in [71], The final expression of the stress σ_c related to the active stiffness thus reads:

$$\sigma_c = d(e_c)\tau_c + \mu_c \dot{e}_c$$

where μ_c denotes a viscosity parameter, while $d(e_c)$ constitutes a correction depending on the Starling effect, i.e. an effect which relates the modulus

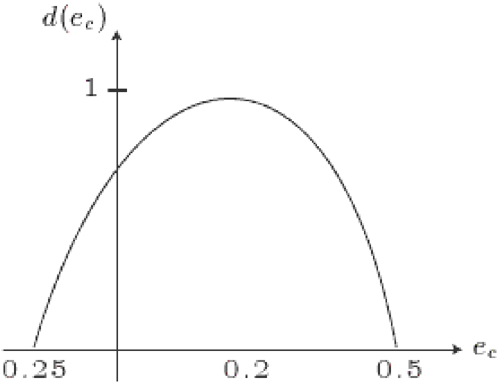

Figure 7.6: d function associated to the Starling effect

of the deformation e_c to the modulus of the contraction, described by the function of figure 7.6.

Remark The correlation between the trans-membrane potential v_m and u is governed by the following affine relation:

$$u = a + bv_m$$

usually, the trans-membrane potential v_m varies between $-80mV$ and $20mV$; the parameters a, b are typically chosen so $u \in [-15, 5]$.

7.3 Rheological model

The rheological behavior of a sarcomere fiber is simply described through the parallel/series assembly of a set of springs and dumpers, thus obtaining the final model in an easier way. In this work the described in [16] and depicted in figure 7.7 is adopted. This model is composed by:

- An active element describing the active behavior of the sarcomere (Bestel-Clèment-Sorine model):

$$\sigma_c = d(e_c)\tau_c + \mu_c \dot{e}_c$$

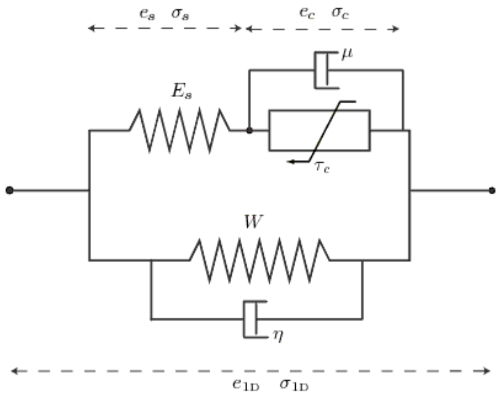

Figure 7.7: Rheological model of a sarcomere fiber

- A spring connected in series with the active element, which allows a contraction of the sarcomere without total deformation, described by:

$$\sigma_s = E_s e_s$$

- A parallel assembly of a spring and a dumper, modeling the passive element and connected in parallel with the previous.

As described in [48], the stress along the sarcomere reads:

$$\begin{aligned} \sigma_c = d(e_c)\tau_c + \mu_c \dot{e}_c = E_s \frac{e_{1D} - e_c}{(1+2e_c)^3}(1+2e_{1D}) \\ e_{1D} = \boldsymbol{a} \cdot \boldsymbol{E} \cdot \boldsymbol{a} \end{aligned}$$

where $\boldsymbol{a}$ represents the fiber direction versor. The second Piola-Kirchoff stress tensor thus becomes:

$$\begin{aligned} \boldsymbol{S} = \boldsymbol{S}^p + \sigma_{1D} \boldsymbol{a} \otimes \boldsymbol{a} \\ \sigma_{1D} = \frac{\sigma_c}{1+2e_s} = \frac{\sigma_s}{1+2e_c} \end{aligned}$$

where $\boldsymbol{S}^p$ represents the passive response.

7.4 Blood circulation model

The external applied force which deforms the heart is represented by the ventricular blood pressure P_V acting on the endocardium and depending on the heart phase. Indeed, when one valve opens, the external pressure depends on the value of the pressure of the exterior circulation (atrium or aorta); conversely, when all valves are closed the ventricular pressure has to balance the isotropic force applied by the heart in its contraction. The ventricular pressure therefore represents an unknown of the problem, requiring the knowledge of the external circulation pressure. Thus a model for the valve dynamics and a model for the external circulation are required. In this regards, the heart model is supplied by the following others:

- The valve model, capable of managing the different heart phases
- The Windkessel model describing in a concentrated manner the the time evolution of the external arterial circulation

Remark As previously remarked, the atrial pressure is supposed a known temporal function

7.4.1 The Valve model

The valve model is used to determine the heart phase and the flow coefficient, depending on the ventricular, atrial and aorta pressures. Clearly, the phase change occurs when the ventricular pressure curve intersect one of the others pressure curves: as a consequence a valve opens or closes and the blood flows from/to the ventricle (diastole, ejection), or stops to flow (systole). The blood flow depends on the following relation:

$$\begin{cases} Q \geq 0 & P^V = P^{ar} \\ Q = 0 & P^{at} < P^V < P^{ar} \\ Q \leq 0 & P^V = P^{at} \end{cases} \tag{7.1}$$

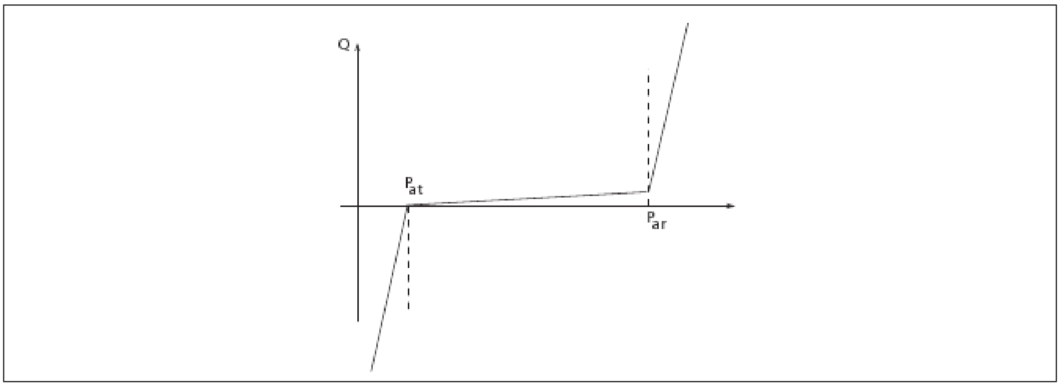

Figure 7.8: Regularized flux vs pressure model

where P^{ar} denotes the arterial pressure, P^{at} denotes the atrial pressure and P^V denotes the ventricular pressure. From (7.1) it is possible to determine the following flow/pressure relation:

$$Q = -\dot{V} = \begin{cases} K_{ar}(P^V - P^{ar}) & P^V \geq P^{ar} \\ 0 & P^{at} < P^V < P^{ar} \\ K_{at}(P^V - P^{at}) & P^V \leq P^{at} \end{cases} \tag{7.2}$$

where $\dot{V}$ represents the ventricle volume variation in time.

Remark For numerical reasons, the isovolumic phase relation appearing in (7.2) is substituted by the following:

$$K_{ar}(P^V - P^{ar}) + K_{iso}(P^{ar} - P^{at})$$

thus generating the regularized function depicted in figure 7.8.

7.4.2 The Windkessel model

The aorta pressure is determined through the Windkessel model, representing a 0D description of the whole circulation as an equivalent electrical circuit. In this work of first order Windkessel model is considered; denoting by P^d the distal pressure (i.e., the pressure measured after the aortic arc) and with

P^{sv} the pressure inside the peripheral vessel net, the Windkessel model reads:

$$\begin{aligned} C_p \dot{P}^{ar} + \frac{P^{ar} - P^d}{R_p} &= Q \\ C_p \dot{P}^d + \frac{P^d - P^{ar}}{R_p} &= \frac{P^{sv} - P^d}{R_d} \end{aligned}$$

The notations are reported in figure 7.9; in the same figure equivalent electrical components for the valves are also depicted.

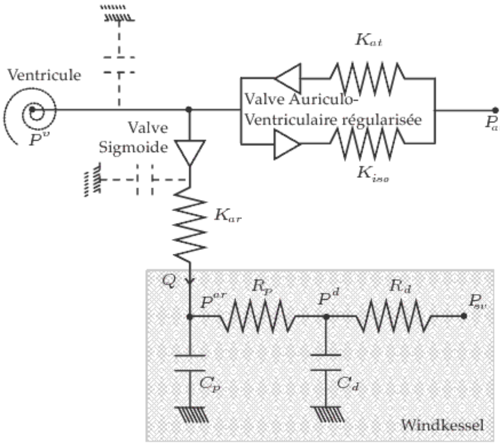

Figure 7.9: Sketch of the complete external circulation; Valves are described as non-linear diodes, while the distal circulation as a RC circuit

7.5 The boundary conditions

The heart is constrained in its position by the neighbor organs, in particular the diaphragm, the sternum, the lungs and partially by the aorta; as a consequence, it is difficult to impose a set of boundary condition capable of reproducing exactly the whole neighbor organs. A viable alternative consists in reproducing the the neighbor tissue behavior through a visco-elastic support, yielding a boundary condition depending on the solution. This model is called ”elastic support“, and will be used in the numerical simulations. Applying the principle of virtual works to the boundary constraint, the following variational forms holds:

$$\mathcal{P}^{ext} = -\int_{\mathcal{B}} \left(a(x)\boldsymbol{d} + b(x)\dot{\boldsymbol{d}} \right) \cdot \boldsymbol{v} dS$$

where $\mathcal{P}^{ext}$ represents the power of the constraint, $a(x)$, $b(x)$ are two functions, determined by the experimental evidence, representing the elastic modulus and the dissipation constant of the support. Usually, this boundary condition is imposed on the region $\mathcal{B}$ representing the contact area between the sternum and the apex.

7.6 The complete heart model

Denoting by $V = H^1_{\Gamma_D}(\Omega_0)$ the Hilbert space of the function square integrable with their first derivatives which vanish at the Dirichlet boundary, the complete heart model to solve is represented by the following system:

$$\begin{aligned}
&\int_{\Omega_0} \rho \ddot{\boldsymbol{d}} \cdot \boldsymbol{v} d\Omega + \int_{\Omega_0} \boldsymbol{S}\left(\boldsymbol{E}, e_c\right) \cdot \boldsymbol{E}(\boldsymbol{v}) d\Omega \\
&\quad + \sum_{i=g,d} \int_{\partial \mathcal{C}_i} P_i^V \boldsymbol{n} \boldsymbol{F}^{-1} \cdot \boldsymbol{v} J dS = 0 \qquad \forall \boldsymbol{v} \in V
\end{aligned} \tag{7.3}$$

$$\boldsymbol{S} = -pJ\boldsymbol{C}^{-1} + \frac{\partial W^e}{\partial \boldsymbol{E}} + \frac{\partial W^v}{\partial \dot{\boldsymbol{E}}} + \sigma_{1D}(e_{1D}, e_c) \boldsymbol{n} \otimes \boldsymbol{n} \tag{7.4}$$

$$\sigma_{1D} = \frac{\sigma_c(1+2e_c)}{(1+2e_{1D})} \tag{7.5}$$

$$\sigma_c = d(e_c)\tau_c + \mu_c \dot{e}_c = E_s \frac{e_{1D} - e_c}{(1+2e_c)^3}(1+2e_{1D}) \tag{7.6}$$

$$e_{1D} = \boldsymbol{n} \cdot \boldsymbol{E} \cdot \boldsymbol{n} \tag{7.7}$$

$$\dot{k}_c = -\left(\alpha |\dot{e}_c| + |u|\right) k_c + k_0 |u|_+ \tag{7.8}$$

$$\dot{\tau}_c = k_c \dot{e}_c - \left(\alpha |\dot{e}_c| + |u|\right) \tau_c + \sigma_0 |u|_+ \tag{7.9}$$

$$\begin{aligned}
Q_i = -\dot{V}_i &= -\int_{\partial \mathcal{C}_i} J \boldsymbol{n} \boldsymbol{F}^{-1} \cdot \boldsymbol{v} \qquad (7.10) \\
&= \begin{cases} K_{ar}(P^V - P^{ar}) & P^V \geq P^{ar} \\ K_{ar}(P^V - P^{ar}) + K_{iso}(P^{ar} - P^{at}) & P^{at} < P^V < P^{ar} \\ K_{at}(P^V - P^{at}) & P^V \leq P^{at} \end{cases} \qquad i = g, d
\end{aligned}$$

$$C_p \dot{P}^{ar} + \frac{P^{ar} - P^d}{R_p} = Q \tag{7.11}$$

$$C_p \dot{P}^d + \frac{P^d - P^{ar}}{R_p} = \frac{P^{sv} - P^d}{R_d} \tag{7.12}$$

Chapter 8

The Heart electro-mechanical coupling

8.1 introduction

Electro-mechanical problems have an important role in medicine, being the experimental investigation by medical devices leaking of informations. Conversely computer investigation furnishes also the informations which are not detectable by medical devices; as a consequence, computer investigation represents a significant tool in the study of heart disease, when addressed to reproduce as accurate as possible the physiology, i.e. to reproduce the same results coming from the experimental investigation.

The heart electrical activity is typically reproduced through the data obtained by the electro-cardiogram (see figure 8.1), a non-invasive medical device furnishing the graphical representation in time of the potential difference between different body locations. An ECG graph is characterized by the following fluctuations (see figure 8.1):

- the P-wave (in the graph not depicted), representing the atrial depolarization;
- the QRS complex representing the ventricle depolarization

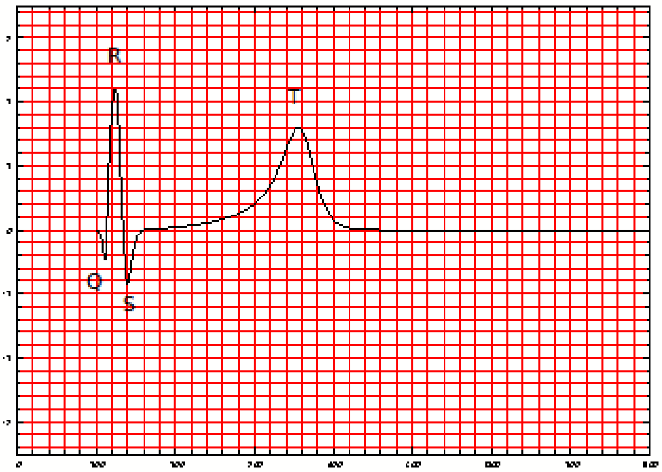

Figure 8.1: ECG of a single heart cycle. The P wave is absent

- the T wave, representing the ventricle repolarization

Remark The analysis of this chapter deals with the ventricles only. As a consequence, the P wave will not be present. Moreover, the atrial pressure will be described through an analytical and known temporal law.

This chapter is devoted to the analysis of the influence of the electro-mechanical coupling on the ECG. Indeed during the heart movement the fiber direction changes and so the electrical propagation properties; as a consequence, the mechanical response also changes, being the active stiffness driven by the electrical stimulus. The problem which arises is non-linear fully coupled, being both solutions (electro physiology and mechanics) depending on each other. By the numerical point of view, this corresponds to implementing an efficient coupling algorithm, capable of managing in an efficient manner the interaction between the two sub-problems.

The ECGs here evaluated are based on the hypothesis of isolated heart (cf. chapter 6) and thus obtained through a transmission matrix furnishing directly the ECG data.

8.2 The Electro-Mechanical coupling algorithm

The problem consists in coupling the two different sub-problems, each one endowed by it's numerical solver, i.e. in implementing an efficient interface between them. The heart mechanics is solved by Heartlab, a matlab finite element library developed by the INRIA MACS team, while the electrical activity is solved by the C++ finite element library LIFEV [1], developed by the INRIA REO team.

These two solvers are considered as two "black box" exchanging informations with the external environment. Indeed, the mechanical solver receives a trans-membrane potential from the external world and returns the heart displacement and the heart velocity, while the electrical solver receives a heart displacement and a heart velocity from the external world and returns the trans-membrane potential.

The coupling algorithm consists in interfacing these two "box", independently on their implementation, in the most efficient way through the exchanged data; by the mathematical point of view, this consists in implementing a (at least locally) contractive function, the (unique) fixed point of which represents the solution of the coupled system.

In this work, two type of function will be constructed: one by "parallelism", in which a vectorial function of the whole unknowns set is considered, so the two problems are solved at the same time, yielding the so called Jacobi-like scheme; the other by "sequentiality", i.e. by solving in sequence the two problems thus generating a composite function, yielding the so called Gauss-Seidel-like scheme.

Let it be:

- $[\boldsymbol{d}, \boldsymbol{w}](\boldsymbol{x}, t) = F(v_m(\boldsymbol{x}, t))$ the function representing the mechanical solver
- $v_m(\boldsymbol{x}, t) = G([\boldsymbol{d}, \boldsymbol{w}](\boldsymbol{x}, t)$ the function representing the electro-physiology solver

The Jacobi scheme consists in finding the fixed point of:

$$\begin{bmatrix} \boldsymbol{d}\left(\boldsymbol{x},t\right) \\ \boldsymbol{w}\left(\boldsymbol{x},t\right) \\ v_m\left(\boldsymbol{x},t\right) \end{bmatrix} = \begin{bmatrix} F_1\left(v_m\left(\boldsymbol{x},t\right)\right) \\ F_2\left(v_m\left(\boldsymbol{x},t\right)\right) \\ G\left(\left[\boldsymbol{d},\boldsymbol{w}\right]\left(\boldsymbol{x},t\right)\right) \end{bmatrix}$$

while the Gauss-Seidel scheme consists in finding the fixed point of:

$$\left[\boldsymbol{d},\boldsymbol{w}\right] = F\left(G\left(\left[\boldsymbol{d},\boldsymbol{w}\right]\left(\boldsymbol{x},t\right)\right)\right)$$

The details of the implementation of the coupling algorithm are described in appendix B

8.3 Numerical results

The results here reported refer as two geometry. The first one (in the following called "ElliBi".) consists in describing the heart geometry through the intersection of two ellipsoids, as depicted in figure 8.2.

The tests performed with this simple geometry analyze the influence of the electro-mechanical feed-back on the mechanical indicators (i.e. the evolution of the ventricular pressure, ventricular volume and mechanical energy) by a comparison of the results obtained with and without feedback and the difference in the distribution of the trans-membrane and the extracellular potential by comparing their maximum value (and, in particular, the spatial location of the maximum value) in time. A model without electro-mechanical feedback means that the electro physiology is resolved on a fixed heart, while the mechanics still governed by the obtained trans-membrane potential.

For the electro-mechanical feed-back two cases are reported: one where sub-iterations are performed until convergence and another where only one sub-iteration is performed.

The second geometry (in the following called "Zygote") was obtained by the INRIA Cardiosense3D team, starting by Computer Tomography data. This geometry is represents a real human heart, as depicted in figure 8.3.

The tests performed with this latter geometry are aimed in studying the impact of the heart movement on the ecg graph.

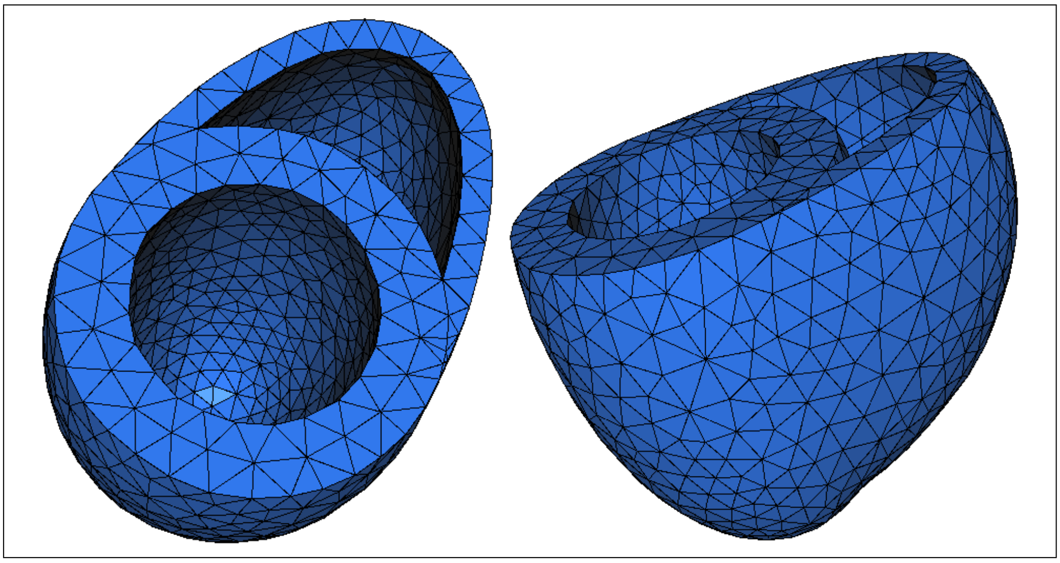

Figure 8.2: ElliBi heart geometry

8.3.1 ElliBi geometry

This simple geometry represents a heart simplification, defined through the intersection of ellipsoids. Typically, this geometry is adopted when testing the algorithm, being the fiber direction and the heart heterogeneity described analytically. Even though simple, the results concerning the ElliBi geometry permit observing whats happen when considering or not the electromechanical feedback.

During the heart motion, the fiber direction changes accordingly to the heart deformations: as a consequence, the preferred electrical wave propagation direction also changes, and the trans-membrane potential distribution will be different from the one obtained without moving the heart, as depicted in figs 8.4, 8.5, 8.6.

The same holds for the extra-cellular potential as depicted in figs. 8.7, 8.8, 8.9 and 8.10. The mechanical indicators also differ; indeed, the

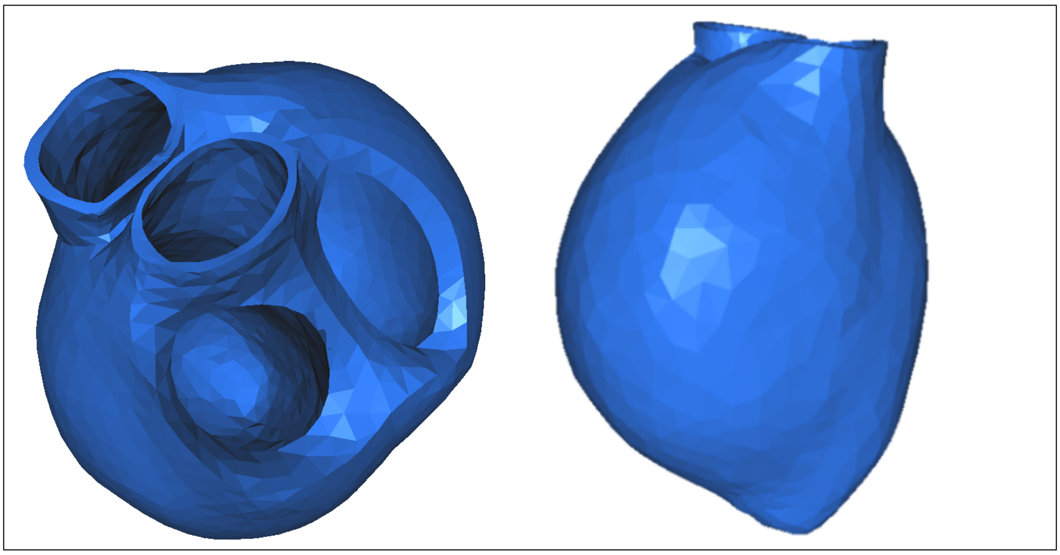

Figure 8.3: Zygote heart geometry

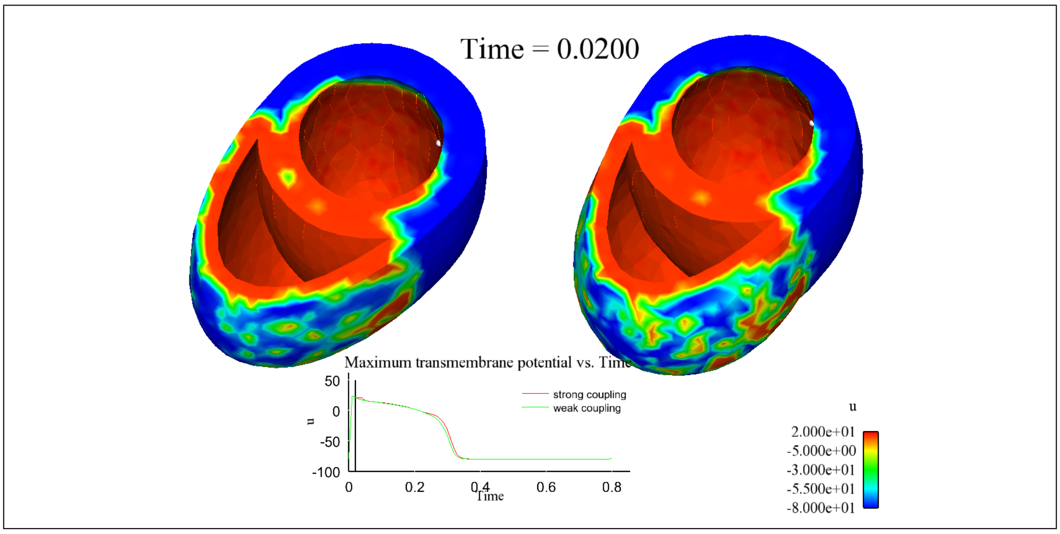

Figure 8.4: Trans-membrane potential for $t = 0.02$ with (right) and without (left) electromechanical feedback. ElliBi geometry, heart period $T = 0.8s$. The white dots (where present) indicate the maximum trans-membrane potential point locations

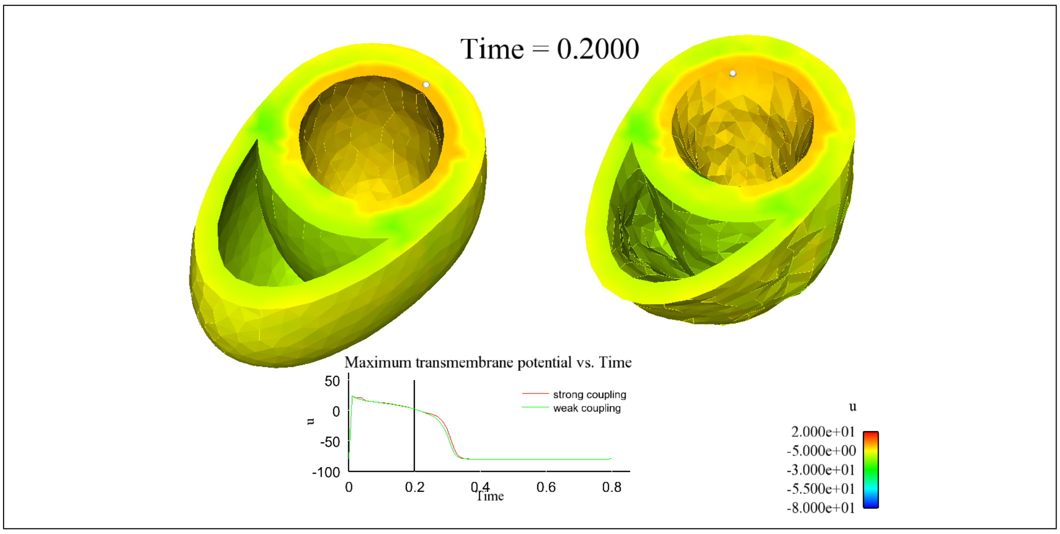

Figure 8.5: Trans-membrane potential for $t = 0.2$ with (right) and without (left) electromechanical feedback. ElliBi geometry, heart period $T = 0.8s$. The white dots (where present) indicate the maximum trans-membrane potential point locations

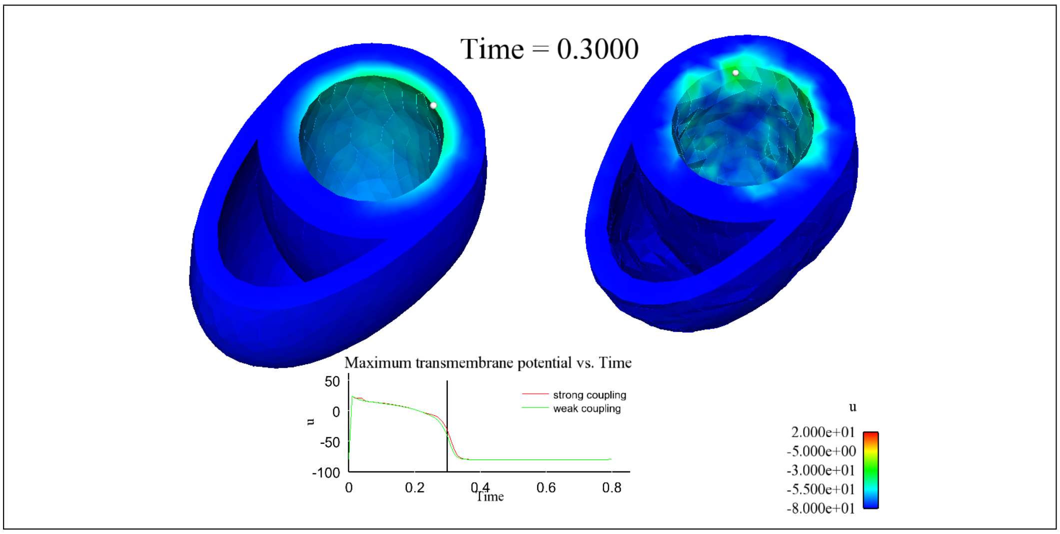

Figure 8.6: Trans-membrane potential for $t = 0.3$ with (right) and without (left) electromechanical feedback. ElliBi geometry, heart period $T = 0.8s$. The white dots (where present) indicate the maximum trans-membrane potential point locations

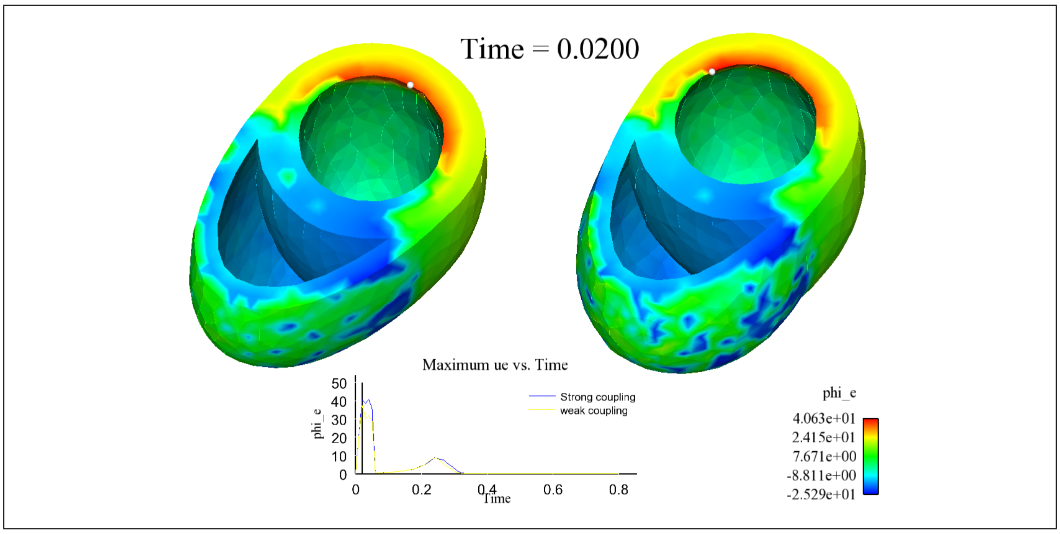

Figure 8.7: Extracellular potential for $t = 0.02$ with (right) and without (left) electromechanical feedback. ElliBi geometry, heart period $T = 0.8s$. The white dots (where present) indicate the maximum extracellular potential point locations

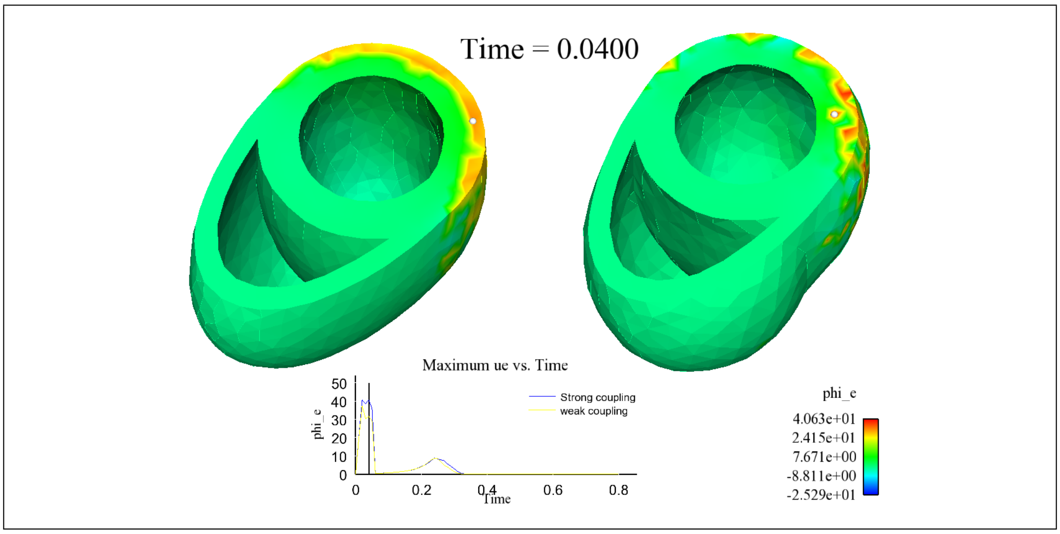

Figure 8.8: Extracellular potential for $t = 0.04$ with (right) and without (left) electromechanical feedback. ElliBi geometry, heart period $T = 0.8s$. The white dots (where present) indicate the maximum extracellular potential point locations

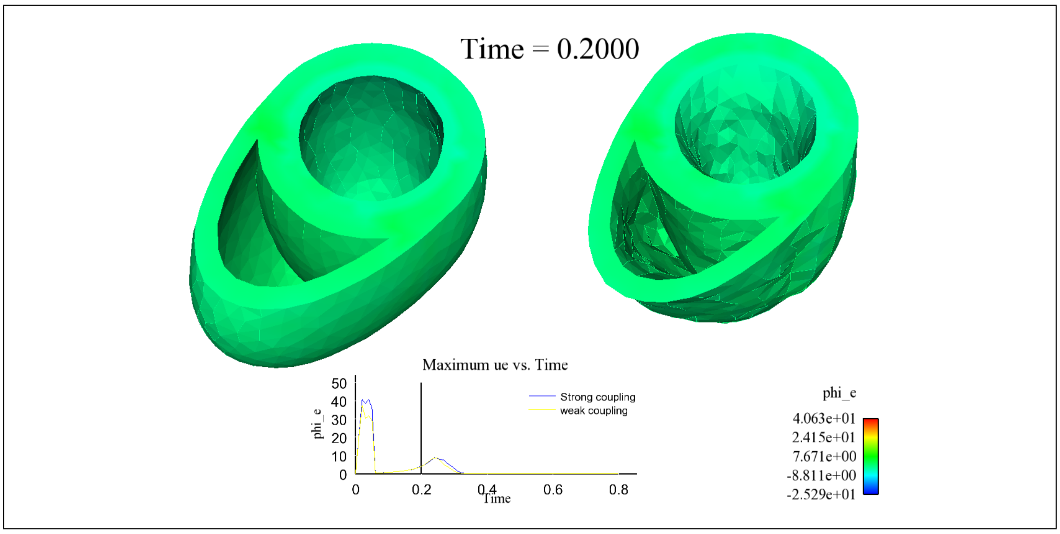

Figure 8.9: Extracellular potential for $t = 0.2$ with (right) and without (left) electromechanical feedback. ElliBi geometry, heart period $T = 0.8s$. The white dots (where present) indicate the maximum extracellular potential point locations

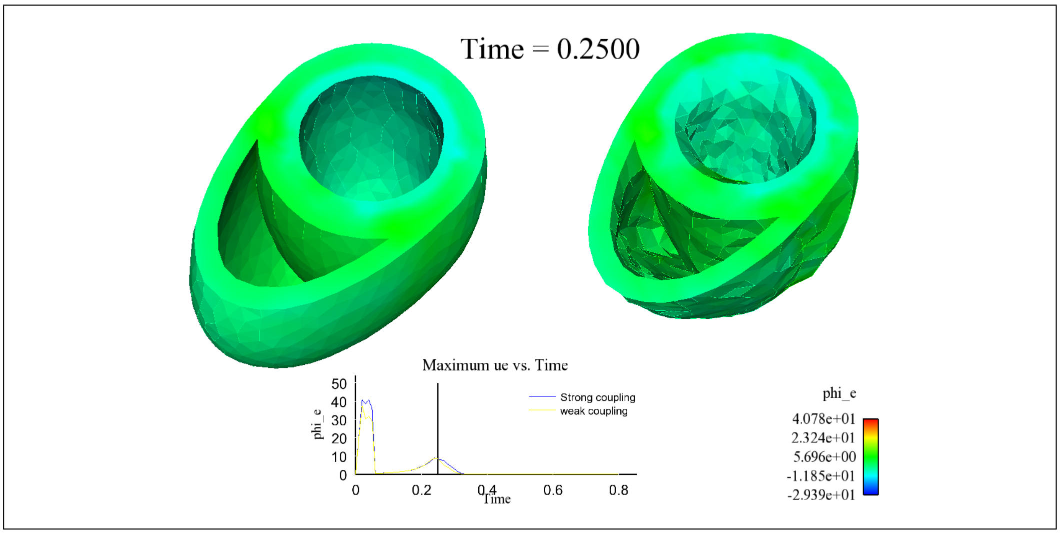

Figure 8.10: Extracellular potential for $t = 0.25$ with (right) and without (left) electromechanical feedback. ElliBi geometry, heart period $T = 0.8s$. The white dots (where present) indicate the maximum extracellular potential point locations

total mechanical energy related to one cycle is greater when the electromechanical feedback is neglected, as depicted in figure 8.11; conversely, the energy transferred to the fluid is less, as depicted in 8.12.

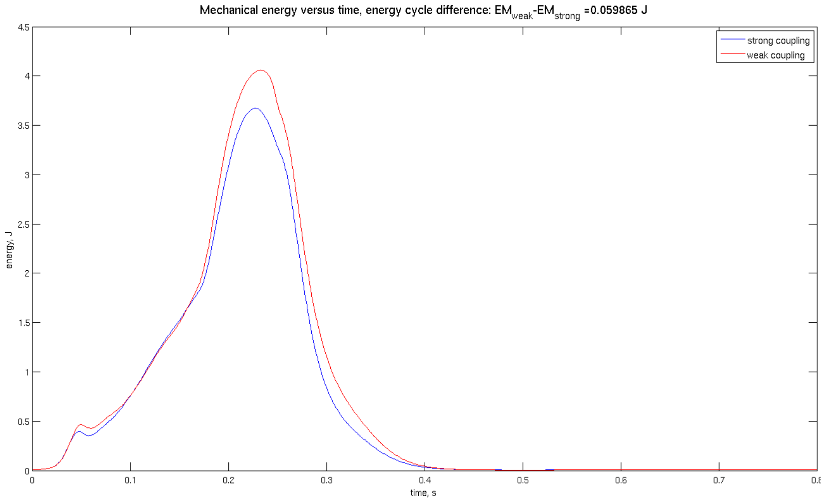

Figure 8.11: Mechanical energy vs time with (blue line) and without (red line) electromechanical feed-back. ElliBi geometry, $T = 0.8s$

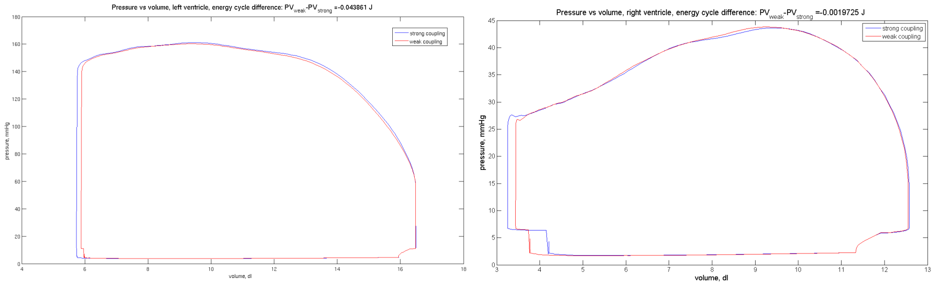

Figure 8.12: Pressure vs volume graph, left ventricle (left) and right ventricle (right) with (blue line) and without (red line) electromechanical feed-back. ElliBi geometry, $T = 0.8s$

In fig. 8.13 the Ventricular pressure vs time is depicted. The three curves are obtained by considering/neglecting the electromechanical feedback, or by considering it through one fixed point iteration only. By the figure one can infer that the convergence velocity is fast (indeed, only two iterations are typically needed to achieve convergence).

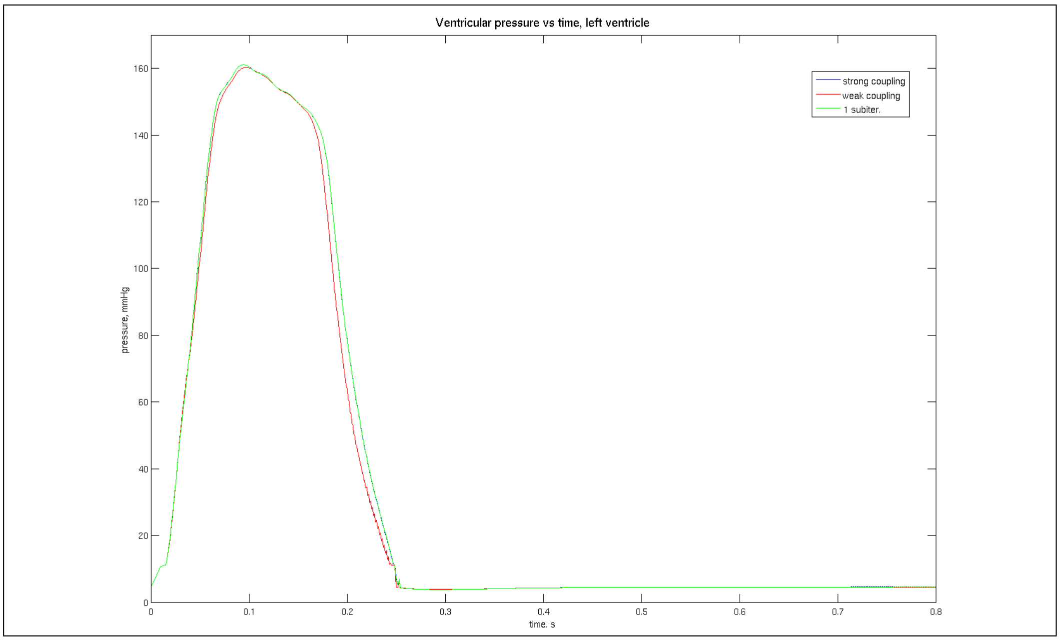

Figure 8.13: Ventricular pressure vs time with (blue line) and without (red line) electromechanical feedback; the green line refers to a electromechanical feedback obtained by only one sub-iteration of the Gauss-Seidel fixed point function. ElliBi geometry, $T = 0.8s$

8.3.2 Zygote geometry

The major effect related to the electro-mechanical feed-back deals with the T wave. As depicted in fig 8.14 on aVF termination the wave is reversed. Moreover, in II and III the amplitude changes, while in V2 presents a larger amplitude and returns to the reference value without oscillations. The same behavior still when changing the heart frequency (as depicted in fig 8.15) The QRS wave is significantly modified in III, aVL, aVF and V3 terminations. In all the other terminations there are no significant modifications.

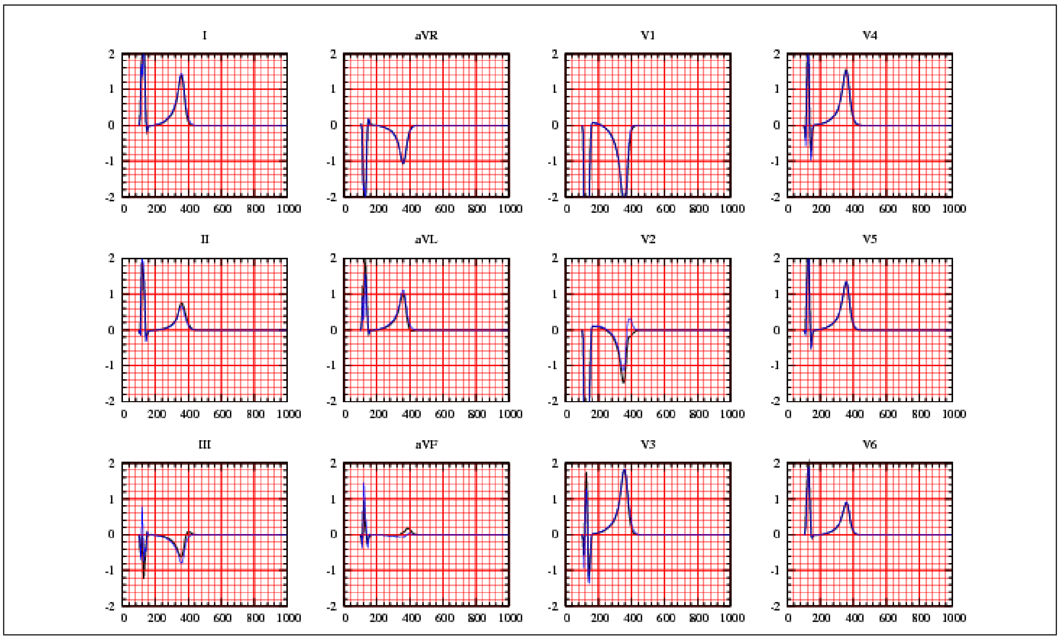

Figure 8.14: ECG with (black line) and without (blue line) electromechanical coupling, for a period $T = 1s$

Clearly, when the heart moves, the fibers direction also change, accordingly to the heart deformation. As a consequence, the electrical wave propagates in a direction different to the one concerning the heart at rest. This is highlighted in figs 8.16, 8.17, 8.18 and 8.19 for the trans-membrane potential and if figs 8.20,8.21, 8.22 and 8.23 for the extracellular potential. Indeed, the positions of the points of maximum value for the trans-membrane potential and for the extracellular potential differ if considering the electromechani-

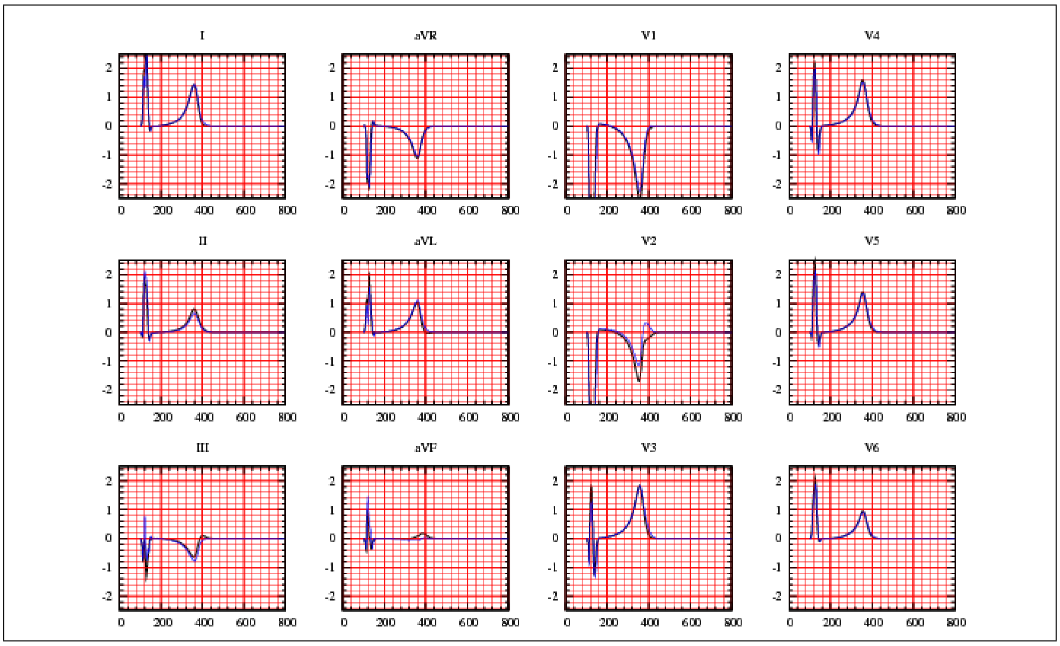

Figure 8.15: ECG with (black line) and without (blue line) electromechanical coupling, for a period $T = 0.8s$

cal feedback or not. In particular, the maximum value responsible of the QRS wave differs of $0.1s$ between the two coupling schemes, as depicted in fig 8.24 for the time values corresponding to the R peak with and without electromechanical feedback.

As far as the mechanical indicator is concerned, the total mechanical energy related to one cycle is greater for the weak coupling, as depicted in figure 8.25; the same holds true for the energy transferred to the fluid, as depicted in 8.26. By comparing the ventricular pressure vs time between the two coupling schemes, it is possible to see a small delay of the weak coupling with respect to the strong coupling (cf fig. 8.27).

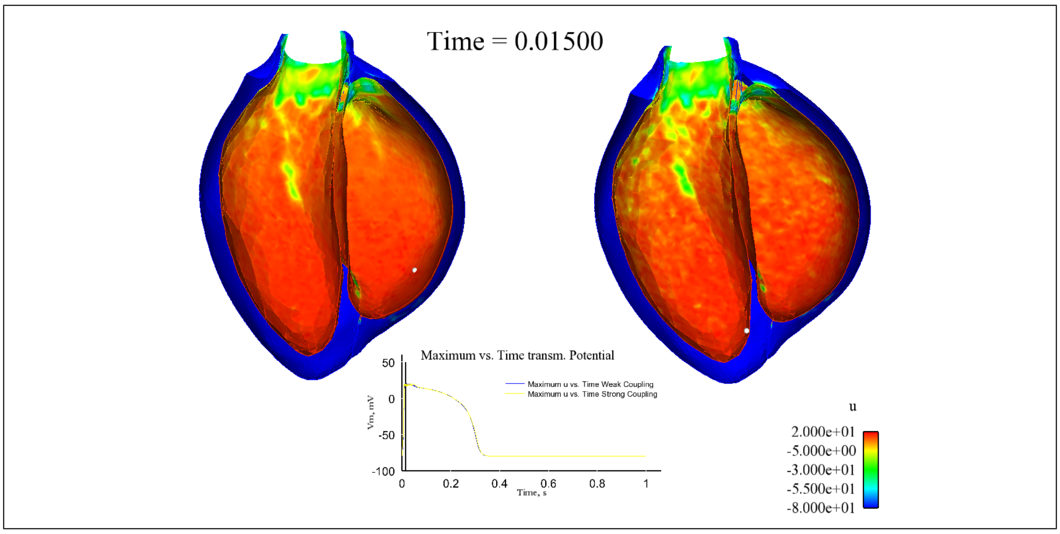

Figure 8.16: Trans-membrane potential for $t = 0.015$ with (right) and without (left) electromechanical feedback. Zygote geometry, heart period $T = 1.0s$. The white dots indicate the maximum trans-membrane potential point locations

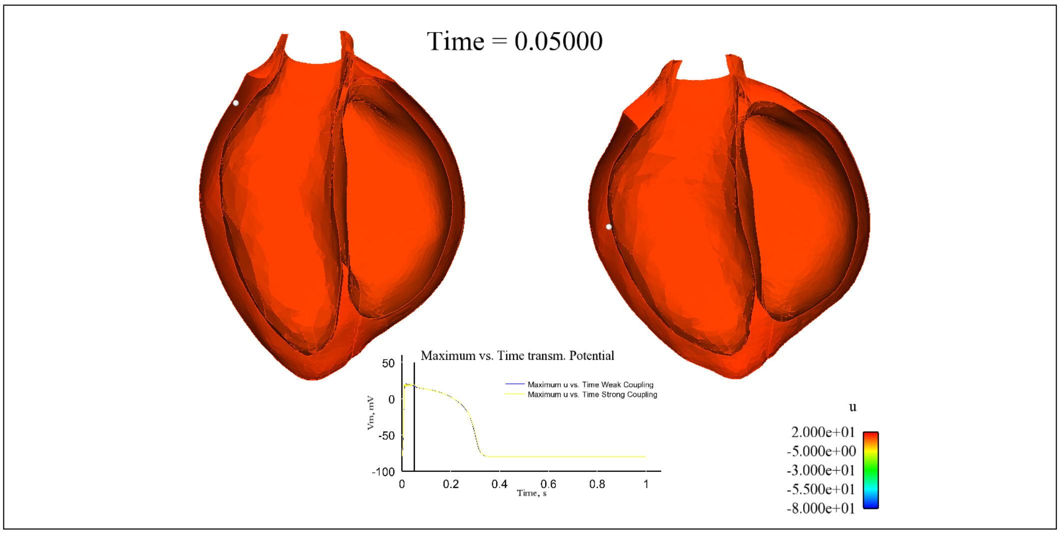

Figure 8.17: Trans-membrane potential for $t = 0.05$ with (right) and without (left) electromechanical feedback. Zygote geometry, heart period $T = 1.0s$. The white dots indicate the maximum trans-membrane potential point locations

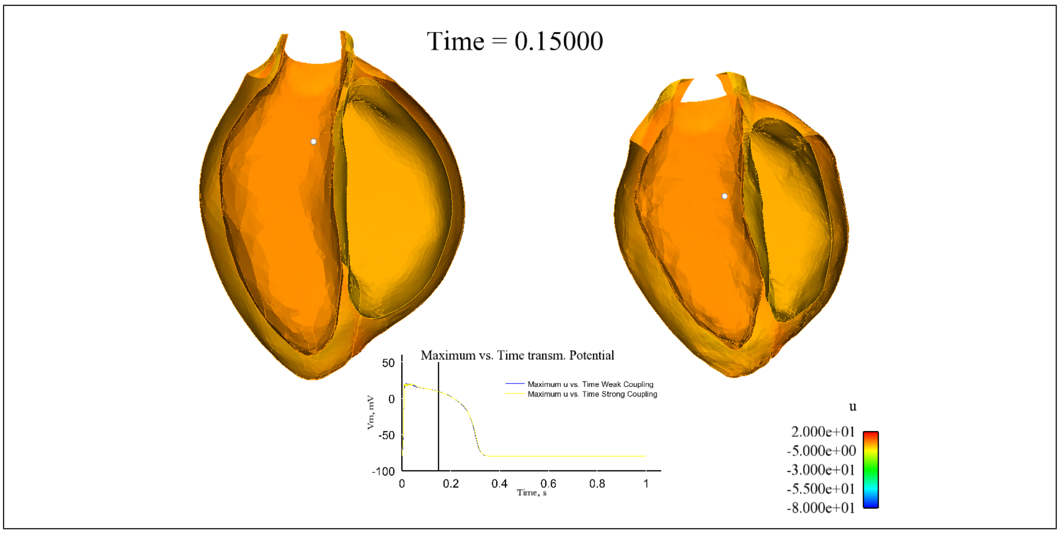

Figure 8.18: Trans-membrane potential for $t = 0.15$ with (right) and without (left) electromechanical feedback. Zygote geometry, heart period $T = 1.0s$. The white dots indicate the maximum trans-membrane potential point locations

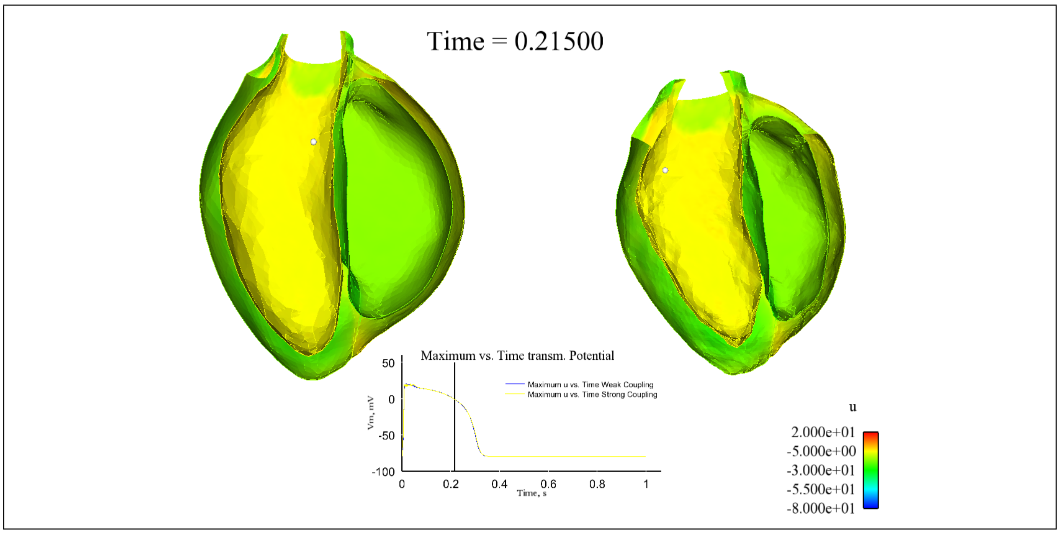

Figure 8.19: Trans-membrane potential for $t = 0.215$ with (right) and without (left) electromechanical feedback. Zygote geometry, heart period $T = 1.0s$. The white dots indicate the maximum trans-membrane potential point locations

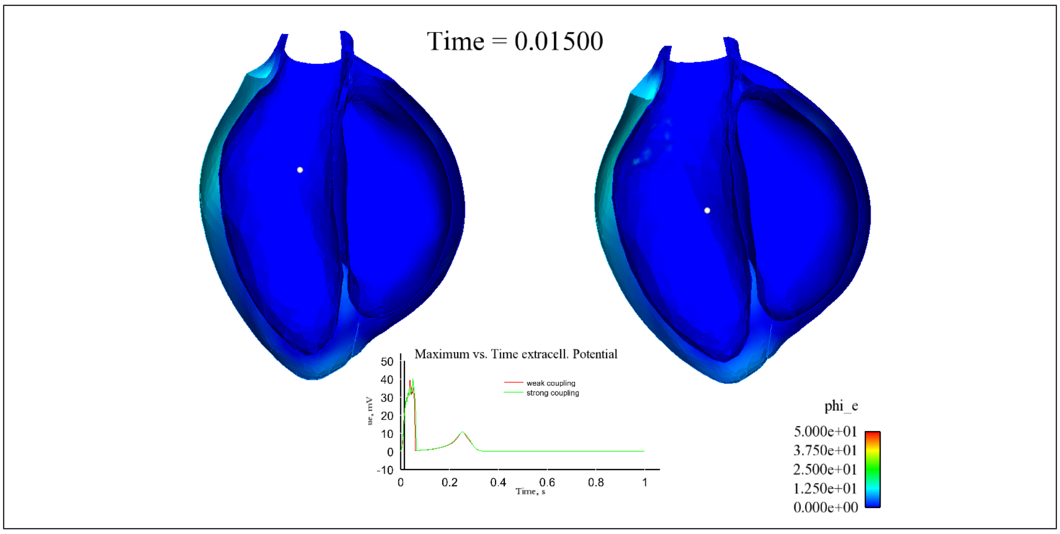

Figure 8.20: Extracellular potential for $t = 0.015$ with (right) and without (left) electromechanical feedback. Zygote geometry, heart period $T = 1.0s$. The white dots (where present) indicate the maximum extracellular potential point locations

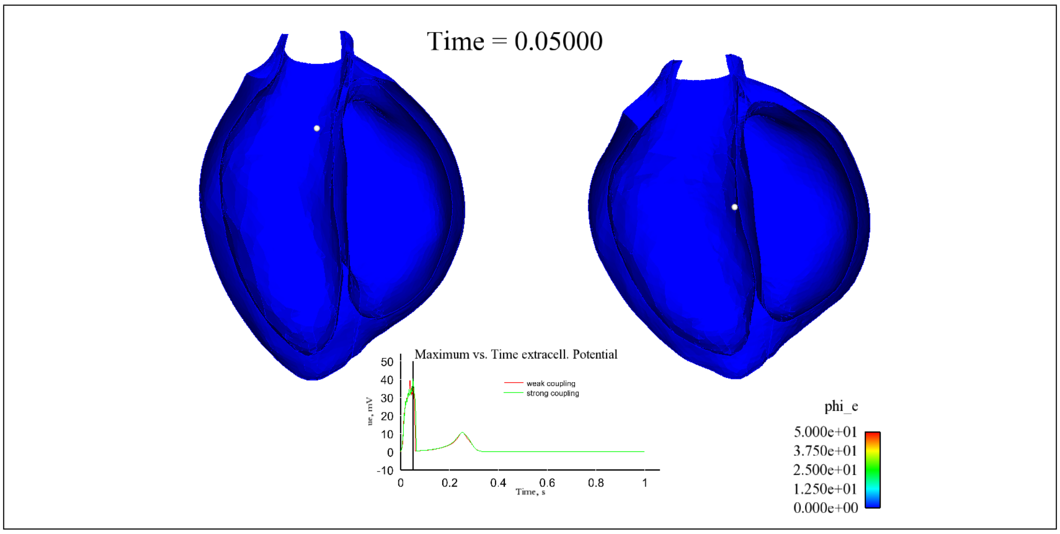

Figure 8.21: Extracellular potential for $t = 0.05$ with (right) and without (left) electromechanical feedback. Zygote geometry, heart period $T = 1.0s$. The white dots (where present) indicate the maximum extracellular potential point locations

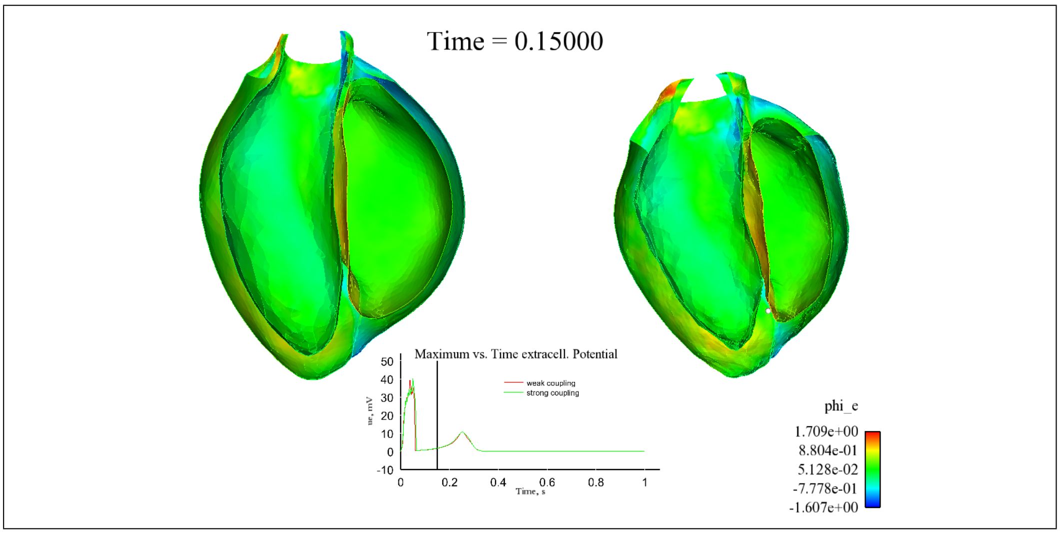

Figure 8.22: Extracellular potential for $t = 0.15$ with (right) and without (left) electromechanical feedback. Zygote geometry, heart period $T = 1.0s$. The white dots (where present) indicate the maximum extracellular potential point locations

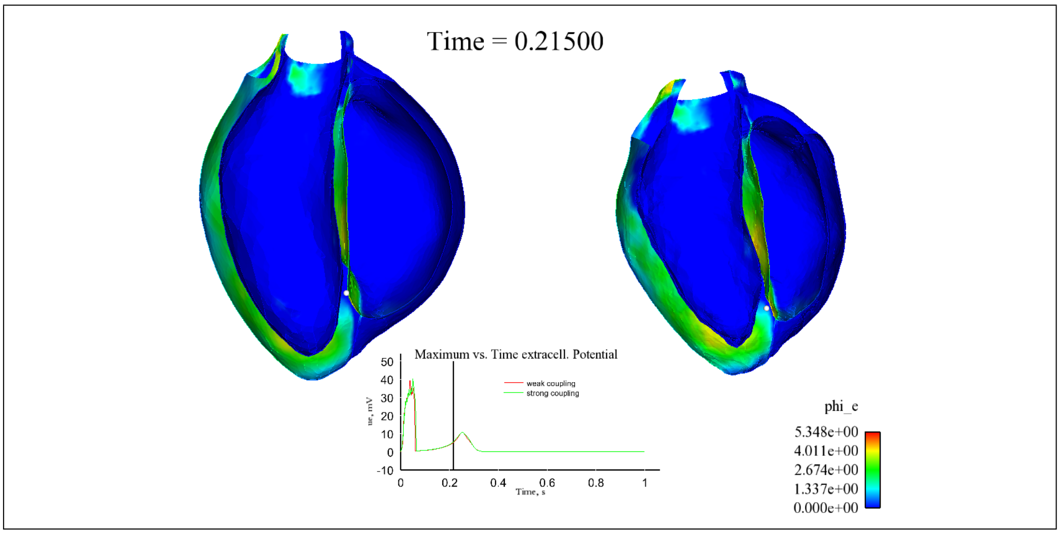

Figure 8.23: Extracellular potential for $t = 0.215$ with (right) and without (left) electromechanical feedback. Zygote geometry, heart period $T = 1.0s$. The white dots (where present) indicate the maximum extracellular potential point locations

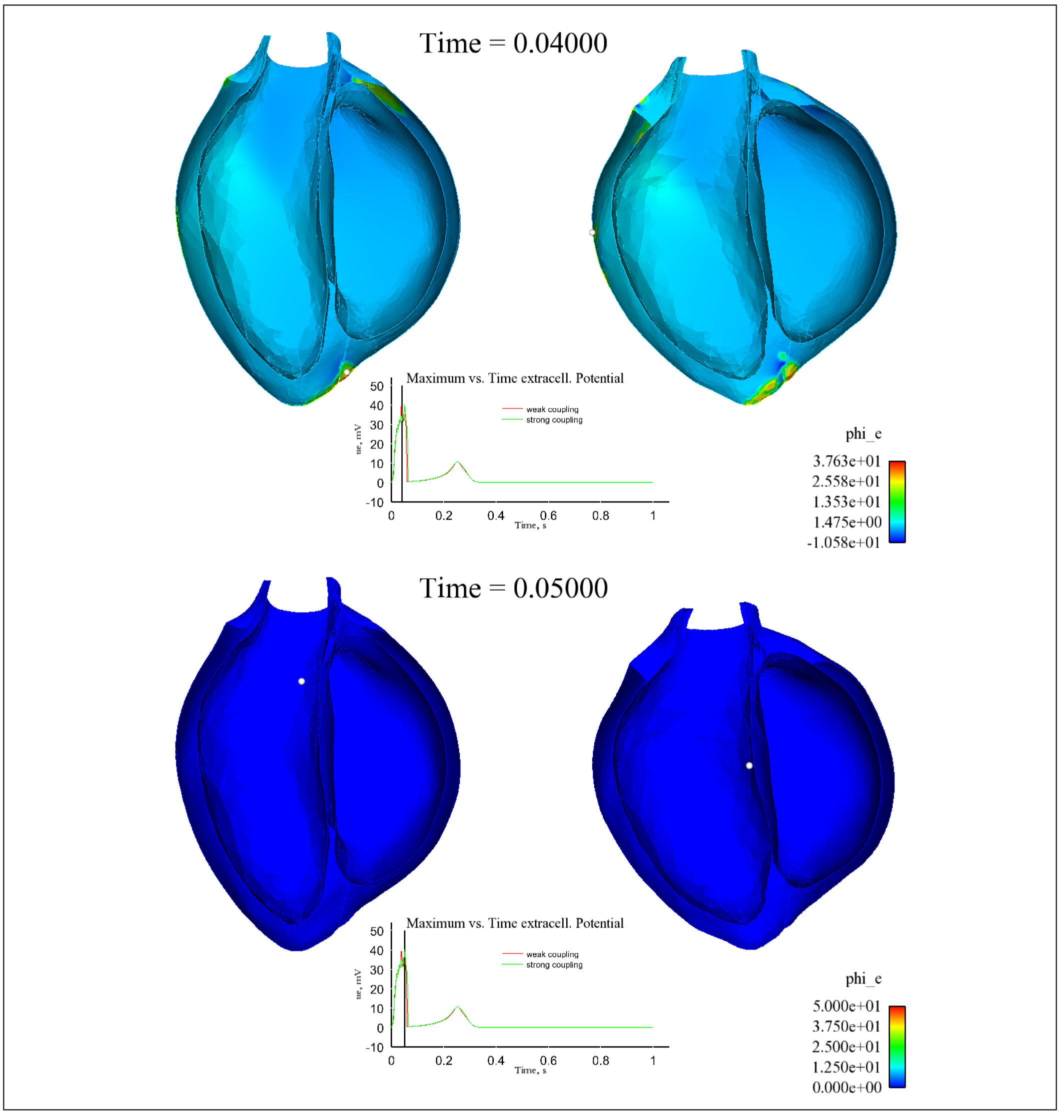

Figure 8.24: Extracellular potential for $t = 0.04s$ and $t = 0.05s$, with (right) and without (left) electromechanical feedback, Zygote geometry and a heart period of $T = 1.0s$. The white dot (where present) indicates the point of maximum transmembrane potential, for each time These two time values correspond to the R peak

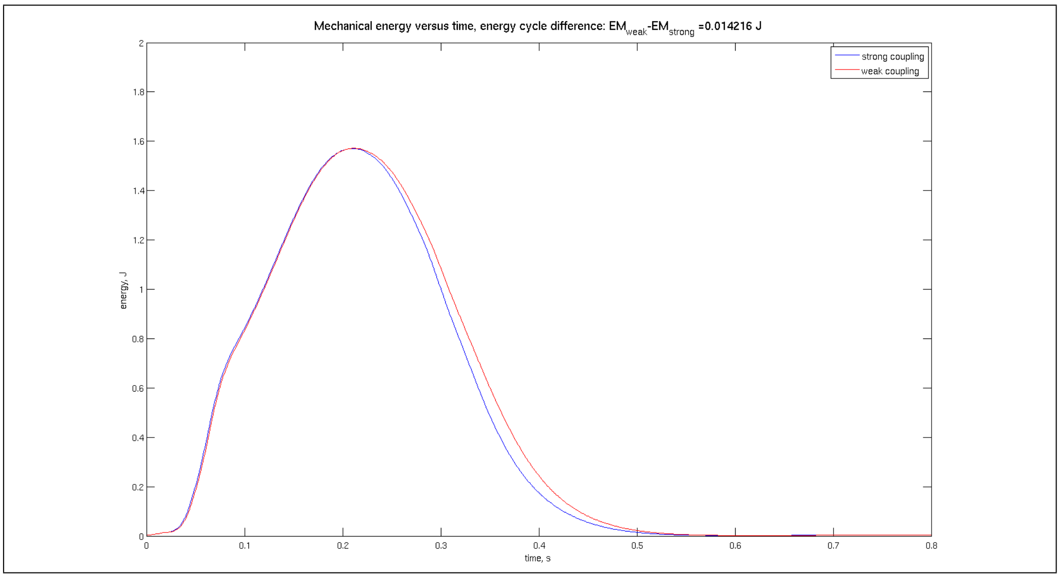

Figure 8.25: Mechanical energy vs time with (blue line) and without (red line) electromechanical feed-back, Zygote geometry, $T = 1s$

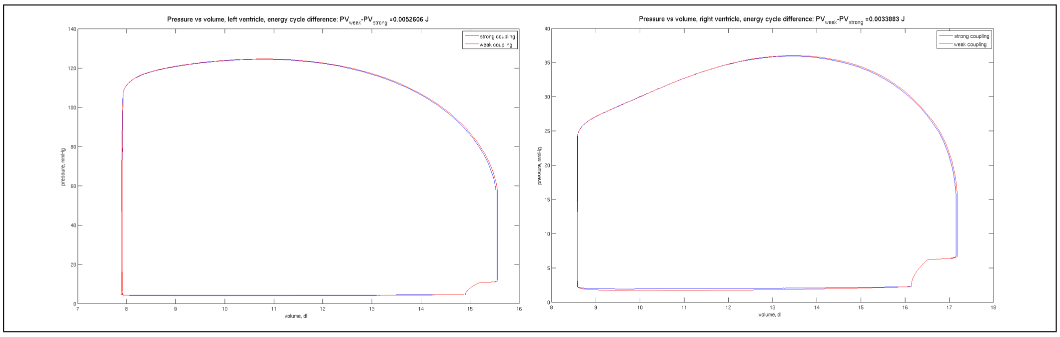

Figure 8.26: Pressure vs volume graph, left ventricle (left) and right ventricle (right) with (blue line) and without (red line) electromechanical feed-back, Zygote geometry, $T = 1s$

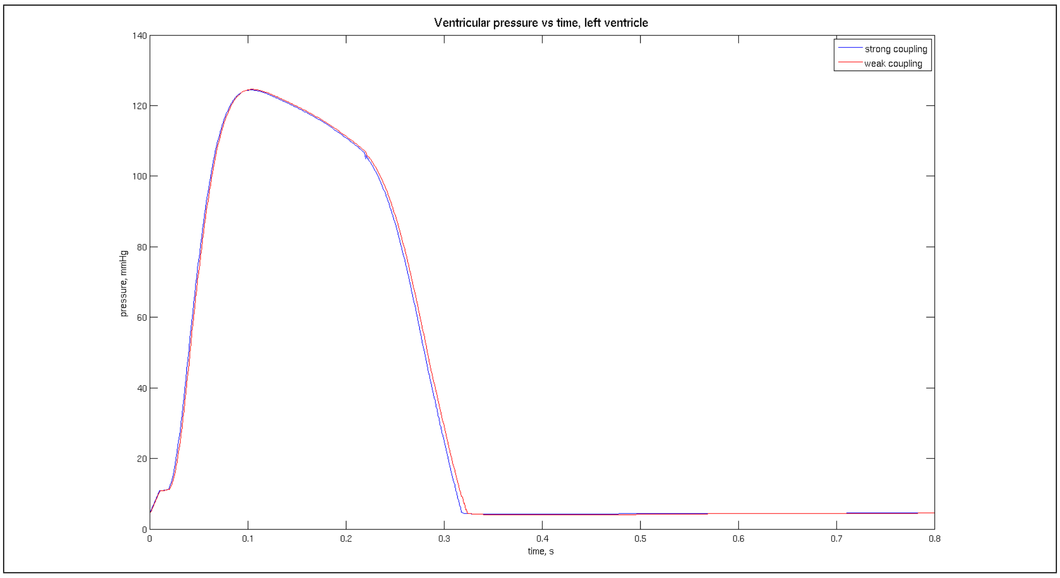

Figure 8.27: Ventricular pressure vs time with (blue line) and without (red line) electromechanical feed-back, Zygote geometry, $T = 1s$

Conclusions

In this thesis we have deeply investigated some aspects related to the mathematical and numerical modeling of the cardiovascular system.

In the first part we have analyzed the problems concerning the unsteady flows in pipe. In this regards, we formulate a new monodimensional scheme capable of reproducing the fluid-structure iteration effects related to the multi-dimensionality of the motion. The base hypothesis is represented by considering the radial variation of pressure and the radial velocity small but not negligible. We have also demonstrate that our model represents a general case of the classical one, by neglecting a posteriori the radial velocity and recasting the classical system. Moreover, we have demonstrated a strict analogy between our model and a classical model where the structure dynamic takes into account of the contribution depending on the time derivative, but with coefficients depending on the fluid-structure interaction. In this regards, we have show the presence of the added mass effect, through a coefficient multiplying a second time derivative of the structure displacement; by numerical examples we have also show the effect on the mechanical response by comparing a solution obtained with the added mass effect and another obtained without the added mass effect.

In the same parts we have determined a new analytical solution dealing with a unsteady flow in a undefined rigid pipe, comprehensive of the transitory effects. We have also demonstrate that with this new solution it is possible to study what happens when the flow is not fully developed to the regime solution and the possibility of estimate the time of assessment. Two examples are introduced, referring as two piratical applications: the former representing the starting of an extracorporeal circulation device, the latter describing the behavior of the flux determined by a sudden decrease of pressure followed by a sudden raise. We have demonstrate that the flow does not adapt instantaneously to the new developed conditions, but needs a time interval depending on the initial conditions.

In the second part we have furnished a stability estimate for the immersed finite element method when the structure is described with a spatial order greater than the first. We have also show that the estimate related to the structural first spatial order is a particular case of our new estimation. Moreover, we have shown for the implicit coupling algorithm that the inertial term could generate instability when the structure density is less than the fluid one. We have also enforced the results with numerical example. In the same section we have also compared the performance between the IFEM method and the ALE method when dealing with immersed structure subjected to large displacement, by considering the number of fixed point sub-iteration needed to achieve convergence at a fixed time step. We have shown that while the ALE computational cost raises when the structural displacement increases, the IFEM computational cost does not depend on the structure displacement.

In the third part we have analyzed the electromechanical feedback when studying the heart electro-physiology. In particular, we have investigated the effects of the heart movement on the electro-cardiogram. We show that the heart deformation has a strong impact on the electrocardiogram graph: indeed , changing the fiber direction when the heart deforms, the electrical wave propagates along preferred directions different from the one of an heart at rest. The major effect related to the electro-mechanical feed-back deals with the T wave, indeed on aVF termination the wave is reversed. Moreover, in II and III the amplitude changes, while in V2 presents a larger amplitude and returns to the reference value without oscillations. Moreover the QRS wave is significantly modified in III, aVL, aVF and V3 terminations. In all the other terminations there are no significant modifications. The changing of the conductivity tensor yields a different distribution for both the transmembrane and the extracellular potentials on the heart; moreover, the transmembrane potential peak concerning the QRS wave is delayed in time when the electromechanical feedback is considered. The same behavior still when changing the heart frequency.

Appendix A

The Womersley solution for the compliant pipe

The structural model adopted for studying the flow field in a compliant pipe is denoted in literature as "independent ring model". The wall of the pipe is modeled as an algebraic membrane without shear stress, similar to the one considered by Koiter [38, 39], which can move only radially.

Following the same procedure described in [51] and neglecting inertial terms, one obtains:

$$
\begin{aligned}
\beta\eta &= f_s \\
\beta &= \frac{h_s E}{(1-\sigma^2)R_0^2}
\end{aligned}
$$

where η is the radial displacement with respect to the reference configuration R_0, E is the Young modulus, σ the Poisson coefficient and h_s is the membrane thickness. The fluid flow field is supposed to be characterized by a general unknown function f of the type:

$$
f(r,z,t) = f_1(r)\exp\left[i\omega\left(t-\frac{z}{c}\right)\right]
$$

where ω is the frequency of pressure changes in time and is c the (unknown) propagation speed of pressure waves in the coupled fluid-structure system. Following the same procedure described in [69], the following radial profiles for the axial and radial velocities are obtained:

$$\begin{aligned}
w_1 &= \frac{A_1}{\rho c} + C_1 \frac{J_0\left(\alpha i^{3/2} y\right)}{J_0\left(\alpha i^{3/2}\right)} \\
u_1 &= \frac{i\omega R_0}{2c}\left(y\frac{A_1}{\rho c} + C_1 \frac{2J_1\left(\alpha i^{3/2} y\right)}{\alpha i^{3/2} J_0\left(\alpha i^{3/2}\right)}\right) \\
y &= \frac{r}{R} \\
\alpha &= R_0\sqrt{\frac{\omega}{\nu}}
\end{aligned}$$

where A_1 is the modulus of the pressure and C_1 is a constant to be determined. In order to couple the fluid-structure system, the following boundary conditions are imposed:

$$v_z = 0 \qquad r = R \tag{A.1}$$

$$v_r = \dot{\eta} \qquad r = R \tag{A.2}$$

$$p = \beta\eta \qquad r = R \tag{A.3}$$

From the condition (A.1) it follows immediately that

$$C_1 = -\frac{A_1}{\rho c}$$

while from (A.2),(A.3) the following system of equations is derived:

$$\frac{i\omega R_0}{2c}\left(1 - F_{10}\left(\alpha\right)\right)\frac{A_1}{\rho c} - i\omega D_1 = 0 \tag{A.4}$$

$$A_1 - \beta D_1 = 0 \tag{A.5}$$

where:

$$\begin{aligned}
\eta &= D_1 \exp\left[i\omega\left(t - \frac{z}{c}\right)\right] \\
F_{10}\left(\alpha\right) &= \frac{2J_1\left(\alpha i^{3/2}\right)}{\alpha i^{3/2} J_0\left(\alpha i^{3/2}\right)}
\end{aligned}$$

In order to have a propagating wave, the system (A.4),(A.5) must be undetermined, in order to admit a nontrivial solution. By imposing the vanishing of its determinant, one finds the following complex propagation speed:

$$c = \sqrt{\frac{\beta\left(1 - F_{10}\left(\alpha\right)\right) R_0}{2\rho}}$$

which takes into account for a pure traveling part by the real value and a dissipative one, by the imaginary value.

The fluid velocity thus becomes:

$$v_z(r, z, t) = \Re\left[\frac{A_1}{\rho c}\left(1 - \frac{J_0\left(\alpha i^{3/2} y\right)}{J_0\left(\alpha i^{3/2}\right)}\right)\exp\left[i\omega\left(t - \frac{z}{c}\right)\right]\right] \tag{A.6}$$

$$v_r(r, z, t) = \Re\left[\frac{i\omega R_0}{2c}\frac{A_1}{\rho c}\left(y - \frac{2J_1\left(\alpha i^{3/2} y\right)}{\alpha i^{3/2} J_0\left(\alpha i^{3/2}\right)}\right)\exp\left[i\omega\left(t - \frac{z}{c}\right)\right]\right] \tag{A.7}$$

$$y = \frac{r}{R}$$

$$\alpha = R_0\sqrt{\frac{\omega}{\nu}}$$

$$c = \sqrt{\frac{\beta\left(1 - F_{10}\left(\alpha\right)\right) R_0}{2\rho}}$$

Repeating the same procedure by replacing ω with $-\omega$ (i.e., by the complex conjugate), summing the two solutions and dividing by two it is possible to find the real solution related to a forcing term of the cosine type.[1]

A.0.3 Radial velocity as a function of wall displacement

In order to determine the radial velocity as a function of the wall displacement, the continuity of radial velocity at interface $r = R$ must be imposed. Denoting by

$$\eta = D_1 \exp\left[i\omega\left(t - \frac{z}{c}\right)\right]$$

the wall displacement, at $r = R$ reads:

$$i\omega D_1 = \frac{i\omega R_0}{2c}\frac{A_1}{\rho c}\left(1 - F_{10}\left(\alpha\right)\right)$$

---

[1] Clearly, with the difference and the division by $2i$ the solution corresponds to a forcing term of the sine type.

so

$$v_r'(r,z,t) = \frac{i\omega D_1}{1-F_{10}\left(\alpha\right)}\left(y - \frac{2J_1\left(\alpha i^{3/2}y\right)}{\alpha i^{3/2}J_0\left(\alpha i^{3/2}\right)}\right)\exp\left[i\omega\left(t-\frac{z}{c}\right)\right]$$

In order to obtain a real number, the complex conjugate solution is evaluated, taking $-\omega$ instead of ω:

$$\overline{v_r'}(r,z,t) = \frac{-i\omega D_1}{1-F_{10}\left(i\alpha\right)}\left(y - \frac{2J_1\left(i\alpha i^{3/2}y\right)}{i\alpha i^{3/2}J_0\left(i\alpha i^{3/2}\right)}\right)\exp\left[-i\omega\left(t-\frac{z}{\overline{c}}\right)\right]$$

clearly, the propagation speed here is the complex conjugate of the previous one. The sum of v_r and $\overline{v_r}$ must be a real number; in particular it should be at $t=0, z=0$, so it is possible to write:

$$\frac{1}{1-F_{10}\left(\alpha\right)}\left(y - \frac{2J_1\left(\alpha i^{3/2}y\right)}{\alpha i^{3/2}J_0\left(\alpha i^{3/2}\right)}\right) = A(y)+iB(y)$$

The radial velocity finally is:

$$\begin{aligned}
v_r(r,z,t) = \frac{1}{2}\Bigg[&(A(y)+iB(y))\left(i\omega D_1\exp\left[i\omega\left(t-\frac{z}{c}\right)\right]\right)\\
&+(A(y)-iB(y))\left(-i\omega D_1\exp\left[-i\omega\left(t-\frac{z}{\overline{c}}\right)\right]\right)\Bigg]\\
&= A(y)\frac{i\omega D_1}{2}\left(\exp\left[i\omega\left(t-\frac{z}{c}\right)\right]-\exp\left[-i\omega\left(t-\frac{z}{\overline{c}}\right)\right]\right)\\
&- B(y)\frac{\omega D_1}{2}\left(\exp\left[i\omega\left(t-\frac{z}{c}\right)\right]+\exp\left[-i\omega\left(t-\frac{z}{\overline{c}}\right)\right]\right)\\
&= A(y)\dot{\eta} - B(y)\omega\eta
\end{aligned}$$

Appendix B

Implementation of the Electro-Mechanical coupling algorithm

A coupled algorithm is generally characterized by the following components:

- Two (or more) codes (in the following called workers) implementing the solvers of each singular subproblem
- A code (in the following called master) managing all the coupling aspects (advancing in time, manipulating the informations arising from the workers, sending the right informations to the workers, checking the convergence of the sub-iterations).
- A message passing interface, capable of exchanging the data between the master and the workers

The interaction between these components is depicted in fig. A-1.

The fixed point functions introduced in section 8.2 correspond to a single data evaluation, as depicted in Figs. A-2, A-3.

Before computing, all the state variables have to be initialized, putting each worker is in a consistent initial state. This is performed as in Fig. A-4.

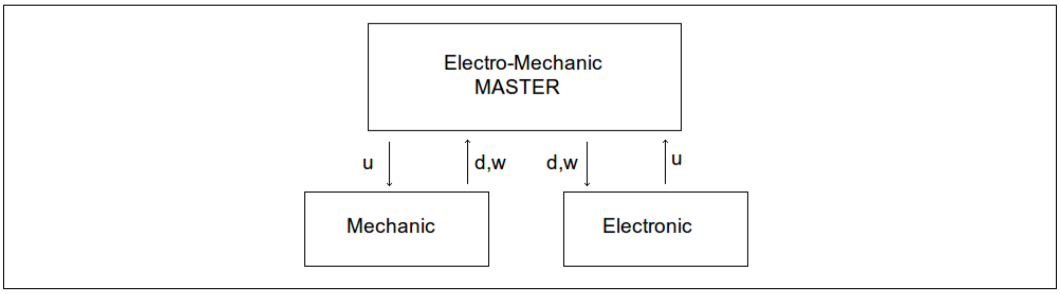

Figure A-1: The coupling algorithm

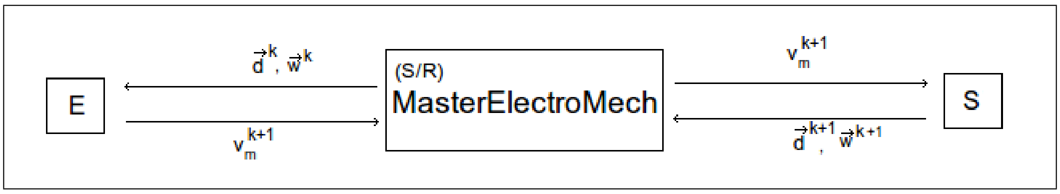

Figure A-2: Gauss-Seidel fixed point function

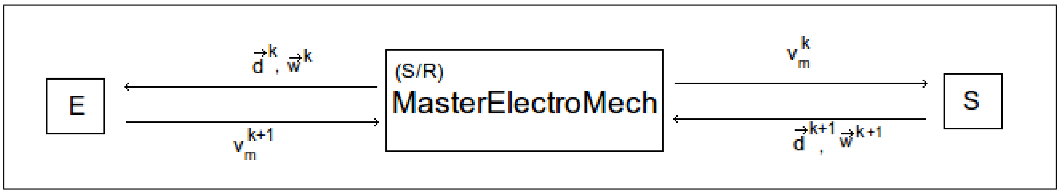

Figure A-3: Jacobi fixed point function

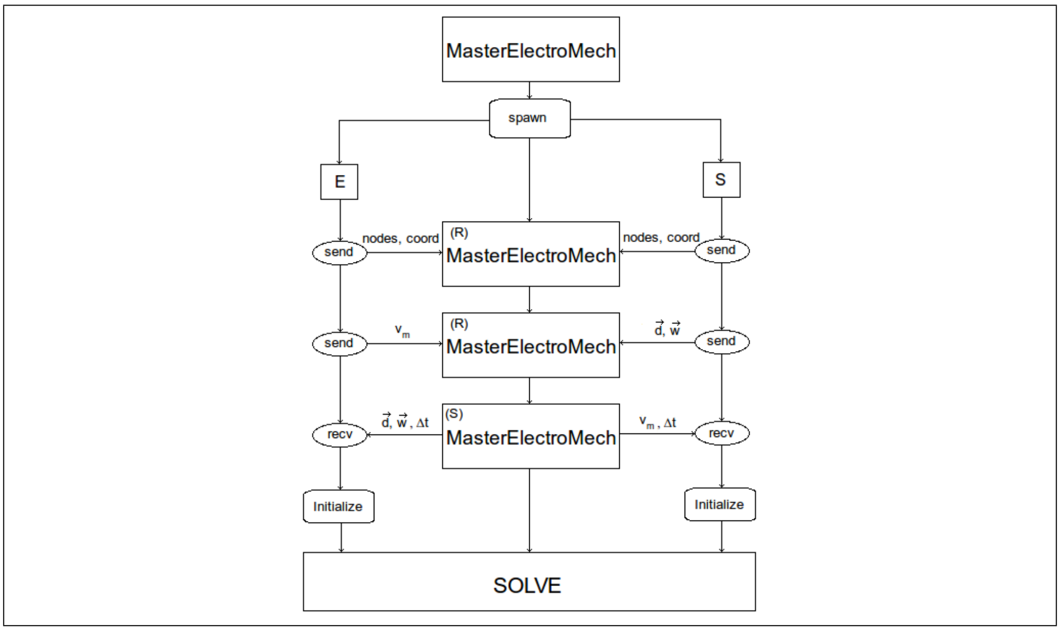

Figure A-4: Initialization of all the variables of the algorithm

At each time step the solution computing is performed as in Fig. A-5 (Gauss-Seidel algorithm); during this, the master has to control the convergence of the global sub-iterations, manipulate the data received by the workers, send the new manipulated variable values to the workers and tell them if advancing in time or not; the updating of the internal variable (the variable of each worker) at a new time step is clearly performed by each worker.

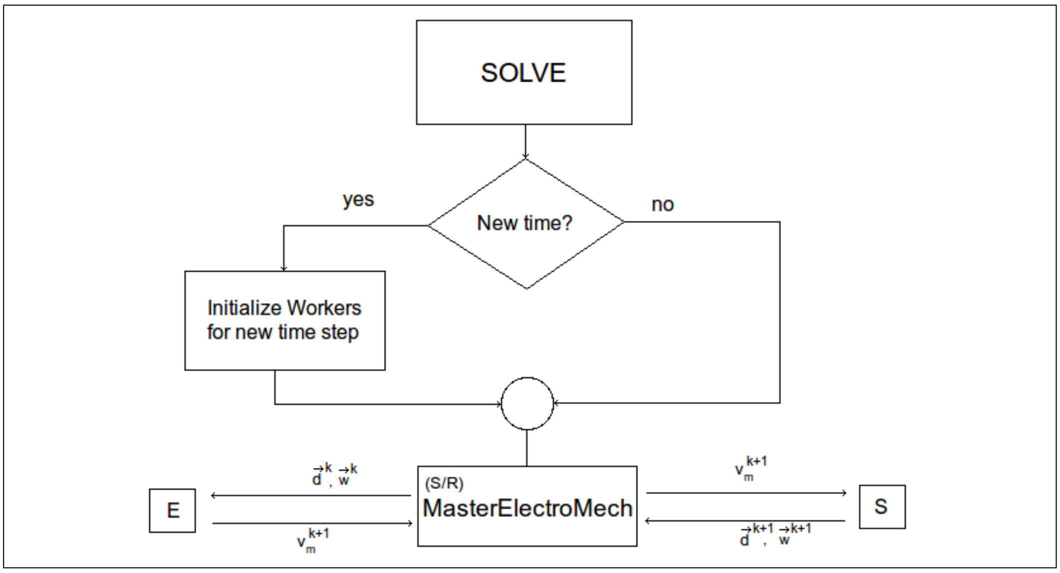

Figure A-5: Iterations

B.1 Different time scales

Structural mechanics and electro-physiology have different characteristic time scale: whereas the former has a characteristic time of $10^{-3}\,s$, the latter has one of typically $10^{-4}s$.

If the problem solution is determined by using a time step of the order of the smaller scale, the computational cost becomes considerable for the huge number of time iterations. Moreover, even though one adopts the smaller time step corresponding to the electro-physiology phenomena, the mechanical solver could require a smaller one during the phase changing.[1]

To overcome these difficulties, both problems are solved by using different time steps, and after re-synchronized at some temporal check-point. This is achieved by changing the structure of the worker, performing a number of internal time iterations (in order to reach the checkpoint) before exchanging the informations with the master. Clearly, at each fixed point sub-iteration the last time window between two subsequent checkpoints has to be re-evaluated.

---

[1] It has be observed that this happens when the aorta valve closes and the heart passes to the isovolumic relaxation.

Bibliography

[1] Life v. URL `www.lifev.org`.

[2] R. Aliev and A. Panfilov. A simple two-variable model of cardiac excitation. *Chaos, Solitons and Fractals*, 7(3):293–301, 1996.

[3] C. Antzelevitch. Cellular basis for the repolarization waves of the ecg. *Ann N. Y. Acad. Sci*, 1080:268–281, 2006.

[4] J. Bestel. *Modèle différentiel de la contraction musculaire contrôlée. Application au système Mo- dèle différentiel de la contraction musculaire contrôlée. Application au système cardio-vasculaire*. PhD thesis, University Paris IX Dauphine, 2000.

[5] J. Bestel, F. Clément, and M. Sorine. *A biomechanical model of muscle contraction*, volume 2208 of *Lecture Notes in Computer Science*. Springer-Verlag, 2001.

[6] D. Boffi and L. Gastaldi. The immersed boundary method: a finite element approach. In *Proceeding of the Second MIT Conference on Computational Fluid and Solid Mechanics*, volume 2, pages 1263–1266. Elsevier, 2003.

[7] D. Boffi, L. Gastaldi, and L. Heltai. A finite element approach to the immersed boundary method. *Comp. & Struct.*, 81(8-11):491–501, 2003.

[8] D. Boffi, L. Gastaldi, and L. Heltai. Stability results and algorithmic strategies for the finite element approach to the immersed boundary

method. In *Proceeding of the Sixth European Conference on Numerical Mathematics and Advanced Applications*, pages 557–566. Springer-Verlag, 2005.

[9] D. Boffi, L. Gastaldi, and L. Heltai. Stability results for the finite element approach to the immersed boundary method. In K. Bathe, editor, *Proceeding of the Third MIT Conference on Computational Fluid and Solid Mechanics*, pages 93–96, 2005.

[10] D. Boffi, L. Gastaldi, and L. Heltai. Numerical stability of the finite element immersed boundary method. *Math. Mod. Meth. Appl. Sci.*, 17 (10):1479–1505, 2007.

[11] D. Boffi, L. Gastaldi, L. Heltai, and C. S. Peskin. On the hyper-elastic formulation of the immersed boundary method. *Comp. Methods App. Mech. Eng.*, 197(25-28):2210–2231, 2008.

[12] M. Boulakia, S. Cazeau, M. A. Fernandez, J. F. Gerbeau, and N. Zemzemi. Matematical modeling of the electrocardiograms: A numerical study. Technical Report RR-6977, INRIA, 2009.

[13] F. Brezzi and M. Fortin. *Mixed and hybrid finite element methods.* Springer-Verlag New York, Inc., New York, NY, USA, 1991. ISBN 0-387-97582-9.

[14] M. L. Buist and A. J. Pullan. The effect of torso impedance on epicardial and body surface potentials: A modeling study. *EEE Trans. Biomed. Eng.*, 50(7):816–824, 2003.

[15] P. Causin, J. F. Gerbeau, and F. Nobile. Added-mass effect in the design of partitioned algorithms for ïňĆuid–structure problems. *Comp. Methods App. Mech. Eng.*, 194:4506–4527, 2005.

[16] D. Chapelle, F. Clément, F. Génot, P. L. Tallec, M. Sorine, and J. Urquiza. *A physiologically-based model for the active cardiac muscle*,

volume 2230 of *Lectures Notes in Computer Science*. Springer-Verlag, 2001.

[17] P. G. Ciarlet and G. Geymonat. *Sur les lois de comportement en élasticité non linéaire*, volume 295 of *Serie II*, pages 423–426. C.R.A.S., 1982.

[18] J. Clements, J. Nenonen, P. Li, and B. M. Horacek. Activation dynamics in anisotropic cardiac tissue via decoupling. *Annals of Biomedical Engeneering*, 32(7):984–990, 2004.

[19] P. Colli-Franzone, P. L. F., and B. Taccardi. *Effects of the anisotropy and transmural heterogeneity on the T-wave polarity of simulated electrocardiograms*, volume 5528 of *Functional Imaging and Modeling of the Heart*, pages 513–523. Springler-Verlag, lecture notes in computer science edition, 2009.

[20] C. E. Conrath and T. Opthof. Ventricular repolarization: an overview of (patho)physiology, sympathetic effects and genetic aspects. *Prog. Biophys. Mol Biol.*, 92(3):269–307, Nov. 2006.

[21] D. Di-Francesco and D. Noble. Simulations of ionic currents and concentration changes. *Phil. Trans R. Soc. Lond.*, pages 353–398, 1985.

[22] J. Donea. An arbitrary lagrangian eulerian finite element method for transient dynamic fluid-structure interaction. *Comp. Methods App. Mech. Eng.*, 33:689–723, 1982.

[23] J. Donea. Arbitrary lagrangian eulerian method. *In Computational Methods for Transient Analysis*, 1 of Computational Method in Mechanics. North Holland, Elsevier, 1983.

[24] R. Fitzhugh. Impulses and physiological states in theoretical models of nerve membrane. *Biophys. Journal*, 1:445–465, 1961.

[25] L. Formaggia and F. Nobile. A stability analisys for the arbitrary lagrangian eulerian formulation with finite elements. *East-West J. Num Math*, 7:105–132, 1999.

[26] L. Formaggia, J. F. Gerbeau, F. Nobile, and A. Quarteroni. Numerical treatment of defective boundary conditions for the Navier-Stokes equation. *SIAM J. Num. Anal.*, 40(1):376–401, 2002.

[27] L. Formaggia, D. Lamponi, and A. Quarteroni. One-dimensional models for blood flow in arteries. *Journal of Engeneering. Mathematics*, 47:251–276, 2003.

[28] L. Formaggia, A. Moura, and F. Nobile. On the stability of the coupling of 3d and 1d fluid-structure interaction models for blood flow simulations. Technical report, MOX, Nov. 2006.

[29] M. R. Franz, K. Bargheer, W. Rafflenbeul, A. Haverich, and P. R. Lichtlen. Monophasic action potential mapping in human subjects with normal electrocardiograms: direct evidence for the genesis of the t wave. *Circulation*, 75(2):379–386, 1987.

[30] J. F. Hale, D. A. McDonald, and J. R. Womersley. Velocity profiles of oscillating arterial flow, with some calculations of viscous drag and the reynolds number. *Journal of Physiology*, 128:629–640, 1955.

[31] F. Hecht, O. Pironneau, A. Le-Hyaric, and K. Ohtsuka. Freefem++. URL `www.freefem.org`.

[32] L. Heltai. On the stability of the finite element immersed boundary method. *Comp. & Struct.*, 86:598–617, 2008.

[33] J. G. Heywood and R. Rannacher. Finite element approximation of the nonstationary Navier-Stokes problem. I. Regularity of the solutions and second-order error estimates for spatial discretization. *SIAM J. Num. Anal.*, 19(2):275–311, 1982.

[34] T. Higuchi and Y. Nakaya. T wave polarity related to the repolarization process of epicardial and endocardial ventricular surfaces. *American Heart Journal*, 108(2):290–295, 1984.

[35] T. J. R. Huges, W. K. Liu, and T. K. Zimmermann. Lagrangian-eulerian finite element formulation for incompressible viscous flows. *Comp. Methods App. Mech. Eng.*, 29(3):329–349, 1981.

[36] A. F. Huxley. *Muscle Structure and theories of contraction*, volume 7 of *Progress in biophysics and biological chemistry*, pages 255–318. Pergamon press, 1957.

[37] *An active pulse transmission line stimulating nerve axon*, 1962. IRE.

[38] W. Koiter. On the foundations of the linear theory of thin elastic shells. *Proc. Kon. Neder. Akad Wet*, B73:169–195, 1970.

[39] W. Koiter. On the non-linear theory of thin elastic shells. *Proc. Kon. Neder. Akad Wet*, B69:1–54, 1996.

[40] W. Krassowska and J. C. Neu. Homogenization of syncitial tissues. *CRC Crit. Rev. Biomed. Eng.*, 21(2):137–199, 1993.

[41] W. Krassowska and J. C. Neu. Effective boundary conditions for syncitial tissues. *IEEE Trans. Biomed. Eng*, 41(2):137–199, 1994.

[42] G. T. Lines. *Simulating the electrical activity in the heart.* PhD thesis, University of Oslo, 1999.

[43] G. T. Lines, M. L. Buist, P. Grottum, A. J. Pullan, J. Sundnes, and A. Tveito. Mathematical models and numerical methods for the forward problem in cardiac electrophysiology. *Comput. Visual. Sci.*, 5(4):215–239, 2003.

[44] W. K. Liu, D. W. Kim, and S. Tang. Mathematical foundations of the immersed finite element method. *J. Comput. Mech.*, 39(3):211–222,

2007. ISSN 0178-7675. doi: http://dx.doi.org/10.1007/s00466-005-0018-5.

[45] J. Malmivuo and R. Plonsey. *Bioelectromagnetism. Principles and applications of bioelectric fields.* Oxford University press, New York, 1995.

[46] D. A. McDonald. *Blood Flow in Arteries.* Edward Arnold Publishers, 1974.

[47] C. C. Mitchell and D. G. Schaeffer. A two-current model for the dynamics of cardiac membrane. *Bulletin Math. Bio*, 65:767–793, 2003.

[48] P. Moireau. *Assimilation de données par ïňĄltrage pour les systèmes hyperboliques du second ordre. Applications à la mécanique cardiaque.* PhD thesis, École doctorale de lâĂŹÉcole Polytechnique, 2008.

[49] M. Mourad. *Description topologique de l'architecture fibreuse et modélisation mécanique du myocarde.* PhD thesis, MSTI de l'INPG. 71, 2003.

[50] F. Nobile. *Numerical approximation of Fluid Structure Interaction problems with application to haemode Lausannedynamics.* PhD thesis, Ecole Polytechnique Fédérale de Lausanne, 2001.

[51] F. Nobile and C. Vergara. An effectvive fluid-structure interaction formulation for vascular dynamics by generalized robin conditions. *SIAM J. Sci. Comput.*, 30(2):731–763, 2008.

[52] E. Page. Cat heart muscle in vitro. part iii. the extracellular space. *J. Gen. Physio.*, 46(1):201–213, 1962.

[53] C. S. Peskin. The immersed boundary method. *Acta Numerica*, 11: 479–517, 2002.

[54] C. Pierre. *Modélisation et simulation de l'activité électrique du coeur dans le thorax, analyse numérique et méthodes de volumes finis.* PhD thesis, LAboratoire J. Leray, Université de Nantes, 2005.

[55] M. Potse, B. Dubé, and R. M. Gulrajani. Ecg simulations with realistic human membrane, heart and thorso model. In *Proceedings of the 25th Annual International Conference of the IEEE EMBS*, pages 70–73, 2003.

[56] M. Potse, B. Dubé, J. Richer, A. Vinet, and R. M. Gulrajani. A comparaison of monodomain and bidomain reaction-diffusion models for action potential propagation in the human heart. *Biomedical Engineering, IEE Transactions on*, 53(12):2425–2435, Dec. 2006.

[57] M. Potse, B. Dubé, and A. Vinet. Cardiac anisotropy in boundary element models for the electrocardiogram. *Med. Biol. Eng Comput*, 2009. doi: 10.1007/s11517-009-0472-x.

[58] A. J. Pullan, M. L. Buist, and L. K. Cheng. Mathematically modelling of the electrical activity of the heart: From cell to body surface and back again. *World Scientific Publishing Co. Pte. Ltd.*, 2005.

[59] A. Quarteroni and L. Formaggia. Mathematical modeling and numerical simulation of the cardiovascular system. *in Modeling of Living Systems, Handbook of Numerical Analysis Series (P.G. Ciarlet and J.L. Lions Eds), Elsevir, Amsterdam 2002*, 2002.

[60] O. H. Schmitt. Biological information processing using the concept of interpenetrating domains. In K. N. Leibovic, editor, *Information Processing in the Nervous System*. Springler-Verlag, 1969.

[61] M. Sermesant, P. Moireau, O. Camara, J. Sainte-Marie, R. Andriantsimiavona, R. Cimrman, D. H. Hill, D. Chapelle, and R. Razavi. Cardiac functions estimation from mri using a heart model and data assimilation: advances and difficulties. *Med. Image Anal.*, 10(4):642–656, Dec. 2006.

[62] D. D. Streeter. Gross morphology and ïňĄber geometry of the heartd. In R. Berne, N. Sperelakis, and S. Geiger, editors, *Handbook Physiology.*

The cardiovascular system. Am. Phys. Soc. gy. The cardiovascu Williams Wilkins, 1979.

[63] J. Sundnes, G. T. Lines, X. Cai, B. F. Nielsen, K. A. Mardal, and A. Tveito. *Computing the electrical activity of the heart*, volume 1 of *Monographs in computational Science and Engineering*. Springler-Verlag, 2006.

[64] C. Taylor and P. Hood. A numerical solution of the navier-stokes equations using the finite element technique. *Computers & Fluids*, 1(1):73–100, 1973. ISSN 0045-7930. doi: DOI: 10.1016/0045-7930(73)90027-3. URL `http://www.sciencedirect.com/science/article/B6V26-480TTGH-3T/2/7adfcd863`

[65] L. Tung. *A bi-domain model for describing the ischemic myocardial D-C potentials*. PhD thesis, MIT, 1978.

[66] E. J. Vigmond and C. Clements. Construction of a computer model to investigate sawtooh effects in Purkinje system. *IEEE Trans. Biomed. Eng*, 54(3):389–399, 2007.

[67] X. Wang and W. K. Liu. Extended immersed boundary method using fem and rkpm. *Comp. Methods App. Mech. Eng.*, 193(12-14):1305–1321, 2004.

[68] J. R. Womersley. Method for the calculation of velocity, rate of flow and viscous drag in arteries when the pressure gradient is known. *Journal of Physiology*, 127:553–563, 1955.

[69] J. R. Womersley. Oscillatory motion of a viscous liquid in a thin-walled elastic tube. I. the linear approximation for long waves. *Philosophical Magazine*, 46:199–221, 1955.

[70] G. X. Yan and C. Antzelevitch. Cellular basis for the normal t wave and the electrocardiographic manifestations of the long-q t syndrome. *Circulation*, 98:1928–1936, 1998.

[71] G. H. Zahalac. A distribution-moment approximation for kinetic theories of muscular contraction. *Mathematical Biosciences*, 114:55–89, 1981.

[72] N. Zemzemi. *Etude théorique et numérique de l'activité électrique du coeur: Applications aux électrocardiogrammes*. PhD thesis, Université Paris-sud 11, Dec. 2009.

[73] L. Zhang, A. GerstenBerger, X. Wang, and W. K. Liu. Immersed finite element method. *Comp. Methods App. Mech. Eng.*, pages 1305–1321, 2004.